Measurement of the top quark pair production cross section with the ATLAS experiment at $\sqrt{s} = 7\,\text{TeV}$

Volker Vorwerk

Institut de Física d'Altes Energies
Universitat Autònoma de Barcelona
Departament de Física
Edifici Cn E-08193 Bellaterra (Barcelona)

May 10, 2011

supervised by
Aurelio Juste Rozas
Institut de Física d'Altes Energies
Edifici Cn E-08193 Bellaterra (Barcelona)

Abstract

The production cross section of top quark pairs with a semi-leptonic final state was measured in proton-proton collisions at $\sqrt{s} = 7\,\text{TeV}$ with the ATLAS experiment at the LHC.

A first measurement was performed with data corresponding to an integrated luminosity of $2.9\,\text{pb}^{-1}$, collected during the early running phase of the LHC. Large efforts were made in order to cope with the low statistics and the restricted understanding of the detector at the early stage of the experiment. Events with exactly one electron or muon, high missing transverse energy and at least three jets were analyzed. Flavor tagging algorithms were used to further increase the purity of the signal in the final selection sample, requiring at least one jet to originate from a b quark. The production cross section was extracted from a maximum likelihood fit to the invariant mass spectrum of the hadronically decaying top quark candidate, yielding $130 \pm 44\,(\text{stat.})\,^{+34}_{-28}\,(\text{syst.})\,^{+16}_{-13}\,(\text{lumi.})\,\text{pb}$.

The analysis was improved using the complete data set recorded with the ATLAS detector in 2011, corresponding to an integrated luminosity of $35\,\text{pb}^{-1}$. An improved fitting method was used that allowed the data to constrain and reduce the impact of the systematic uncertainties on the measurement. In order to achieve this the data was categorized into 18 exclusive channels depending on the lepton flavor, the jet multiplicity, and the number of heavy-flavor tagged jets. In the improved analysis a top quark pair production cross section of $156\,^{+20}_{-18}\,(\text{stat.+syst.}) \pm 5\,(\text{lumi.})\,\text{pb}$ was measured, representing one of the most precise measurements to date corresponding to $35\,\text{pb}^{-1}$.

Contents

1 Introduction **1**

2 The Standard Model of Particle Physics **4**
2.1 Gauge Theories 4
2.2 The Electroweak Interaction 5
2.3 The Strong Interaction 9
2.4 The Higgs Mechanism 11
2.5 Open Questions of the Standard Model 13

3 Top Quark Physics **16**
3.1 The Top Quark 16
3.1.1 Indirect Evidence 16
3.1.2 Indirect Constrains on the Top Quark Mass 18
3.1.3 Observation of the Top Quark 19
3.1.4 Top Quark Properties 20
3.2 Top Quark Physics at the LHC 22
3.2.1 Top Quark Production 23
3.2.2 Top Quark Decay 28
3.2.3 Backgrounds 31
3.2.4 Event Generation 34
3.2.5 Monte Carlo Samples 38

4 The Experimental Setup **41**
4.1 The Injector Chain 41
4.2 The LHC 42
4.3 The ATLAS Detector 44
4.3.1 Interaction of Particles with Matter 46
4.3.2 Inner Detector 47
4.3.3 Calorimeters 50
4.3.4 Muon Spectrometer 57
4.3.5 Magnet System 60
4.3.6 The Forward Detectors 60
4.3.7 Trigger and Data Acquisition 62

4.3.8 Detector Simulation 65

5 Event Reconstruction and Object Identification 67
5.1 Track Identification 67
5.2 Vertex Reconstruction 68
5.3 Electrons and Photons 68
5.4 Muons 69
5.4.1 Standalone Muons 69
5.4.2 Combined Muons 70
5.4.3 Tagged Muons 70
5.5 Jets 70
5.5.1 Jet Energy Calibration 72
5.5.2 Jet Energy Resolution 75
5.5.3 b-jet Identification 75
5.6 Missing Transverse Energy 77

6 Data Streams and Trigger Selection 80

7 Evidence for $t\bar{t}$ Production at $\sqrt{s}$=7 TeV 83
7.1 Physics Object Definitions 84
7.1.1 Electrons 84
7.1.2 Muons 85
7.1.3 Jets and Flavor Tagging 86
7.1.4 Missing Transverse Energy 86
7.2 Event Selection 86
7.2.1 Selection Requirements 86
7.2.2 Monte Carlo Correction Factors 87
7.2.3 Signal Selection Efficiency 95
7.3 Background Estimation 95
7.3.1 Estimation of the QCD Multijet Background 95
7.3.2 Estimation of the W+jets Background 109
7.4 Selected Events 110
7.5 Top Quark Mass Reconstruction 114
7.5.1 Algorithm and Performance 114
7.5.2 Estimation of the QCD Multijet Background Shape . 119
7.5.3 Estimation of the W+jets Background Shape 121
7.6 The Fit Method 123
7.6.1 Systematic Uncertainties 125
7.6.2 Expected Performance 131
7.7 Results 133
7.7.1 Measured Uncertainties 134
7.7.2 Template Fit Results 135
7.7.3 W+jets Comparison to Other Studies 135
7.7.4 Significance Calculation 138

7.8 Summary 140

8 Measurement of the $t\bar{t}$ Cross Section. 142
8.1 Physics Object Definition 143
8.1.1 Electrons 143
8.1.2 Muons 143
8.1.3 Jets and Flavor Tagging 144
8.1.4 Missing Transverse Energy 144
8.2 Event Selection and Event Yields 144
8.3 Systematic Uncertainties 146
8.4 Profile Likelihood Fit 151
8.4.1 Method 151
8.4.2 Analysis Strategy 153
8.5 Results 154
8.5.1 Expected Performance of the Profile Likelihood Fit . . 154
8.5.2 Cross Section Measurement 159
8.5.3 Comparison Between Measurements 163
8.6 Summary 168

9 Summary and Prospects 171

A Parton Density Functions 173

B Luminosity 176

C Monte Carlo Samples 177

D Expected Uncertainties 184

E Measured Uncertainties 186

F Control Plots and Correlation Matrix. 188

Bibliography 197

Acknowledgement 205

List of Figures

2.1 Measurements of the 18 free parameters of the Standard Model. 14

3.1 Virtual top quark loops contributing to W/Z propagators. . . 18
3.2 Virtual Higgs boson loops contributing to W/Z propagators. 19
3.3 Comparison of the indirect constrains on m_W and m_t. 20
3.4 Trend of the limits on the top quark mass or its measurements. 21
3.5 Total hadronic cross section with variation of μ_f and μ_r. . . . 24
3.6 Factorization for the hard-scattering cross sections. 24
3.7 The LO Feynman diagrams for top quark pair production. . . 25
3.8 Different measurements of the top quark cross section. 26
3.9 The Feynman diagrams for the single top quark production. . 27
3.10 Feynman diagram for semi-leptonic decay of a top quark pair. 30
3.11 Angular correlation in the decay of a spin up top quark. . . . 31
3.12 Cross sections and event rates versus center-of-mass energy. . 32
3.13 Feynman diagram for W boson production with jets. 33
3.14 Feynman diagram of a dijet event. 33
3.15 Feynman diagram for the production of two W bosons. . . . 34
3.16 $pp \to t\bar{t}H$ with ISR, FSR, underlying events, hadronization. . 35
3.17 Summary of the final +jets sample composition. 40

4.1 The injection complex of the LHC. 42
4.2 The underground structure of the LHC. 43
4.3 The sectional diagram of the ATLAS Detector. 45
4.4 Sectional sketch of particles crossing the different sub-detectors. 46
4.5 Cut-away view of the ATLAS inner detector. 48
4.6 View of the active sections of the inner detector. 48
4.7 A cut-away view of the ATLAS calorimeter. 51
4.8 Detector material in units of radiation length X_0 versus $|\eta|$. . 53
4.9 Detector material in units of interaction λ length versus $|\eta|$. . 54
4.10 Schematically drawing of one of the 64 wedges of the TileCal. 55
4.11 Schematically $|\eta| - z$ view of the HEC. 56
4.12 Cross section of the barrel muon spectrometer. 59
4.13 Peak delivered instantaneous luminosity. 63

4.14 Block diagram of the ATLAS TDAQ system. 63

5.1 Flow chart of the jet reconstruction. 71
5.2 Jet multiplicity VS. $L/\sigma(L)$ and tracks per secondary vertex. 78

6.1 Cumulative luminosity delivered and recorded by ATLAS. . . 81

7.1 Distribution of probe muons used for trigger efficiencies. . . . 89
7.2 Reconstruction and identification efficiency for electrons. . . . 90
7.3 Distribution of probe muons for reconstruction efficiencies. . . 91
7.4 Distributions of muon identification efficiencies. 92
7.5 $\mathrm{SF}_{\mathrm{flavor}}$ as function of p_T of the tagged jet. 94
7.6 ϵ_{real} as a function of $|\eta|$. 99
7.7 ϵ_{fake} as a function of $|\eta|$. 100
7.8 Distribution with estimated QCD after all full selection. . . . 101
7.9 Distribution of data events and background with two jets. . . 102
7.10 Distributions with 1, 2 jets, with and without triangular cut. 103
7.11 Transverse muon impact parameter significance. 104
7.12 QCD events vs jet multiplicity with Matrix Method. 105
7.13 Fit results and control plots for the anti-electron model. . . . 107
7.14 Fit results for the jet-electron model. 108
7.15 Jet multiplicity without and with b-tag. 113
7.16 p_T, E_T^{miss}, and $m(W)_T$ for =3 jets, untagged. 115
7.17 p_T, E_T^{miss}, and $m(W)_T$ for =3 jets, b-tagged. 116
7.18 p_T, E_T^{miss}, and $m(W)_T$ for ≥ 4 jets, untagged. 117
7.19 p_T, E_T^{miss}, and $m(W)_T$ for ≥ 4 jets, b-tagged. 118
7.20 3-jet mass for Matrix Method and inverted-lepton selection. . 120
7.21 Per-jet TRF in the e+jets and μ+jets channels. 121
7.22 H_T and three-jet mass distributions. 122
7.23 3-jet mass shape for W-jets, data estimation and MC. 123
7.24 Template distributions used in the fit. 124
7.25 m_{jjj}, leading jet and second jet p_T for different W+jets MCs. 129
7.26 Three-jet mass distribution for MC and variations. 130
7.27 Linearity and pull for $k_{t\bar{t}}$ and $k_{W+\mathrm{jets}}$. 132
7.28 Three-jet mass for data and prediction (separate channels). . 136
7.29 Three-jet mass for data and prediction (channel combination). 137
7.30 Three-jet mass with full combination. 137
7.31 Fit of $k_{t\bar{t}}$ distribution for background-only pseudo-experiments. 139
7.32 $t\bar{t}$ cross section measurements at ATLAS with $2.9\,\mathrm{pb}^{-1}$. . . . 141

8.1 Transverse mass of reconstructed W for the electron channel. 149
8.2 Transverse mass of reconstructed W for the muon channel. . 150
8.3 Top mass and number of jets including one σ variations. . . . 155
8.4 Top mass and number of jets including one σ variations. . . . 157
8.5 Number of b-tagged jets including one σ variation of $\epsilon_{b\text{-tag}}$. . . 158

8.6 $k_{t\bar{t}}$ and $k_{W+\text{jets}}$ from 10,000 pseudo-experiments. 159
8.7 Cross checks of the profile likelihood fit. 160
8.8 Ability of fit to take possible shifts of systematic into account. 162
8.9 Invariant mass distributions used for fit, electron channel. . . 164
8.10 Invariant mass distribution used for fit, muon channel. 165
8.11 Summary of $t\bar{t}$ cross section measurements with $35\,\text{pb}^{-1}$. . . . 169
8.12 Results for $\sigma_{t\bar{t}}$ from the TEVATRON and the LHC. 169

A.1 Proton structure function F_2 from HERA. 174
A.2 CTEQ6.6 for different Q^2. 175

F.1 Electron candidates p_T for the electron channel. 189
F.2 Electron candidates p_T for the muon channel. 190
F.3 Missing transverse energy for the electron channel. 191
F.4 Missing transverse energy for the muon channel. 192

List of Tables

2.1 The elementary particles of the Standard Model. 6
2.2 The three quantum numbers for leptons and quarks. 7
2.3 Measured properties of the gauge bosons of the EW interaction. 7

3.1 List of all decay channels of the top quark pair. 29

4.1 Main parameters of the inner detector. 49
4.2 Granularity of the EM and the hadronic calorimeter. 52
4.3 Parameters of the three FCal modules. 57
4.4 Main parameters of the muon spectrometer. 58
4.5 Parameters of the sub-systems of the Muon Spectrometer. . . 59
4.6 Main parameters of the ATLAS magnet system. 61
4.7 Latencies and output rates for the three trigger levels. 64

5.1 Parameters for jet energy resolution. 75
5.2 Track selection criteria used by the SV0 tagging algorithm. . 77

6.1 Triggers used for electron channel with corresponding runs. . 82
6.2 Triggers used for muon channel with corresponding runs. . . . 82

7.1 Trigger efficiencies for the muon triggers. 88
7.2 Scale factors used for electrons and muons. 92
7.3 Muon momentum scale and resolution parameter. 93
7.4 Event selection efficiency after all MC correction factors. . . . 95
7.5 Probabilities for QCD events with ≥ 1 b-tag. 100
7.6 Number of predicted QCD events in the muon channel. . . . 106
7.7 Estimation of QCD events used for the muon channel. 106
7.8 Number of predicted QCD events for data. 109
7.9 Estimation of QCD events used for the electron channel. . . . 109
7.10 Selected events for the electron channel (pre-tagged). 111
7.11 Selected events for the muon channel (pre-tagged). 111
7.12 Selected events for the electron channel (b-tagged). 112
7.13 Selected events for the muon channel (b-tagged). 112
7.14 Correlated and uncorrelated uncertainties for QCD. 126

7.15 Expected results of the combined fit. 133
7.16 Results of the combined fit. 134
7.17 Measured inclusive $t\bar{t}$ cross section for full combination. . . . 135
7.18 Comparison of W+jets measurement with counting method. . 138
7.19 Inclusive $t\bar{t}$ cross section measured at ATLAS. 140

8.2 Selected events for the electron channel with no b-tagged jet. 147
8.3 Selected events for the electron channel with one b-tagged jet. 147
8.4 Selected events for the electron channel with $\geq 2b$-tagged jet. 147
8.5 Selected events for the muon channel with no b-tagged jet. . . 148
8.6 Selected events for the muon channel with one b-tagged jet. . 148
8.7 Selected events for the muon channel with $\geq 2b$-tagged jet. . 148
8.8 Correlated uncertainties on normalization of QCD background.151
8.9 Expected results of the nuisance parameters fit. 156
8.10 Results of the nuisance parameters fit to data. 161
8.11 Measured $t\bar{t}$ cross section for full combination with $35\,\mathrm{pb}^{-1}$. . 162
8.12 Event yields measured with the profile likelihood fit. 166
8.13 Simultaneous fit in =3, =4, ≥5-jet, zero-tag, =1-tag, ≥2-tag. 167
8.14 Comparison of measurement with $2.9\,\mathrm{pb}^{-1}$ and $35\,\mathrm{pb}^{-1}$. . . . 168

C.1 Top-pair and single top MC samples used in this analysis. . . 178
C.2 Diboson MC samples used in this analysis. 179
C.3 W+jets MC samples used in this analysis. 179
C.4 W+jets MC samples used in this analysis. 179
C.5 W+heavy flavor+jets MC samples used in this analysis. . . . 180
C.6 Z+jets MC samples used in this analysis. 180
C.7 Light-quark QCD MC samples used in this analysis. 181
C.8 Light-quark QCD MC samples used in this analysis. 182
C.9 QCD $b\bar{b}$ MC samples used in this analysis. 182
C.10 QCD $b\bar{b}$ MC samples used in this analysis. 183

D.1 Expected uncertainties for the object modeling systematics. . 184
D.2 Expected uncertainties for the background rate systematics. . 185
D.3 Expected uncertainties for background modeling systematics. 185
D.4 Expected uncertainties for the $t\bar{t}$ signal modeling systematics. 185

E.1 Measured uncertainties for the object modeling systematics. . 186
E.2 Measured uncertainties for the background rate systematics. . 187
E.3 Measured uncertainties for background modeling systematics. 187
E.4 Measured uncertainties for the $t\bar{t}$ signal modeling systematics. 187

F.1 Expected correlation Matrix for profile likelihood fit. 193

Chapter 1

Introduction

Already the ancient Greeks invented the concept of elementary particles, the $\alpha\tau o\mu o\varsigma$, as the "un-cuttable" building blocks of matter. With Joseph J. Thomson's discovery of the electron in 1897 [1], the first evidence for a sub-atomic structure was found. During the following decades more and more details about the atomic sub-structure came to light and further elementary particles were discovered. By the middle of the 20^{th} century several elementary particles where known, such that physicists found themselves confronted with a "particle zoo" of supposed elementary particles.

Looking for a theoretical model to describe the observations, in the 1960s the Standard Model was formulated [2, 3, 4] which gave a common frame work to all these particles. Therein matter is explained by fermions and forces are mediated via bosons. Two types of fermions are distinguished, leptons and quarks, both sub-divided into three families.

After the discovery of the bottom quark in 1977 [5], the existence of the top quark was predicted in order to complete the third quark family. Indirect evidence came from measurements of the branching ratio of the Z boson to hadrons, which agrees with the theoretical prediction including the top quark in the Standard Model [6]. The top quark was finally discovered directly in 1995 with the CDF [7] and DØ [8] experiments at the TEVATRON proton anti-proton collider. Its prediction and subsequent discovery was a great success for the Standard Model.

The top quark is special in comparison to other fermions, because its large mass of approximately $173\,\text{GeV}$[1], which is of almost the electroweak scale. The large mass causes an almost immediate decay such that the spin is transferred directly to its daughters before the hadronization of the top quark. An inside view of the top quark, not masked by Quantum Chromo Dynamics effects, is thus possible. Being the heaviest particle of the Standard Model discovered up to now, the top quark plays an important role within higher-order corrections of other Standard Model processes.

[1] Natural units are used within this measurement, assuming $c \equiv 1$ and $\hbar \equiv 1$.

Also because of its large mass, the top quark is expected to play an active role in the spontaneous breaking of the electroweak symmetry, the most prominent explanation for the origin of masses in the Standard Model. In searches for physics beyond the Standard Model the top quark becomes one of the main background processes as well as a potential window to new phenomena. Therefore, detailed studies of the top quark are expected to yield critical insights on how nature operates at the most fundamental level.

The work presented here is one of the first studies of top quarks with the ATLAS experiment at the Large Hadron Collider (LHC), colliding protons at a center-of-mass energy of 7 TeV. A data sample corresponding to a luminosity of $2.9\,\mathrm{pb}^{-1}$ collected in the early stage of the experiment was analyzed. The limited available statistics made it especially challenging to fully validate the reconstruction of the used objects. Also the correction factors, applied to account for the differences between data and simulation, were hard to estimate. Also the modeling of the background contribution was only partially estimated from real data, given the constrains from low statistics.

Within the Standard Model, the top quark decays almost 100% of the time into a bottom quark and a W boson, which successively decays into a quark or lepton pair. In this analysis the semi-leptonic decay of the top quark pair was analyzed, with an electron or a muon in the final state: $t\bar{t} \to e\,\nu_e q\,\bar{q}'\,b\,\bar{b}'$ and $t\bar{t} \to \mu\,\nu_\mu q\,\bar{q}'\,b\,\bar{b}'$. All parts of the ATLAS detector were used in this study to reconstruct the final state: the tracking detector, the calorimeters, and the muon spectrometer. Flavor tagging algorithms were used to distinguish the bottom quarks from lighter quark flavors. Energy not accounted to any reconstructed object was assigned as missing transverse energy, signaling the neutrino (ν_e and ν_μ).

To measure the cross section the reconstructed top quark mass from simulated Monte Carlo samples was fitted to the data. The contribution from Quantum Chromo Dynamic processes, one of the main background contributions, was estimated from real data, while the contribution from the main physics background of W bosons in association with jets was taken from simulation. An event selection was applied to separate the signal from the background, exploiting the flavor tagging to suppress contributions from W bosons with associated jets. To suppress the contribution from Quantum Chromo Dynamics a minimum missing transverse energy was asked for. For the result a wide range of systematic uncertainties was taken into account.

After successfully running the LHC during the year 2010, a data set corresponding to $35\,\mathrm{pb}^{-1}$ became available. The larger statistics allowed the enhancement of the object reconstruction as well as the background estimation, increasing the precision of the measurement. To fully exploit the ten-fold increase in the data set, the maximum likelihood fit was extended to a profile likelihood fit, using nuisance parameters in order to allow the data to restrict the contribution from systematic uncertainties. This further

decreases the contributions from systematic uncertainties.

This dissertation is organized as follows. The Standard Model is introduced in Chapter 2. In Chapter 3 various aspects of top quark physics are explained, from its observation, production, and decay at hadron colliders to the background process mimicking its final state. The experimental setup used for this measurement, i.e. the LHC and the ATLAS detector, are introduced in Chapter 4. Chapter 5 explains in detail the event reconstruction and the identification of the physical objects used in this study. The data sample used is introduced in Chapter 6. Finally, the first measurement of the top quark pair production cross section with the ATLAS detector with a data sample corresponding to an integrated luminosity of $2.9\,\mathrm{pb}^{-1}$ is presented in Chapter 7. Here the events selection and estimation of the background events is explained, as well as the reconstruction of the mass of the hadronically decaying top quark candidate. The extraction of the top quark pair production cross section with the maximum likelihood fit method using the top mass is elucidated and its results are presented. An improved measurement with a data sample corresponding to an integrated luminosity of $35\,\mathrm{pb}^{-1}$ is exposed in Chapter 8. The used profile likelihood fit is explained and the final result is presented. A summary and prospects are drawn in Chapter 9.

The results presented in this work have been published in the European Physical Journal C [9].

Chapter 2

The Standard Model of Particle Physics

In this chapter the Standard Model of particle physics is discussed briefly. After introducing the basic ideas of gauge theories in Sec. 2.1, the interactions between the elementary particles that are mediated by gauge fields (Sec. 2.2 and 2.3) are described. Also the Higgs mechanism, generating the masses of the particles, is introduced shortly in Sec. 2.4. Finally, open questions of the Standard Model are mentioned in Sec. 2.5. For more detailed information see [10, 11, 12, 13, 14].

2.1 Gauge Theories

Since the early 1930s a plethora of new particles was discovered so that at the beginning of the 1960s physicists found themselves confronted with a large spectrum of different particles, often referred to as a "particle zoo", unable to gather and describe them in a common model.

During the 1960s the Standard Model was formulated [2, 3, 4], a sophisticated theory providing a framework for this particle zoo. It is confirmed in many different experiments to a high accuracy (see for example [15] and Fig. 2.1) and can be described by means of a quantum field theory, representing particles by interacting matter-fields.

The Standard Model is a gauge field theory which means that its Lagrangian is invariant under local gauge transformations. These transformations describe symmetries, which form Lie-groups, or gauge groups. The algebra associated with a Lie-group consists of group generators, that are identified as the vector or gauge fields. These symmetries yield the existence of conservation laws, as predicted by the Noether theorem [16], as for example the conservation of electrical charge.

Since quantities in quantum fields theories may have ultraviolet divergences when calculating their observables, so-called renormalization param-

eters are introduced to consistently eliminated these. The Standard Model is such a renormalizable theory. Its coupling constants are renormalized which makes them dependent on the energy scale they are observed at. This dependence is often referred to as "running of the coupling".

When the field theory is quantized, the gauge fields are referred to as gauge bosons, the particles that carry the force of the gauge fields. For an exact gauge invariance these gauge bosons must be massless, which is in contradiction to the observation in experiments. The spontaneous breaking of the symmetries results into masses for the gauge bosons. Nevertheless, this symmetry breaking preserves the renormalizability.

The Standard Model includes the electroweak (EW) interaction and the strong interaction, which are explained in the following sections.

The elementary particles of the Standard Model are leptons and quarks, fermions with spin-1/2, arranged in three pairs of "generations" (see Table 2.1), and bosons of spin-1 (see Table 2.3) forming the visible matter of our universe. Also fermions have to be massless in order to satisfy the exact gauge invariance, which is like for the bosons in contradiction to the observation (e.g. $m_e = 0.511\,\mathrm{MeV}$, $m_\mu = 105.66\,\mathrm{MeV}$, and $m_\tau = 1.78\,\mathrm{GeV}$).

2.2 The Electroweak Interaction

The EW interaction is the unification of Quantum Electro Dynamics (QED) and the weak interaction. The symmetry of the QED interaction is the $U(1)_Q$ group with the charge operator Q as its generator. For the weak interaction the symmetry is the $SU(2)$ group which describes the transformations of the weak isospin T for the left-handed doublets. The generators of the $SU(2)$ group are the weak isospin operators, the Pauli-matrices τ_i $(i = 1, 2, 3)$, or $T = \tau/2$. The fact that the T_i do not commute makes this gauge group non-Abelian.

Both interactions can be unified introducing the $U(1)_Y$ gauge symmetry with the conserved quantum number Y, the hyper-charge. Together with a left-handed structure of the weak interaction resulting in the gauge group $SU(2)_L$, the symmetry group for the EW theory is $SU(2)_L \times U(1)_Y$. The three charges, namely the electromagnetic charge Q, the hyper-charge Y, and the weak isospin T are coupled via the Gell-Mann-Nishijima relation

$$Q = T_3 + \frac{Y}{2}\,, \tag{2.1}$$

where T_3 is the third component of the isospin.

The corresponding gauge fields for the hyper-charge operator Y are B_μ and the Yang-Mills gauge fields W^i_μ $(i = 1, 2, 3)$ for the isospin. The gauge

Table 2.1: The elementary particles of the Standard Model, categorized in singlets and doublets, depending on their transformation properties under the electroweak symmetry group.

Leptons			Quarks		
I	II	III	I	II	III
$\begin{pmatrix}\nu_e\\ e\end{pmatrix}_L$	$\begin{pmatrix}\nu_\mu\\ \mu\end{pmatrix}_L$	$\begin{pmatrix}\nu_\tau\\ \tau\end{pmatrix}_L$	$\begin{pmatrix}u\\ d'\end{pmatrix}_L$	$\begin{pmatrix}c\\ s'\end{pmatrix}_L$	$\begin{pmatrix}t\\ b'\end{pmatrix}_L$
ν_{eR}, e_R	$\nu_{\mu R}$, μ_R	$\nu_{\tau R}$, τ_R	u_R, d_R	c_R, s_R	t_R, b_R

transformations for theses fields are defined as

$$B'^{\mu} = B^{\mu} - \partial^{\mu}\chi(x)\,, \tag{2.2}$$

$$W_i'^{\mu} = W_i^{\mu} - \partial^{\mu}\beta_i(x) - g\,\varepsilon_{ijk}\,\beta_j(x)\,W_k^{\mu}\,, \tag{2.3}$$

where the Levi-Civita symbol ε_{ijk} is the structure constant of the $SU(2)_L$ symmetry group, g the coupling constant, and $\chi(x)$ and $\beta(\vec{x})$ are phases.

The Lagrangian for free (non-interacting) massless fermion fields ψ_f can be written as

$$\mathcal{L} = \sum_f \bar{\psi}_f\, i\,\gamma_\mu\,\partial^\mu\,\psi_f\,, \tag{2.4}$$

with the anti-fermion defined as $\bar{\psi}_f = \psi_f^\dagger\gamma^0$. Fermions are characterized by their spin orientation, chirality, and their quantum numbers[1], i.e. the electric charge, the hyper-charge, and the isospin, respectively (see Table 2.1 and 2.2). The fermion fields can be split up into their chiralities ("handedness"), i.e.

$$\psi = \frac{1-\gamma_5}{2}\psi + \frac{1+\gamma_5}{2}\psi = \psi_L + \psi_R\,, \tag{2.5}$$

Similar, the helicity is the alignment between the spin orientation and the direction of motion. In case of massless particles the helicity corresponds to the chirality.

Interactions between fermions and the gauge fields B_μ and W_μ^i are implemented in the Lagrangian (see Eq. 2.4) via the replacement of ∂_μ in the free Lagrangian with the covariant derivation

$$D^\mu = \partial^\mu + i\,g\,\vec{T}\cdot\vec{W}^\mu + i\,\frac{g'}{2}YB^\mu\,, \tag{2.6}$$

where g and g' are the EW coupling constants for $SU(2)_L$ and $U(1)_Y$ groups, respectively. The gauge bosons are linear combinations of the vector-fields

[1]The anti-fermions have opposite sign quantum numbers and the same masses.

Table 2.2: The three quantum numbers for leptons and quarks, divided into left-handed and right-handed fermions.

fermion	electric charge Q	hyper-charge Y	Isospin T_3
e_R, μ_R, τ_R	-1	-2	0
ν_{eL}, $\nu_{\mu L}$, $\nu_{\tau L}$	0	-1	$+1/2$
e_L, μ_L, τ_L	-1	-1	$-1/2$
u_R, c_R, t_R	$+2/3$	$+4/3$	0
d_R, s_R, b_R	$-1/3$	$-2/3$	0
u_L, c_L, t_L	$+2/3$	$+1/3$	$+1/2$
d'_L, s'_L, b'_L	$-1/3$	$+1/3$	$-1/2$

Table 2.3: Measured properties of the gauge bosons of the EW Interaction [17].

Property	γ	W	Z
mass [GeV]	$< 1 \cdot 10^{-27}$	80.399 ± 0.023	91.176 ± 0.0021
lifetime $[s]$	∞	$\sim 3 \cdot 10^{-25}$	$\sim 3 \cdot 10^{-25}$
range $[m]$	∞	$\sim 10^{-18}$	$\sim 10^{-18}$
spin	1	1	1
charge $[e]$	$< 1 \cdot 10^{-35}$	± 1	0

$\vec{W}_\mu$ and B_μ, such that the mass eigenstates can be written as

$$W^\pm \equiv W^{\pm\mu} = 1/\sqrt{2}\,(W_1^\mu \pm W_2^\mu)\,, \tag{2.7}$$

$$\gamma \equiv A^\mu = W_3^\mu \sin\theta_W + B^\mu \cos\theta_W\,, \tag{2.8}$$

$$Z \equiv Z^\mu = W_3^\mu \cos\theta_W - B^\mu \sin\theta_W\,, \tag{2.9}$$

where θ_W is the weak mixing angle or Weinberg angle. A brief summary of the measured properties of the gauge bosons of the EW interaction is listed in Table 2.3.

The weak mixing is defined in terms of the EW coupling constants g and g':

$$\cos\theta_W = \frac{g}{\sqrt{g^2 + g'^2}} \qquad \text{and} \tag{2.10}$$

$$\sin\theta_W = \frac{g'}{\sqrt{g^2 + g'^2}}\,. \tag{2.11}$$

It can also be expressed using the three most accurately known weak-interaction observables: the EW coupling constant $\alpha_{\text{EW}} = \sqrt{g/4\pi}$ [18], the

Fermi constant G_F [19], and the mass of the Z boson m_Z [6] as

$$\sin\theta_W \equiv \left(\frac{4\pi\alpha_{\rm EW}}{\sqrt{2}G_F m_Z^2}\right). \tag{2.12}$$

Summarizing, the Lagrangian of the EW interaction can be written as

$$\mathcal{L} = \mathcal{L}_{\rm fermion} + \mathcal{L}_{\rm boson} + \mathcal{L}_{\rm interaction}\,. \tag{2.13}$$

Here $\mathcal{L}_{\rm fermion}$ represents the kinetic energies of the fermions:

$$\mathcal{L}_{\rm fermion} = \bar{L}\,\gamma^\mu i\,\partial_\mu L + \bar{R}\,\gamma^\mu i\,\partial_\mu R\,, \tag{2.14}$$

where L are the left-handed fermion doublets and R the right-handed fermion singlets. The kinetic energies and self-interactions of the W and the Z bosons can be written as

$$\mathcal{L}_{\rm boson} = -\frac{1}{4}\vec{W}_{\mu\nu}\vec{W}^{\mu\nu} - \frac{1}{4}B_{\mu\nu}B^{\mu\nu}\,, \tag{2.15}$$

where $\vec{W}_{\mu\nu} = \partial_\mu\vec{W}_\nu - \partial_\nu\vec{W}_\mu - g\vec{W}_\mu \times \vec{W}_\nu$. The interactions of the fermions with the bosons is represented in the term

$$\mathcal{L}_{\rm interaction} = \bar{L}\,\gamma^\mu(-g\frac{1}{2}\tau\vec{W}_\mu - g'\,\frac{Y}{2}B_\mu)L + \bar{R}\,\gamma^\mu(-g'\,\frac{Y}{2}B_\mu)R\,. \tag{2.16}$$

The absence of $\vec{W}_\mu$ in the interaction part with right-handed leptons in Eq. 2.16 represents the vector minus axial vector ($V-A$) structure of the charged weak current (see Eq. 2.5). The interaction mediated by W bosons only involves left-handed (right-handed) fermions (anti-fermions).

A feature of the EW interaction is that the weak eigenstates with the same quantum numbers (Q, Y, T_3) can mix with each other. The fundamental quark states of the EW theory can be transformed by unitary matrices to the mass eigenstates

$$\begin{pmatrix} u'_1 \\ u'_2 \\ u'_3 \end{pmatrix} = U \begin{pmatrix} u \\ c \\ t \end{pmatrix} \quad \text{and} \quad \begin{pmatrix} d'_1 \\ d'_2 \\ d'_3 \end{pmatrix} = D \begin{pmatrix} d \\ s \\ b \end{pmatrix}. \tag{2.17}$$

Transforming the bi-linear terms $\bar{u'_{iL}}\gamma^\mu d'_{iL}$, with $i = 1,2,3$, in the charged-currents of the weak interaction to the mass eigenstates introduces the Cabibbo-Kobayashi-Maskawa (CKM) matrix $V \equiv U_L^\dagger D_L$. Electromagnetic and neutral weak currents are not affected by the mixing since $U_L^\dagger U_L = 1$. The mixing of quarks is only possible if they are left-handed, since right-handed quarks do not couple to the W boson.

The matrix elements V_{ij} are free parameters of the Standard Model and have to be determined experimentally. The standard parametrization as

proposed in [20] is the product of three rotation matrices and can be written as

$$V = \begin{pmatrix} c_{12}c_{13} & s_{12}c_{13} & s_{13}e^{-\delta} \\ -s_{12}c_{23} - c_{12}s_{23}e^{\delta} & c_{12}c_{23} - s_{12}s_{23}s_{13}e^{\delta} & s_{23}c_{13} \\ s_{12}s_{23} - c_{12}c_{23}s_{13}e^{\delta} & -c_{12}s_{23} - s_{12}c_{23}s_{13}e^{\delta} & c_{23}c_{13} \end{pmatrix}, \quad (2.18)$$

where $c_{ij} = \cos\theta_{ij}$ and $s_{ij} = \sin\theta_{ij}$ for $i < j = 1, 2, 3$. The Euler angles θ_{12}, θ_{13}, and θ_{23} are the mixing angles between the quark generations. The overall phase δ describes CP violation and explains its appearance in kaon and B meson decay.

In the Standard Model the CKM matrix is almost a diagonal matrix and can be written using powers of a parameter λ, yielding the parametrization introduced by Wolfenstein [21] which is defined as

$$V = \begin{pmatrix} 1 - \lambda^2/2 & \lambda & A\lambda^3(\rho - i\eta) \\ -\lambda & 1 - \lambda^2/2 & A\lambda^2 \\ A\lambda^3(1 - \rho - i\eta) & -A\lambda^2 & 1 \end{pmatrix}, \quad (2.19)$$

with $s_{12} = \lambda$, $s_{23} = A\lambda^2$, $s_{13}e^{-i\delta} = A\lambda(\rho - i\eta)$. In this approximation the number of parameters needed to measure reduces to four [17]:

$$\lambda = 0.2253 \pm 0.0007\,, \qquad A = 0.808 \pm {}^{0.022}_{0.015}\,, \quad (2.20)$$

$$\rho = 0.132 \pm {}^{0.00026}_{0.00020}\,, \qquad \eta = 0.341 \pm 0.013\,. \quad (2.21)$$

After discovery of neutrino oscillation [22], implying non-zero neutrino masses, the mixing in the lepton sector, in analogy to the quark sector, was accepted. The mixing matrix of the lepton sector is the Maki-Nakagawa-Sakata (MNS) matrix. This mixing leads to the violation of the originally introduced lepton number of the individual flavors as a quantum number. The total lepton number however remains conserved.

2.3 The Strong Interaction

A large number of baryons and mesons was found in the middle of the last century, indicating an underlying sub-structure. The strong interaction, described by the theory of Quantum Chromo Dynamics (QCD), was constructed to explain baryons and mesons as combinations of three quarks and two quarks, respectively. A "strong" force was demanded, that overrules the repulsion of the quarks due to its electromagnetic charge.

Another puzzle appeared for the wave function of the Δ^{++}-baryon (uuu), which is symmetric under permutations of two quarks, although quarks have spin-1/2. This lead to the introduction an additional "hidden" quantum number, to fulfill the Pauli principle[2]. The Yang-Mills theory based on the

[2]Two fermions having the same quantum numbers may not occupy the same quantum state simultaneously.

$SU(3)$ symmetry group was introduced, such that the symmetry for the Standard Model can be written as

$$SU(3)_C \times SU(2)_L \times U(1)_Y \,. \tag{2.22}$$

The $SU(3)_C$ group gives the quarks three additional degrees of freedom, the so-called color-charge of red, blue, and green. The strong interaction is mediated by fields G^a_μ.

The generators of the $SU(3)_C$ group are the eight Gell-Mann-matrices λ_i which are the 3-dimensional equivalents of the Pauli matrices τ_i, the generators of the $SU(2)_L$ group. The wave function for quarks is the product of the Dirac wave function ψ and a 3-dimensional color-spinor χ_C

$$\Psi = \psi\,\chi_C \,. \tag{2.23}$$

The Lagrangian of the strong interaction can be written as

$$\mathcal{L} = \bar{\Psi} i\gamma_\mu D^\mu \Psi - \frac{1}{4} G^a_{\mu\nu} G^{\mu\nu}_a \,, \tag{2.24}$$

where the covariant derivative is defined in analogy to the EW theory (see Eq. 2.3) as

$$D_\mu = \partial_\mu + i g_s \lambda_a G^a_\mu \,. \tag{2.25}$$

Here g_s is the strong coupling, in analogy to the EW couplings g and g'. The index a specifies the eight degrees of freedom of the gluon field G^a_μ. The bosons of the QCD are the eigenstates of G^a_μ, the gluons. Their name originates from the confinement properties of the QCD interaction: Quarks do not exist as free particles but only as colorless compositions and are thus "glued". $F^{\mu\nu}_a$ is the field strength tensor, defined as

$$[D_\mu, D_\nu] = i g_s \lambda_a G^a_{\mu\nu} \,, \tag{2.26}$$

or more explicitly

$$G^a_{\mu\nu} = \partial_\mu G^a_\nu - \partial_\nu G^a_\mu - g_s f_{abc}\, G^b_\mu G^c_\nu \,. \tag{2.27}$$

The nonlinear terms in the Yang-Mills Lagrangian (Eq. 2.24) appear in the derivative (Eq. 2.25) where they are proportional to λ_i and the structure constants f_{jkl} of the $SU(3)_C$ group. These nonlinear interactions of the vector fields with itself are proportional to the commutators of the generators G^a_μ and thus explicitly require the non-Abelian nature of the $SU(3)_C$ symmetry group.

Gluons are massless and thus stable particles and as mentioned before do couple to themselves. They have spin-1 and carry neither electromagnetic charge nor hyper-charge or isospin. The coupling of the strong interaction

$$\alpha_s = \frac{{g_s}^2}{4\pi} \,, \tag{2.28}$$

depends on the momentum scale Q^2 of the interaction. This is characterized in a leading order approximation by the parametrization

$$\alpha_s(Q^2) = \frac{12\pi}{(33 - 2n_f) \cdot \ln(Q^2/\Lambda^2)}\,, \tag{2.29}$$

at the QCD scale $\Lambda \ll Q^2$ and with the number of flavors n_f. The scaling of α_s with Q is referred to as "running" of the coupling constant. Since the coupling decreases towards zero for $Q^2 \to \infty$, the quarks can propagate as if they were free (asymptotic freedom). For low Q^2 the coupling α_s diverges, a phenomenon which is called confinement. This is the case for distances larger than roughly 1 fm at which a quark anti-quark pair is energetically preferred compared to single quarks.

Since in perturbative theory, when calculating physics processes, virtual loops occur, infinities are induced in the calculation, so-called ultraviolet divergences. To solve that, a renormalization procedure is applied (see e.g. [11, 12]), which implies the scaling of the coupling constant. An artificial scale μ_r is introduced, at which α_s is measured experimentally. The value of α_s at a different scale Q^2 can be obtained through

$$\alpha_s(Q^2) = \frac{\alpha_s(\mu_r^2)}{1 + \alpha_s(\mu_r^2)\, b\, \ln(Q^2/\mu_r^2)}\,, \tag{2.30}$$

with $b = (33 - 2n_f)/12\pi$, where n_f defines the number of fermion generations.

2.4 The Higgs Mechanism

Since the discovery of the W boson [23] and the Z boson [24] in the early 1980s, both are known as massive particles with masses of the order of 100 GeV (see Table 2.3). However, only massless vector fields fulfill the gauge invariance under local transformations of the EW Lagrangian (see Eq. 2.13). Additional mass terms as for instance $1/2 m^2 B_\mu B^\mu$ are not gauge invariant and can thus not introduce directly masses for the gauge bosons, which contradicts the experimental observations. The same is valid for fermions.

A scalar doublet containing four real fields ϕ_i $(i = 1, \ldots, 4)$, invariant under $SU(2)$ transformations, is introduced

$$\phi = \begin{pmatrix} \phi^+ \\ \phi^0 \end{pmatrix} = \frac{1}{\sqrt{2}} \begin{pmatrix} \phi_1 + i\phi_2 \\ \phi_3 + i\phi_4 \end{pmatrix}. \tag{2.31}$$

The corresponding potential, the so-called Higgs potential, is chosen as

$$V(\phi) = -\mu^2|\phi|^2 + \lambda^2|\phi|^4\,. \tag{2.32}$$

By selecting $\mu^2 < 0$ and $\lambda > 0$, the minimum of the potential is not at $|\phi_0| = 0$, but at $|\phi_0|^2 = \frac{\mu^2}{2\lambda^2} \equiv \frac{v}{\sqrt{2}}$, referred to as the vacuum expectation

state of ϕ. This yields an infinite set of ground states for the Higgs potential, satisfying

$$(\phi_1^2 + \phi_2^2 + \phi_3^2 + \phi_4^2) = -\frac{\mu^2}{2\lambda}\,. \tag{2.33}$$

By choosing one in particular, e.g.

$$\phi_0 = \frac{1}{\sqrt{2}}\begin{pmatrix}0\\ v\end{pmatrix}, \tag{2.34}$$

the potential $V(\phi)$ is no longer invariant under $SU(2)_L \times U(1)_Y$. It is said, that the $SU(2)_L \times U(1)_Y$ symmetry of the Higgs potential is spontaneously broken and the gauge invariance is hidden.

Expanding $\phi(x)$ around the minimum, representing ground state fluctuations $h(x)$ around the vacuum state, the Higgs doublet can be expressed as

$$\phi(x) = \frac{1}{\sqrt{2}}\begin{pmatrix}0\\ v + h(x)\end{pmatrix}. \tag{2.35}$$

The contribution of the scalar Higgs doublet to the Lagrangian of the Standard Model represents the masses of the bosons and their couplings:

$$\mathcal{L}_{\text{Higgs}} = (D^\mu\phi)^\dagger(D_\mu\phi) - V(\phi)\,. \tag{2.36}$$

With D_μ as defined as in Eq. 2.6, the Lagrangian can be expressed as

$$\begin{aligned}\mathcal{L}_{\text{Higgs}} = \frac{1}{4}g^2W^+W^-(v+h(x))^2 + \frac{1}{8}(g^2+g'^2)ZZ(v+h(x))^2 \\ + \frac{1}{2}(\partial h(x))^2 - V\left[\frac{1}{2}(v+h(x))^2\right].\end{aligned} \tag{2.37}$$

This allows to define the boson masses as

$$m_W = \frac{1}{2}vg \qquad \text{and} \qquad m_Z = \frac{1}{2}v\sqrt{g^2+g'^2}\,. \tag{2.38}$$

The chosen vacuum expectation value for $\phi^+ = 0$ results in an invariance under the $U(1)_{\text{EM}}$ group and a massless photon field, consistent with the measurements [25]. Of the original four degrees of freedom in form of the Goldstone fields ϕ_i, three have been converted into the mass, and thus the longitudinal polarization of the vector bosons. The remaining degree of freedom $h(x)$ is the physical Higgs field, corresponding to the Higgs boson of mass

$$m_H = \sqrt{2\lambda v}\,. \tag{2.39}$$

Using Eq. 2.10 and 2.38, the mixing between the vector fields W_μ^3 and B_μ, resulting in the difference of the W and the Z boson mass eigenstates, can be described depending on the Weinberg angle:

$$\frac{m_W}{m_Z} = \cos\theta_W\,. \tag{2.40}$$

Furthermore v can be defined with Eq. 2.12 and 2.38 as

$$v = \frac{2m_W}{g} = (\sqrt{2}G_F)^{-1/2} = 246\,\text{GeV}\,. \tag{2.41}$$

By introducing a Yukawa interaction between the Higgs and the fermion fields,

$$\mathcal{L}_{\text{Yukawa}} = -\lambda_f \bar{L}\phi R - \lambda_f \bar{R}\phi^\dagger L\,, \tag{2.42}$$

where L denotes a left-handed fermion doublet and R a right-handed fermion singlet, fermions acquire masses as well upon breaking of the electroweak symmetry:

$$m_f = \frac{v\lambda_f}{\sqrt{2}}\,, \tag{2.43}$$

for each fermion f. The Yukawa couplings, and thus the fermion masses, are not predicted by the theory and have to be measured.

The Higgs boson has not been discovered yet and its mass is not predicted by the theory. Limits have been set at its mass by direct searches at the Large Electron-Positron Collider (LEP) $m_H > 114.4\,\text{GeV}$ [15, 26], and at the Tevatron $158 < m_H < 175\,\text{GeV}$ [27]. As it will be discussed in Sec. 3.1.2, the precise measurement of the W boson mass and the top quark mass allow to place indirect constrains on the Higgs boson mass via quantum corrections to electroweak observables.

2.5 Open Questions of the Standard Model

Although the Standard Model has been successfully tested to a very high degree of accuracy (see Fig. 2.1), a number of open questions remain. Those suggest that the Standard Model is nothing but an effective theory at low energies and new physics should emerge at higher scales, which would require a more fundamental description.

- The Higgs boson which is supposed to generate the mass of the Standard Model particles without spoiling the renormalizability (see Sec. 2.4) has not been discovered yet.

- The Hierarchy Problem of the Standard Model appears due to the renormalization of fundamental parameters, as for example the couplings. One example is the fact that for a Standard Model Higgs boson with a mass $m_H \lesssim 1\,\text{TeV}$ the contributions from higher order terms

  $$m_H^2 = m_0^2 + \lambda\frac{\Lambda^2}{16\pi^2}\,, \tag{2.44}$$

  have to become very small at the Planck Scale $\Lambda_{\text{Planck}}/\sqrt{8\pi} = 10^{18}\,\text{GeV}$, at which gravitational effects should no longer be negligible. This is

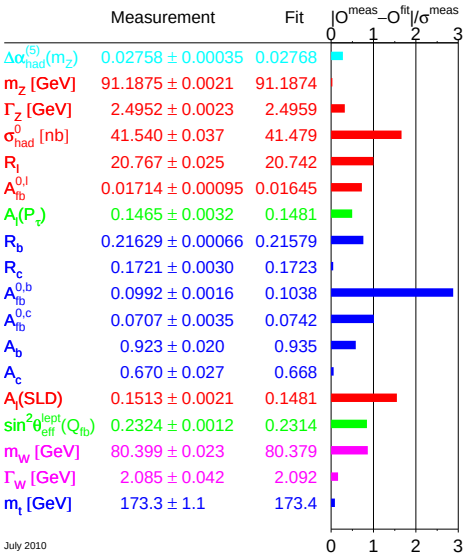

Figure 2.1: Measurements of 18 free parameters of the Standard Model that are not a priori determined. The 19$^{\text{th}}$ is the Higgs boson mass. The differences between the measured values and the fit using Standard Model predictions divided by the measurements uncertainty are shown. The measured values are obtained from a fit to all measurements [15]. Since the deviation of the measurements is for almost all parameters within its uncertainties, the Standard Model is in agreement with its expectations.

needed such that the Higgs boson mass is of the order of the W and Z boson mass and thus ensures the cancellation of diagrams in perturbation theory occur at sufficiently low energy. To achieve a Higgs boson mass of that order a fine-tuning of the scale of

$$\frac{\mu}{\Lambda} \approx 10^{-16}\,, \tag{2.45}$$

is needed at the Planck scale, which is very "unnatural" and therefore disfavored.

- The hierarchical mass structure of the Standard Model fermions, ranging from not yet directly measured masses of neutrinos up to about 173 GeV of the top quark, is not understood. Also the question why exactly three families of fermions exist remains unsolved.

- Dark matter, required to explain the almost constant rotation velocity of spiral galaxies up to large radii [28], accounts for about 30% of the matter in the known universe. It gives also an explanation to the origin of the galaxy clustering in the early universe. The origin of dark

matter is not known yet, although some theories are able to resolve this problem, the existence of a supersymmetry, which associates every Standard Model fermion with a supersymmetric boson and every Standard Model boson with a supersymmetric fermion. Depending on the supersymmetric model the lightest supersymmetric particle is stable, neutral, and only weakly interacting, and is therefore a good dark matter candidate. So far no evidence for the existence of supersymmetric particles has been found.

- An unification of the EW theory and QCD is aspired by physicists to obtain a gran unified theory, in which the $SU(3)_C$, $SU(2)_L$, and $U(1)_Y$ groups have a common origin in a larger symmetry group G. It is expected that at a high energy scale these symmetries are unbroken and that their coupling constants become one: $\alpha_1 = \alpha_2 = \alpha_s = \alpha_G$. This is not realized in the Standard Model, however, some supersymmetric models predict the unification of the coupling constants. Still missing though would be an unification of these three forces with the Gravitation in a so-called Theory of Everything.

As it will be discussed in Chapter 3, it is hoped that detailed studies of the top quark may provide some clues that will eventually help to solve some of the open questions of the Standard Model.

Chapter 3

Top Quark Physics

The top quark is one of the most recently discovered particles[1] of the Standard Model, for the first time observed in 1995 at the CDF [7] and DØ [8] experiments at the TEVATRON proton anti-proton collider. It was one of the last missing pieces in the set of fermions forming the visible matter of the known universe. The top quark contributes to quantum corrections to standard model processes and is thus crucial for precision test of the EW theory. Due to its large mass of about 173 GeV, comparable to the vacuum expectation value v, it is strongly coupled to the Higgs boson and can potentially play an active role in the EW symmetry breaking. The top quark furthermore can serve as a window to new physics directly related to EW symmetry breaking and strongly coupled to it.

In this section the top quark is introduced in more detail, starting with its prediction and the resulting observation (Sec. 3.1). After motivating its special role among the Standard Model fermions, its properties are discussed (Sec. 3.1.4). The top quark production (Sec. 3.2.1) and decay processes (Sec. 3.2.2) at the LHC are explained. Finally, possible background when measuring it (Sec. 3.2.3) are introduced.

3.1 The Top Quark

3.1.1 Indirect Evidence

After the discovery of the b quark in 1977 [5], several arguments suggested the existence of a weak isospin partner, the top quark. The most convincing argument originates from the measurements of the process $Z \to b\bar{b}$ at LEP and Stanford Linear Accelerator Center (SLAC). For this process the

[1] The last discovered elementary particle was the tau neutrino by the DONUT collaboration in 2000 [29].

interaction of the Z boson to the b quarks can be described by

$$\frac{-ig}{\cos\theta_W}\gamma^\mu\frac{1}{2}(v_b - a_b\gamma^5)\,, \tag{3.1}$$

with the vector and axial vector couplings v_b and a_b defined as

$$v_b = [T_3^L(b) + T_3^R(b)] - 2\,Q_b\sin^2\theta_W\,, \quad \text{and} \tag{3.2}$$
$$a_b = [T_3^L(b) + T_3^R(b)]\,, \tag{3.3}$$

where $Q_b = -1/3$ is the electrical charge of the b quark and the $T_3^L(b)$ and $T_3^R(b)$ are the third components of the weak isospin for left- and right-handed b quark fields (see Sec. 2.2). Using the (improved) Born approximation, the decay rate of the Z boson into a b quark pair for the limit of a zero b quark mass can be expressed as

$$\Gamma_{b\bar{b}} \equiv \Gamma_{Z\to b\bar{b}} = \frac{G_F m_Z^3}{2\sqrt{2}\,\pi}(v_b^2 + a_b^2)\,, \tag{3.4}$$

where G_F is the Fermi constant and m_Z the mass of the Z boson. In the case of an isospin singlet b quark, i.e. $T_3^L(b) = 0$, this decay rate would be much smaller than the actual measured value at LEP of the ratio $\Gamma_{b\bar{b}}/\Gamma_{\text{had}} = 0.21629 \pm 0.00066$ [6]. These results are in very good agreement with the Standard Model prediction of 0.2158, including a top quark.

A second argument is the desired renormalizability of the Standard Model. It can be shown generally [30] that the Standard Model of EW interactions is renormalizable if the sum of the weak hyper-charges Y_i of all left-handed fermions equals zero, i.e.

$$\sum_{f_L} Y_i = 0\,. \tag{3.5}$$

Consulting Table 2.1, Eq. 3.5 is fulfilled if every quark exists in three color versions (see Sec. 2.3) and the number of quarks equals to the number of leptons.

A more general proof for the renormalizability of a gauge theory can be applied if the gauge theory is free from chiral anomalies. Those appear in closed loops of fermions with gauge-bosons, that couple differently to left and right-handed fermions. To achieve the cancellation of fermion loops that cause such anomalies, an odd number of axial vector couplings is required. This is satisfied for the EW interaction with $SU(2)\times U_Y(1)$ if the following condition is fulfilled:

$$d_{abc} = \sum_{\text{fermions}} Tr\left[\hat{\lambda}_a\{\hat{\lambda}_b,\hat{\lambda}_c\}_+\right] = 0\,, \tag{3.6}$$

with the three Pauli matrices $\hat{\lambda}_i = \sigma_i$ for $i = 1,2,3$ and the hyper-charge $\hat{\lambda}_4 = \hat{Y} = 2(\hat{Q} - \hat{T}_3)$ (See Eq. 2.1). It can be shown that Eq. 3.6 is satisfied

for three colors and equal number of lepton and quark doublets [31]. From the fact that three lepton doublets have been observed, the lack of anomalies therefore requires the existence of three quark doublets, hence the top quark.

Furthermore, the existence of the top quark and thus an isospin doublet provides a natural way to suppress flavor changing neutral current (FCNC) interactions, which have not been observed.

3.1.2 Indirect Constrains on the Top Quark Mass

In addition to the arguments discussed in Sec. 3.1.1, various indirect measurements have constrained the mass of the top quark. The best-measured EW quantities are the electromagnetic coupling constant α, the Fermi constant G_F, and the mass of the Z boson (see Sec. 2.2). Rewriting Eq. 2.10 as

$$\sin^2\theta_W = 1 - \frac{m_W^2}{m_Z^2}\,, \tag{3.7}$$

the mass of the W boson can be expressed [32] as

$$m_W = \left(\frac{\pi\alpha}{\sqrt{2}\,G_F}\right)^2 \frac{(1+\Delta r/2)}{\sin\theta_W}\,, \tag{3.8}$$

where Δr includes one-loop contributions from the top quark Δr_{top} (see Fig. 3.1) and from the Higgs boson Δr_{Higgs} (see Fig. 3.2).

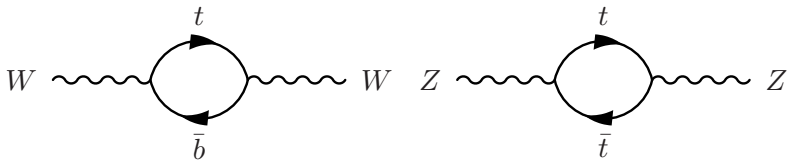

Figure 3.1: Virtual top quark loops contributing to the W and Z boson propagators.

The contribution from the top quark is

$$\Delta r_{\text{top}} \simeq -\frac{3\,G_F\,m_t^2}{8\sqrt{(2)}\,\pi^2\tan^2\theta_W}\,, \tag{3.9}$$

whereas the contribution from the Higgs boson is

$$\Delta r_{\text{Higgs}} \simeq \frac{3\,G_F\,m_W^2}{8\sqrt{2}\,\pi^2}\left(\ln\frac{m_H^2}{m_Z^2} - \frac{5}{6}\right)\,. \tag{3.10}$$

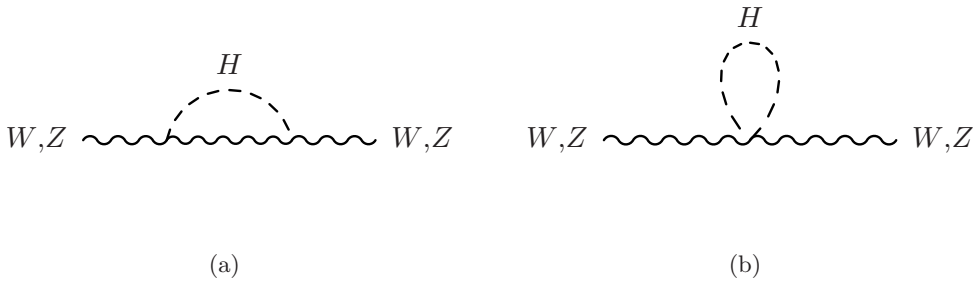

(a) (b)

Figure 3.2: Virtual Higgs boson loops contributing to the W and Z boson propagators.

Comparing Eq. 3.9 and Eq. 3.10 it becomes clear that the inferred constrains on the Higgs boson mass m_H are much weaker than for the top quark mass m_t, since the former only contributes logarithmically, while the dependence on latter is quadratic. Figure 3.3 shows indirect constrains on the W boson mass m_W and the top quark mass m_t based on LEP-I and SLD data. Also results from direct measurements at LEP-II and the TEVATRON are drawn [33]. The prediction of m_W and m_t for different Higgs boson masses are drawn as well, showing a clear preference of lower Higgs boson masses. The fit was performed on five parameters: the hadronic contribution to the QED vacuum polarization $\delta\alpha^{(5)}_{\text{had}}(m_Z^2)$, the strong coupling constant $\alpha_s(m_Z^2)$, the mass of the Z boson m_Z, the mass of the top quark m_t, and $\log_{10}(m_H/\text{GeV})$. A good agreement with the Standard Model prediction using the measurements of m_t and m_W is observed. For a more detailed description see [33].

Using the most recent results of the Z-pole data together with the direct measurement of the W boson mass and total width as well as several other EW quantities, the indirect determination of the top quark mass yields [33]

$$m_t = 179.1^{+12}_{-9}\,\text{GeV}\,. \tag{3.11}$$

3.1.3 Observation of the Top Quark

Finally, in 1995, the top quark was for the first time observed at the CDF [7] and the DØ [8] experiments at the TEVATRON in proton anti-proton collisions at $\sqrt{s} = 1.96\,\text{GeV}$. The successful prediction of the top quark before its discovery was a great success of the Standard Model and gave confidence in the precision and predictive power of radiative corrections, e.g. for the yet not observed Higgs boson.

In the last years, measurements of the top quark mass (see Fig. 3.4) have gained in accuracy, such that today it is measured with better relative precision (0.61%) than for any other quark [34].

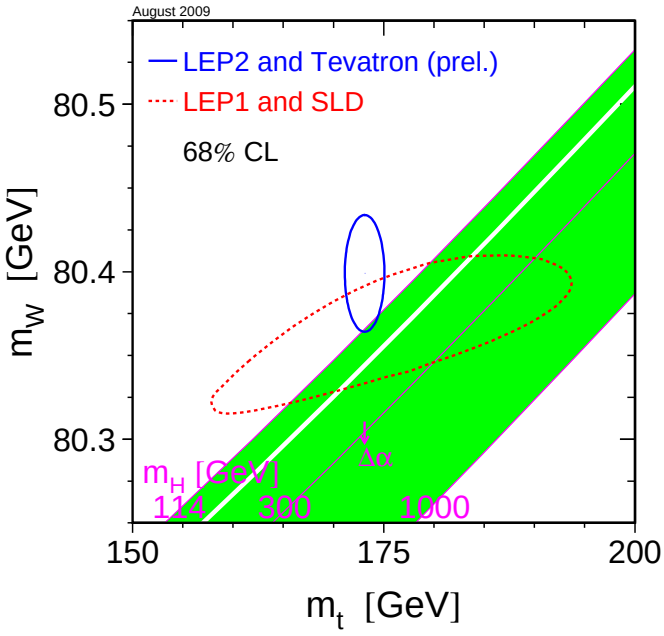

Figure 3.3: Comparison of the indirect constraints on the W boson mass m_W and the top quark mass m_t based on LEP-I and SLD data and the direct measurements from the LEP-II and the TEVATRON experiments. In both cases the 68% CL contours are shown. Also shown is the dependence on the masses as a function of the Higgs boson mass predicted by the Standard Model [33].

The latest measurement of the top quark mass from DØ and CDF with data corresponding to an integrated luminosity of up to $5.6\,\mathrm{fb}^{-1}$ is [34]

$$m_t = 173.3 \pm 0.6\,(\mathrm{stat.}) \pm 0.9\,(\mathrm{syst.})\,\mathrm{GeV}\,. \tag{3.12}$$

3.1.4 Top Quark Properties

The top quark is special in comparison to the other fermions of the Standard Model, not only due to its much larger mass but also regarding to other properties which are discussed in this section.

3.1.4.1 Decay Width, Lifetime and V_{tb}

Within the Standard Model the top quark decays 100% of the times into a W boson and a b quark. Neglecting the b quark mass, the decay width for

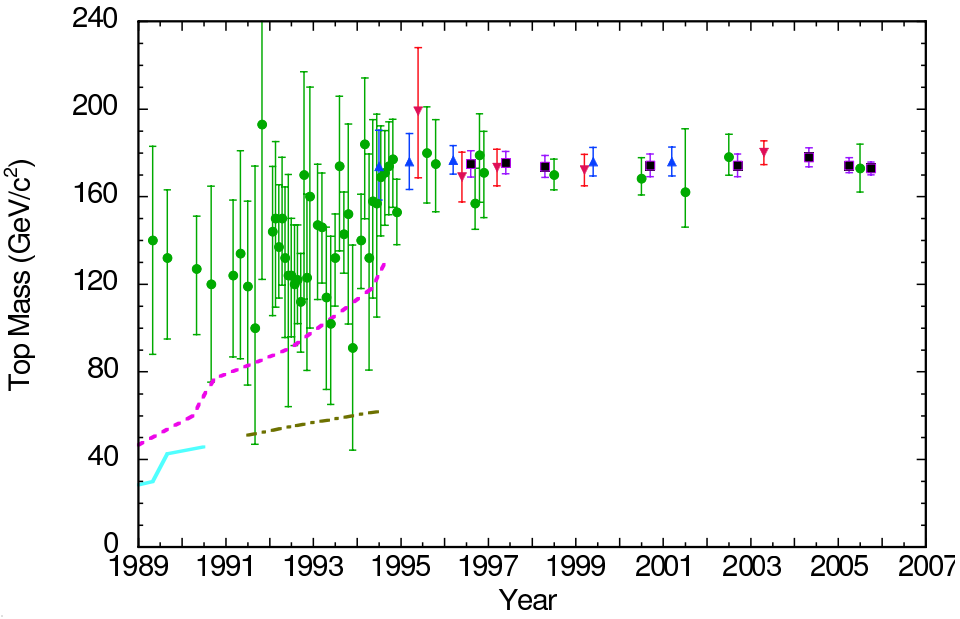

Figure 3.4: The trend of the limits on the top quark mass or its measurements [35, 36, 17]: (●) Indirect bounds from precision EW data, (■) World-average of direct measurements, (▲) published by CDF, and (▼) published by DØ. Lower bounds from $p\bar{p}$ colliders Sp$\bar{p}$S and the TEVATRON are shown as dash-dotted and dashed lines, respectively, and lower bounds from e^+e^- colliders (PETRA, TRISTAN, LEP and SLAC) are shown as a solid light gray line.

the process $t \to Wb$ can be written at leading order (LO) as

$$\Gamma_{\mathrm{LO}}(t \to Wb) = \Gamma_0 |V_{tb}|^2 (1-y)^2 (1+2y)\,, \tag{3.13}$$

with $\Gamma_0 = \frac{G_F\, m_t^3}{8\pi\sqrt{2}}$ and $y = (m_W/m_t)^2$. This partial width is proportional to the CKM matrix element $|V_{tb}|^2$ for which combined results of the unitarity triangle, assuming three fermion generations and an unitary CKM matrix, yield an allowed value of [17]

$$V_{tb} = 0.999152^{+0.000030}_{-0.000045}\,. \tag{3.14}$$

Including one-loop QCD corrections to the decay rate [37] in Eq. 3.13 becomes

$$\Gamma(t \to Wb) = \Gamma_{\mathrm{LO}} \cdot \left[1 - \frac{2\alpha_s}{3\pi} \cdot f(y)\right]\,, \tag{3.15}$$

with $f(y) = \frac{2\pi^2}{3} - 2.5 - 3y + 4.5y^2 - 3y^2 \ln y$. The QCD corrections of order α_s decrease the LO decay width by about 10%, yielding $\Gamma_t = 1.34\,\mathrm{GeV}$

at $m_t = 173\,\text{GeV}$. Corrections from EW interaction δ_{EW} and from taking into account the finite width of the W boson δ_Γ, both of the order of 1.5%, approximately cancel each other [31].

The corresponding top quark live time is $\tau = 1/\Gamma \approx 4 \times 10^{-25}\,\text{s}$. This is about an order of magnitude smaller than the hadronization time $\tau_{\text{had}} = 1/\Lambda_{\text{QCD}} = 3 \times 10^{-24}\,\text{s}$. Since the top quark decays before it can hadronize, it transfers its spin to the decay daughters.

With the direct observation of the single top quark at the TEVATRON the direct measurement of V_{tb} without assuming the unitarity of the CKM matrix became possible. The combined result of the CDF and the DØ experiment is $V_{tb} = 0.88 \pm 0.07$, with a lower bound of 0.77 at 95% confidence level [38]. The measured single top quark cross section and ratio of branching ratios in top quark decays $\frac{B(t\to Wb)}{B(t\to Wq)}$ can be used to obtain an indirect determination of the top quark width to be $\Gamma_t = 1.99^{+0.69}_{-0.55}\,\text{GeV}$ [39], in agreement with theoretical predictions.

3.1.4.2 Electric Charge

So far the top quark is the only quark whose electric charge wasn't directly measured. This is mainly due to the fact that neither DØ nor CDF associate the b, $\bar{b}$, and the $W^\pm$ to the top or anti-top quark such that the decays $t \to W^+\bar{b}$ and $t \to W^-b$ are not yet excluded. This leaves the possibility of the existence of an exotic quark Q_4 with charge $-4/3$ open. However, recent searches indicate that the Standard Model top quark is strongly favored and exclude a charge $-4/3$ top quark at the 95% C.L. [40].

3.1.4.3 Yukawa Coupling

The top quark is the Standard Model fermion most strongly coupled to the Higgs boson. With $v = 246\,\text{GeV}$ (see Eq. 2.41) and the latest measurement of the top quark mass (see Eq. 3.12), the Yukawa coupling for the top quark can be estimated using Eq. 2.43 as

$$\lambda_t = \frac{\sqrt{2}m_t}{v} = 1.0003 \pm 0.0035\,(\text{stat.}) \pm 0.0052\,(\text{syst.})\,. \tag{3.16}$$

3.2 Top Quark Physics at the LHC

After years of successfully measuring the top quark and its properties directly at the TEVATRON, finally the LHC started operating (see Sec. 4.2). With an center-of-mass energy of $\sqrt{s} = 7\,\text{TeV}$, the expected cross section for the top quark pair production is 165 pb, about a factor of 20 larger than at the Tevatron. This will provide a large sample of top quark pair events so that the statistical uncertainties will become negligible and will allow a detailed study of top quark physics.

3.2.1 Top Quark Production

The dominant production mode for top quark pairs is via the strong interaction. Additionally, single top quarks can be produced with a smaller rate via the EW interaction. In hadron-hadron collisions, perturbative QCD calculations of the hard scattering process are possible by invoking the Factorization Theorem, that establishes that the physics at high and low energy scales can be separated. Therefore, the top quark pair production cross section in pp collisions can be expressed as

$$\sigma_{pp\to t\bar{t}} = \sum_{i,j=q,\bar{q},g} \int dx_i dx_j f_i(x_i,\mu^2) f_j(x_j,\mu^2) \cdot \hat{\sigma}_{ij\to t\bar{t}}(\hat{s},\mu^2)\,. \tag{3.17}$$

The Parton Density Function (PDF) $f_i(x_i,\mu^2)$ describes the probability density to find a parton i inside the proton carrying the momentum fraction x_i. The PDFs are discussed in more detail in Appendix A. The cross section $\hat{\sigma}_{ij\to t\bar{t}}$ for the hard-scatter process is calculated in powers of the strong coupling constant α_s, describing the short distance interaction of the incoming partons. Both, the PDF and $\hat{\sigma}_{ij\to t\bar{t}}$, depend on the factorization scale μ_f and renormalization scale μ_r, which are usually taken to be the same $\mu_f = \mu_r \equiv \mu$. Figure 3.5 shows the dependence of the top quark pair cross section for different values of μ_f/m_t and μ_r/m_t. Usually, μ is chosen to equal the four-momentum transfer Q. Figure 3.6 shows a sketch of the factorization of a hard-scattering cross section.

The threshold on x_i and x_j for the top quark pair production is, assuming $x_i \approx x_j \approx x_{\text{thr}}$, a top quark mass of $m_t = 173\,\text{GeV}$, and the center-of-mass energy[2] $\sqrt{s} = 7\,\text{TeV}$ for the LHC [43],

$$x_{\text{thr}} \approx \frac{2m_t}{\sqrt{s}} = 0.05\,. \tag{3.18}$$

In Appendix A in Fig. A.2 PDFs for three different values of Q^2 for CTEQ6.6 are shown. Gluons start to dominate the top quark production for $x < 0.15$. At the LHC the production of $t\bar{t}$ will therefore be mainly ($\sim 90\%$) mediated via gluon-gluon fusion $gg \to t\bar{t}$, since there the production threshold is much smaller than 0.15 (see Eq. 3.18). Since the top quark mass is rather large in comparison to the center-of-mass energy at the TEVATRON ($\sqrt{s} = 1.96\,\text{TeV}$), and thus $x_{\text{thr}} \approx 0.176 > 0.15$, the top quark pair production there is dominated ($\sim 87\%$) by quark-antiquark annihilation $q\bar{q} \to t\bar{t}$. For the actual short distance production process the possible LO Feynman diagrams are shown in Fig. 3.7 for both, quark-antiquark annihilation and gluon fusion.

[2]The center-of-mass energy for two particles of masses m_1 and m_2 can be written as $\sqrt{s} = \sqrt{(E_1+E_2)^2 - (\vec{p}_1+\vec{p}_2)^2}$,where $E_i = \sqrt{\vec{p}_i^{\,2} + m_i^4}$ and $\vec{p}_i$ is the momentum of the i-th particle.

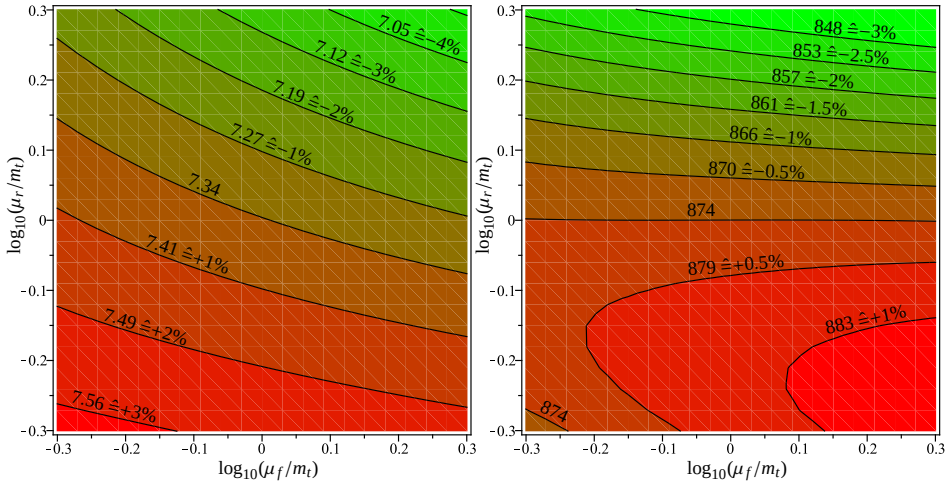

(a) (b)

Figure 3.5: Total hadronic cross section for the top quark pair production from the independent variation of the renormalization and factorization scale μ_r and μ_f for (a) the TEVATRON ($\sqrt{s} = 1.96\,\text{TeV}$) and (b) the LHC (here: $\sqrt{s} = 14\,\text{TeV}$) with CTEQ6.6. The μ_r and μ_f are varied between $m_t/2$ and $2m_t$ [41].

The large top quark mass, and thus the short lifetime (see Sec. 3.1.4.1), ensures that the top quark pair production is a short-distance process and that the perturbative expansion, given by a series in powers of the QCD coupling constant $\alpha_s(m_t) \sim 0.1$, converges rapidly. Applying this expansion to the cross section from Eq. 3.17 yields

$$\hat{\sigma}_{ij}(\rho, m_t^2, \alpha_s(\mu^2), \mu^2) = \frac{\alpha_s^2(\mu^2)}{m_t^2} f_{ij}(\rho, \alpha_s^2(\mu^2), \mu^2/m_t^2)\,, \tag{3.19}$$

with $\rho = {}^{4m_t^2}/_{\hat{s}}$ and $\hat{s} = x_i\, x_j\, s$. The dimensionless scaling functions f_{ij} are

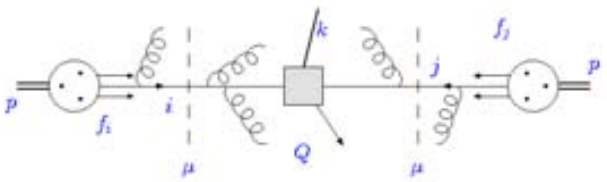

Figure 3.6: Factorization for the hard-scattering cross sections in the QCD improved parton model [42].

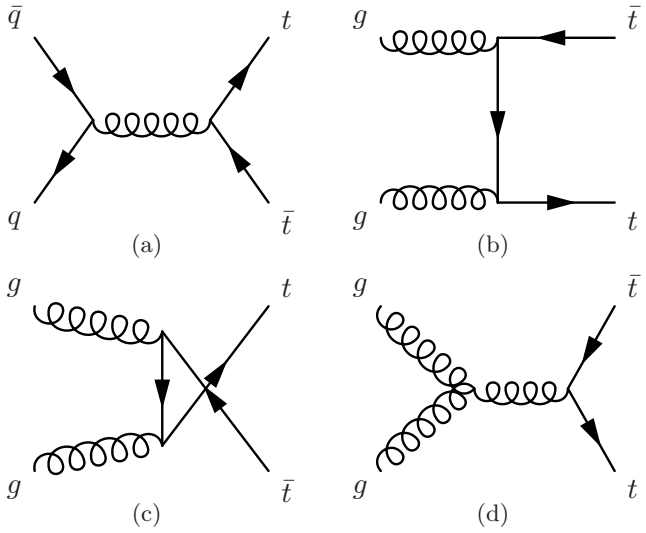

Figure 3.7: The LO Feynman diagrams for the actual hard scattering top quark pair production process. (a) shows the quark-antiquark annihilation, dominating at the TEVATRON, (b),(c), and (d) the gluon-gluon fusion, dominant at the LHC.

perturbatively computable and can be expanded in α_s as [44]

$$\begin{aligned} f_{ij}(\rho, \alpha_s(\mu^2), \mu^2/m_t^2) &= f_{ij}^{(0)}(\rho) \\ &+ 4\pi\,\alpha_s(\mu^2)\left[f_{ij}^{(1)}(\rho) + \bar{f}_{ij}^{(1)}(\rho)\ln\frac{\mu^2}{m_t^2}\right] \\ &+ \sum_{n=2}^{\infty}\alpha_s^n(\mu^2) f_{ij}^{(n)}(\rho, \mu^2/m_t^2)\,. \end{aligned} \tag{3.20}$$

Here $f_{ij}^{(0)}$ is the LO, $f_{ij}^{(1)}$ and $\bar{f}_{ij}^{(1)}$ the next-to-leading order (NLO) and $f_{ij}^{(2)}$ the next-to-next-to-leading order (NNLO) contribution. The NLO in the QCD coupling has been calculated in [45] taking into account the full spin dependence of the top quarks. For the next-to-leading logarithm (NLL) soft-gluon emissions were taken into account [46]. A complete set of velocity-enhanced terms for the NNLO near the partonic threshold was derived in [47], taking into account also potential-gluon exchanges. It was also proven that there are no enhancements due to sub-leading soft-gluon couplings multiplying the leading Coulomb singularity. The most recent theoretical prediction for the top quark pair production cross section yields $\sigma_{t\bar{t}} = 164.6 \pm {}^{11.4}_{15.7}\,\text{pb}$ [41, 47, 48] for a top quark mass of 172.5 GeV.

The different measurements of the top quark production cross section at the TEVATRON and expected results for the LHC as a function of the

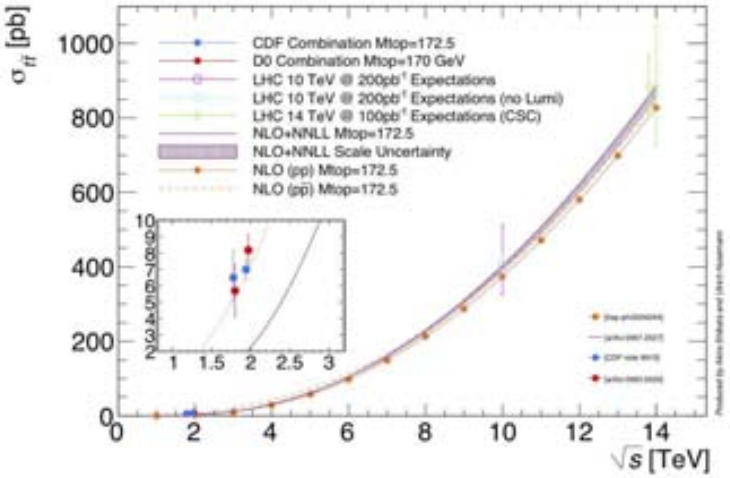

Figure 3.8: Different measurements of the top quark production cross section at the TEVATRON and expected results for the LHC as a function of the center-of-mass energy [49].

center-of-mass energy are shown in Figure 3.8.

The production of a single top quark via the EW interaction involving the tWb vertex is also possible. Three different production modes are distinguished, depending on the virtuality ($Q^2 = -q^2$) of the associated W boson:

- t-channel ($q^2 = \hat{t}$): a virtual, space-like W boson converts a b quark into a top quark (see Fig. 3.9 (a) and (b)). This is the dominant process at the TEVATRON and the LHC. The theoretical prediction for the production cross section at the LHC is $\sigma_{\text{t-channel}} = 66\,\text{pb}$ [50, 51];

- s-channel ($q^2 = \hat{s}$): a time-like W boson with $q^2 \geq (m_t + m_b)^2$ is produced by the fusion of two quarks of the same $SU(2)$-isospin doublet (see Fig. 3.9 (c)) The theoretical prediction for the production cross section at the LHC is $\sigma_{\text{s-channel}} = 4\,\text{pb}$ [50, 51];

- associated production ($q^2 = m_W^2$), or Wt-channel: the top quark is produced in association with a real W boson with $q^2 = m_W^2$ (see Fig. 3.9 (d)). This process is suppressed at the TEVATRON. However, at the LHC this process exceeds the s-channel. The theoretical prediction for the production cross section at the LHC is $\sigma_{Wt\text{-channel}} = 15\,\text{pb}$ [50, 51, 52].

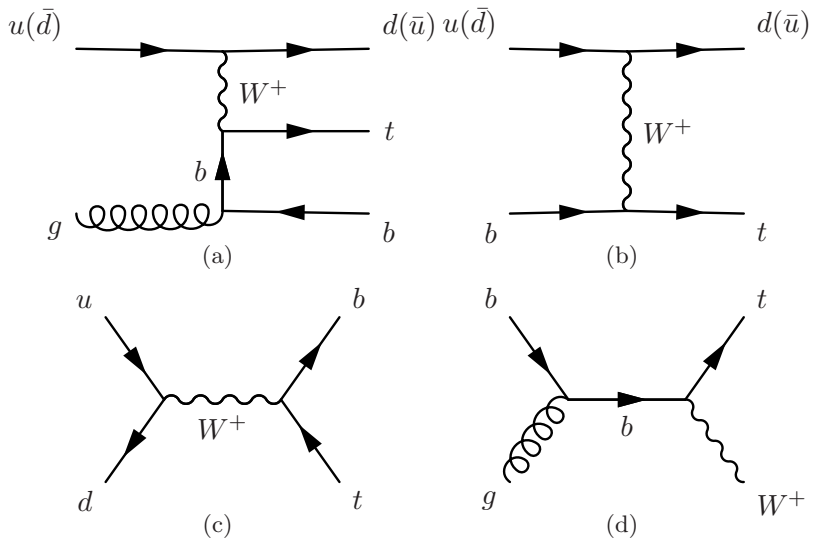

Figure 3.9: The Feynman diagrams for single top quark production: (a) and (b) t-channel, (c) s-channel, and (d) associated production (Wt-channel).

3.2.1.1 Non-Standard Model Production

At leading order in perturbative QCD top quark pair production is symmetric under charge conjugation. Higher order radiative corrections at $\mathcal{O}(\alpha^3)$ generate a charge asymmetry for the production via quark-antiquark annihilation. Thereby the top quark becomes more abundant in the direction of the incoming light quark. The total asymmetry in the top quark pair rest frame is defined as

$$A^{t\bar{t}} = \frac{N(\Delta y > 0) - N(\Delta y < 0)}{N(\Delta y > 0) + N(\Delta y < 0)}\,, \tag{3.21}$$

where $\Delta y = y_t - y_{\bar{t}}$ is the rapidity difference between the top and the anti-top quark, identified by the lepton charge. Recent measurements at the CDF experiment yielded an asymmetry in the $t\bar{t}$ rest frame of $A^{t\bar{t}} = 0.158 \pm 0.075$ [53]. This is about two standard deviations above the predicted NLO value of 0.058 ± 0.009 and could represent a first indication of physics beyond the Standard Model.

An example for top quark production involving physics beyond the Standard Model is the production of a heavy neutral boson Z' with a subsequent decay into a top quark pair (for details see e.g. [54]). No such process were observed at the Tevatron and limits on Z' were set by the CDF [55] and the DØ collaboration [56].

3.2.2 Top Quark Decay

The top quark decays via the weak interaction almost always into a b quark and a W boson, since

$$\frac{BR(t \to Wb)}{BR(t \to Wq)} = \frac{|V_{tb}|^2}{(\sum_q |V_{tq}|^2)} = |V_{tb}|^2 \simeq 1\,, \tag{3.22}$$

with $q = b, s, d$. This assumes three fermion families and the unitarity of the CKM matrix. Due to this strong CKM-suppression only the dominant channel $t \to Wb$ is considered in the further discussion. The decay width of the top quark was discussed in Sec. 3.1.4.1.

With the assumption of $|V_{tb}| = 1$, three different decay channels of top quark pairs are distinguished which are determined by the decay mode of the W boson:

- di-leptonic channel: $t\bar{t} \to \bar{\ell}\,\nu_\ell\,b\,\ell'\,\bar{\nu}_{\ell'}\,\bar{b}$ with a relative contribution of 10.3% [17],
- semi-leptonic channel: $t\bar{t} \to q\,\bar{q}'\,b\,\ell\,\bar{\nu}_\ell\,\bar{b} + \bar{\ell}\,\nu_\ell\,b\,q\,\bar{q}'\,\bar{b}$ with a relative contribution of 43.5% [17],
- fully hadronic channel: $t\bar{t} \to q\,\bar{q}'\,b\,q''\,\bar{q}'''\,\bar{b}$ with a relative contribution of 46.2% [17].

For the relative contributions the cases $\tau \to e\,\nu_e\nu_\tau$ and $\tau \to \mu\,\nu_\mu\nu_\tau$ are considered as $\ell = e, \mu$. Table 3.1 lists in detail the possible decay channels and their branching ratios at the Born level, i.e. at LO.

In Fig. 3.10 a complete LO Feynman diagram is shown for the top quark pair production via gluon-gluon fusion and its further decay into the semi-leptonic channel. The signature of the semi-leptonic decay is one charged lepton ℓ (e or μ) from the leptonic W boson decay, missing transverse energy (E_T^{miss}) signaling the neutrino ν_ℓ (see Sec. 5.6), two b quarks and two quarks of the first or second quark generation (u, d, c, or s) from the hadronic W boson decay. Additional partons may appear due to initial state radiation (ISR) or final state radiation (FSR).

In Sec. 2.2 the concept of quark mixing was introduced, mentioning that this feature depends on the fact, that the W boson does not couple to right-handed fermions. This suggests the study of decay angular distributions to directly check the $V - A$ nature of the tWb coupling as well as the relative coupling of longitudinal and transverse W bosons to the top quark. The ratios of the decay rates into the three W boson helicity-states longitudinal $h^W = 0$, left-handed $h^W = -1$, and right-handed $h^W = +1$ are given at LO by

$$\Gamma(h^W = -1) : \Gamma(h^W = 0) : \Gamma(h^W = +1) = 1 : \frac{m_t^2}{2m_W^2} : 0\,. \tag{3.23}$$

Table 3.1: List of all decay channels of the top quark pair assuming $|V_{tb}| = 1$ at the Born level. The assignation to di-leptonic, semi-leptonic and fully-hadronic channel in the first row does not reflect the actual assignment used in this analysis for leptonic τ decays (see text for explanation).

channel	decay mode	BR at LO
di-leptonic	$t\bar{t} \to e^+\nu_e\, e^-\bar{\nu}_e\, b\,\bar{b}$	$1/81$
	$t\bar{t} \to e^+\nu_e\, \mu^-\bar{\nu}_\mu\, b\,\bar{b}$	$2/81$
	$t\bar{t} \to e^+\nu_e\, \tau^-\bar{\nu}_\tau\, b\,\bar{b}$	$2/81$
	$t\bar{t} \to \mu^+\nu_\mu\, \mu^-\bar{\nu}_\mu\, b\,\bar{b}$	$1/81$
	$t\bar{t} \to \mu^+\nu_\mu\, \tau^-\bar{\nu}_\tau\, b\,\bar{b}$	$2/81$
	$t\bar{t} \to \tau^+\nu_\tau\, \tau^-\bar{\nu}_\tau\, b\,\bar{b}$	$1/81$
semi-leptonic	$t\bar{t} \to e^+\nu_e\, q\,\bar{q}'b\,\bar{b}$	$12/81$
	$t\bar{t} \to \mu^+\nu_\mu\, q\,\bar{q}'b\,\bar{b}$	$12/81$
	$t\bar{t} \to \tau^+\nu_\tau\, q\,\bar{q}'b\,\bar{b}$	$12/81$
fully hadronic	$t\bar{t} \to q\bar{q}'q''\,\bar{q}''b\,\bar{b}$	$36/81$

This yields a decay ratio of 70% into longitudinal, 30% into left-handed, and no decay into right-handed W bosons.

Because of the short life time of the top quark, the helicity is propagated to the decay products. It can be measured via the decay angular distribution in the rest frame of the top quark as [57]

$$\frac{1}{\Gamma}\frac{d\,\Gamma}{d(\cos\theta_i)} = \frac{1}{2}(1 + \alpha_i \cos\theta_i)\,, \qquad \alpha_i = \begin{cases} +1.0 & \ell^+ \text{ or } \bar{d} \text{ quark} \\ -0.31 & \bar{\nu} \text{ or } u \text{ quark} \\ -0.41 & b \text{ quark} \end{cases} \tag{3.24}$$

where θ_i is the angle between the top quark spin and the i-th decay product. The degree of correlation for each decay product is given by α_i, such that the largest effects appear in the angular distribution between the top quark spin and the charged lepton. Figure 3.11 illustrates the case of the decay of a spin up top quark.

For the production via the strong interaction the spin between top and anti-top quarks is significantly correlated, depending on the top quark pair production mechanism. This offers a possibility to probe the dominant production process realized in an experiment. As can be seen in Eq. 3.24, the $\ell^+\ell^-$ final state is favored to estimate the spin correlation. The spin correlation for top quark pairs can be expressed with the following normalized double-differential distribution [59]

$$\frac{1}{\sigma}\frac{d^2\sigma}{d(\cos\theta_i)d\cos(\bar{\theta}_{\bar{i}})} = \frac{1 + C\,\alpha_i\,\bar{\alpha}_{\bar{i}}\cos\theta_i\cos\bar{\theta}_{\bar{i}}}{4}\,, \tag{3.25}$$

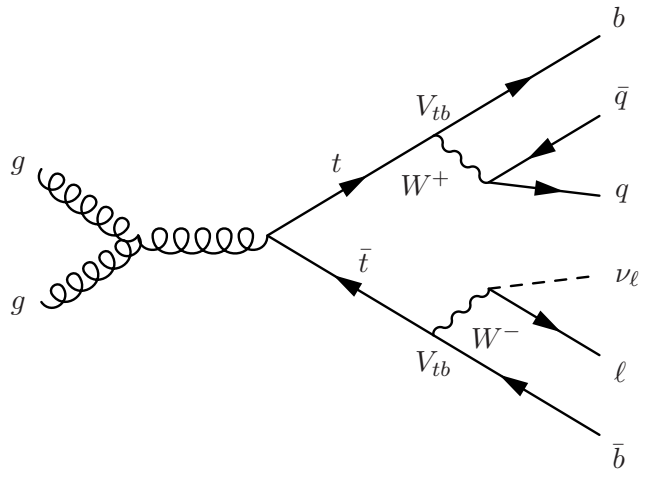

Figure 3.10: The Feynman diagram for the top quark production via gluon-gluon fusion and the further decay in the semi-leptonic channel.

with α_i as defined in Eq. 3.24 (inverted for $\bar{t}$) and θ_i ($\bar{\theta}_{\bar{i}}$) the angle between the i-th particle and the top (anti-top) quark spin direction. The coefficient C gives the degree of the spin correlation between top and anti-top quarks. In the helicity basis it is defined as

$$C = \frac{N(t_L\bar{t}_L + t_R\bar{t}_R) - N(t_L\bar{t}_R + t_R\bar{t}_L)}{N(t_L\bar{t}_L + t_R\bar{t}_R) + N(t_L\bar{t}_R + t_R\bar{t}_L)}\,. \tag{3.26}$$

where N denotes the number of events of top pairs with corresponding spin. At the LHC the coefficient C is about 0.332 at lowest order in α_s [59]. The spin-correlation coefficient can be affected by physics processes beyond the Standard Model and its measurement is therefore of interest in searches for new physics.

Non-Standard Model Decays: FCNC decays in the Standard Model are highly suppressed by the Glashow-Iliopoulos-Maiani (GIM) mechanism, with the largest expected branching ratio being for the top quark decay $t \to cg$ of $\mathcal{O}(10^{-12})$. Since this value is not in the reach of present collider experiments, any measured value of FCNC branching rations would be a signal for new physics. In optimistic scenarios of for instance supersymmetric models, two-Higgs doublet or quark-singlet models predict values of $\mathcal{O}(10^{-4})$ to $\mathcal{O}(10^{-5})$. For more details see for example [60].

In the Minimal Supersymmetric extension of the Standard Model (MSSM) five physical Higgs bosons exist, among those a charged Higgs boson pair $H^{\pm}$. In the case of low masses of this charged Higgs bosons, i.e. $m_{H^{\pm}} < m_t - m_b$, the top quark can decay as $t \to bH^+$, in competition to $t \to bW^+$. Recently limits on that process have been set by the CDF [55]

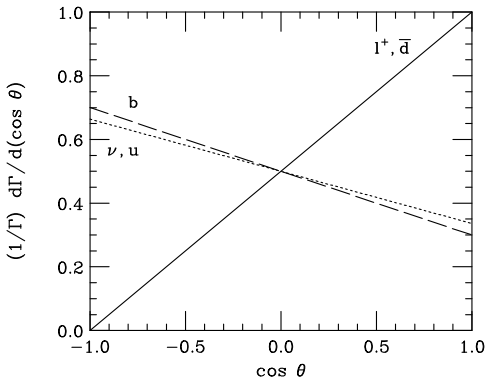

Figure 3.11: Angular correlation in the decay of a spin up top quark. Shown is the angle between the spin axis of the top quark and the particle in the rest frame of the top quark (see labels) [58].

and the DØ collaboration [61] and excluded branching ratios larger than 0.1 to 0.3 for charged Higgs boson masses of 60 GeV to 150 GeV [55].

3.2.3 Backgrounds

In experiments only the final decay products can be measured. This means, that the final states of the different top quark pair decay channels listed in Table 3.1 can be mimicked by other processes.

The distinction is drawn between physics and instrumental backgrounds which mimic the top quark pair final state signature. Physics backgrounds are characterized by having the same final state particles as the signal process, in case of this analysis the semi-leptonic decay $t\bar{t} \to \ell\nu_\ell q\,\bar{q}\,b\,\bar{b}$. Instrumental backgrounds originate from mis-identification of physical objects. Another source for instrumental backgrounds could be the incomplete coverage of the detector around the interaction, such that parts of the final state particles may escape without being detected.

Figure 3.12 shows the cross sections and the resulting event rates as a function of the center-of-mass energy $\sqrt{s}$ for some of those backgrounds as well as for the top quark pair construction. The gap between cross sections of some processes, e.g. the top quark pair production, originates from the different initial particles at the TEVATRON and the LHC. Unlike at the LHC, at the TEVATRON protons and anti-protons are collided.

3.2.3.1 Vector Boson with Associated Jets

An important physics process at high energy hadron colliders is the production of a W or a Z boson in association with jets (see Fig. 3.13). The production of a W boson in association with at least four jets results in

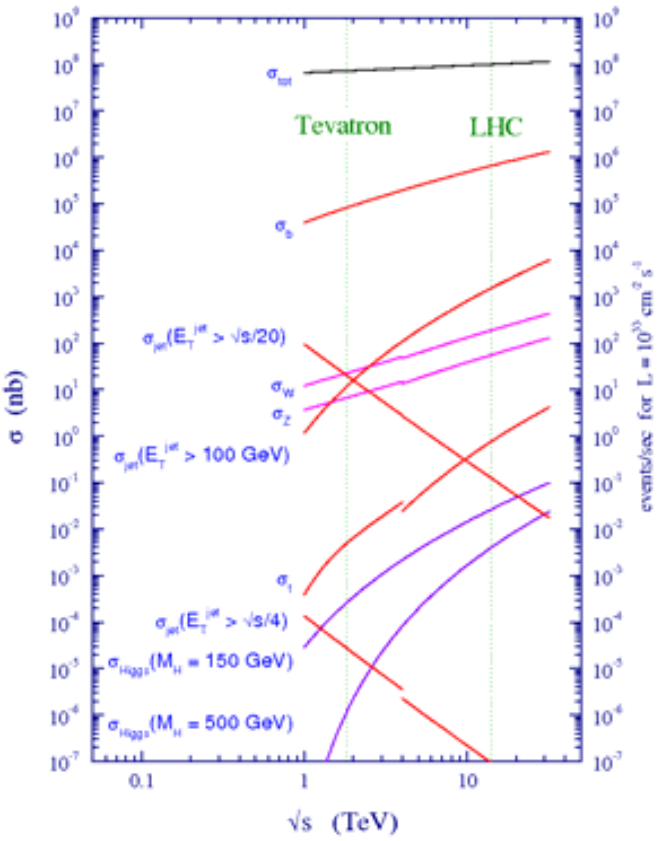

Figure 3.12: Cross sections and event rates per second as a function of the center-of-mass energy for different physics processes [62].

the same final states as the semi-leptonic top quark pair decay described in Sec. 3.2.2 such that the W boson with associated jets is a physics background.

This process turns out to be one of the main backgrounds for top quark pairs which requires a thorough understanding of such W boson plus n jets events (from now on W+n jets). However, the total rate for W+4 jets is poorly predicted by event generators because of the LO description, although NLO calculations recently became available [**?**]. The W boson plus jets background can be estimated via data-driven methods (see Sec. 7.3.2). A method, based on recursion relation, was introduced in [63]. The large uncertainties on this method for higher jet multiplicities can be controlled profiting from the relation of the cross sections for W+n jets and W+(n+1) jets

$$\alpha = \frac{\sigma(W + (n+1))_{\text{jets}})}{\sigma(W + n_{\text{jets}})}\,, \tag{3.27}$$

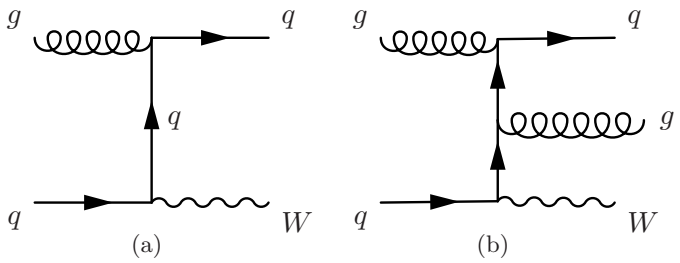

Figure 3.13: Subset of Feynman diagrams for the production of a W boson in association with (a) one and (b) two jets in the final state.

where α at lowest order ($n = 0$) refers to α_s. This method is referred to as Berends scaling [63].

The production of a Z boson in association with jets has a contribution a factor of 10 smaller than those with a W boson, a factor three just due to the branching ratio for the decay of the boson into leptons.

3.2.3.2 Multijets

Another major source of background is the production of QCD multijet events via the strong interaction which have an extremely large cross sections (see Fig. 3.12). The production of a quark pair (dijet) in association with additional jets from FSR is drawn in Fig. 3.14.

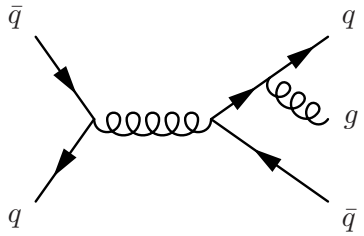

Figure 3.14: Feynman diagram of a dijet event with a gluon radiated in the final state.

Quarks and gluons can be misidentified as electrons due to electromagnetic (EM) fluctuations in the fragmentation of the jets. During this fragmentation many electromagnetically charged particles appear inside this jet, mostly pions. Inside jets also π^0's appear, which decay into two photons which eventually can mimic an electron inside the detector.

Furthermore, c and b quarks can yield to a charged lepton and a neutrino, i.e. missing transverse energy, in the final state. For example an isolated muon, i.e. with only a few electromagnetic activities around the

reconstructed object, can appear originating from a b quark decay. Another source of missing transverse energy, that leads to a similar final state as the semi-leptonic top quark decay, is the mis-reconstruction of a jet or the mis-measurement of the muon transverse momentum.

Large efforts are made to suppress the contribution of this reducible background, which eventually needs to be measured directly in data, since no theoretical prediction of it is accurate enough.

3.2.3.3 Single Top

The process of single top quark production was introduced in Sec. 3.2.2. At the LHC the main contribution comes from the t-channel (see Fig. 3.9 (a) and (b)) and the s-channel is the most suppressed one. In case of additional gluon radiation and the leptonic decay of the associated W boson, this channel is a physics background to the top quark pair decay process. It is a small contribution in comparison to the former introduced backgrounds.

3.2.3.4 Dibosons

The associated production of two weak bosons (WW, WZ, and ZZ) is a small background. The largest predicted cross section corresponds to W^+W^- production (see Fig. 3.15). In this case the signal final state can be mimicked one W boson decays leptonically and the other hadronically, together with ISR or FSR.

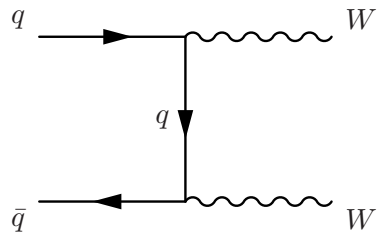

Figure 3.15: Subset of Feynman diagrams for the associated production of two W bosons.

3.2.4 Event Generation

In order to study the topology and characteristics of top quark pair events Monte Carlo (MC) simulations are performed and compared with the data collected with the detector. The generation of those MC events consists of the production of a set of particles produced during the collisions. Each generated event contains the particles from a single interaction with a vertex located at the geometric origin. In these events the truth refers to a history

of the interactions from the generator, including incoming and outgoing particles. A record is kept for every particle, whether it is later to be passed through the detector simulation (see Sec. 4.3.8) or not.

In order to take the substructure of the protons as initial particles into account, a PDF is used the first stage of the event generation when selecting the partons of the hard scattering process. The PDFs are discussed in Appendix A.

The hard scattering processes describes the interaction of the incoming and the production of outgoing partons. Before and after this process, QCD radiation of the initial and final states, i.e. ISR and FSR, occurs. Also the breakup of the colliding protons, i.e. beam remnants of partons which did not take part of the hard interaction, have to be taken into account and are referred to as underlying events. All these semi-hard interactions interfere due to the color connection with the main event and may thus influence the observables of the final state particles. Figure 3.16 shows a sketch of the process $pp \to t\bar{t}H$ including all these effects.

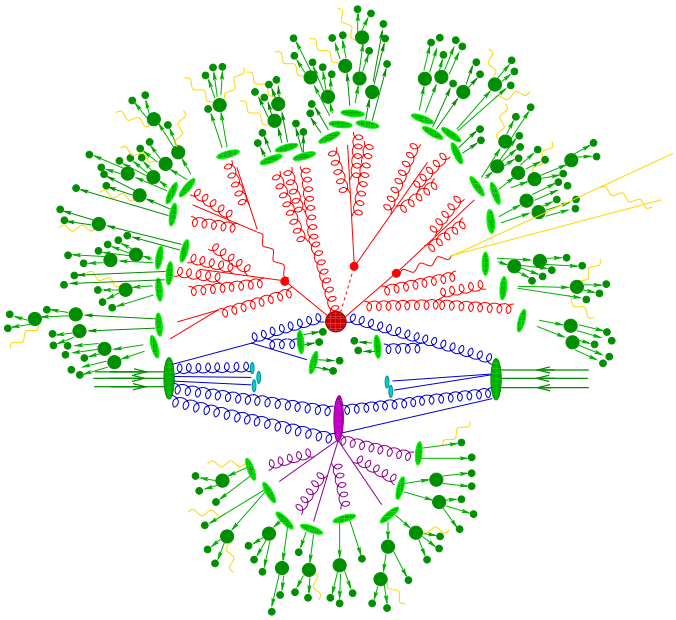

Figure 3.16: Sketch of a $pp \to t\bar{t}H$ event produced by an event generator. The hard interaction (big red blob) is followed by the decay of both top quarks and the Higgs boson (small red blobs). Additional hard QCD radiation is produced (red) and a secondary interaction takes place (purple blob), i.e. representing an underlying event, before the final-state partons hadronize (light green blobs) and hadrons decay (dark green blobs). Photon radiation occurs at any stage (yellow). ISR (blue) and FSR (red) occurs before and after the hard interaction [64].

At high instantaneous luminosity multiple proton-proton collisions in the same bunch crossing, referred to as minimum bias events, can occur. Minimum bias events can not be reliably calculated since these processes are soft and thus dominated by non-perturbative interactions. In the analysis of data corresponding to an integrated luminosity of $35\,\mathrm{pb}^{-1}$, minimum bias contributions were taken into account in the MC simulation. By taking the number of vertices as a measure for the number of additional proton-proton interactions, the MC samples were re-weighted in order to fit the simulation to data.

Dedicated event generators with parameter tunes to data are used in order to model the underlying event and pile-up contributions.

3.2.4.1 Hadronization

For short distance interactions QCD perturbation theory is valid for the description of partons outgoing from the hard scattering process. With growing distance, the QCD interaction becomes very strong and the perturbation theory breaks down. In this so-called confinement regime, quarks and gluons form color-less hadrons. This transition is referred to as hadronization or fragmentation, and is governed by soft non-perturbative processes that can not be calculated accurately. For details see for example [14].

Three different models exist to describe the hadronization process: for Pythia [65] the string fragmentation model is used, for Herwig [66] and Sherpa [67] the cluster fragmentation model. The independent fragmentation is implemented in Isajet [68], but is not used for this analysis.

In case of the string fragmentation model a string of gluons, a so-called gluon tube, is created, which represents the color field between two outgoing partons. With a growing separation of the two partons, the potential energy of the gluon tube increases. The gluon tube breaks up when enough energy is available to create additional quark anti-quark pair. This process is repeated until a hadron is formed from the quarks.

The cluster fragmentation is performed in the pre-confinement regime. Clusters are formed of nearby quarks while remaining gluons are split up into quark anti-quark pairs. Each cluster decays into hadrons, depending on the phase space available to the decay products.

Many hadrons are unstable and decay into lighter particles, including charged leptons and neutrinos. The particle shower, which appears based on the fragmentation process, is referred to as a jet. The total momentum of a jet corresponds roughly to the momentum of the initially emitted quark and is therefore taken as its representational final state in the event.

3.2.4.2 Generators

A large variety of generators are implemented within the A Toroidal LHC ApparatuS (ATLAS) event generation framework, divided into general purpose generators as for example Pythia [65], Herwig [66], and Sherpa [67], and specialized generators, as e.g. Alpgen [69], MC@NLO [50], and AcerMC [70], while their usage depend on the physics process. Details on which generator was used for the samples used in this study can be found in Sec. 3.2.5.

General Purpose Generators: General purpose generators produce complete events starting from the proton-proton initial state and can be used standalone or, in order to improve the description of certain final states, with specialized generators.

Pythia [65], extensively tested at e^+e^- and hadron colliders and providing a large number of built-in processes, starts with a hard scattering process, calculated to the lowest order in QCD, where additional QCD and QED radiation can be added in form of shower approximations. The accuracy of this approximation depends on the emission angle and gets worse with increasing angles.

Herwig [66] also comes with a large number of built-in process and was tested and tuned at the Tevatron. For underlying event generation it is used together with the Jimmy [71] package. Although other generators are used for specific final states, Herwig and Pythia act as the benchmarks [72].

Sherpa [67] is written in C++, in contrary to Herwig and Pythia, which are written in Fortran. It implements the prescription of duplicated removal described in [73] to match fixed-order QCD matrix elements to QCD showers. It is therefore expected to better describe events with large multiplicity of isolated jets than for example Herwig and Pythia.

Specialized Generators: Specialized generators are used to improve the accuracy of specific decays or final states and are used in conjunction with general event generators.

Alpgen [69] is used for the generation of events with several well-separated hadronic final states. For those the fixed order QCD matrix element is expected to give a better approximation than the shower approximation of Herwig and Pythia. It is however interfered to Herwig and Pythia, which are used to generate parton shower and subsequent hadronization. It also includes an algorithm to reject events in order to avoid double counting of contributions generated by both, the matrix element calculation and parton showering.

MC@NLO [50] produces hard scattering processes at NLO. Its generated events are used as input for Herwig. For example for top quark pair

production, the description of the transverse momentum distribution of the tops quarks is expected to be better modeled than for general purpose generators. Due to the fact that MC@NLO used one loop corrections, events with positive and negative weight are generated.

In order to avoid the negative weights used by MC@NLO, the Positive Weight Hardest Emission Generator (POWHEG) generator [74] can be used. It generates first the hardest radiation with a technique that results on into positive weighted events by using the exact NLO matrix elements.

AcerMC [70] is primarily dedicated to the production of W or Z bosons in association with several jets, including those originating from b quarks. After producing a partonic final state by running it standalone, Pythia is used for the showering.

3.2.5 Monte Carlo Samples

All Monte Carlo (MC) samples have been generated at a center-of-mass energy of 7 TeV. The effect of pile-up, i.e. additional proton-proton interactions in the same beam crossing, has not been simulated in the MC samples used for the measurement with an integrated luminosity of $2.9\,\mathrm{pb}^{-1}$. This was however done for the measurement with the complete data set collected during 2011 ($35\,\mathrm{pb}^{-1}$). Subsequent detector and trigger simulation, followed by offline reconstruction, has been performed with standard ATLAS software making use of GEometry ANd Tracking 4 (GEANT4) (see Sec. 4.3.8).

To generate $t\bar{t}$ signal and single top quark events, MC@NLO v3.41 [50] was used with the PDF set CTEQ6.6 [75], assuming a top quark mass of 172.5 GeV and normalizing the $t\bar{t}$ cross-section to the prediction of 160 pb at approximate NNLO [41, 76]. For single top the s-channel, t-channel, and Wt-channels were included, normalized to the MC@NLO cross-section. The diagram removal scheme [77] for Wt was used to remove overlaps with the $t\bar{t}$ final state. Those diagrams occur at higher order corrections of the Wt-channel. They can be interpreted as a top anti-top quark pair at LO with a subsequent decay of the anti-quark into a $b\bar{W}$ pair. This yields an interference between Wt and $t\bar{t}$ production and is therefore suppressed.

In the study of systematic uncertainties $t\bar{t}$ samples have been generated also with Powheg, using Herwig and Pythia for the hadronization. To estimate the uncertainty due to ISR and FSR, samples with AcerMC and Pythia have been generated.

The W+jets, Z+jets, QCD multijet, and diboson sample have been generated with Alpgen v2.13 [69] and the PDF set CTEQ6L1 [78]. For the hadronization Herwig was used. The MLM matching scheme [73] with matching parameters `RCLUS`=0.7 and `ETCLUS`=20 was used to remove overlaps between samples with $n+1$ and n jets. For the MLM (or CKKW) matching scheme a jet multiplicity n is selected according to a probability

function proportional to the tree-level cross section for that jet multiplicity divided by the sum of the cross section for all N possible multiplicities (currently $N = 6$). The jet momenta are distributed following the matrix element and their resolution is determined via the anti-k_t algorithm.

The W + jets samples are generated separately for W + light-flavor jets, $Wb\bar{b}$+jets, $Wc\bar{c}$+jets and Wc+jets. In the light-flavor jets sample hard jets from matrix elements arising from gluons, u, d, s, and c quarks are included and treated as massless. However, the $Wb\bar{b}$ + jets and W + light-flavor jets have an overlap of about 4% resulting in a double counting of events. The same is valid for those events with c-quarks. Therefore, these samples have been combined applying a procedure to avoid double-counting of heavy-flavor final states between the matrix element calculation and the parton shower by vetoing certain classes of events in each sample.

The so-called jet based overlap removal exploits the different strengths of the matrix element and the parton shower. The matrix element is better suited for large opening angles between the quarks, whereas the parton shower describes the collinear gluon splitting much better. These properties can be included by considering reconstructed quantities like jets. The matrix-element heavy-flavor quark pairs are required to be matched to different reconstructed jets, while heavy-flavor quark-pairs from the parton shower are required to be inside one reconstructed jet. The definition of the matching is done with a simple geometric cut, $\Delta R < R_0$, where R_0 is the cone size of the jet algorithm in use and ΔR is the distance between the jet axis and the heavy flavor quark in the $\eta - \phi$ plane.

To handle the unmatched jets (for cone $R = 0.4$ about 50%), a ΔR-based overlap removal is applied in addition to the jet based one. In this algorithm the matching is performed by considering the distance ΔR between two heavy flavor quarks. For the migration of event, that occurs in these schemes, only an upgrading of events was consider, such that events can only move from lighter quark samples to heavier quark samples. Figure 3.17 shows a summary of how the final samples are built.

Both, the W + jets and the Z + jets samples, were normalized with a k-factor of 1.22. This is done to achieve an agreement of the normalization to NNLO calculations with FEWZ [80] for W+jets and the MCFM [81] for Z+jets. For the Z/γ^* + jets the phase space has been restricted to $m(\ell^+\ell^-) > 40\,\text{GeV}$.

For the QCD multijet samples the generator-level p_T of the leading parton must be at least 35 GeV. QCD multijet events have also been subjected to filtering prior to the full event simulation: events must have either a true muon within $|\eta| < 2.8$ with a $p_T \geq 10\,\text{GeV}$, or contain at least three true jets (reconstructed from simulated stable particles after hadronization with the anti-k_T algorithm with parameter R=0.4) with a $p_T \geq 25\,\text{GeV}$, as well as an additional true jet with a $p_T \geq 17\,\text{GeV}$. The QCD multijet samples were normalized using the ALPGEN prediction. All events were hadronized with

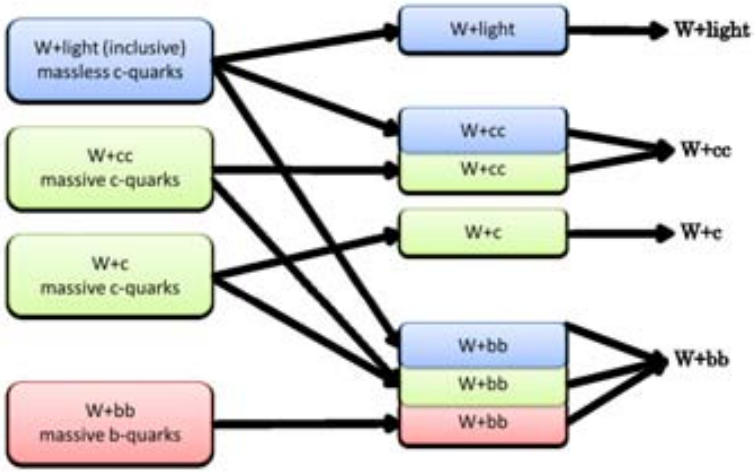

Figure 3.17: Summary of the final W + jets sample composition [79].

Herwig, using Jimmy for the underlying event model. The QCD multijet Monte Carlo is used in this analysis only to perform validation studies of the procedure to predict its normalization and shape. Otherwise, the QCD multijet background is fully estimated in data as discussed in Sec. 7.3.1.

Appendix C summarizes the different Monte Carlo samples that have been used throughout the analysis.

Chapter 4

The Experimental Setup

This chapter describes the experimental setup used for this measurement, mainly consisting of the ATLAS detector. This multipurpose detector allows to study proton-proton collisions at the Large Hadron Collider (LHC). The LHC is hosted and operated by the European Organization for Nuclear Research (CERN), the world's largest particle physics laboratory. CERN was founded in 1954 and hosted already several accelerators, among those the Synchrocyclotron (1957-1991), the Low Energy Antiproton Ring (LEAR) (1982-1996), and the Large Electron-Positron Collider (LEP) (1989-2000).

This chapter is organized as follows: in Sec. 4.1 the complete sequence of the LHC injector chain and in Sec. 4.2 the final acceleration of the protons in the LHC to the center-of-mass energy of 7 TeV are described. In Sec. 4.3 the ATLAS detector with all its subsystems is explained, introducing also the particle interaction and the detector simulation.

4.1 The Injector Chain

Protons are injected in the LHC trough a chain of accelerators (see Fig. 4.1) discussed in the following. The Linear Accelerator 2 (LINAC2) is an Alvarez Proton Linac which accelerates protons beams coming from the Radio Frequency Quadrupole (RFQ) from 750 keV up to 50 MeV with a frequency of 50 MHz [82]. It is basically the same machine that was originally built for the Proton Synchrotron Booster (PSB) and launched in 1978 [83].

The PSB was built in 1972 and consists of four superimposed synchrotron rings, each of 25 m circumference. It collects the incoming protons in 8 bunches, each of $1.8 \cdot 10^{12}$ protons. The four bunches of the four rings are transferred to the Proton Synchrotron (PS) with an energy of 1.4 GeV [85].

In the PS these bunches are accelerated to 25 GeV. To accomplish the required bunch spacing of 25 ns as needed by the Super Proton Synchrotron (SPS) and the LHC the injected bunches are de-bunched by lowering the radio frequency voltage. The beam is recaptured at a bunch spacing of 25 ns

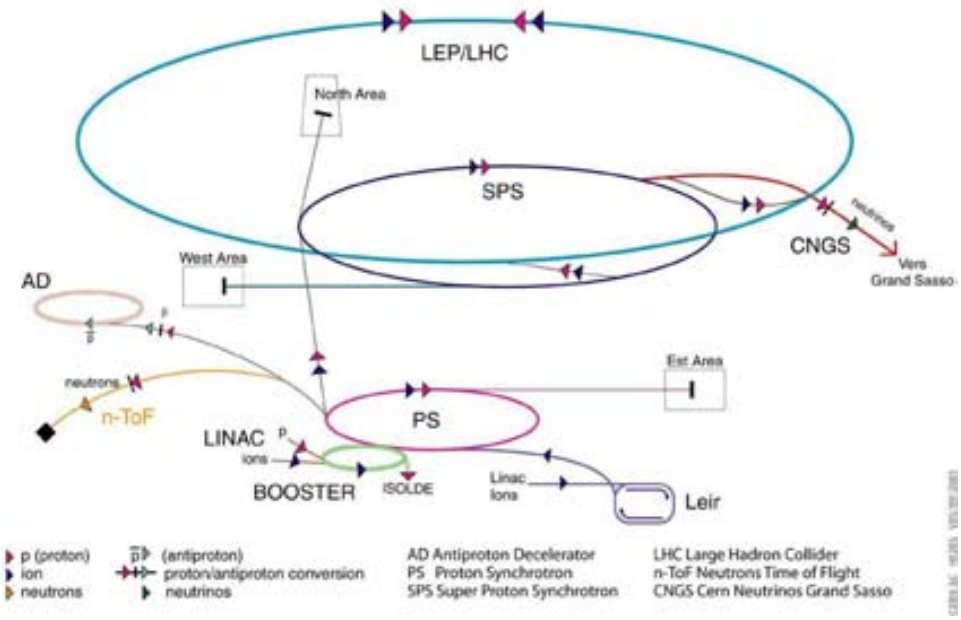

Figure 4.1: The injection complex of the LHC [84]

with 84 bunches, each with a length of 4 ns.

The PS was the actual first major accelerator at CERN which first operated in 1959. Several upgrades have been made since then.

The SPS is the machine that eventually injects the proton bunches into the LHC. It is filled with 3 PS pulses separated by 3.6 s. These are accelerated to an energy of 450 GeV. The SPS was built in 1976 and consists of an accelerator ring of 6.9 km circumference [86].

4.2 The LHC

The LHC is the world's largest particle accelerator with a center-of-mass energy of $\sqrt{s} = 7\,\text{TeV}$, the highest ever produced by mankind. It was designed to achieve a center-of-mass of $\sqrt{s} = 14\,\text{TeV}$ with an instantaneous luminosity of $10^{34}\,\text{cm}^{-2}\text{s}^{-1}$ (see Appendix B). Its design energy was reduced after an incident on 19 September 2008 to 7 TeV. On 30 March 2010 the first planned collision at 7 TeV were achieved. With only short technical stop at the end of 2011, the LHC will run until the end of 2012. After 2012 a long shutdown is foreseen to prepare the machine for higher energy running starting in 2014.

The LHC is installed in a tunnel of a circumference of 27 km buried around 50 to 175 m underground, partially below the Jura mountains. The tunnel was formerly used by the LEP collider.

The LHC hosts four experiments: two multi purpose experiments ATLAS and Compact Muon Solenoid (CMS), as well as Large Hadron Collider beauty (LHCb) for B-physics and A Large Ion Collider Experiment (ALICE) for heavy-ion physics. Fig. 4.2 shows the underground structure of the LHC with the four experiments mounted at the four intersection points.

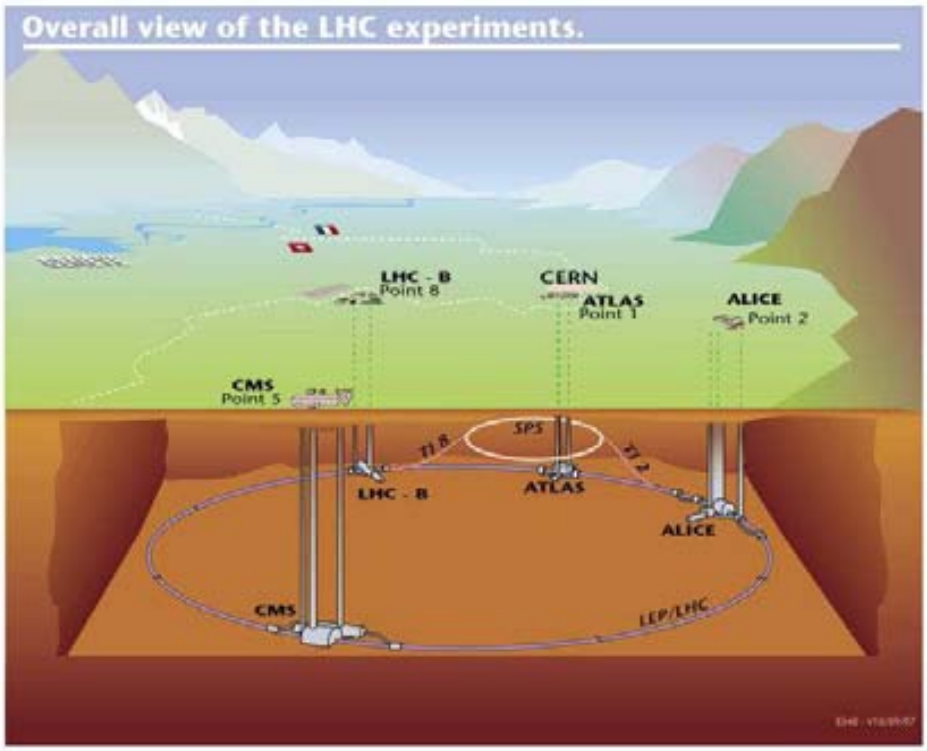

Figure 4.2: The underground structure of the LHC. It shows the injection accelerator SPS, the main LHC ring and the four hosted experiments: ATLAS, CMS, ALICE, and LHCb [87].

Coming from the SPS at an energy of 450 GeV, the protons are accelerated in the LHC to 3.5 TeV, yielding a center-of-mass energy at the intersection points of 7 TeV.

The proton beams are injected in two parallel beam pipes, that accelerate them in opposite direction. 1232 super-conducting dipole magnets bend the beams such that they keep circulating in the ring and accelerates each to 3.5 TeV. To achieve this energy a magnetic field of 8.33 T is required and magnets have to be cooled down to 1.9 K by liquid helium. The beam is focused by 858 super-conducting quadrupole magnets [88].

In two straight sections of the ring the LHC collimation system is placed.

It consists of 54 collimators with a maximum magnetic field of 1.53 T. Its purpose is the cleaning of the beam and the protection against beam loss [88].

When the beam reaches the minimal intensity, the protons are dumped in the LHC dumping system consisting of a graphite block encased in concrete [88].

Heavy Ion Physics: In addition to the proton acceleration and collision the LHC contains a heavy ion accelerator chain. Pb ions coming from the Laser Ion Source (LIS) are accelerated in the same way as described for protons. Before entering the PS, the Low Energy Ion Ring (LEIR) accumulates the linear accelerator pulses to provide the necessary intensity. Two bunches with 72 MeV/nucleon, each containing $4.5 \cdot 10^8$ ions are injected into the PS [89].

The lead beams will be collided at the intersection point of ALICE, as well as of ATLAS and CMS.

4.3 The ATLAS Detector

The A Toroidal LHC ApparatuS (ATLAS) detector surrounds the collision point and was conceived to detect particles in a wide range of energy and with the largest possible coverage around the interaction point.

The ATLAS detector was designed with focus on the search for new physics at the TeV scale and the so far undiscovered Higgs boson. A variety of new physics searches are foreseen and already ongoing, such as searches for super-symmetric particles, new heavy bosons, or fourth family fermions. A wide range of precision measurements of the Standard Model parameters are also an important point of the physics program.

The ATLAS detector is the largest detector ever built for a collider experiment, measuring 42 m in length and 11 m in radius, and weighting some 7,000 tonnes. It is a multipurpose detector consisting of three main layers, beginning from the beam pipe: the inner detector, subdivided into the Pixel Detector, the Semiconductor Tracker (SCT), and the Transition Radiation Tracker (TRT) (Sec. 4.3.2), the Calorimetry, subdivided into EM and hadronic calorimeters (Sec. 4.3.3.1 and 4.3.3.2), and the Muon Spectrometer (Sec. 4.3.4). Furthermore two magnets, the Inner Solenoid (Sec. 4.3.5.1) and Outer Toroidal (Sec. 4.3.5.2), are mounted within the ATLAS detector. A simplified sectional diagram is shown in Fig. 4.3. All components were designed to cope with the high interaction rate and the enormous radiation at the LHC.

As in the case of most other multi-purpose detectors, cylindrical coordinates are used in ATLAS to describe the topology of events. Each point in the three dimensional space in uniquely defined by:

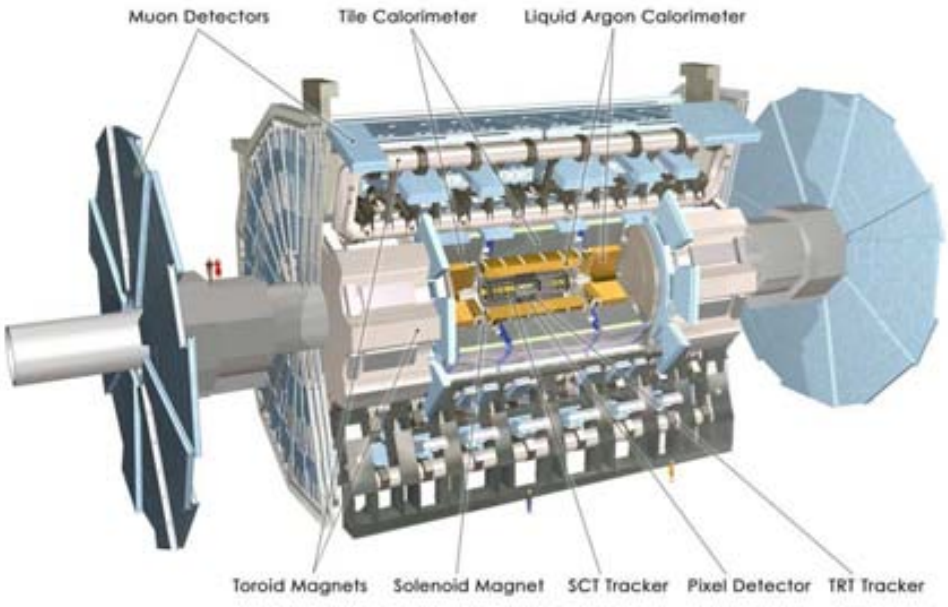

Figure 4.3: The ATLAS Detector as a simplified sectional diagram, showing the different sub-detectors, the tracker, the calorimeters, the muon spectrometer, and the magnets [90].

- z, the distance from the center of the detector along the beam-pipe, where the positive z denotes counterclockwise;
- ϕ, where $\phi = 0$ corresponds to the positive x-axis and ϕ increases clockwise looking into the positive z direction;
- θ, the opening angle, measured from the positive z axis on.

Instead of θ usually the pseudo-rapidity η is used, defined as

$$\eta := -\ln(\tan(\theta/2)). \tag{4.1}$$

In the case of a massless particle, the pseudo-rapidity agrees with the rapidity, which is invariant under Lorentz transformations along the beam axis. The coordinate ϕ is already invariant under such operations. This simplifies transformations between the center-of-mass system and the laboratory frame. The distance between two points in ϕ–η space is defined as

$$\Delta R = \sqrt{(\Delta\phi)^2 + (\Delta\eta)^2}\,, \tag{4.2}$$

where $\Delta\phi$ and $\Delta\eta$ are the separation in ϕ and η, respectively.

In this study all sub-systems of the ATLAS detector are used in order to reconstruct the topology and all final state particles arising in semi-leptonic top quark pair decays.

4.3.1 Interaction of Particles with Matter

The principle of particle detection and measurement of its properties is based on the interaction of the particles with the matter of the detector. Different sub-detectors, dedicated to measure the different properties, are combined in the multipurpose ATLAS detector. Figure 4.4 shows a sketch of particles crossing the detector and the sub-detectors used for these measurements.

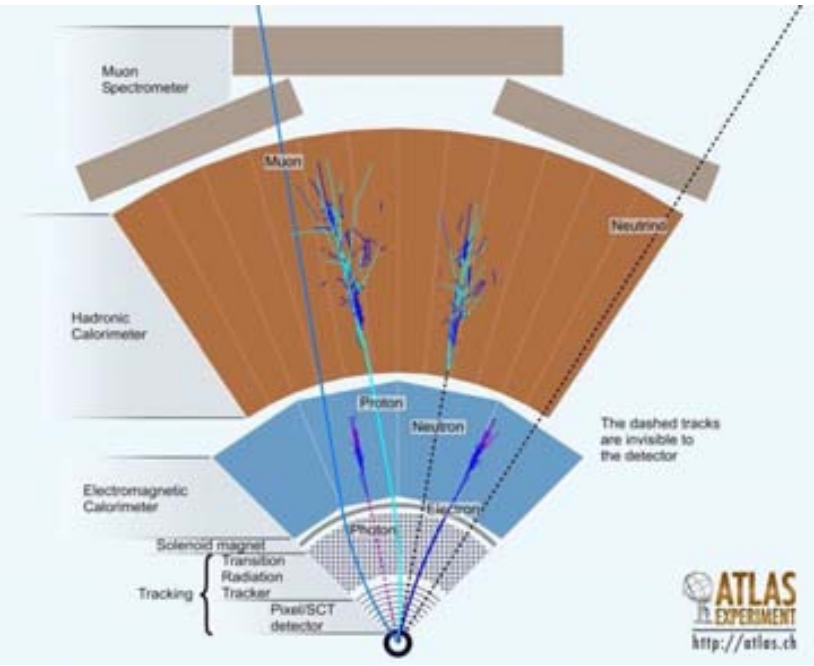

Figure 4.4: Sectional sketch of particles crossing the different sub-detectors [91].

The tracker measures the ionization and energy deposit of crossing charged particles and allows thus the reconstruction of tracks in three dimensions. Their bending within the magnetic field of the inner solenoid magnet allows to identify the charge of the particles as well as to measure their momenta.

Within the EM calorimeter the energy and the direction of electromagnetically interacting particles are measured. The particles loose energy through bremsstrahlung and ionization. In the process of bremsstrahlung photons are emitted and decay into electron-positron pairs which in turn emit photons, resulting in EM showers. Below a critical energy the energy loss is dominated by ionization, until the energy is totally absorbed. Due to multiple scattering, which yields only small energy loss in comparison to bremsstrahlung and ionization, a Gaussian smearing of the particle's direction of flight is caused. This affects the resolution of the momentum measurement. The distance of EM interactions is given by radiation length

X_0, which is the mean path length required to reduce the electromagnetically interacting particle's energy by $1/e$.

Heavy particles colliding with a light target will lose energy without any significant change in their direction of flight. They are measured in the hadronic calorimeter. The energy loss is caused by inelastic hadronic collisions yielding π^0's and η's, as well as charged particles like π^+, p, and so on. π^0's and η's subsequently decay into high energy photons which generated high-energy EM cascades. On the other hand, π^+ deposit energy via ionization and excitation or interact with the nuclei. The hadronic calorimeter totally absorbs all the energy of the heavy particles and thus stops them. To estimate the range of heavy particles, the interaction length λ is used, also defined as the mean path length required to reduce the particle's energy by $1/e$.

The characteristics of muons are measured with the Muon Spectrometer. A combination with results from the tracker is also applied. Muons are considered as stable particles within the range of the detector and loose only small parts of their energy within the calorimeters, primarily via ionization. When crossing the Muon Spectrometer energy is deposited and allows the reconstruction tracks. An additional bending within the magnetic field of the toroidal magnet allows to determine their momenta.

4.3.2 Inner Detector

The inner detector was designed to measure with a high resolution the momenta and the vertices of the large number of tracks, originating from particles that emerge from the collisions. A proper identification of the vertices is crucial to identify heavy flavor jets (i.e. those originating from b or c quarks; see Sec. 5.5.3).

The inner detector is mounted around the beam pipe at a distance of 36 mm and is subdivided into the Pixel Detector (see Sec. 4.3.2.1), the Semiconductor Tracker (see Sec. 4.3.2.2) and the Transition Radiation Tracker (see Sec. 4.3.2.3). A cut-away view of the ATLAS inner detector is shown in Fig. 4.5. The inner detector is situated inside the Inner Solenoid (see Sec. 4.3.5) which provides a magnetic field of 2 T to bend the particles when crossing the inner detector. This allows to measure the momentum of the particle tracks.

The main parameters of the inner detector are listed in Table 4.1. In Figure 4.8 (a) the thickness of the Inner Detector in units of radiation length X_0 is shown. For a more detailed description of the inner detector see [92].

4.3.2.1 Pixel Detector

The silicon Pixel Detector is part of the precision tracking system (Pixel Detector and SCT). It covers a region around the interaction point up

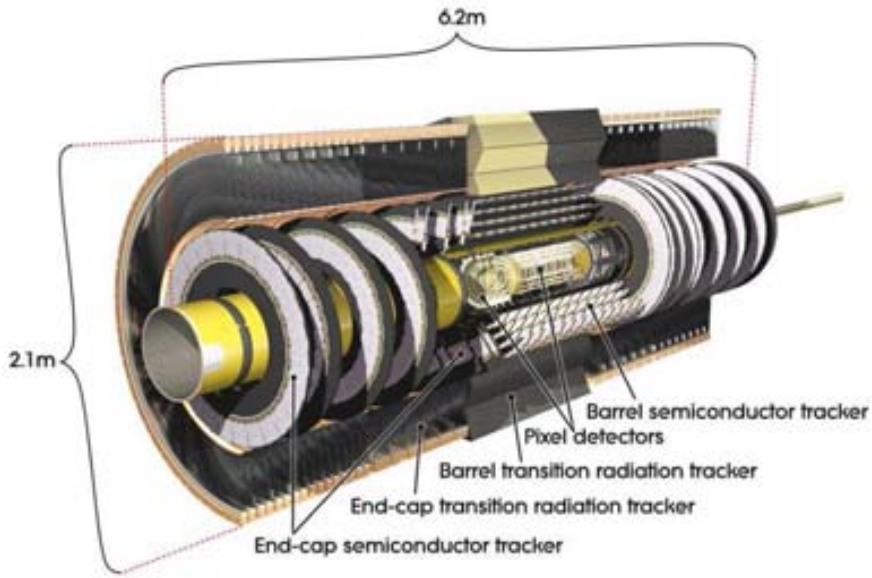

Figure 4.5: Cut-away view of the ATLAS inner detector [92].

to $|\eta| = 2.5$ (see Fig. 4.6). As listed in Table 4.1, the Pixel Detector is

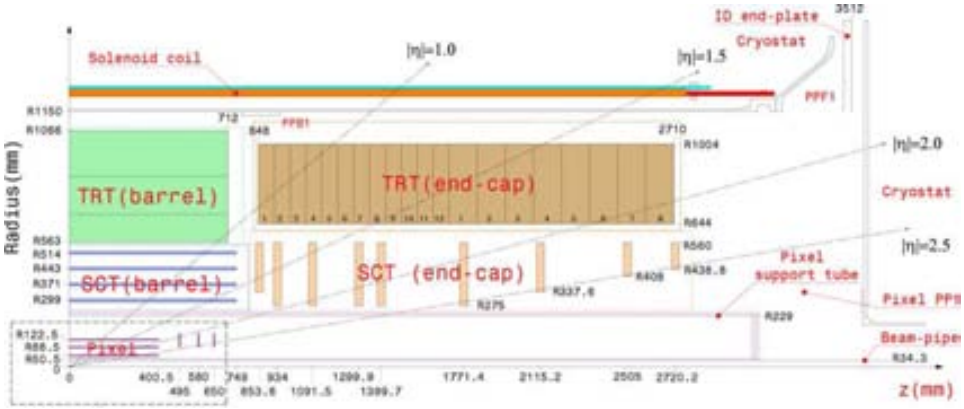

Figure 4.6: View of the active sections of the ATLAS inner detector [92].

divided into the barrel and the end-cap region. The barrel region consists of three concentric cylinders installed around the beam pipe. On the other hand, in the end-cap region the pixels are placed in the form of three disks perpendicular to the beam axis.

The barrel and the disks consist of 1456 and 288 modules, respectively, each has size of $62.4 \times 21.4\,\mathrm{mm}^2$ with 46080 pixel elements. All modules are equal and the size of the smallest pixels is $50 \times 400\,\mu$m with all pixel layers

Table 4.1: Main parameters of the inner detector [92].

Item		Radial extension (mm)	Length (mm)
Pixel Detector		$45.5 < R < 242$	$0 < \|z\| < 3092$
3 cylindrical layers	barrel	$50.5 < R < 122.5$	$0 < \|z\| < 400.5$
2×3 disks	end-cap	$88.8 < R < 149.6$	$495 < \|z\| < 650$
SCT	barrel	$255 < R < 549$	$0 < \|z\| < 805$
	end-cap	$251 < R < 610$	$810 < \|z\| < 2797$
4 cylindrical layers	barrel	$299 < R < 514$	$0 < \|z\| < 749$
2×9 disks	end-cap	$275 < R < 560$	$839 < \|z\| < 2735$
TRT	barrel	$554 < R < 1082$	$0 < \|z\| < 780$
	end-cap	$617 < R < 1106$	$827 < \|z\| < 2744$
73 straw planes	barrel	$563 < R < 1066$	$0 < \|z\| < 712$
160 straw planes	end-cap	$644 < R < 1004$	$848 < \|z\| < 2710$

segmented in $R-\phi$ and z. A total of about 80.4 million readout channels are installed to record the information provided by the Pixel Detector, which has its highest granularity around the vertex region using silicon pixel sensors.

The intrinsic accuracy of the Pixel Detector in both the barrel and the end-cap regions is of $10\,\mu$m in $R-\phi$ and $115\,\mu$m in z and R, respectively. The innermost layer of the Pixel Detector barrel region is known in ATLAS jargon as the B-layer, since it provides the critical vertexing information used in ATLAS to reconstruct the displaced vertices as for instance from b quark decays (see Sec. 5.5.3).

4.3.2.2 Semiconductor Tracker

The Semiconductor Tracker (SCT) performs eight precision measurements per crossing particle yielding four space points. This is done by eight silicon microstrip detectors.

In the barrel region these detectors consist of small angle (40 mrad) stereo strips. One set of strips in each layer is mounted parallel with the beam line to measure $R-\phi$. Each silicon strip has a size of $6.36 \times 6.40\,\text{cm}^2$ and is connected to 780 readout strips. The end-cap modules are similar to the barrel ones, with a set of strips running radical and another set of stereo strips at an angle of 40 mrad.

The intrinsic accuracy per module is $17\,\mu$m in $R-\phi$ and $580\,\mu$m in z and R for both, the barrel and the end-cap.

4.3.2.3 Transition Radiation Tracker

The Transition Radiation Tracker (TRT) measures up to a maximum of 36 hits per track. It consists of straw tubes of a diameter of 4 mm, each containing a gold-plated wolfram rhenium wire. Covering a region up to $|\eta| = 2$ it only measures the $R - \phi$ coordinate of tracks. These drift time measurements are performed with an accuracy of 130 μm per straw.

The TRT is composed of about 500,000 straws in the barrel, each with a length of 144 cm centered at $|z| = 0$ and aligned parallel to the beam line. In the end-cap the TRT consists of 320,000 straws, arranged in 18 wheels, mounted radically to the beam line.

A Xenon gas mixture of Xe (20%), CO_2 (27%), and O_2 (3%), allows to detect transition radiation photons originating from the cracks between the straws.

4.3.3 Calorimeters

The calorimeter of the ATLAS Detector allows to measure the energy of charged and neutral particles in a large range of energy, from a few GeV up to TeV, with a high resolution and linearity. It measures the energy of crossing particles which produce EM and hadronic showers due to interactions with the absorber material (see Sec. 4.3.1). Only long lived and weakly-interacting particles such as muons are not fully stopped within the calorimeters and thus reach the Muon Spectrometer.

The ATLAS calorimeters cover the range of $|\eta| < 4.9$ around the interaction point, where different techniques are used to cope with the widely varying requirements of physics processes of interest and of the radiation environment. A cut-away view of the calorimeter system is shown in Fig. 4.7.

The calorimeter is divided into the EM (Sec. 4.3.3.1) and the hadronic sections (Sec. 4.3.3.2), the latter surrounding the former. Both are divided into the barrel and the end-cap or extended barrel range for the EM and the hadronic calorimeter, respectively. In addition, the Forward Calorimeter (Sec. 4.3.3.3) covers the range of $3.1 < |\eta| < 4.9$ and also consists of a EM and a hadronic section.

4.3.3.1 Electromagnetic Calorimeter

The EM calorimeter provides the measurement of the momentum and direction for photons and electrons as well as contributes to the reconstruction of jets together with the hadronic calorimeter. It is a lead Liquid Argon (LAr) detector with accordion-shaped Kapton electrodes and lead absorber plates and is housed in cryostats.

The barrels are made of 1024 of such accordion-shaped absorbers, interleaved with readout electronics. The accordion geometry provides a full

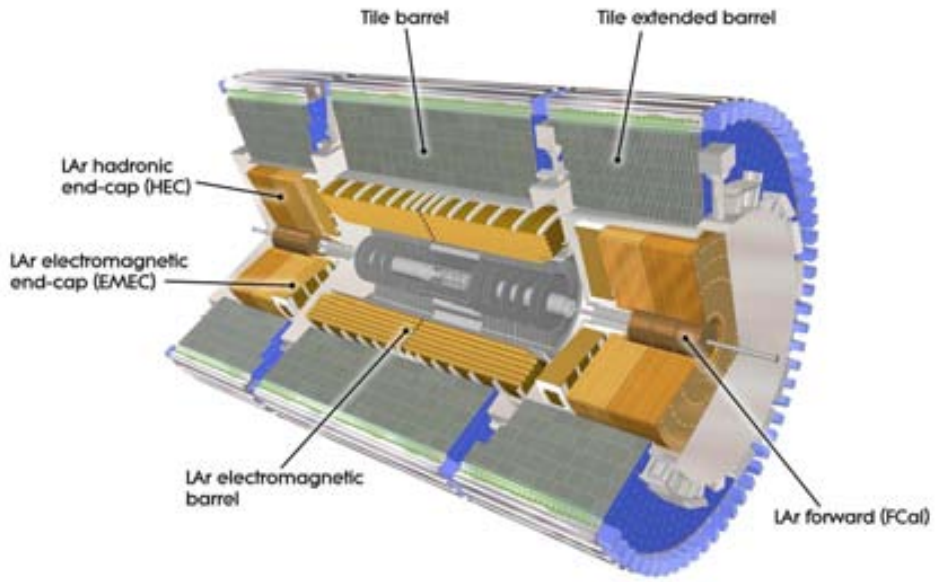

Figure 4.7: A cut-away view of the ATLAS calorimeters showing the different EM and hadronic sections [90].

symmetry in ϕ without azimuthal cracks. Furthermore, it allows a fast read-out of the signal at the front or the rear of the electrodes. The end-caps consist of two coaxial wheels, divided into eight wedge-shaped modules. These modules are made of 768 absorbers which are interleaved with the read-out electronics. The lead thickness in the absorber plates was optimized over η in terms of performance in energy resolution to account to the amount of material crossed by particles with increasing η,

A pre-sampler detector is mounted at $|\eta| < 1.8$ inside the barrel and corrects for energy lost by electron and photon upstream of the calorimeter. It consists of active LAr layers with a thickness of 1.1 cm and 0.5 cm in the barrel and the end-cap, respectively.

The thickness in terms of radiation length of the EM calorimeter as a function of the pseudo-rapidity is shown in Fig. 4.8 (a-c). It ranges from $22\,X_0$ to $33\,X_0$.

The EM Calorimeter is subdivided into the barrel ($|\eta| < 1.475$) and two end-caps ($1.375 < |\eta| < 3.2$), all mounted in their own cryostats. Both are housed in one vacuum vessel to reduce the energy loss due to the material of the central solenoid, which is mounted in front of the EM calorimeter (see Sec. 4.3.5.1). This design avoids two vacuum walls. The barrel consists of two half-barrels, separated at $z = 0$ by 4 mm while each end-cap is divided by 3 mm into two coaxial wheels of $1.375 < |\eta| < 2.5$ and $2.5 < |\eta| < 3.2$.

Table 4.2: Granularity of the EM and the hadronic calorimeter for $\Delta\eta \times \Delta\phi$ versus $\Delta|\eta|$ [90].

		Barrel		End-cap	
Pre-sampler		0.025×0.1	$\lvert\eta\rvert < 1.52$	0.025×0.1	$1.5 < \lvert\eta\rvert < 1.8$
Calorimeter	1st layer	$0.025/8 \times 0.1$	$\lvert\eta\rvert < 1.40$	0.050×0.1	$1.375 < \lvert\eta\rvert < 1.425$
		0.025×0.025	$1.40 < \lvert\eta\rvert < 1.475$	0.025×0.1	$1.425 < \lvert\eta\rvert < 1.5$
				$0.025/8 \times 0.1$	$1.5 < \lvert\eta\rvert < 1.8$
				$0.025/6 \times 0.1$	$1.8 < \lvert\eta\rvert < 2.0$
				$0.025/4 \times 0.1$	$2.0 < \lvert\eta\rvert < 2.4$
				0.025×0.1	$2.4 < \lvert\eta\rvert < 2.5$
				0.1×0.1	$2.5 < \lvert\eta\rvert < 3.2$
	2nd layer	0.025×0.025	$\lvert\eta\rvert < 1.40$	0.050×0.025	$1.375 < \lvert\eta\rvert < 1.425$
		0.075×0.025	$1.40 < \lvert\eta\rvert < 1.475$	0.025×0.025	$1.425 < \lvert\eta\rvert < 2.5$
				0.1×0.1	$2.5 < \lvert\eta\rvert < 3.2$
	3rd layer	0.050×0.025	$\lvert\eta\rvert < 1.35$	0.050×0.025	$1.5 < \lvert\eta\rvert < 2.5$
TileCal	First two layers	0.1×0.1	$\lvert\eta\rvert < 1.0$	0.1×0.1	$0.8 < \lvert\eta\rvert < 1.7$
	Last layer	0.2×0.1	$\lvert\eta\rvert < 1.0$	0.2×0.1	$0.8 < \lvert\eta\rvert < 1.7$
Hadronic end-cap	First two layers			0.1×0.1	$1.5 < \lvert\eta\rvert < 2.5$
	Last layer			0.2×0.2	$2.5 < \lvert\eta\rvert < 3.2$

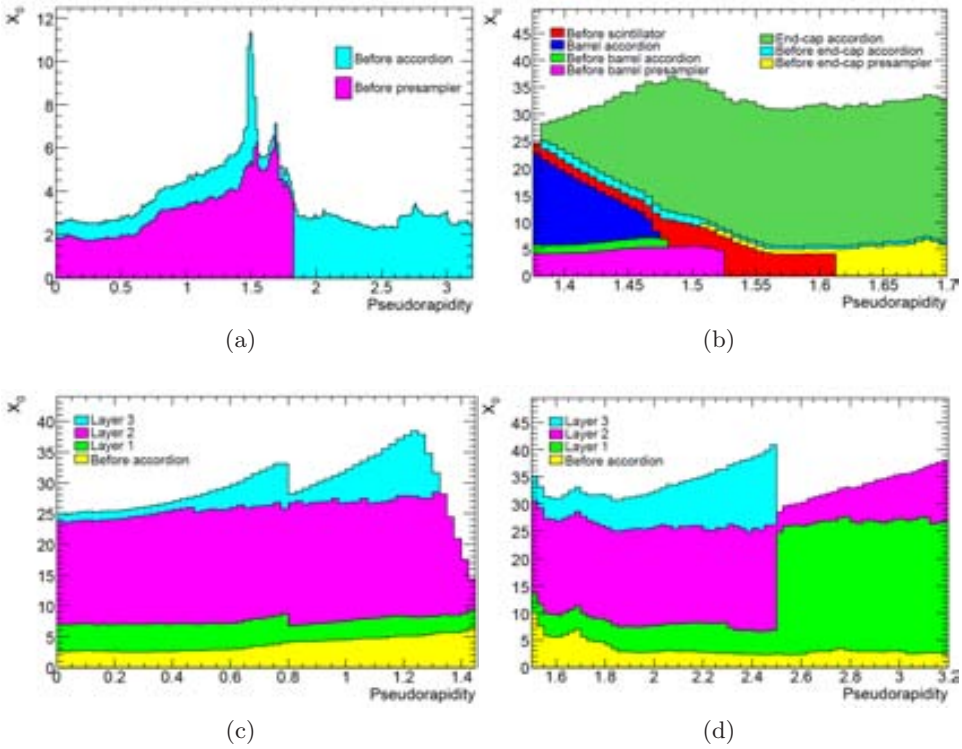

Figure 4.8: Cumulative amount of material, in units of radiation length X_0 and as a function of $|\eta|$, in front of and in the EM calorimeter. (a) shows separately the total amount of material in front of the pre-sampler layer and in front of the accordion itself. (b) shows the details of the crack region between the barrel and end-cap cryostats, both in terms of material in front of the active layers and of the total thickness of the active calorimeter. The two bottom figures show separately for (c) the barrel and (d) the end-cap, the thicknesses of each accordion layer as well as the amount of material in front of the accordion [90].

In the region of precision physics ($|\eta| < 2.5$) the EM calorimeter consists of three sections in depth, whereas for $|\eta| > 2.5$ the outer wheel consists of two sections with a coarser granularity (see Table 4.2).

4.3.3.2 Hadronic Calorimeter

The hadronic calorimeter of the ATLAS detector is divided into the central Tile Calorimeter (TileCal), the LAr Hadronic End-cap Calorimeter (HEC), and the LAr Forward Calorimeter (FCal). It is designed to measure the hadronic showers which are just faintly absorbed in the EM calorimeter.

Apart from long-lived particles such as muons, all particle showers will be completely absorbed within the Hadronic Calorimeter.

Tile calorimeter: The Tile Calorimeter (TileCal) is a sampling calorimeter consisting of steel absorber and scintillator as active medium, mounted in a self-supporting way. It is separated into the central barrel and two alike extended barrels. As shown in Fig. 4.9, the TileCal has a radial depth in terms of interaction length of about $8 - 10\,\lambda$, ensuring the complete absorption of the hadronic showers inside the Hadronic Calorimeter.

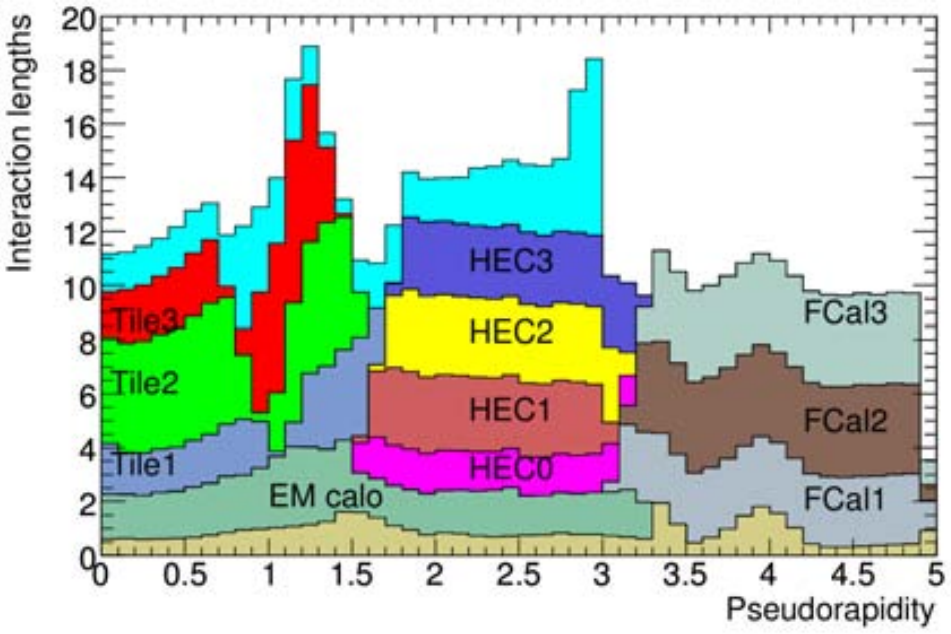

Figure 4.9: Cumulative amount of detector material in units of interaction length λ and as a function of $|\eta|$. The material in front of the EM calorimeter, the EM calorimeter itself, the hadronic tile and end-cap calorimeter, as well as the forward calorimeter is shown [90].

It covers the region up to $|\eta| < 1.7$ and is located around the EM calorimeter. All barrels have an inner (outer) radius of 2.28 m (4.25 m). The inner barrel is 5.8 m long whereas the extended barrels measure 2.6 m.

Each barrel is compound of 54 equal modules, so-called wedges. The wedges of size $\Delta\phi \approx 0.1$ are made of steel plates and scintillator tiles. A schematic drawing of such a wedge is shown in Fig. 4.10. The scintillator tiles are mounted radially and normal to the beam line with the result of an almost seamless azimuthal calorimeter coverage. The grouping of the readout fibers into the readout photomultiplier tubes provides an approximately projective geometry in pseudo-rapidity (see. Table 4.2).

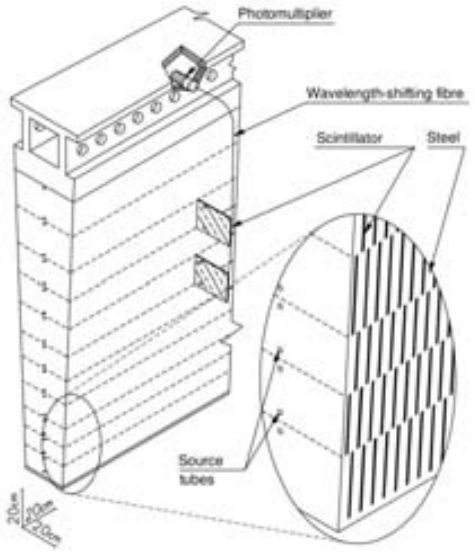

Figure 4.10: Schematically drawing of one of the 64 wedges of the TileCal. It shows the tiles, the fibers, and the photo-multipliers [93].

In the gap region between the barrel and the extended barrel special modules of steel scintillator sandwiches are used. Its sampling fraction is equal to the rest of the TileCal. In addition, thin scintillator counters are mounted in regions of less available space, such that the energy loss in the gab region can be partially recovered.

Hadronic end-cap calorimeter: The Hadronic End-cap Calorimeter (HEC) is a copper/LAr sampling calorimeter which covers the region of $1.5 < |\eta| < 3.2$. Two independent wheels for each end-cap are mounted directly behind the end-cap EM calorimeter. In order to decrease the amount of material, the HEC shares the cryostat in the end-cap together with the EM calorimeter and the FCal. Furthermore, the HEC overlaps partially with the EM calorimeter and the FCal in η (see Fig. 4.9).

Each wheel consists of 32 wedge-shape modules and each module itself is divided into two segments of depth. As a result the two wheels per side split into four layers per end-cap: HEC1, HEC2, HEC3, and HEC4 (see Fig. 4.9).

The inner wheel (closest to the interaction point) is made of 25 mm copper plates, while the outer wheel uses 50 mm ones. Copper plates are interleaved with 8.5 mm LAr gaps as active medium for sampling. Three electrodes divide these gaps into four separate drift zones, each of 1.8 mm.

The read-out cells are defined by pads providing a semi-pointing geometry with a granularity in $\Delta\eta \times \Delta\phi$ of 0.1×0.1 for the first two layers and 0.2×0.1 for the rest (see Table 4.2).

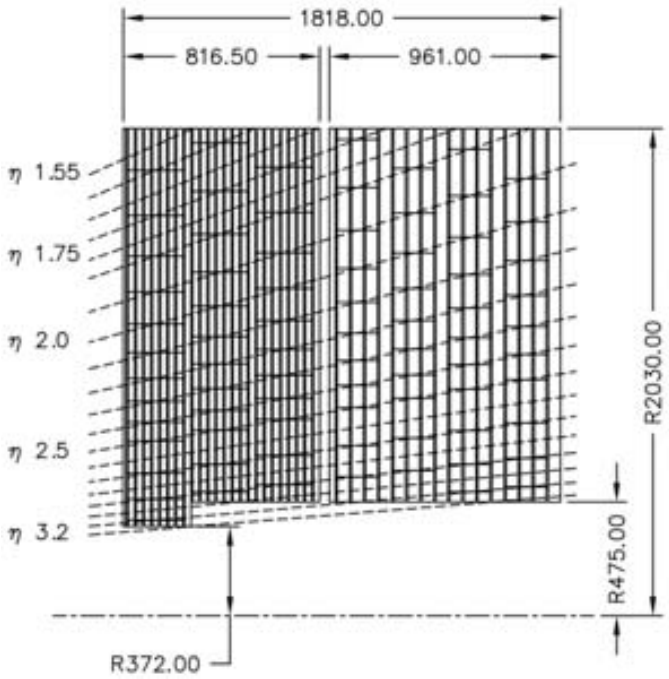

Figure 4.11: Schematic $|\eta| - z$ view of the HEC showing the two independent wheels, the layer depth, and the overlap with the EM calorimeter at low η and with the FCal at large η. Dimensions are given in mm [90].

4.3.3.3 Forward Calorimeter

The FCal consists of an EM and a hadronic section covering the range of $3.1 < |\eta| < 4.9$ in order to provide a hermetic coverage around the interaction point and to reduce the radiation background level in the Muon Spectrometer at large $|\eta|$. It is mounted at a distance of about 4.7 m from the interaction point. It is separated into three 45 cm deep modules, one EM part (FCal1), and two hadronic modules (FCal2, FCal3).

The FCal uses LAr as ionization medium and is made of copper plates, which provide a good resolution and optimize the heat removal. The hadronic part (FCal2, FCal3) has an increased amount of tungsten which provides a good containment and minimizes lateral spread of hadronic showers. A copper alloy is mounted behind the FCal to shield the muon system. The parameters of the FCal are listed in more detail in Table 4.3.

The copper plates of the FCal1 are stacked one behind another with 12,260 holes drilled into them. An electrode structure was inserted into the holes, made of coaxial copper rods and a copper tube, separated by precision radiation hard plastic fiber wound around the rod.

FCal2 and FCal3 consist of two copper plates of a thickness of 2.35 m.

Table 4.3: Parameters of the three FCal modules [90].

Function	FCal1	FCal2	FCal3
Main absorber material	Copper	Tungsten	Tungsten
LAr gap width (mm)	0.269	0.376	0.508
Radiation length (X_0)	27.6	91.3	89.2
Absorption length (λ)	2.66	3.68	3.60

They are optimized for high absorption length by its amount of tungsten (see Table 4.3). To achieve this the amount of tungsten was maximized, choosing it as material for the electrode rods. Apart from that, the structure is similar to the one of the FCal1.

4.3.4 Muon Spectrometer

The outermost component of the ATLAS detector is the Muon Spectrometer, covering the region of $|\eta| < 2.7$ and consisting of separated high-precision tracking and trigger chambers. Its purpose is to detect muons exiting the barrel and end-cap calorimeters as well as to trigger on those particles (for $|\eta| < 2.4$). The used strategy is based on the magnetic deflection of muon tracks in the toroidal magnet.

In the region of $|\eta| < 1.4$ the bending is caused by the barrel solenoid magnet whereas for $1.6 < |\eta| < 2.7$ the bending is preformed by the end-cap toroidal magnet. In the so-called transition region of $1.4 < |\eta| < 1.6$ the fields of both magnet systems overlap (see Table 4.4). The magnets are discussed in Sec. 4.3.5.

In the barrel region the precision tracking chambers are mounted on and between the eight coils of the toroidal magnet (see Fig. 4.12 (a)). In the end-cap region the chambers are mounted in front and behind the end-cap toroidal magnet. The ϕ-symmetry imposed by the toroidal magnet suggests the structure of eight octants. Each octant is subdivided into two sectors in the azimuthal direction, a small (even numbers in Fig. 4.12 (a)) and a large sector (odd numbers) with an overlap in ϕ.

All chambers in the barrel are arranged in three concentric cylindrical shells around the beam axis at 5 m, 7.5 m, and 10 m (see Fig. 4.12 (b)). In end-caps the chambers are installed in wheels perpendicular to the z-axis at 7.4 m, 10.8 m, 14 m, and 21.5 m.

A gap in the chamber coverage was left at $|\eta| \approx 0$ for services to the solenoid magnet, the calorimeters and the inner detector. A possible high energy and thus straight muon can therefore not be detected in a small angel of $|\eta| < 0.08$ and $|\eta| < 0.04$ in the large and the small sector, respectively. Additional gaps are located for the support structure in sector 12 and 14 (see. Fig. 4.12 (a)).

Table 4.4: Main parameters of the muon spectrometer [90].

Monitored drift tubes	MDT
Coverage	$\|\eta\| < 2.7$ (innermost layer: $\|\eta\| < 2,0$)
Number of chambers	1,150
Number of channels	354,000
Function	Precision tracking
Cathode strip chambers	CSC
Coverage	$2.0 < \|\eta\| < 2,7$
Number of chambers	32
Number of channels	31,000
Function	Precision tracking
Resistive plate chambers	RPC
Coverage	$\|\eta\| < 1.05$
Number of chambers	606
Number of channels	373,000
Function	Triggering, second coordinate
Thin gap chambers	TGC
Coverage	$1.05 < \|\eta\| < 2.7$ (2.4 for triggering)
Number of chambers	3,588
Number of channels	318,000
Function	Triggering, second coordinate

The precision measurement of the muon track is performed by the Monitored Drift Tubes (MDT). They were designed to yield a high accuracy for the measurement with consideration of the predictability of mechanical deformations and the simplicity of its construction. The MDT spreads over the region of $|\eta| < 2.7$, whereas the innermost end-cap layer covers only the region of $|\eta| < 2.4$. Between three and eight drift tubes in each chamber at an operating pressure of 3 bar offer a resolution of 80 μm per tube which results in 35 μm per chamber (see Table 4.5).

In the forward region ($2.0 < |\eta| < 2.7$) the Cathode Strip Chamber (CSC) offers a higher rate capability and a higher time resolution. It is made of multi-wired proportional chambers, consisting of cathode planes segmented into strips in the orthogonal direction and provides a measurement in η and ϕ. The resolution amounts 40 μm per chamber in the bending plane and 5 mm in the transverse plane (see Table 4.5).

As mentioned at the beginning of this subsection, the Muon Spectrometer also includes the ability to trigger on muon tracks with a system of fast trigger chambers. In the region of $|\eta| < 1.05$ Resistive Plate Chambers (RPCs) are used, while for $1.05 < |\eta| < 2.4$ Thin Gap Chambers (TGCs) are used. Their main parameters are listed in Table 4.5.

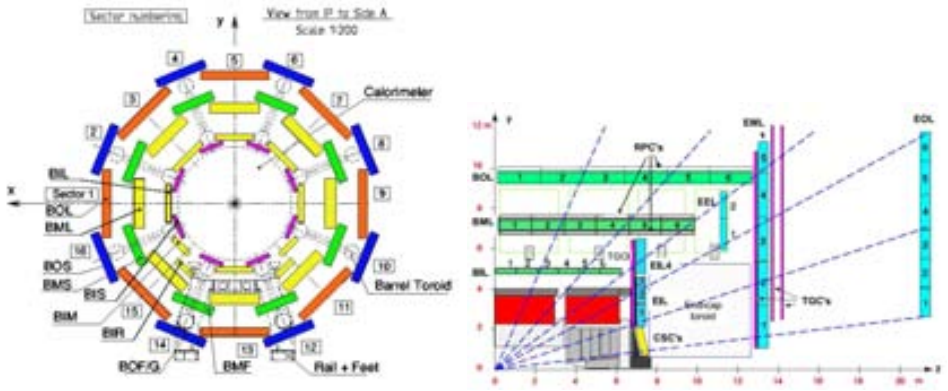

(a) (b)

Figure 4.12: Cross section of the barrel muon spectrometer (a) perpendicular to the beam-axis (no-bending plane), and (b) in the plane containing the beam-axis (bending plane) [90].

Table 4.5: Parameters of the four sub-systems of the Muon Spectrometer. The quoted spatial resolutions (columns 2, 3) do not include chamber-alignment uncertainties. Column 4 lists the intrinsic time resolution of each chamber type, to which contributions from signal-propagation and electronics contributions need to be added [90].

	Chamber resolution (RMS) in			Measurements/track	
Type	z/R	ϕ	time	barrel	end-cap
MDT	35 mm (z)	–	–	20	20
CSC	40 mm (R)	5 mm	7 ns	–	4
RPC	10 mm (z)	10 mm	1.5 ns	6	–
TGC	$2-6$ mm (R)	$3-7$ mm	4 ns	–	9

Both, the RPCs and the TGCs, deliver signals with a spread of $15-25$ ns which allows the system to tag on the beam-crossing. The trigger chambers measure both coordinates, in the bending plane (η) and in the non-bending plane (ϕ). The hits recorded by the MDT and the trigger chambers are matched for the bending plane coordinate. In case of the non-bending plane coordinate, it is adopted from the trigger chambers measurement, if only one track was reconstructed per chamber pair. In the opposite case, the combination with the track measurement by the inner detector (see Sec. 4.3.2) is performed to solve the ambiguity in the η and ϕ assignment.

4.3.5 Magnet System

The Magnet System of the ATLAS detector is made of a solenoid magnet and three toroid magnets and stores a total amount of 1.6 GJ. The magnetic field of the solenoid provides the bending for particle tracks within the inner detector (see Sec. 4.3.2) whereas toroid magnets bend the muon tracks within the muon system (see Sec. 4.3.4) and allows so to measure their momenta.

4.3.5.1 Inner Solenoid

Aligned to the beam axis (see Fig. 4.3), the solenoid magnet establishes a field of 2 T for the inner detector. Its layout was carefully designed to minimize the amount of un-instrumented material in front of the calorimeters, such that its thickness amounts only to $0.66\,X_0$.

The solenoid windings and the LAr calorimeter share a common vacuum vessel to minimize the amount of material due to the vacuum walls. An aluminum heat shield of 2 mm is mounted between the LAr calorimeter and the solenoid. In Table 4.6 a detailed list of the solenoid's parameters can be found.

4.3.5.2 Outer Toroidal

The toroidal magnets, responsible for the bending of particles crossing the Muon Spectrometer, establish a magnetic field of 0.5 T in the central region and 1 T in the end-cap region.

The Barrel Toroid Magnet is of a cylindrical volume surrounding the calorimeters and end-cap toroid (see Fig. 4.3). Eight coils are encased in a stainless-steal vacuum vessel. It is 25.3 m long and its inner (outer) diameter amounts 9.4 m (20.1 m). The parameters of the barrel toroid magnet are stated in Table 4.6.

The End-cap Toroid Magnet is formed by two toroid magnets mounted on the two end-caps to optimize the bending power in the Muon Spectrometer (see Sec. 4.3.4). They consist of a single cold mass built up from eight flat, square coil units and eight keystone wedges. Table 4.6 shows the parameters of the end-cap toroid magnet.

4.3.6 The Forward Detectors

The ATLAS Forward Detector system consists of three sub-detectors which together give a good coverage in the very forward region.

The LUminosity measurement using Cerenkov Integrating Detector (LUCID) consists of 20 aluminum tubes mounted around the beam-pipe towards the interaction point and is primarily dedicated to the online luminosity monitoring. To estimate the luminosity the number of particles

Table 4.6: Main parameters of the ATLAS magnet system [90].

Property	Feature	Unit	Solenoid	Barrel toroid	End-cap toroids
Size	Inner diameter	m	2.46	9.4	1.65
	Outer diameter	m	2.56	20.1	10.7
	Axial length	m	5.8	25.3	5.0
	Number of coils		1	8	2×8
Mass	Conductor	t	3.8	118	2×20.5
	Cold mass	t	5.4	370	2×140
	Total assembly	t	5.7	830	2×239
Coils	Turns per coil		1154	120	116
	Nominal current	kA	7.73	20.5	20.5
	Magnet stored energy	GJ	0.04	1.08	2×0.25
	Peak field in the windings	T	2.6	3.9	4.1
	Field range in the bore	T	0.92.0	0.22.5	0.23.5
Conductor	Overall size	mm^2	30 x 4.25	57 x 12	41×12
	Ratio Al:Cu:NbTi		15.6:0.9:1	28:1.3:1	19:1.3:1
	Number of strands (NbTi)		12	3840	40
	Strand diameter (NbTi)	mm	1.22	1.3	1.3
	Critical current (at 5 T and 4.2 K)	kA	20.4	58	60
	Operating/critical-current ratio at 4.5 K	%	20	30	30
	Residual resistivity ratio (RRR) for Al		> 500	> 800	> 800
	Temperature margin	K	2.7	1.9	1.9
	Number of units $\times$ length	m	4×2290	$8 \times 4 \times 1730$	$2 \times 8 \times 2 \times 800$
	Total length (produced)	km	10	56	2 x 13

entering a Cerenkov tube are counted. The 1.5 m long tubes with a diameter of 15 mm are placed in an aluminum gas vessel filled with C_4F_{10} at a pressure of $1.2 - 1.4$ bar It is mounted at about 17 m on both sides from the interaction point at a radial distance of 10 cm from the beam-line ($|\eta| \approx 5.8$).

The Absolute Luminosity For ATLAS (ALFA) detector is a scintillating-fiber tracker, mounted 237 m away from the interaction point, designed for the very small scattering angle of about 3 μrad. In order to fulfill the spatial resolution requirements, the detector is built of ten double-sided modules, each with 64 fibers arranged in stereo $u - v$ geometry on both sides.

The third Forward Detector is the Zero-Degree Calorimeter (ZDC) which is mounted at 140 m from the interaction point. Its primary purpose is to detect forward neutrons with $|\eta| > 8.3$ in heavy-ion collisions.

The optical theorem connects the elastic-scattering amplitude in the forward direction $A(0)$ to the total cross-section σ_{tot} [94]

$$\sigma_{\text{tot}} = \frac{4\pi}{k}\text{Im}(A(0))\,, \tag{4.3}$$

were k is the wave number of the crossing particle. Together with the elastic (σ_{elastic}) and the total cross section (σ_{tot}), which both can be measured, the inelastic cross section can be estimated as

$$\sigma_{\text{inelastic}} = \sigma_{\text{tot}} - \sigma_{\text{elastic}} \tag{4.4}$$

This allows to extract the luminosity via

$$\mathcal{L} = \frac{R}{\epsilon\,\sigma_{\text{inelastic}}}\,, \tag{4.5}$$

for a rate R and an efficiency ϵ. Figure 4.13 shows the peak delivered instantaneous luminosity delivered per day at the ATLAS detector for the beam declared stable and unstable by the LHC.

More details on the Forward Detectors can be found in [96].

4.3.7 Trigger and Data Acquisition

The design bunch crossing rate of the LHC of 40 MHz, together with 25 proton-proton collisions at an instantaneous luminosity of $10^{34}\,\text{cm}^{-2}\text{s}^{-1}$ per bunch crossing, yield an event production rate of about 1 GHz. The Data Acquisition (DAQ) system can store events on tape only at a rate of $300 - 400$ Hz, taking into account that each event has a size of about 1.3 Mbyte.

To cope with these requirements a highly sophisticated filtering has to be applied. This is achieved by the ATLAS trigger system which is made up of three trigger levels: Level 1 (L1), Level 2 (L2), and the Event Filter (EF). L2 and EF are combined into the High Level Trigger (HLT). Each trigger level makes its decision based on the previous level and refines this information.

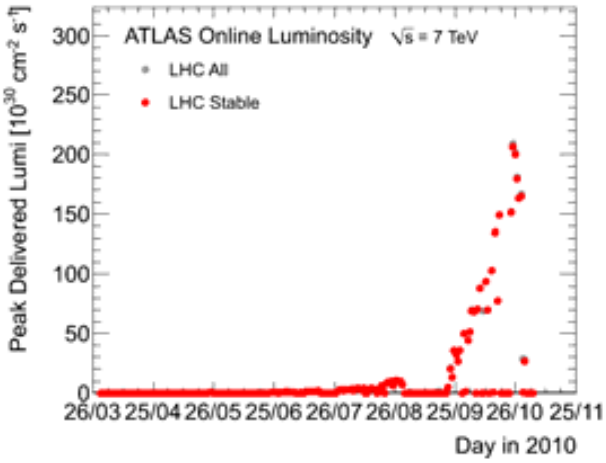

Figure 4.13: Peak delivered instantaneous luminosity per day at the ATLAS detector for the beam declared stable and unstable by the LHC [95].

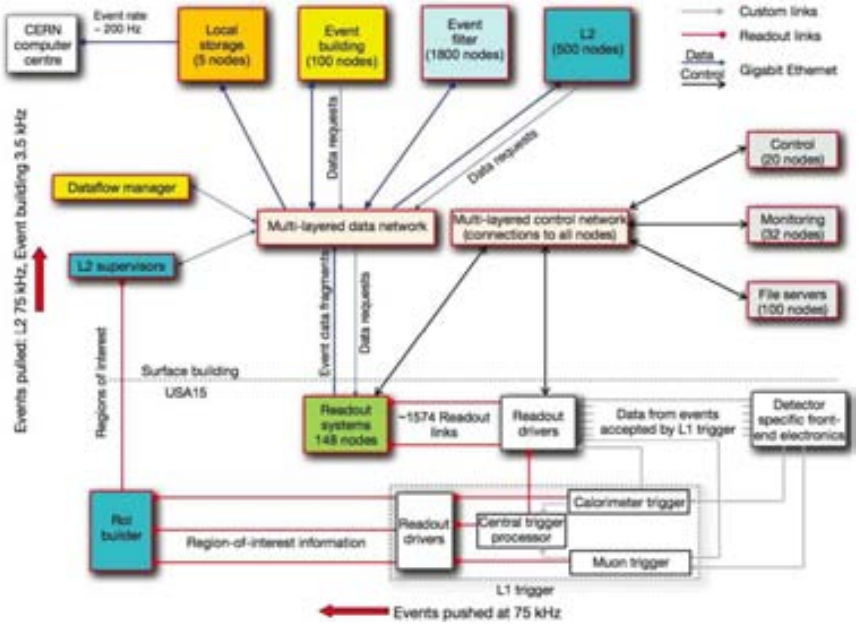

Figure 4.14: Block diagram of the ATLAS TDAQ system [90].

A block diagram of the ATLAS Trigger and Data Acquisition (TDAQ) system is shown in Fig. 4.14. The DAQ system steers the transfer of data from the Read-Out Drivers (RODs) to mass storage. Furthermore, it initializes, controls and monitors the data taking.

Table 4.7: Latencies and output rates for the three trigger levels [97].

Trigger Level	latency	output rate
L1	2.5 μs	75 kHz
L2	40 ms	3.5 kHz
EF	4 s	200 Hz

A detailed description of the TDAQ system can be found for instance in [90] and [97].

L1 Trigger: The L1 trigger level is composed of custom made electronics and filters events with interesting physics processes. Another essential function of the L1 trigger level is the unambiguous identification of bunch crossings of interests, which is challenging taking in mind a crossing interval of about 25 ns. Furthermore, a pre-scaling for optimal use of the available bandwidth can be applied as instantaneous luminosity and background conditions change.

The L1 searches for high transverse momentum muons in the trigger systems of the muon spectrometer, i.e. the RPCs and TGCs (see Sec. 4.3.4) and objects such as electrons, photons, jets, and taus decaying hadronically, in the calorimeters (see Sec. 4.3.3). For the calorimeter based objects a reduced granularity of $\Delta\eta \times \Delta\phi = 0.1 \times 0.1$ [98] is considered.

For the decision taking a Region of Interest (ROI) is created for regions containing interesting features and required to pass a certain threshold. These ROIs contain the η and ϕ coordinates as well as the type information, which is sub-sequentially used and refined by the higher level triggers, e.g. energy and passed threshold.

L2 Trigger: The L2 trigger is seeded by the ROIs reconstructed at L1. It uses a higher granularity and precision together with all available detector data for this region. A processing farm, executing the event selection, lowers the event rate to 3.5 kHz (see Table 4.7). Using the ROIs brings the advantage that only about 2% of the detector data has to be processed.

The decision taking is a series of steps, each refining the existing information by acquiring additional data from increasingly more detectors. Signature and sequence tables are built of a list of physics signatures, so-called trigger chains, the event reconstruction, and the selection algorithms. Finally, a hypothesis algorithm determines whether the trigger criteria are satisfied or not. This procedure is common to both HLT trigger levels, i.e. L2 and EF.

Event Filter: The last trigger level is the Event Filter (EF). It is also a processing farm, but unlike L2, the event selection is based on the standard ATLAS event reconstruction. This allows for example to used the track information of the inner detector (see Sec. 4.3.2) which significantly enhances the particle identification, e.g. to distinguish between electrons and photons.

Beside lowering the output rate to the requested 200 Hz, the EF tags the events according to the classification criteria for the ATLAS physics streams. The different physics streams for the corresponding objects are defined by the trigger menus. In general an event is filled into a stream if any of the corresponding object triggers has been satisfied in this event.

The events are split-up into different physics streams, as for instance electron/photon, muon, jet/missing transverse energy, and minimum bias. This design reduces the user load on individual data sets. Recorded data sets are transferred separately for each stream to the ATLAS Tiers, the ATLAS part of the LHC computing grid. In addition to the physics-motivated streams, streams for calibration and debugging as well as an express stream exist. The express stream fully overlaps with all other streams and contains a representative selection of events [97].

4.3.8 Detector Simulation

The GEANT4 package [99, 100] was developed for the simulation of the passage of particles through matter by means of MC methods. In addition to the description of the detector geometry and the tracking of particles through it, the material of the detector constituents is described and visualized. Furthermore, the response of all sensitive elements of the detector is simulated and recorded.

Every particle produced during the event generation (see Sec. 3.2.4) is passed to the GEANT4 simulation, where the large amount of physics processes, occurring when crossing the detector, is simulated. The so-called hits are generated which correspond to the total energy deposition, the position in the detector, and the time.

To control the CPU time used to process an event, range cuts can be specified. They control the production of secondary particles, as for instance electrons or photons during bremsstrahlung, and suppress them in case their range is below 1 mm. This value differ for some sub-detectors as for example the Pixel Detector or the Forward Calorimeter [72].

In order to simulated underlying events and pile-up, various types of events are read in (see Sec. 3.2.4), and hits from each type are overlaid with the simulated hard-scattering process.

The simulated events are translated into so-called digits to study their detector response. These digits are produced when the voltage or current of a particular read-out channel of a sub-detector exceeds a pre-configured threshold within a time-window. For some sub-detectors the digits include

the signal shape over time, while others just record a signal exceeding of the threshold.

The peculiarities of each sub-detector's charge collection, including cross-talk, electronic noise and channel-dependent variations in detector response are modeled in sub-detector-specific digitization software. The properties of the digitization algorithms were tuned to reproduce the detector response characterized in test beam data and cosmic ray. Dead channels and noise rates are read from database tables to reproduce conditions seen in a particular run.

The effects of multiple proton-proton interactions, beam gas, and other pile-up effects, that are simulated separately as described before, are merged in the digitization step.

The digits of all sub-detectors are written out as Raw Data Objects (RDOs) that are used as input to the object reconstruction (see Chapter 5).

For more details on the ATLAS detector simulation see [72].

Chapter 5

Event Reconstruction and Object Identification

The ATLAS detector and reconstruction software allow the identification and measurement of tracks, vertices, electrons, muons, taus, photons, jets (including their flavor) and missing transverse energy.

The object reconstruction as well as its identification is optimized to achieve the highest possible efficiency while keeping the misidentification rate low enough to guarantee an adequate performance in most physics analysis.

5.1 Track Identification

The reconstruction using the inner detector (see Sec. 4.3.2) is based on a modular and flexible software, designed to reconstruct tracks and vertices, also in combination with the muon spectrometer, whenever required. The software combines various reconstruction tools for track extrapolation, track fitting including material corrections, and vertex fitting [101]. The track reconstruction is logically sub-divided into the three following stages: the pre-processing, the track-finding, and the post-processing.

In the pre-processing stage the space-points are reconstructed from SCT clusters. In the track-finding stage the high granularity of the pixel detector and the SCT are exploited, looking for prompt tracks originating from the interaction point.

After combining space-points from the three pixel layers with those from SCT to form track candidates, these are fitted, outliers removed, cluster-to-track association ambiguities solved, and mis-reconstructed tracks removed. This is achieved by applying quality cuts on the number of associated clusters. After extending the candidate tracks into the TRT, resolving left-right ambiguities using the associated drift-circle information, the tracks are refitted with the full information of all three inner detector sub-detectors. Bad

fits, spotted comparing the fit with the silicon-only track candidate, are labeled as outliers.

5.2 Vertex Reconstruction

After the reconstruction of the tracks, in a post-processing stage, a dedicated vertex finder is used to find primary vertices, followed by secondary vertices. In a typical event, several vertices are produced, originating from the primary hard-scattering interaction or decays of long-living particles. To distinguish an event from minimum bias events and pile-up processes, a primary vertex is searched among all these vertices.

The ATLAS experiment uses a vertex finder tool based on the Billoir method [102]. To find the primary vertex, a basic track selection [103], applying minimal requirements on the transverse momentum ($p_T > 100\,\mathrm{MeV}$) and the number of hits (at least four hits in SCT, at least six in TRT, and at least one in the Pixel Detector), is passed to the vertex finding tool. A fit, that returns a vertex candidate and a list of used tracks, is performed, minimizing

$$\chi^2 = \sum_i \Delta\, q_i^T W_i \Delta\, q_i\,, \tag{5.1}$$

with $\Delta q_{ij} = q_{ij}^{\mathrm{measured}} - F_j(V, p_i)$. The parameters q_{ij} $(j = 1, \ldots, 5)$ are functions $F_j(V, p_i)$ of the vertex position $V = V(x, y, z)$ and the track momenta p_i, that characterize the i-th track. W_i is their weight matrix, the inverse of the covariance matrix. In the case, that the q_i are linearly related to the variations δV and δp_i^0, $F_j(V, p_i)$ can be expanded as

$$F(V^0 + \delta V, p_i^0 + \delta p) = F(V^0, p_i^0) + \frac{\partial F_j(V, p_i)}{\partial V_n}\,\delta V + \frac{\partial F_j(V, p_i)}{\partial p_{im}}\,\delta p_i\,, \tag{5.2}$$

where $n = 1, \ldots, 3$ and $m = 1, \ldots, 3$ are the three dimensions of the track candidate momentum. The χ^2 function can be minimized for δV and δp_i, such that it gives the solution for the vertex position V. For more details see [104].

A second track selection is applied, based on the χ^2 of the fit, to eliminate outliers. Tracks with $\chi^2 > 4$ contributions are removed and the vertex is refitted with the remaining tracks.

5.3 Electrons and Photons

The reconstruction of electrons and photons is seeded by a sliding window algorithm with a size of 5×5 cells in the middle layer of the EM calorimeter. A cluster is reconstructed around the seed.

In the case of electron candidates the energy in a cluster of size 3×7 in the middle layer of the EM calorimeter barrel is collected, corresponding

to 0.075×0.175 in $\Delta\eta \times \Delta\phi$. In the end-cap, the energies in the cells of the sliding windows (5×5 cells) in layer 2 are summed. The number of cells used results from an optimization between collecting all energy of the electron and rejecting energy from hard bremsstrahlung photons. Finally, the energy of all layers is collected.

In the case of photon candidates, that are not labeled as converted, the cluster size of 3×5 is used in the barrel, and 5×5 in the end-cap. Unconverted photons are treated as electrons.

After this step, position corrections are applied, taking into account the different response of the cells at their edges. These corrections however are only of the order of 1% in η and 0.4% in ϕ [90].

A match of a track reconstructed with the inner detector to the reconstructed electron (photon) candidate is performed yielding a well-defined separation between electrons and photons together with the flag, indicating a photon conversion in the inner detector: electrons have an associated track and are not labeled as originating from conversion, while photons do not have an associated track and can be labeled.

5.4 Muons

The ATLAS experiment was designed to measure a broad spectrum of muons, from non-isolated muons originating from b quark jets up to high-momentum and isolated muons arising from W and Z boson decays, covering a momentum range from 3 GeV up to 3 TeV.

Three approaches exist on ATLAS to identify muons. Standalone muons are reconstructed by finding a track in the muon spectrometer which is extrapolated to the beam line. Combined muons are standalone muons matched to nearby inner detector tracks. In contrast, tagged muons start from inner detector tracks and are extrapolated to nearby hits in the muon spectrometer. For each identification type two reconstruction algorithms exists, the so-called Staco and MuID, defined below.

5.4.1 Standalone Muons

Track segments are built up from the four muon spectrometer sub-systems, the MDTs and CSCs, as well as the trigger chambers, RPCs and TGCs, and linked to tracks.

In the case of the MuID, the Moore algorithm [**?**] performs the extrapolation of the track to the beam line and assigns energy loss based on material crossing in the calorimeter. In addition, it includes the calorimeter energy measurements, if they are significantly larger than the most probable value for the muon energy loss and if the muon appears to be isolated.

5.4.2 Combined Muons

Both algorithms pair the muon spectrometer tracks with those from the inner detector. The match is performed using a χ^2 including vectors T of five track parameters and their covariance matrices C for the muon spectrometer (MS) and the inner detector (ID) tracks:

$$\chi^2_{\text{match}} = (T_{\text{MS}} - T_{\text{ID}})^T (C_{\text{ID}} + C_{\text{MS}})^{-1} (T_{\text{MS}} - T_{\text{ID}}) \,. \tag{5.3}$$

The difference between Staco and MuID is, that the former does a statistical combination of Inner Detector and Muon Spectrometer track vectors:

$$T = (C_{\text{ID}}^{-1} + C_{\text{MS}}^{-1})^{-1} (C_{\text{ID}}^{-1} T_{ID} + C_{\text{MS}}^{-1} T_{\text{MS}}) \,, \tag{5.4}$$

while the latter performs a fit accounting for multiple scattering and energy loss in the material, as well as the magnetic field inside the calorimeter and the muon spectrometer.

5.4.3 Tagged Muons

The tagging algorithms (MuTag and MuGirl) propagate all inner detector tracks with sufficient momentum to the first layer of the muon spectrometer and search for nearby segments. While MuTag defines a tag χ^2 using the difference between any nearby segment and its prediction from the extrapolated track, MuGirl uses an artificial neural network to define a discriminant. A track in the inner detector is tagged as a muon track if a segment sufficiently close to the predicted track position is found. Tagged muons are not used in this study, since they are optimized for low momenta.

5.5 Jets

Various jet reconstruction algorithms exist in ATLAS to cope with the variety of physics processes of interest at the LHC. The input to those so-called jet finders can be any object with a four momentum representation, as for instance calorimeter cells, tracks or MC truth objects.

A flow chart of the jet reconstruction for calorimeter jets from towers or clusters is drawn in Fig. 5.1. Towers are formed by collecting cells into bins of a regular $\Delta\eta \times \Delta\phi = 0.1 \times 0.1$ grid, taking into account overlaps. To suppress detected noise, towers with negative energy are recombined with nearby towers until their energy is positive, so that they have a physical four-vector representation.

Alternatively, clusters of energy (topological clusters) are reconstructed, whereby nearest neighbors of a cell with an energy four times larger than the noise level ($|E_{\text{cell}}| > 4\sigma_{\text{cell}}$) are collected, independent of the magnitude of their signal. In case that $|E_{\text{cell}}| > 2\sigma_{\text{cell}}$ for these neighbors, they are treated

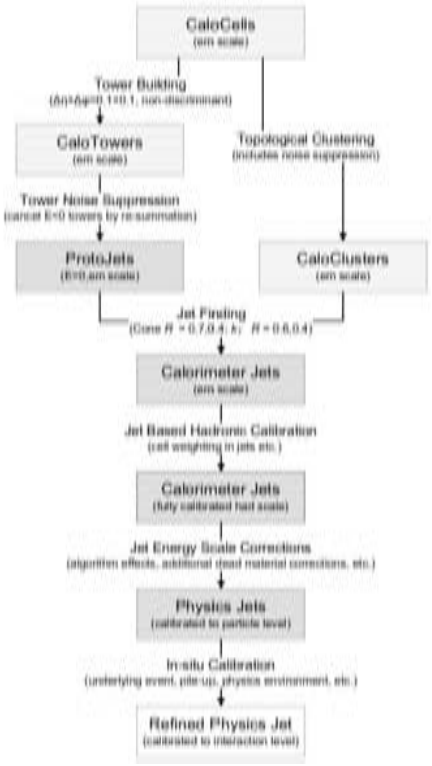

Figure 5.1: Flow chart of the jet reconstruction for jets from towers or clusters, reconstructed with the cone or the anti-k_t jet finding algorithm [90].

as secondary seeds and also their neighbors are attached to the topological cluster. Subsequently, all surrounding cells are added as well. In case of more than one cluster maximum, the topological cluster is split up. Topological clusters contain substantially less noise and to include less cells than tower clusters.

Two main jet finding algorithms exist at ATLAS, a seeded fixed cone algorithm and a successive recombination (anti-k_t) algorithm. The first one associates clusters (or towers) in a cone around the highest p_T cluster. Two input parameters are required, the transversal energy threshold of the clusters, which at ATLAS is $E_T^{\text{threshold}} = 1\,\text{GeV}$, and the size R of the cone (see Eq. 4.2). A narrow ($R = 0.4$) and a wide ($R = 0.7$) cone size are used at ATLAS. For the so-called split-and-merge step an overlap fraction threshold of 50% is chosen. Since the cone jet algorithm with this configuration is fast, it is used for the high level trigger (see Sec. 4.3.7).

The anti-k_t algorithm only needs the cone size R as input. In ATLAS a narrow ($R = 0.4$) and a wide cone ($R = 0.6$) are used. Two distances are

defined:

$$d_{ij} = \frac{\Delta R_{ij}^2}{\max(p_{T,i}^2, p_{T,j}^2)} \qquad \text{and} \qquad d_{iB} = p_{T,i}^{-2}\,, \tag{5.5}$$

where $p_{T,i}$ is the transverse momentum of the i-th cluster, ΔR_{ij} is the distance between the i-th and the j-th cluster. In the case that $d_{ij} < d_{iB}$ the two clusters are combined as cluster i, else the cluster i is considered to be the final state, i.e. a reconstructed jet. The anti-k_t algorithm favors hard particles and expands through soft sub-jets. The resulting jet has a circular cone-like form, preferred by experimentalist to correct for imperfect detector coverage. An important advantage of the anti-k_t algorithm is that it is infrared- and collinear-safe. It is efficient even for a rather large number of input objects and avoids the usual pre-cluster steps, such that its performance is similar to the cone algorithm. For more details on jet algorithms see [105].

To find jets at particle level all stable neutral and charged particles in the final state within $|\eta| < 5.0$ are considered. These can originate from the hadronization of the hard scattering process, from ISR and FSR, as well as underlying events. The four vectors for these particles are taken at their generation vertex.

The jet finding at the reconstruction level is followed by the calibration procedure (see following section). The result is a physics jet object, fully calibrated to the particle level.

5.5.1 Jet Energy Calibration

Reconstructed jets are calibrated to the EM scale, applied to each calorimeter cell. The corrections at the EM scale are measured by the electromagnetic and the hadronic calorimeter using test-beam measurements for electrons and muons in both calorimeters. While the corrections at the EM scale account correctly for electrons and photons, the following effects are not corrected for:

- lower and non-linear response of the calorimeters to hadrons than to electrons and photons;
- energy losses in un-instrumentalized regions (dead-material);
- an offset in the cells energy caused by additional pp interactions;
- the finite size of the jet cone sized used for its reconstruction;
- bending of charged particles out of the jet cone;
- neutrinos from the decay of particles inside the jet;

The jet energy scale (JES) is estimated in MC simulation and is applied both, MC and data, to correct these effects. Together, the EM scale and JES correct the measured jet energy in the calorimeter to the particle level.

The so-called EM-JES calibration scheme was chosen for top quark analysis at the ATLAS experiment. It consists in a per-jet multiplicative factor that corrects the jet energy at the EM scale to the particle level. The EM-JES scheme is applied to the jet energy and transverse momentum in order to restore the energy of the jets at particle level. For the estimation of the JES isolated jets[1], reconstructed from noise-suppressed towers built of cells from topological clusters, were considered.

The correction is performed for the response of the transverse momentum of the jet. A response function is parametrized as a function of the transverse momentum of the jet at particle level $p_T^{\text{MC truth jet}}$ and η:

$$R^{\text{EM}}(p_T^{\text{MC truth jet}}, \eta) = \frac{p_T^{\text{jet,EM}}}{p_T^{\text{MC truth jet}}} , \tag{5.6}$$

where $p_T^{\text{jet,EM}}$ is the transverse momentum of the reconstructed jet measured in the calorimeter, corrected to the EM scale. The numerical inversion method parametrizes R as function of $p_T^{\text{jet,EM}}$ and η [106]:

$$R^{\text{EM}}(p_T^{\text{jet,EM}}, \eta) = \sum_{i=0}^{4} \frac{a_i(\eta)}{(\ln(p_T^{\text{jet,EM}}[\text{GeV}]))^i} . \tag{5.7}$$

The four vector of each jet is scaled with the parametrized response function. The response function is estimated for jets matched to particle level jets in the MC simulation truth within $\Delta R = 0.3$ around the jet axis.

Effects such as different quark or gluon content, jet flavor, jet isolation and out-of-cone fluctuations require additional corrections which are not included in this study.

Uncertainty: Several sources of uncertainty for the estimation of the JES have been taken into account (see Sec. 7.6.1.2), including jets with a transverse momentum at particle level of $p_T^{\text{MC truth jets}} > 20\,\text{GeV}$ and at calorimeter level of $p_T^{\text{jet}} > 10\,\text{GeV}$. No isolation criteria have been taken into account.

For the uncertainty due to an imperfect detector description the following sources have been considered:

- the effect of a distortion of the detector and additional dead material by evaluating different geometry models, yielding an p_T independent downward shift of the response function of 2%;

[1] No other jet with $p_T > 4\,\text{GeV}$ within $\Delta R < 2.5 \cdot R^{\text{algo}}$.

- the threshold of the topological clusters noise, varying the value up and down by 10%, yielding an upward shift at of 4% (2%) for a lower (higher) noise threshold;

- a shifted beam-spot by $(x, y, z) = (1.5, 2.5, -9)\,\text{mm}$, covering the actual shift of $(x, y, z) = (-0.4, 0.62, -1.3)\,\text{mm}$, yielding an uncertainty of less than 1%.

An uncertainty of 3% (4%) on EM scale, flat in p_T and η, has been considered for the electromagnetic (hadronic) calorimeter.

A closure test with QCD multijet samples generated with Pythia was performed and the largest deviation between the restored jet p_T at calorimeter and particle level were taken into account. In the barrel region ($0.3 < |\eta| < 0.8$) a deviation of 2% (1%) for jets with $p_T < 50\,\text{GeV}$ ($p_T > 50\,\text{GeV}$) was considered. In the end-cap region a closure better than 1% was observed. This accounts also for differences originating from the fact that not-isolated jets where used for the uncertainty estimation.

Due to a better understanding of the barrel region, the uncertainties for the end-cap ($1.2 < |\eta| < 2.8$) have been extrapolated from the barrel region. This introduces additional uncertainty of about 2%.

Since the hadronic showering within the calorimeter influences the energy deposit, different showering models have been tested. An contribution of 4% (2%) in the central (barrel) region for the model, that yields a lower jet response, was taken into account. For the model yielding a higher jet response an uncertainty of 2% was considered.

Finally, the impact of the MC event generator, the fragmentation, and the underlying even model have been studied. The Alpgen generator, interfacing Herwig and jimmy has been compared to Pythia with Perugia and Professor tunes of the underlying event to data. First yields the largest deviation in response with a downward shift of 4% (2%) for jets with $p_T > 50\,\text{GeV}$ in the central (end-cap) region.

In both studies, i.e. with an integrated luminosity of $2.9\,\text{pb}^{-1}$ and $35\,\text{pb}^{-1}$, the same sources of uncertainty have been considered. The here listed values refer to the analysis with $2.9\,\text{pb}^{-1}$.

A total uncertainty between 6% and 10% has been taken into account for the study with $2.9\,\text{pb}^{-1}$. For more details see [106].

In the analysis with $35\,\text{pb}^{-1}$ the uncertainty on the JES decreased mainly due to a reduced calorimeter response uncertainties, based on measurements of the single hadron response, a more detailed study of the uncertainties associated to neutral hadrons and the recalibration of the EM scale [107]. The total uncertainty varies in the range of 4% to 6% [107, 108].

Table 5.1: Parameters for the jet energy resolution from data-driven techniques [106].

	N	S	C
dijet balance	4.0 ± 0.4	0.87 ± 0.03	0.060 ± 0.001
bi-sector	4.6 ± 0.4	0.85 ± 0.04	0.064 ± 0.002

5.5.2 Jet Energy Resolution

In order to estimate the energy resolutions of jets at the EM+JES scale, two data-driven techniques were used. The dijet balance method measures the asymmetry A of the two transverse momenta ($p_{T,1}$ and $p_{T,2}$) in dijet events, were both jets are supposed to have the same transverse momentum:

$$A = \frac{p_{T,1} - p_{T,2}}{p_{T,1} + p_{T,2}} \,. \tag{5.8}$$

Requiring both jets being in the same η region, the resolution can be estimated by $\sigma_{p_T}/p_T = \sqrt{2}\sigma_A$.

The bi-sector method uses a imbalance transverse vector $\vec{P}_T$ as the sum of the p_T of the two leading jets. This vector defines a new plane (Ψ, η), where Ψ is the direction that bisects $\Delta\phi_{12} = \phi_1 - \phi 2$. The resolution can been defined with the variance of Ψ and η as

$$\frac{\sigma_{p_T}}{p_T} = \frac{\sqrt{\sigma_{\Psi}^{2,\mathrm{calo}} - \sigma_{\eta}^{2,\mathrm{calo}}}}{\sqrt{2}\langle P_T \rangle |\cos \Delta\phi_{12}|} \,, \tag{5.9}$$

The transverse jet momentum is parametrized as

$$\frac{\sigma_{p_T}}{p_T} = \frac{N}{p_T} \otimes \frac{S}{\sqrt{p_T}} \otimes C \,, \tag{5.10}$$

where N,S, and C denote the noise, stochastic and constant term, respectively. The obtained parameters a listed in Table 5.1 and are in agreement for both methods.

In the study with $2.9\,\mathrm{pb}^{-1}$, an uncertainty of 14% was taken into account for the jet energy resolution [106]. A decreased uncertainty of 10% was considered for the analysis with $35\,\mathrm{pb}^{-1}$.

5.5.3 b-jet Identification

Large efforts are made to identify jets arising from heavy flavor quarks, especially from b quarks. Distinguishing those from jets originating from c quarks, lighter quarks, and gluons is important for top quark studies, as well as to searches for new physics, such as the Higgs boson and supersymmetry.

For instance, the information about which jet originates from b quarks can be exploited to suppress physical backgrounds, as well as an aid in the mass reconstruction to reject combinatorial background. For instance, the possible combinations to reconstruct the hadronic top quark candidate in the top quark pair decay final states can be restricted having the two b quark jets identified, e.g. by a factor of two in case of only four jet candidates, but already by a factor of almost seven for five jet candidates.

The identification is based on the long lifetime of the b quark, the large mass of B-hadrons, and the large branching ratio into leptons. The main discrimination between b and light quark jets is the lifetime. Flavor tagging algorithms are defined based on L, d_0, z_0, the secondary vertex properties and the properties of the leptons reconstructed inside the jet. They provide a tagging weight, specifying the probability of a jet being of a certain flavor.

In ATLAS the following taggers have been developed [90]:

- TrackCounting: based on the impact parameter significance d_0/σ_{d_0} of tracks within the jet, where σ_{d_0} is the uncertainty on the impact parameter d_0. The transverse impact parameters d_0 defined as the closest approach of a track and the primary vertex, i.e. its transversal (r/ϕ) projection. It is signed by the jet direction within the calorimeter;
- JetProb: based on the impact parameter resolution function $R(d_0/\sigma_{d_0})$ of prompt tracks;
- SV0: based on a cut on signed decay length significance L/σ_L of the reconstructed secondary vertex. For the b quark the long lifetime results in a significant flight path length L;
- IP3D+SV1: based on the sum of SV1 and IP3D probability weights;
  - SV1: probability weight based on secondary vertex tagger;
  - IP3D: probability weight based on the transverse (d_0) and longitudinal impact parameter (z_0) significances of all tracks. z_0 represents the z-coordinate of a track at the point of the closest approach of the track to the primary vertex.
- JetFitterComb: based on a vertexing algorithm using a Kalman filter;
- Soft Muon: based on the identification of a reconstructed muon within a jet.

This measurement is based on the SV0 tagger, which is discussed in detail in [109, 110]. It starts with the reconstruction of secondary vertices from B-hadron decay products by combining track pairs that form a good vertex. Table 5.2 list the requirements on those tracks. Two-track vertices, that have a mass incompatible with K_s^0 and Λ decays and photon conversion,

Table 5.2: Track selection criteria used by the SV0 tagging algorithm [109].

p_T	$> 0.5\,\text{GeV}$
d_0	$< 2\,\text{mm}$
$z_0 \sin\theta$	$< 2\,\text{mm}$
σ_{d_0}	$< 1\,\text{mm}$
σ_{z_0}	$< 5\,\text{mm}$
χ^2/ndof	< 3
Number of Pixel hits	≥ 2
Number of SCT hits	≥ 4
Number of Pixel+SCT hits	≥ 7

are merged into a common vertex by a robust χ^2 base fitting algorithm. Tracks with large contributions to χ^2 are iteratively removed until the fit probability of the reconstructed secondary vertex is greater than 0.001, a vertex mass less than 6 GeV, and the largest χ^2 contribution being below seven. In the case that a two-track vertex is at a radius consistent with the radius of one of the three Pixel Detector layers it is not considered, since it likely originates from material interactions.

All tracks from the remaining two-track vertices are combined to one secondary vertex. The tagging of the jet flavor with the SV0 algorithm is performed by requiring a cut on the tag weight. The tag weight is defined as the signed decay length significance $L/\sigma(L)$. Figure 5.2 shows three-dimensional decay length significance for all secondary vertices reconstructed in data events and the number of tracks in secondary vertices for the SV0 tagger algorithm.

In this measurement the SV0 algorithm was used with a tag weight cut of 5.72 (5.85) for the analysis with $2.9\,\text{pb}^{-1}$ ($35\,\text{pb}^{-1}$) yielding an average efficiency of about 50% in simulated top quark pair events.

5.6 Missing Transverse Energy

The measurement of the missing transverse energy E_T^{miss} is important for the study of the top quark pair decays, as well as for many new physics searches, since it can be used to signal the presence of particles that go undetected through the detector, such as neutrinos. To achieve a good performance, efforts are made to minimize the impact of limited detector coverage, the finite detector resolution, dead regions, and noise.

Two algorithms are available in ATLAS to reconstruct the missing transverse energy, the cell-based and the object-based algorithms. Both use the same noise suppression, which is important, since the electronic noise alone from the around 200,000 read-out channels of the calorimeter contribute $\sim 13\,\text{GeV}$ to the width of the missing transverse energy distribu-

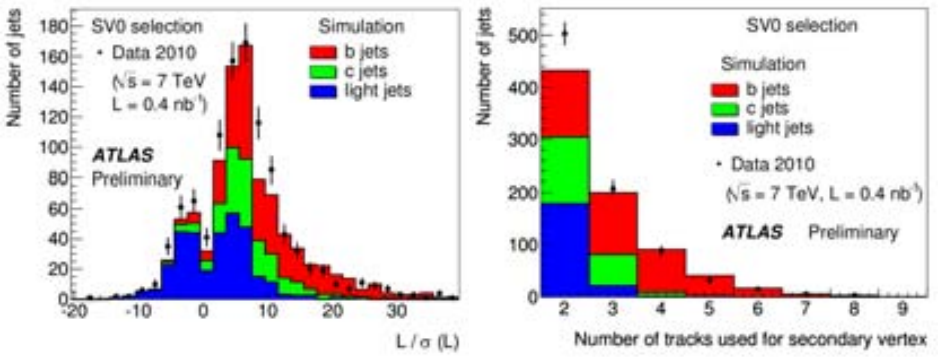

(a) (b)

Figure 5.2: Shown are (a) the three-dimensional decay length significance, signed with respect to the calorimeter jet axis, for all secondary vertices reconstructed in data events (markers) and (b) the number of tracks in secondary vertices for the SV0 tagger algorithm [109].

tion [90]. The method used for the noise suppression uses the cells from topological clusters which survive a noise suppression of σ_{noise} (see Sec. 5.5).

In this study the object-based algorithm was used and is discussed in the following. For the estimation of E_T^{miss} the calibrated cells from reconstructed objects are used in the following order: electrons, photons, taus, jets, and finally muons. In case that a cells belongs to more than one object, only the first association is used. Because the initial cell energy is replaced with a more refined calibration, one referrers to $E_T^{\text{miss,RefFinal}}$. Cells not included in any object are treated in an additional term. Each contribution corresponds to the negative sum of the calibrated object cells inside the respective object, i.e. electrons, jets, muons, and unused cells. The calorimeter cells are calibrated at the EM scale. Only electrons that are isolated are taken into account.

Since the jet calibration on EM scale does not take into account instrumental effects, the p_T of the jets used for the E_T^{miss} estimation are calibrated with the numerical inversion (see Sec. 5.5.1).

The contribution from muons is estimated from the p_T of combined muons, which are measured in the muon spectrometer and require a track match within $|\eta| < 2.5$ with the inner detector, to reduces contributions from mis-identified muons. These can for example arise from high hit multiplicities in the muon spectrometer in events with very energetic jets. Outside the coverage of the inner detector ($|\eta| > 2.5$) no matched track is required. In that case the momentum of standalone muons momentum is used.

For more details see [111].

At the early stage of the analysis with a luminosity of $2.9\,\text{pb}^{-1}$, no correc-

tions are available for photons and taus, such that their energies effectively are accounted in the CellOut and RefJet term. Also the corrections from the cryostat between the EM and the hadronic calorimeter, which correspond to about half a radiation length, are not yet accounted.

In the measurement of the top quark pair cross section with $35\,\mathrm{pb}^{-1}$ also photons and taus are taken into account. Furthermore soft jets, corrected at the EM scale, contribute to the missing transverse energy calculation [112].

Chapter 6

Data Streams and Trigger Selection

The ATLAS detector covers nearly the entire solid angle around the collision point with layers of tracking detectors, calorimeters and muon chambers. All these detectors play important roles in the reconstruction of $t\bar{t}$ event candidates. Only data collected while all sub-detector systems were fully operational was used. Applying these requirements to data collected in stable beam conditions until 30^{th} August 2010 results in a data sample corresponding to an integrated luminosity of $2.9\,\text{pb}^{-1}$. This integrated luminosity estimate has an uncertainty of 11%, which is dominated by the uncertainty on the LHC beam current [113]. In the complete 2010 run data corresponding to an integrated luminosity of $35\,\text{pb}^{-1}$ an uncertainty of 3.4% was recorded. The main contribution originates from the bunch charge product (3.1%) which was reduced by updating the set of beam-separation scans [114].

Figure 6.1 shows the accumulated luminosity with the ATLAS detector until 3rd November 2010. The ratio of the recorded to delivered luminosity gives the ATLAS data taking efficiency (weighted by luminosity) of 93.6%. The inefficiency accounts for the turn-on of the high voltage of the Pixel, SCT and some of the muon detectors (2.0%) and any inefficiencies due to dead-time or due to individual problems with a given sub-detector that prevent the ATLAS data taking to proceed (4.4%). An additional $0.8\,\text{pb}^{-1}$ of integrated luminosity was delivered by the LHC between the request for ATLAS to turn off the sensitive detectors and the end of stable beam conditions [115].

Data Quality (DQ) requirements are applied in order to remove events containing unphysical objects, which may occur due to malfunction of parts of the detector. The DQ flags are saved per luminosity block and are used to form Good Runs Lists (GRLs).

Primary DQ flags indicate if the detectors, combined performance ob-

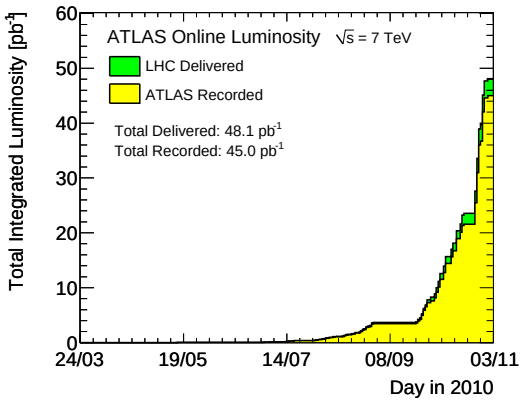

Figure 6.1: Cumulative luminosity versus day delivered to (green), and recorded by ATLAS (yellow) during stable beams and for pp collisions at 7 TeV center-of-mass energy [115].

jects, and triggers were performing well. The combined performance DQ flags are set by looking at the distribution of various observables associated with the combined performance objects, but without considering the state of the detectors or triggers. The final decision on whether a combined performance object is good for physics is taken by combining the relevant primary DQ flags to form a virtual flag. GRLs are produced by specifying a combination of virtual flags based on the physical objects needed for various analysis.

This measurement uses the electron and muon data streams. The different physics streams for the corresponding objects are defined by the trigger menus. In general an event is filled into a stream if any of the corresponding object triggers has been satisfied in this event.

Trigger requirements have been made more restrictive with increasing instantaneous luminosity, as listed in Table 6.1 and 6.2. Starting from an instantaneous luminosity of $10^{30}\,\mathrm{cm}^{-2}\mathrm{s}^{-1}$, single electron and muon triggers with a 10 GeV threshold are used. Since the HLT was not working properly, only L1 triggers have been used for early runs. For the electron channel a track match was required for the second half of the data, approximating the trigger object definition to the selected electron candidate.

For the rest of the 2010 data set, the transverse momentum requirement was increased for the electron trigger (`EF_e15_medium`). Also the quality cuts of the muon trigger have been tightened (`EF_mu13_tight`).

In MC studies `EF_e10_medium` and `EF_mu10_MSonly` have been used for the electron and muon channel, respectively. This is motivated by reasons of simplicity at the analysis level and is justified by the fact that in any case a scale factor on the trigger efficiency on simulation is needed. `Medium`

Table 6.1: Trigger used for the electron channel for the various runs with the corresponding runs, as well as the integrated luminosity for that period [116].

trigger	period	first run	last run	$\mathcal{L}_{\text{int}}[\text{nb}^{-1}]$
L1_EM10	A-D	152166	159224	295.3
EF_g17_etcut	E	160387	161948	1002.3
EF_e10_medium	F	162347	162882	1588.7
total				2886.3
EF_e15_medium	G1-I2	165591	167844	32422.6
total				35308.9

Table 6.2: Trigger used for the muon channel for the various runs with the corresponding runs, as well as the integrated luminosity for that period [116].

trigger	period	first run	last run	$\mathcal{L}_{\text{int}}[\text{nb}^{-1}]$
L1_MU10	A-E3	152166	160879	763.9
EF_mu10_MSonly	E4-F	160899	162882	2122.4
total				2886.3
EF_mu13_tight	G1-I2	165591	167844	32422.6
total				35308.9

refers to an electron trigger object with shower shape requirements and a track matching to the inner detector. MSonly means that only the Muon Spectrometers was used.

Chapter 7

Evidence for Top Quark Pair Production at $\sqrt{s} = 7\,\text{TeV}$

In this chapter we present the first study of top quark pair production in the lepton plus jets final state. The cross section $\sigma_{t\bar{t}}$ is measured using data corresponding to an integrated luminosity of $\mathcal{L}_{\text{int}} = 2.9\,\text{pb}^{-1}$ collected with the ATLAS detector at the LHC in pp collisions at $\sqrt{s} = 7\,\text{TeV}$. The signal cross section can be calculated as

$$\sigma_{t\bar{t}} = \frac{N_{\text{data}} - N_{\text{bkg}}}{\epsilon \cdot \mathcal{L}_{\text{int}}}\,, \tag{7.1}$$

where N_{data} is the number of selected data events, N_{bkg} is the estimated background contribution, and ϵ represents the overall event selection efficiency.

Flavor tagging algorithms were used to identify jets originating from b quarks, in order to suppress the contribution from physical backgrounds. The cross section is extracted from a likelihood fit to the invariant mass distribution of the hadronic top quark candidate, exploiting the characteristic resonant structure in this variable of signal events as compared to the backgrounds. An extended list of systematic uncertainties is taken into account for the cross section measurement.

The definition of the objects used to select the top quark pair candidates is introduced in Sec. 7.1. These objects are further used to separate signal from background events. This event selection is presented in Sec. 7.2. One of the main backgrounds that mimic the final state of top quark pairs are QCD multijet events, which are hard to simulated. Their estimation from data is explained in Sec. 7.3.1. The main physics background, W bosons in association with jets, was estimated from simulated events (see Sec. 7.3.2). After presenting the selected events used in this study in Sec. 7.4, the reconstruction of the top quark mass is explained in Sec. 7.5, followed by the description of the fitting method in Sec. 7.6. The expected and measured

impact of the systematic uncertainties on the measured top quark pair production cross section are discussed in Sec. 7.6.2 and 7.7.1, respectively.

Finally, the results of the cross section measurement are presented in Sec. 7.7 with the significance calculation for this result given in Sec. 7.7.4. A summary is given in Sec. 7.8.

7.1 Physics Object Definitions

This measurement exploits the information from the majority of the subsystems of the ATLAS detector, since it requires the identification of electrons, muons, jets (including their flavor) and missing transverse energy. The object definition criteria introduced in Chapter 5 are used. In order to reconstruct the signal final state with a high purity, further optimizations of the object definitions are applied.

In this section the physical object candidates which are used within this analysis are defined.

7.1.1 Electrons

Electron candidates are required to have a reconstructed transverse energy of $E_T > 20\,\text{GeV}$ and to satisfy also the fiducial requirements for the cluster pseudo-rapidity of $|\eta_{\text{cluster}}| < 2.47$, excluding the crack region at $1.37 < |\eta_{\text{cluster}}| < 1.52$ (see Sec. 4.3.3.1). In order to suppress jets or photons mis-identified as electrons, the following variables are exploited (for further details see [117]):

- shower shape:
  - the hadronic leakage, i.e. the ratio R_{had1} of the E_T in the first layer of the hadronic calorimeter to the E_T of the EM cluster (used over the range $|\eta| < 0.8$ and $|\eta| > 1.37$), as well as the ratio R_{had} with E_T in the complete hadronic calorimeter;
  - the ratio R_η of cell energies in 3×7 over 7×7 cells in the second layer of the EM calorimeter as a function of the pseudo-rapidity;
  - the lateral width w_{η^2} of the shower from the second layer of the EM calorimeter. It is calculated in a window of 3×5 cells using the energy weighted sum over all cells

$$w_\eta^2 = \sqrt{\frac{\sum E_i \times \eta^2}{\sum E_i} - \left(\frac{\sum E_i \times \eta}{\sum E_i}\right)^2}\,, \tag{7.2}$$

    with E_i the energy of the i-th cell;

  - the total shower width w_{stot} in the first layer of the calorimeter, determined in a window $\eta \times \phi = 0.0625 \times 0.2$ as

$$w_{\text{stot}} = \sqrt{\frac{\sum E_i \times (i - i_{\text{max}})^2}{\sum E_i}}, \tag{7.3}$$

    with i being the strip number and i_{max} the strip number of the first local maximum;
  - the ratio of the energy difference E_{ratio} associated with the largest and second largest energy deposit over the sum of these energies from the first layer of the EM calorimeter;

- central tracks spatially matched to the calorimeter clusters satisfying requirements on:
  - the number of hits in the pixel detector (≤ 1), the number of hits in the pixel detector and SCT (≤ 7), as well as the transverse impact parameter ($d_0 < 5\,\text{mm}$);
  - $\Delta\eta_1$ between the cluster and the track ($\Delta\eta_1 < 0.01$);
  - the ratio of the cluster energy to the track momentum (E/p) being compatible with that from electrons;
- calorimeter isolation: the transverse energy deposit in the calorimeter in a cone of $R = 0.2$ (Etcone20 $< 4\,\text{GeV} + 0.023 \cdot E_T$), except the E_T of the electron cluster;
- veto on photon conversion: at least one B-layer hit (see Sec. 4.3.2.1), in regions with known dead modules.

7.1.2 Muons

Muon candidates are selected from combined muons reconstructed with the MuID algorithm. This is done to be consistent with the muon object definition used for the missing transverse energy calculation (see Sec. 7.1.4). The candidates are required to have a transverse momentum of $p_T > 20\,\text{GeV}$ and the pseudo-rapidity to be within the inner detector acceptance ($|\eta| < 2.5$). Isolation criteria are used to reject muons that do not originate from W decays but for instance from heavy (b and c) flavor decays and in-flight-decays of π and K:

- the distance between the muon candidate and the closest accepted jet candidate (see Sec. 7.1.3) of $\Delta R > 0.4$, considering jets with $p_T > 20\,\text{GeV}$ and within $|\eta| < 2.5$;
- the transverse energy deposit in the calorimeter within a cone of $R = 0.3$ around the cluster (Etcone30 $< 4\,\text{GeV}$), excluding the transverse energy of the calorimeter cells associated with the muon;

- the sum of track transverse momentum measured within a cone of $R = 0.3$ around the track (Ptcone30 < 4 GeV), excluding the track p_T of the muon;

7.1.3 Jets and Flavor Tagging

Jet candidates are reconstructed with the anti-k_t algorithm and calibrated at the particle level (see Sec. 5.5.1). Jets are considered to be mis-identified and rejected if any of the following three criteria is satisfied:

- less than six energy-ordered cells accounting for at least 90% of the jet energy and a fraction of the jet energy larger than 0.8 in the HEC;
- a fraction of the jet energy from calorimeter cells with a bad fit quality larger than 0.8 and a fraction of the jet energy in the EM calorimeter larger than 0.95;
- a jet time with respect to the bunch crossing larger than 50 ns, calculated with an energy weighted sum of the timing from all the cells associated to the corresponding jet.

For more details on the jet quality requirements see [118].

Since by default all reconstructed electron objects are also reconstructed as jets, these two classes of objects do overlap. To avoid double counting of the electron candidate as a jet, the closest jet to an accepted electron candidate (see Sec. 7.1.1) within $\Delta R < 0.2$ is rejected.

Candidate b quark jets are identified by using the SV0 tagging algorithm and requiring a weight larger than 5.72, corresponding to an average efficiency of 50% for b quark jets in $t\bar{t}$ events.

7.1.4 Missing Transverse Energy

The missing transverse energy E_T^{miss} is constructed from the vector sum of all calorimeter cells, resolved into the transverse plane (see Sec. 5.6). Cells associated with jets are taken at the corrected energy scale that was used for jets, while the contribution from cells associated with electrons are replaced by the calibrated transverse energy of the electron. Finally, the transverse momentum of muons passing selection requirements are included, also removing the contribution of any calorimeter cell associated with the muon.

7.2 Event Selection

7.2.1 Selection Requirements

An event selection is applied in order to obtain a set of events with the highest possible purity and acceptance for signal events. In the following we

distinguish between the electron and the muon channels, depending on the selected lepton (see listing below).

Events satisfying the single isolated electron trigger (electron channel) or the muon trigger (muon channel) criteria corresponding to the data taking period analyzed (see Chapter 6) have been selected. Furthermore, selected events must have a reconstructed primary vertex with at least four associated tracks, to ensure that the correct hard-scattering primary vertex is selected and the proper reconstruction of the objects used in the analysis. In addition, the following criteria are applied to the objects defined in Sec. 7.1:

- exactly one (no) electron candidate and no (exactly one) muon candidate for the electron channel (muon channel). In case of the electron channel the selected candidate has to match the corresponding trigger object[1];
- a missing transverse energy of $E_T^{\text{miss}} > 20\,\text{GeV}$;
- satisfy the so-called triangular cut: $E_T^{\text{miss}} + m_T(W) > 60\,\text{GeV}$. The transverse mass of the W boson is defined as $m_T(W) = \sqrt{2\,p_T^{\ell}\,E_T^{\text{miss}}\,(1 - \cos\phi(\ell, E_T^{\text{miss}}))}$;
- the event contains either exactly three jets with $p_T > 25\,\text{GeV}$ (referred to as three jets exclusive channel) or at least four jets with $p_T > 25\,\text{GeV}$ (referred to as four jets inclusive channel) within a pseudo rapidity of $|\eta| < 2.5$;
- at least one of the selected jets should be tagged as a b quark jet, i.e. have a SV0 tagging weight larger than 5.72.

The requirements on the lepton and the missing transverse energy (including the triangular cut) are effective to suppress the contribution from QCD multijet background (see Sec. 7.3.1). The requirements on the jet multiplicity and the jet flavor are important for the rejection of events originating from physical backgrounds, in particular from W+jets.

7.2.2 Monte Carlo Correction Factors

Differences between data and its description with the MC simulation can appear for the trigger as well as the reconstruction and identification efficiencies of the leptons. In order to correct for those differences, scale factors have been estimated using the tag and probe technique on $Z \to ee$ and $Z \to \mu\mu$. This technique requires one lepton that satisfies the complete set of object definition requirements (tag) and a second one on which the efficiency for those selection requirements, or a subset of them, can be tested (probe).

[1] Due to a software error, the corresponding information for the muon object was not available in early data.

Table 7.1: Trigger efficiencies for the muon triggers [116]. The efficiencies are given for data and MC.

	L1_MU10	EF_mu10_MSonly	EF_mu10_MSonly
	Data		MC
Barrel	$74.62^{+3.01}_{-3.17}\%$	$70.56^{+1.80}_{-1.84}\%$	$77.85^{+0.12}_{-0.13}$
End-caps	$84.80^{+2.40}_{-2.62}\%$	$87.69^{+1.26}_{-1.84}\%$	$89.97^{+0.08}_{-0.09}$

7.2.2.1 Trigger Efficiency

For the MC samples only a single trigger was used for each channel, i.e. EF_e10_medium and EF_mu10_MSonly respectively. For data various triggers were used depending on the run period (see Chapter 6). The trigger efficiency was measured in data and the MC corrected for the observed discrepancies.

The trigger efficiency $\epsilon_{\text{trigger}}$ is estimated with the tag-and-probe method on Z boson decays. Therefore one lepton was asked to match the trigger requirements and the second one is tested for it. The probe lepton was also asked to be spatially matched to a trigger object with $\Delta R = 0.2$ for L1 and $\Delta R = 0.15$ for EF.

For the electron triggers, the probe electron is required to have a transverse energy above 20 GeV within the fiducial η region, i.e. $0 < |\eta| < 1.37$ or $1.52 < |\eta| < 2.47$. Due to the low thresholds and the plateau position in the trigger turn-on curve, the electron triggers are highly efficient. The efficiency for data is $99.66^{+0.16}_{-0.24}\%$ and $98.95 \pm 0.06\%$ for MC [116].

For the muon trigger a muon object is selected as the tag muon and a match with a ROI muon object is required. A second muon object of opposite electric charge is probed to form together with the first one the invariant mass of the Z boson in a mass window of 12 GeV. The efficiencies are listed in Table 7.1. Figure 7.1 shows the trigger efficiency for muons comparing data and the MC simulation.

For more details on the trigger efficiency estimation see [116].

7.2.2.2 Electron Reconstruction and Identification Efficiency

The reconstruction and identification efficiency for electrons is estimated with the tag-and-probe method on $Z \to ee$ data and MC events. The tag electron satisfies the electron candidate requirements. The following requirements have to be fulfilled by the probe electron: the minimum transverse momentum $p_T > 20$ GeV and the η-fiducial cuts ($|\eta| < 2.47$ and $1.37 < |\eta| < 1.52$). All electrons satisfying the requirements on the hadronic leakage, R_η, w_{η^2} are taken into account (see Sec. 7.1.1). The tag and probe electron combinations are required to be of opposite charge and

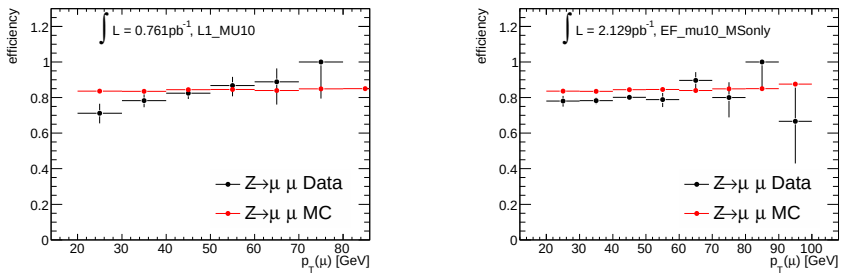

(a) (b)

Figure 7.1: Trigger efficiency as a function of the p_T of the muon for (a) the `L1_MU10` trigger and (b) for `EF_mu10_MSonly`. [116]

to form an invariant mass between 80 and 100 GeV to match the Z boson mass. The background in the data is estimated by taking the average of the same-sign pairs in the Z boson mass sidebands at $60 - 80$ GeV and $100 - 120$ GeV, whereas for the MC studies only simulated $Z \to ee$ samples are used.

Figure 7.2 shows the combined reconstruction and identification efficiency and shape distribution of the transverse electron energy E_T, the pseudo-rapidity $|\eta|$, the number of selected jet candidates, and isolation criteria (Etcone20 $< 4\,\text{GeV} + 0.023 \cdot E_T$). The comparison of MC and data is based on electrons originating from Z boson decays, which differ for those originating from the decay of top quark pairs. As can be seen in Fig. 7.2, electrons from top quark decays have a broader energy spectrum, are relatively more central, and appear in events with more jets present. However, comparing the resulting efficiency from true top quark pair with Z boson electrons only the resulting efficiencies as a function of the jet multiplicity differ significantly.

The scale factors (applied only to MC) express the differences between simulated MC and the recorded data at the trigger, reconstruction, and identification stages. In Table 7.2 the resulting scale factors are summarized.

7.2.2.3 Electron Energy Scale and Resolution

The MC has been corrected for differences in the electron energy scale and resolution. The electron energy scale is derived from the invariant mass peak of the Z boson in $Z \to ee$ events, with a systematic uncertainty of $\pm 3\%$. To account for the uncertainty of the energy resolution the following smearing was applied [116]:

$$E_s = E \cdot \left(1 + g\left(0, \frac{0.11}{\sqrt{E}}\right) + g(0, 0.011)\right), \tag{7.4}$$

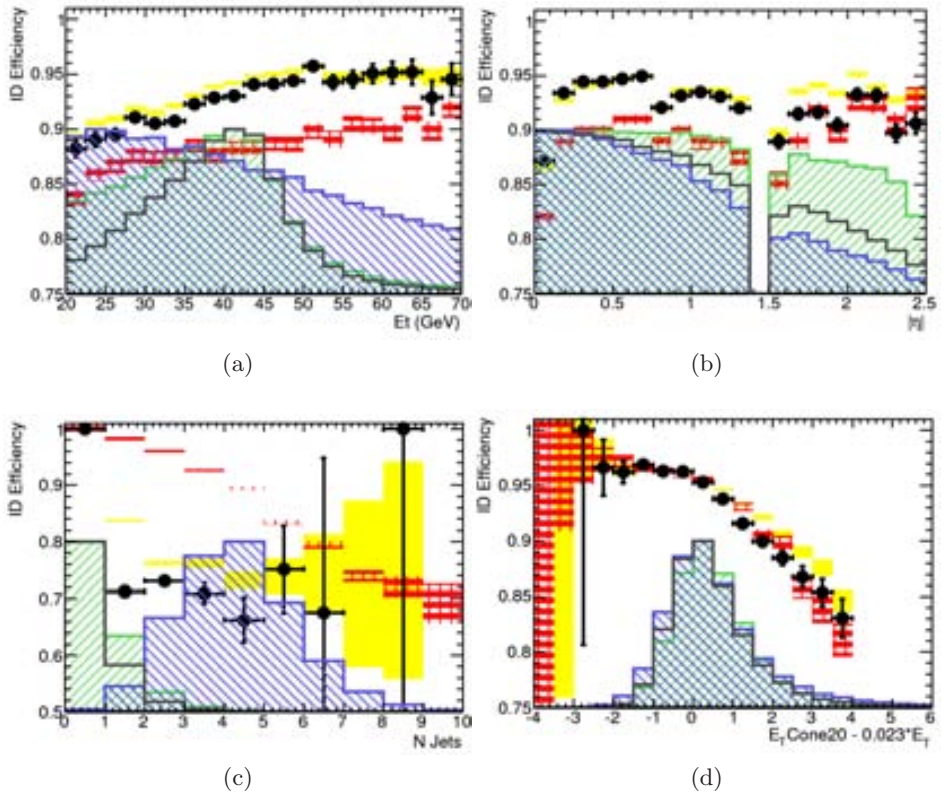

(a) (b)

(c) (d)

Figure 7.2: Distributions of (a) E_T, (b) $|\eta|$, (c) number of jets, and (d) modified isolation are shown. The shapes are drawn for true electrons originating from Z boson (green line), top quark pair decays (blue line), and from data using the tab-and-probe method (black line). The corresponding efficiencies are drawn in yellow, red, and black line with dots, respectively. All is shown as a function of (a) E_T, (b) $|\eta|$, (c) number of jets, and (d) modified isolation [116].

where $g(a, b)$ refers to a Gaussian random variable with mean of a and a sigma of b.

7.2.2.4 Muon Reconstruction and Identification Efficiency

For the estimation of the reconstruction efficiency the tag muon is the object candidate defined in Sec. 7.1. The probe muon is required to have:

- an inner detector track with at least one hit in the pixel detector and at least six hits in the SCT;
- a $p_T \geq 22\,\text{GeV}$, to allow for mismatches between the muon spectrome-

ter and the inner detector due to tracking resolution effects and avoid boundary effects around $p_T = 20\,\text{GeV}$;

- $|d_0| \leq 0.05\,\text{mm}$;
- $|m_{\text{tag+probe}} - m_Z| \leq 10\,\text{GeV}$;
- $\Delta\phi(\text{tag-probe}) \geq 1.5\,\text{rad}$;
- opposite electric charge with respect to the tag muon.

The condition on the transverse impact parameter d_0 of the track with respect to the first reconstructed primary vertex in the event ensures that the two tracks come from the same vertex and rejects backgrounds such as π and K decays in flight. Further checks against interactions originating from pile-up at higher instantaneous luminosities, when more than one primary vertices was reconstructed, where performed. A loose cut on $\Delta\phi$(tag-probe) is chosen in order not to bias the selection towards events with a low jet multiplicity in which the Z boson is less boosted and the muon pair more often in a back-to-back configuration.

Figure 7.3 shows the comparison of the muon reconstruction efficiency measured with the tag and probe method for both, data and the MC simulation.

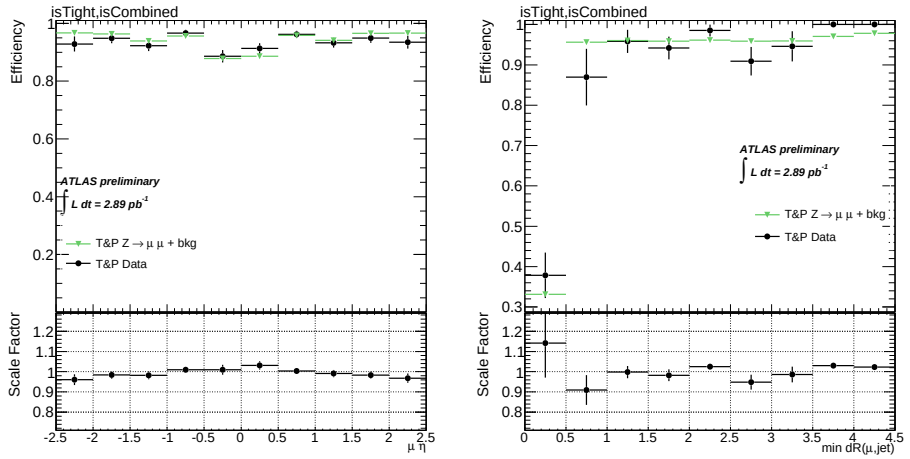

(a) (b)

Figure 7.3: The muon reconstruction efficiency measured with the tag and probe method on data (black dots) and on simulation (dark green dots), as a function of (a) $\eta(\mu)$ and (b) $\Delta R(\mu, \text{closest jet})$. The MC includes all background contributions. In the bottom part the scale factor SF_{reco} is drawn [116].

To estimated the identification efficiency the following requirements were asked to be satisfied by the probe muon in addition to the muon object

Table 7.2: Scale factors (SF) used for lepton trigger, reconstruction and identification efficiencies [116].

Step	Electron SF	Muon SF
Trigger	1.007 ± 0.004	($\|\eta\|$ <1.05:) 0.92±0.02
		($\|\eta\|$ >1.05:) 0.97±0.02
Reconstruction	1.00 ± 0.02	1.00 ±0.02
Identification	0.98 ± 0.02	0.996 ±0.006

definition (see Sec. 7.1.2), except the isolation cuts (Etcone20 and Ptcone20) and the requirement on the closest jet:

- $|m_{\text{tag+probe}} - m_Z| \leq 10\,\text{GeV}$;
- $\Delta\phi(\text{tag-probe}) \geq 1.5\,\text{rad}$;
- opposite electric charge with respect to the tag muon.

Figure 7.4 shows the comparison of the muon identification efficiency measured with the tag and probe method for both, data and the MC simulation.

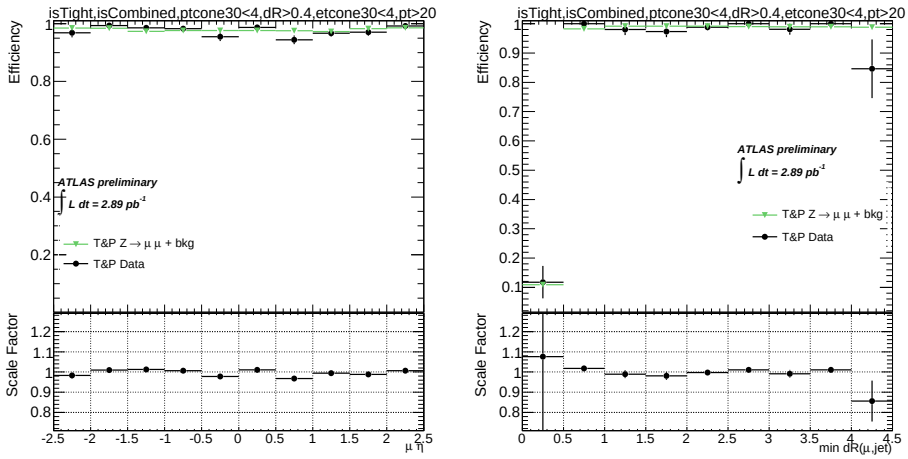

(a) (b)

Figure 7.4: The muon identification efficiency measured with the tag and probe method on data (black dots) and on simulation (dark green dots), as a function of (a) $\eta(\mu)$ and (b) $\Delta R(\mu, \text{closest jet})$. The MC includes all background contributions. In the bottom part the scale factor SF_{reco} is drawn [116].

The scale factors that are applied to the MC are listed in Table 7.2.

Table 7.3: Muon momentum scale and resolution parameter [116].

	C_1	C_2
$\|\eta\| < 1.05$	0.992 ± 0.010	0.031 ± 0.020
$1.05 < \|\eta\| < 2.5$	0.980 ± 0.012	0.063 ± 0.031

7.2.2.5 Muon Momentum Scale and Resolution

The width of the reconstructed Z boson mass peak in $Z \to \mu\mu$ events is larger in data than in simulated MC events. This originates mainly from differences in the material budged and the alignment of the various detectors. In order to achieve agreement of data and MC, the muon momentum is smeared with the following function:

$$(1/p_T)_s = 1/C_1 \times (1/p_T)_{\mathrm{MC}} \times (1 + g(0,1) \times C_2)\,, \tag{7.5}$$

where $(1/p_T)_s$ is the smeared and $(1/p_T)_{\mathrm{MC}}$ the simulated muon curvature. C_1 is the momentum scale term and C_2 the additional momentum resolution (smearing) term. The factor $g(0,1)$ is a random number generated with a Gaussian distribution with zero mean and variance one. The numbers in Table 7.3 yield a good agreement of data and MC. The systematic uncertainty on the momentum scale (resolution) parameter has been taken into account in the measurement as uncertainty on the momentum scale (resolution).

7.2.2.6 Flavor Tagging Efficiency

The flavor tagging efficiency was estimated using di-jet samples taken from data, enriched in $b\bar{b}$ production by requiring an away jet tagged with a SV0 weight above one. The transverse momentum of the muon perpendicular to the jet axis from different jet flavor templates is fitted to the data yielding the number of b quark jets. The comparison of the result before and after applying the b-tagging algorithm yields the efficiency $\epsilon^{\mathrm{MC}}(p_T, |\eta|)$ and $\epsilon^{\mathrm{data}}(p_T, |\eta|)$ for MC and data, respectively, as a function of the transverse momentum p_T and the pseudo-rapidity η. The ratio of the two efficiencies yields the per jet scale factors (SF)

$$\mathrm{SF}_{\mathrm{flavor}}(p_T, |\eta|) = \frac{\epsilon^{\mathrm{data}}(p_T, |\eta|)}{\epsilon^{\mathrm{MC}}(p_T, |\eta|)}\,, \tag{7.6}$$

which is used for b-tagged jets in order to correct for the flavor tagging efficiency difference between data and MC. Figure 7.5 shows the scale factor $\mathrm{SF}_{\mathrm{flavor}}$ as a function of the transverse momentum of the jet. The same scale factor was used for c quark jets. For not-tagged jets from b and c quark in

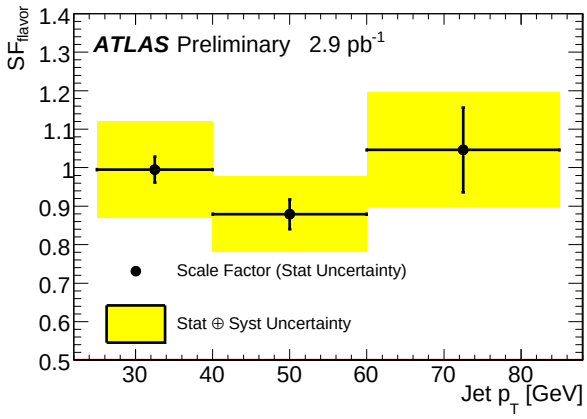

Figure 7.5: $\mathrm{SF}_{\mathrm{flavor}}$ as a function of the transverse momentum of the tagged jet [119].

the simulation, the corresponding scale factor is given by

$$\begin{aligned} \mathrm{SF}_{\mathrm{flavor}}^{\text{not-tagged}}(p_T, |\eta|) &= \frac{1-\epsilon^{\mathrm{data}}(p_T, |\eta|)}{1-\epsilon^{\mathrm{MC}}(p_T, |\eta|)}\,, \\ &= \frac{1-\mathrm{SF}_{\mathrm{flavor}}(p_T, |\eta|)\cdot\epsilon^{\mathrm{MC}}(p_T, |\eta|)}{1-\epsilon^{\mathrm{MC}}(p_T, |\eta|)}\,. \end{aligned} \tag{7.7}$$

In Eq. 7.7 a parametrization of ϵ^{MC} for b and c quarks in $t\bar{t}$ events was used.

Also light flavor jets can result as tagged if they have a high decay length significance. This may originate from a limited detector resolution, long lived light-particle decays (λ, K_s) or interactions with the detector material. Two methods are combined to estimate the mis-tagging rate.

The first estimates the mis-tagging rate from an negative inclusive tagging rate by reversing the decay length significance of the contributing tracks. Correction factors accounting for differences of b, c and light quarks and asymmetries of negative and positive decays length significance are applied.

To determine the number of light flavor jets in data, the second method compares the results obtained with a fit of the secondary vertex mass before and after performing the flavor tagging The fitted number of heavy flavor jets is correct by scale factors and subtracted.

Mis-tag scale factors of 1.27 ± 0.26 (1.07 ± 0.25) have been obtained for jets with $p_T < 40\,\mathrm{GeV}$ ($p_T > 40\,\mathrm{GeV}$) [119].

Table 7.4: Event selection efficiency after applying all MC correction factors.

	$= 1$ jet	$= 2$ jets	$= 3$ jets	≥ 4 jets
electron channel				
not-tagged	0.3%	1.8%	4.2%	8.3%
≥ 1 b-tagged	0.2%	1.0%	2.7%	5.8%
muon channel				
not-tagged	0.4%	1.9%	4.2%	8.3%
≥ 1 b-tagged	0.1%	1.0%	2.3%	5.8%

7.2.3 Signal Selection Efficiency

Table 7.4 show the signal efficiencies for the selection requirements listed in Sec. 7.2.1 for both electron and muon channels. The efficiencies are obtained after applying all correction factors on the MC (see Sec. 7.2.2) and are listed for different jet multiplicities.

About 90% of the selected $t\bar{t}$ events originate from true semi-leptonic decays. Only around 5% of these events contain mis-identified leptons, almost all being mis-identified taus. About 10% of the selected events originate from top quark decays with both W bosons decaying leptonically.

7.3 Background Estimation

The two main backgrounds for this measurement are QCD multijet events and W bosons in association with jets. The estimation of their contribution need special attention in order to reach a precise measurement of the signal cross section. All other backgrounds yield small contributions and are taken from MC simulation.

7.3.1 Estimation of the QCD Multijet Background

Misidentified and non-prompt leptons allow a QCD multijet event to mimic the signal final state (see Sec. 3.2.3.2). Since this background is difficult to accurately model with simulation, data-driven methods are developed to estimate the expected number of QCD events in the final selection sample.

The so-called "Matrix Method" was used for the muon channel, estimating needed efficiencies from the low missing transverse energy region or from the muon impact parameter significance. To model the QCD multijet background contribution for the electron channel the Matrix Method is more difficult to apply properly. This is because the heavy flavor jets are not the only source of mis-identified electrons but also photon conversion and jets with high electromagnetic fraction. Therefore two different approaches

are exploited to obtain a data-driven estimation of the QCD multijet background in the electron channel: the selection of so-called jet-electrons from jet-triggered events, and the so-called anti-electron selection from the e/γ-triggered stream. For details on the trigger and the streams see Chapter 6.

7.3.1.1 Muon Channel

The Matrix Method was developed at the DØ experiment [120] and employs a system of linear equations that describes the relation between two different samples, differing in the lepton identification criteria used. This way the contribution of mis-identified lepton events, i.e. QCD multijet events, in the final selection sample can be predicted from the data.

The two samples are obtained by applying a "loose" and a "tight" selection, with the latter being a subset of the former. This yields N^{loose} (N^{tight}) events fulfilling the loose (tight) selection. The tight selection sample is chosen to be the final event selection for this analysis (see Sec. 7.2). Both selection samples consist of contributions from events with a real and a mis-identified lepton fulfilling the lepton criteria, N_{real} and N_{fake} respectively. This allows to write the total number for the loose and the tight sample as

$$N^{\text{loose}} = N^{\text{loose}}_{\text{real}} + N^{\text{loose}}_{\text{fake}}\,, \tag{7.8}$$

$$N^{\text{tight}} = N^{\text{tight}}_{\text{real}} + N^{\text{tight}}_{\text{fake}}\,. \tag{7.9}$$

Using the efficiencies for loose lepton to also fulfill the tight lepton requirements

$$\epsilon_{\text{real}} = \frac{N^{\text{tight}}_{\text{real}}}{N^{\text{loose}}_{\text{real}}} \qquad \text{and} \qquad \epsilon_{\text{fake}} = \frac{N^{\text{tight}}_{\text{fake}}}{N^{\text{loose}}_{\text{fake}}}\,. \tag{7.10}$$

Eq. 7.9 can be written as

$$N^{\text{tight}} = \epsilon_{\text{real}} \cdot N^{\text{loose}}_{\text{real}} + \epsilon_{\text{fake}} \cdot N^{\text{loose}}_{\text{fake}}\,, \tag{7.11}$$

Solving the linear system for $N^{\text{tight}}_{\text{real}}$ and $N^{\text{tight}}_{\text{fake}}$ in Eq. 7.8 and 7.9 together with Eq. 7.11 yields

$$N^{\text{tight}}_{\text{real}} = \frac{\epsilon_{\text{real}}}{\epsilon_{\text{real}} - \epsilon_{\text{fake}}} \left(N^{\text{tight}} - \epsilon_{\text{fake}}\, N^{\text{loose}}\right) \tag{7.12}$$

$$N^{\text{tight}}_{\text{fake}} = \frac{\epsilon_{\text{fake}}}{\epsilon_{\text{real}} - \epsilon_{\text{fake}}} \left(\epsilon_{\text{real}}\, N^{\text{loose}} - N^{\text{tight}}\right). \tag{7.13}$$

This allows to estimate the number of events in a tight selection sample with real and mis-identified leptons. The following conditions must be satisfied for the method to work with reasonable precision:

- both efficiencies must be sufficiently different numerically so that the statistical precision of the mis-identified background estimation is not compromised by the term $1/(\epsilon_{\text{real}} - \epsilon_{\text{fake}})$;

- both efficiencies should be as independent of the event topology as possible, in such a way that they can be determined in control samples and be applied to the analysis sample (e.g. ϵ_{real} must be similar for leptons origination from W+jets, Z+jets, and $t\bar{t}$);
- any significant dependence of the efficiencies on the kinematics or topology must be parametrized.

These conditions can be met by carefully selecting the loose lepton definition (for a given fixed tight lepton definition).

An event-by-event based weighting of the complete data sample is possible. This offers the possibility to estimate the contribution from QCD multijet events for any chosen quantity, independent of the parameter used to estimate ϵ_{real} and ϵ_{fake}. The number of "loose-not-tight" events is defined as

$$N^{\text{loose-not-tight}} = N^{\text{loose}} - N^{\text{tight}} \,. \tag{7.14}$$

and is combined with Eq. 7.13, such that the number of mis-identified lepton events in a tight sample can be expressed as

$$N^{\text{tight}}_{\text{fake}} = \frac{\epsilon_{\text{real}} \cdot \epsilon_{\text{fake}}}{\epsilon_{\text{real}} - \epsilon_{\text{fake}}} N^{\text{loose-not-tight}} + \frac{\epsilon_{\text{fake}}(\epsilon_{\text{real}} - 1)}{\epsilon_{\text{real}} - \epsilon_{\text{fake}}} N^{\text{tight}} \,. \tag{7.15}$$

This allows to weight events that fulfill the loose but not the tight requirements with

$$w_{\text{loose-not-tight}} = \frac{\epsilon_{\text{real}} \cdot \epsilon_{\text{fake}}}{\epsilon_{\text{real}} - \epsilon_{\text{fake}}} \,, \tag{7.16}$$

and those, that fulfill the tight requirements with

$$w_{\text{tight}} = \frac{\epsilon_{\text{fake}}(\epsilon_{\text{real}} - 1)}{\epsilon_{\text{real}} - \epsilon_{\text{fake}}} \,, \tag{7.17}$$

yielding a prediction of the contribution from QCD multijet events.

The knowledge and a good understanding of ϵ_{real} and ϵ_{fake} is need for that method. It turned out, that the efficiencies are mainly depending on the pseudo-rapidity η of the lepton, which is used in this study for the parametrization.

Estimation of ϵ_{real} and ϵ_{fake} in a low E_T^{miss} region: A sample enriched with QCD multijet events was used to measure ϵ_{fake}. Therefore a tight selection equal to the object definition of muons (see Sec. 7.1.2) was applied. The isolation criteria (Etcone30 $< 4\,\text{GeV}$ and Ptcone30 $< 4\,\text{GeV}$) were dropped to obtain the loose selection. These criteria have been proven to be useful for reducing the topology dependence of the measured mis-identification efficiency ϵ_{fake}. The control region for the mis-identification rate estimate is obtained by selecting events with one lepton, at least one jet, and low missing transverse energy ($E_T^{\text{miss}} < 10\,\text{GeV}$).

However, these requirements do not lead to a sufficiently pure QCD multijet sample, and contamination from real leptons from W and Z decays can bias the ϵ_{fake} measurement. Such real lepton contamination must explicitly be corrected for on a statistical basis. Assuming the cross sections for W/Z+jets production or the total integrated luminosity may not be accurately known, an iterative method has been developed to empirically calibrate the W/Z+jets MC to data and to subtract this contamination.

Before the subtraction of the real lepton contamination (referred to as "iteration 0"), the mis-identification efficiency ϵ^0_{fake} is given by

$$\epsilon^0_{\text{fake}} = \left(\frac{N^{\text{tight}}}{N^{\text{loose}}} \right)_{E_T^{\text{miss}}<10\,\text{GeV}} . \tag{7.18}$$

Such a biased efficiency can be used to obtain a first estimate of the existing W/Z+jets background in the sample without applying a cut on missing transverse energy. The corresponding scaling factor, necessary to correct the MC to match such an estimate, can be written as

$$k^0_{W/Z+\text{jets}} = \frac{N^{\text{tight}} - N^{0,\,\text{tight}}_{\text{fake}} - N^{\text{tight, MC}}_{t\bar{t}}}{N^{\text{tight}}_{W+\text{jets, MC}} + N^{\text{tight}}_{Z+\text{jets, MC}}} , \tag{7.19}$$

where $N^{0,\,\text{tight}}_{\text{fake}}$ is computed using ϵ^0_{fake} in Eq. 7.13. For the following iteration ($i > 0$), ϵ_{fake} is computed with $E_T^{\text{miss}} < 10\,\text{GeV}$ as

$$\epsilon^i_{\text{fake}} = \left(\frac{N^{\text{tight}} - k^i_{W/Z+\text{jets}} \cdot (N^{\text{tight}}_{W+\text{jets, MC}} + N^{\text{tight}}_{Z+\text{jets, MC}}) - N^{\text{tight}}_{t\bar{t},\text{MC}}}{N^{\text{loose}} - k^i_{W/Z+\text{jets}} \cdot (N^{\text{loose}}_{W+\text{jets, MC}} + N^{\text{loose}}_{Z+\text{jets, MC}}) - N^{\text{loose}}_{t\bar{t},\text{MC}}} \right)_{E_T^{\text{miss}}<10\,\text{GeV}} , \tag{7.20}$$

where

$$k^i_{W/Z+\text{jets}} = \frac{N^{\text{tight}} - N^{i-1,\text{tight}}_{\text{fake}} - N^{\text{tight, MC}}_{t\bar{t}}}{N^{\text{tight}}_{W+\text{jets, MC}} + N^{\text{tight}}_{Z+\text{jets, MC}}} . \tag{7.21}$$

A combination of simulated QCD multijet, W+jet, Z+jet, and $t\bar{t}$ events, weighted with their corresponding cross sections, is used to simulate a real data sample. This iterative procedure typically converges after the second iteration yielding an estimated ϵ_{fake} very close to the true one predicted by the QCD multijet simulation. It also makes the estimation more robust against the choice of upper E_T^{miss} cut which was introduced to enrich the sample in QCD multijets [121].

Figure 7.6 shows the efficiency for real muons, that pass the loose selection criteria, to pass the tight one for $Z \to \mu\mu$ events in data and in the combined MC samples as a function of $|\eta|$. Both distributions agree very well with an average of $\epsilon_{\text{real}} = 0.990 \pm 0.003$ measured in MC.

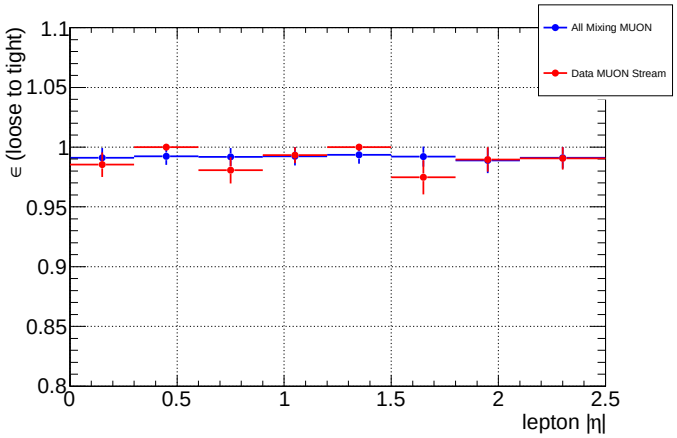

Figure 7.6: ϵ_{real} as a function of $|\eta|$ measured using $Z \to \mu\mu$ events in data (red points) and the combined MC samples (blue points) [121].

The distribution of ϵ_{fake} as a function of E_T^{miss} is almost flat below about 30 GeV, such that no large dependence on the missing transverse energy requirement is observed. Figure 7.7 shows the estimation of ϵ_{fake} in data as a function of $|\eta|$ for several steps of the iterative procedure. A transverse missing energy of $E_T^{\text{miss}} < 10\,\text{GeV}$ was required. The Matrix Method uses the values obtained in the second iteration step as a function of $|\eta|$. This corresponds to the average $\epsilon_{\text{fake}} = 0.382 \pm 0.007$.

The result of the application of the Matrix Method to the data is illustrated in Fig. 7.8 for events with one jet after full selection and before the triangular cut and without requiring any b-tagged jet, which significantly suppresses the contribution from QCD multijets. Figure 7.9 shows similar distributions for events with exactly two jets. A reasonable agreement between the prediction and data is observed.

The matrix method can be applied to the tagged sample, in order to predict QCD multijet contribution in a sample where at least one jet is required to be identified as a b-jet. However, the number of events after tagging is too small in the present data sample ($2.9\,\text{pb}^{-1}$) to provide sufficient statistics for such an approach. In order to handle this restriction, the predicted QCD multijet background rate before tagging is multiplied by the fraction of QCD multijet events with at least on b-tagged jet. The latter is measured in a sample of events selected by removing the requirement on the missing transverse energy and requiring that only the loose-not-tight lepton selection is satisfied.

Table 7.5 shows the resulting b-tagging probabilities for multijet events as a function of jet multiplicity. Figure 7.10 shows the transverse mass distribution of the W boson candidate after b-tagging for events with exactly one and two jets. This shows a good description of the data also for the

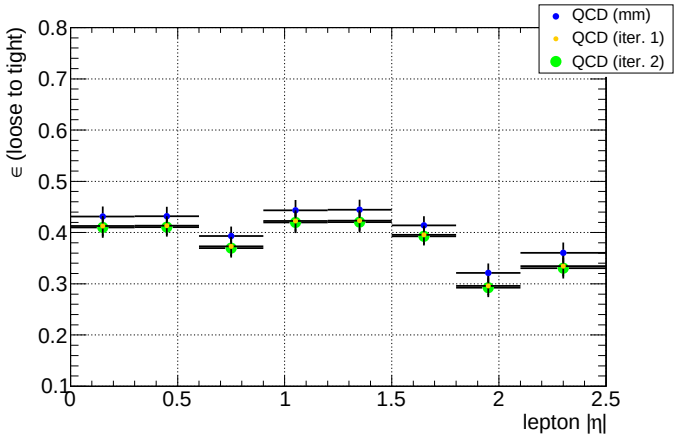

Figure 7.7: ϵ_{fake} as a function of $|\eta|$. Blue points show ϵ_{fake} without correction for the real muon contamination of $E_T^{\text{miss}} < 10\,\text{GeV}$ region, yellow points correspond to the first and green ones to the second and final iteration used in the Matrix Method [121].

Table 7.5: Probabilities for a QCD multijet event to have at least one b-tagged jet as a function of jet multiplicity, measured from loose but not tight data control sample with no requirement on the transverse energy. The quoted uncertainties include both statistical and systematic contributions.

Channel	1-jet	2-jet	3-jet	4-jet
μ+jets	0.09±0.02	0.17±0.03	0.23 ± 0.06	0.31±0.10

b-tagged selection.

Estimation of ϵ_{real} and ϵ_{fake} using the muon impact parameter significance: Studies in MC simulation showed that the dominant contribution to QCD multijet events in the muon channel is heavy flavor decay, with other contributions (e.g. decay-in-flight) being less than 5% to the total QCD multijet background. This offers the possibility to use the impact parameter significance $d_0^{\text{sign}} = d_0/\sigma_{d_0}$ (see d_0 in Sec. 5.5.3) of the muon to discriminate between a mis-identified and a real muon enriched sample. This allows to estimate ϵ_{real} and ϵ_{fake} and thus the application of the Matrix Method as described in Sec. 7.3.1.1. The distribution of d_0^{sign} for the signal and various QCD multijet samples is drawn in Fig. 7.11. An advantage of this method in comparison with the estimation of the efficiencies at low missing transverse energy is that it can be applied at high E_T^{miss}, which is the actual region used for the top quark pair cross section.

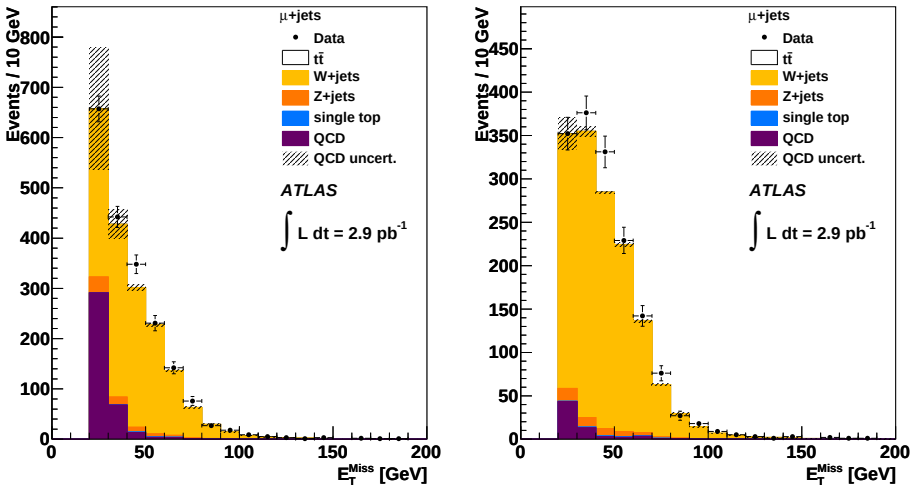

(a) (b)

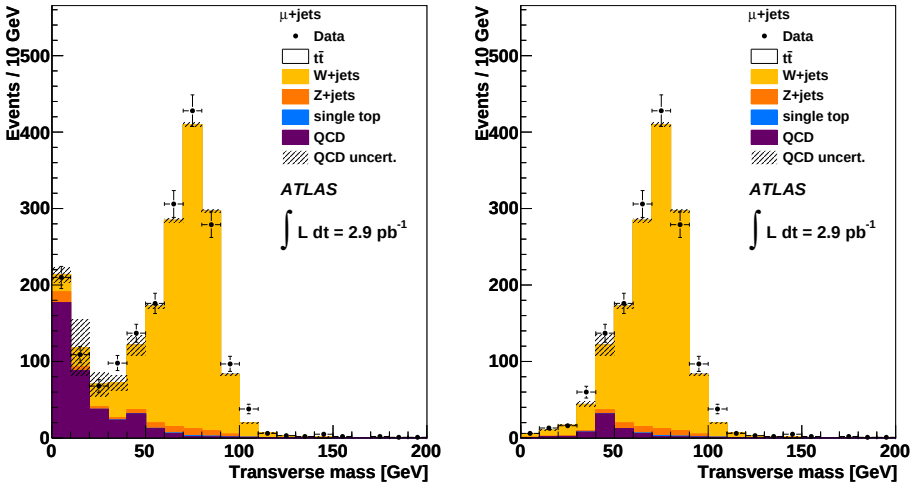

(c) (d)

Figure 7.8: Distributions of events with exactly one jet before b-tagging, before the triangular cut (left column) and after the full selection (right column) for the missing transverse energy (upper row) and the transverse mass of the reconstructed W boson candidate (bottom row). QCD multijet contribution is evaluated using Matrix Method [121].

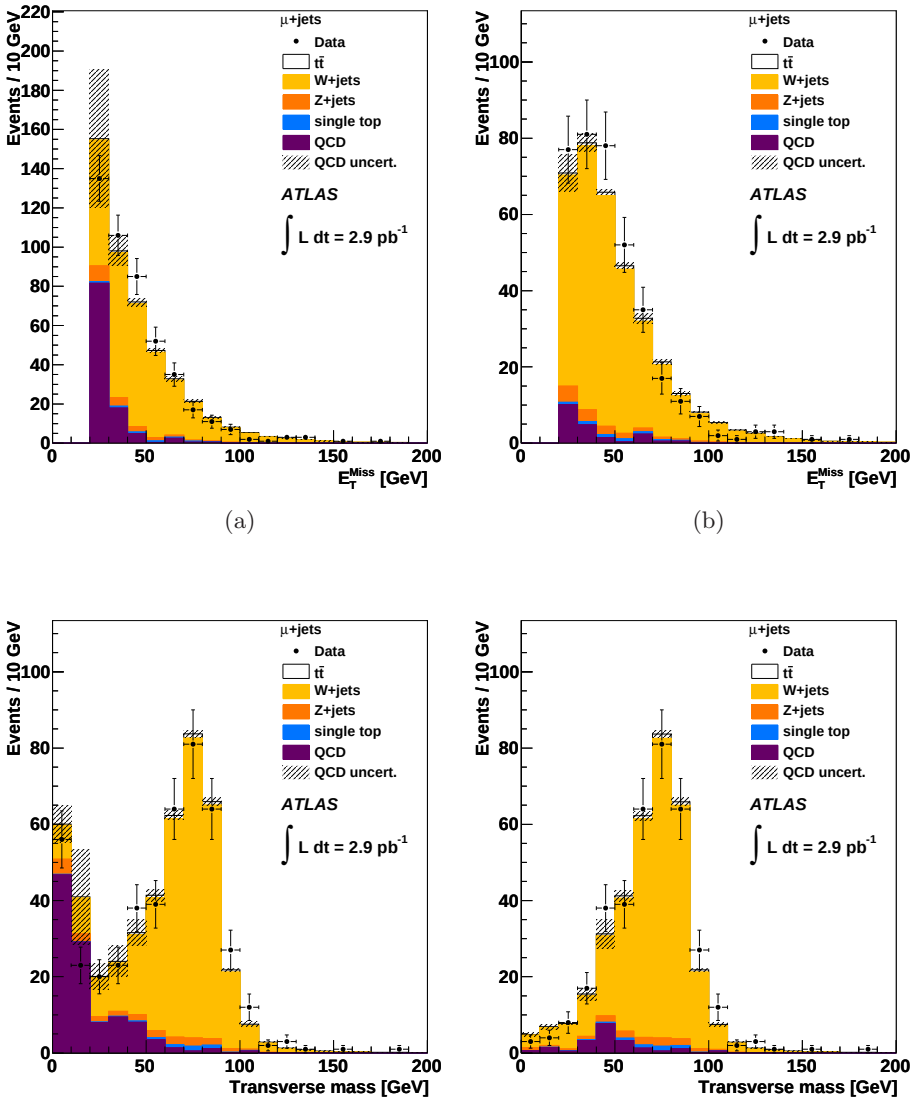

Figure 7.9: Distributions of events with exactly two jets before b-tagging, before the triangular cut (left column) and after the full selection (right column) for the missing transverse energy (upper row) and the transverse mass of the reconstructed W boson candidate (bottom row). QCD multijet contribution is evaluated using the Matrix Method [121].

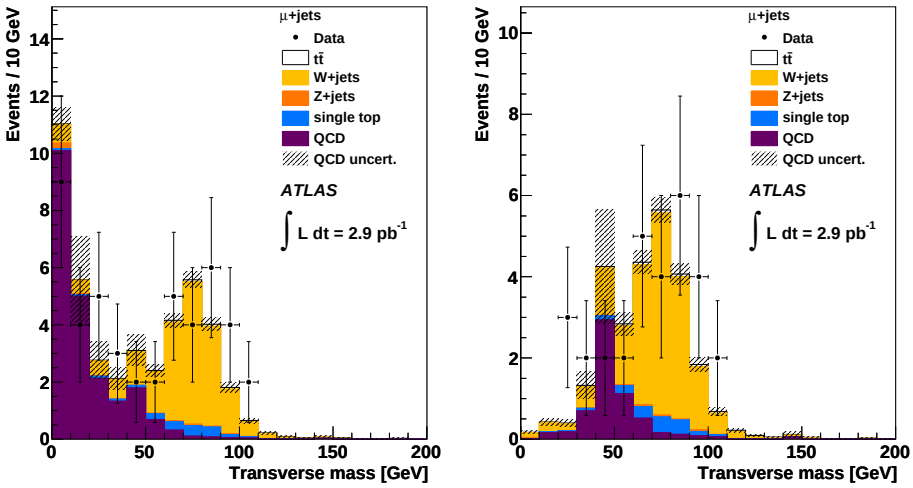

(a) (b)

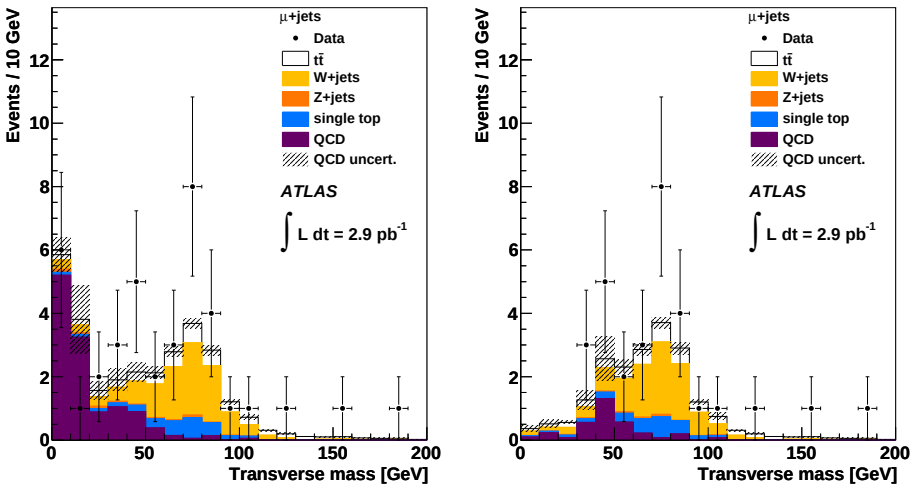

(c) (d)

Figure 7.10: Distributions of events with exactly one jet (top) and exactly two (bottom) before the triangular cut (left column) and after the full selection (right column), requiring at least on b-tag. The QCD multijet contribution is evaluated using the Matrix Method [121].

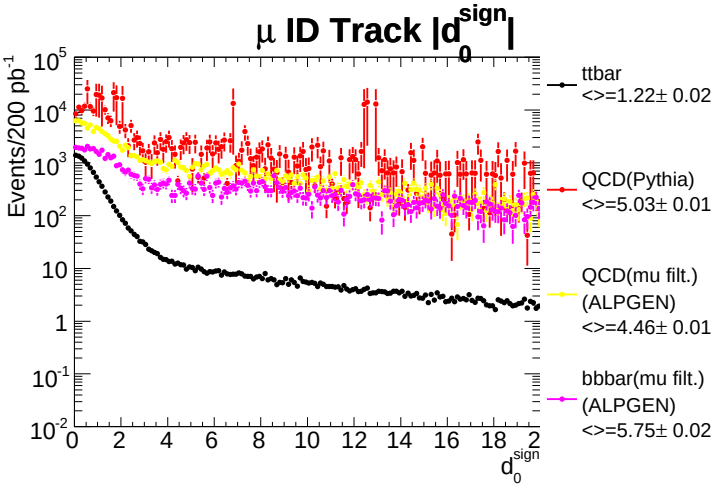

Figure 7.11: Transverse impact parameter significance for $t\bar{t}$, QCD multijet PYTHIA and ALPGEN events. The direct $b\bar{b}$ component of the QCD multijet ALPGEN background is also shown separately. The number of events is normalized to an integrated luminosity of 200 pb^{-1} [121].

Due to the limited statistics available to perform the Matrix Method after the triangular cut, ϵ_{fake} is estimated without this requirement.

The QCD multijet estimates in the pre-tag and tagged samples after all cuts, and for each jet multiplicity, are given in Table 7.6. For more details see [121].

Systematic Uncertainties:

Low E_T^{miss}: To study the systematic uncertainties introduced by the Matrix Method, the prediction obtained by a QCD multijet MC simulation sample was compared to the result of the Matrix Method taken from a pseudo-data sample, a mixture of all used MC samples, weighted by their cross sections. Figure 7.12 shows that for all jet multiplicities the Matrix Method predicts a multijet contribution with an accuracy better than 30%.

The procedure used to predict the number of b-tagged jets also contributes to the systematic uncertainty of the Matrix Method result. A study using QCD multijet MC simulation samples was performed to make sure that such selection cuts do not introduce a bias in the measured tagging rate. The latter was compared in the samples selected by requiring a tight muon or a loose but not tight muon and $E_T^{\text{miss}} < 10\,\text{GeV}$, $E_T^{\text{miss}} > 20\,\text{GeV}$, $E_T^{\text{miss}} > 20\,\text{GeV}$ together with triangular cut, and no E_T^{miss} requirement. Tagging rates were found to be consistent within statistical uncertainties in

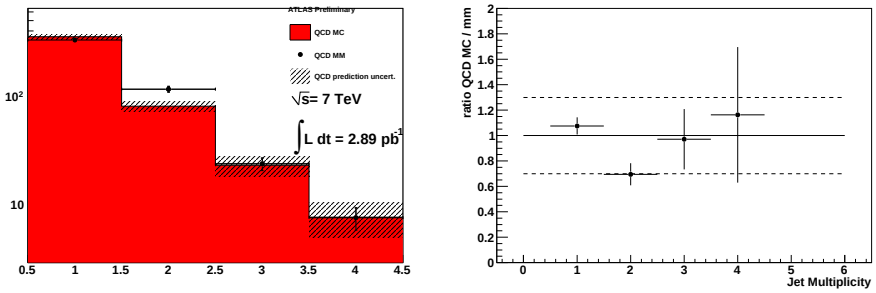

(a) (b)

Figure 7.12: Number of QCD multijet events in dependence on the jet multiplicity predicted by the Matrix Method compared to true QCD multijet rate for jets with $p_T > 20\,\text{GeV}$ [121].

all these samples. The loose but not tight sample without E_T^{miss} cut has been chosen for the tagging rate measurement due to its larger statistics. Additional systematic uncertainty of 20% is assigned to cover for possible biases.

Other sources of systematic uncertainties do not contribute significantly, among those the statistical uncertainties on ϵ_{real} (0.4%) and ϵ_{fake} (2%) determination and the uncertainty from the variation of the E_T^{miss} cut region between 10 GeV and 20 GeV (3%).

Impact Parameter Significance: A systematic on the QCD multijet event tagging rate (30%) was assumed. In analogy to the estimation at low missing transverse energy, a comparison of the prediction from simulated QCD multijet MC samples with the Matrix Method results was performed, yielding an uncertainty of 16%. This is mainly introduced by the fact, that the Matrix Method is applied before the triangular cut. A small contribution comes from non-QCD multijet background contribution, mainly W+jets, yielding 1.8%.

QCD Multijet Contribution for the Muon Channel: The estimated contribution of QCD multijet events obtained with the Matrix Method and using the impact parameter significance are given in Table 7.6. They are listed for the pre-tag and b-tagged samples after all cuts as a function of the jet multiplicity. In this study, the average of both methods was used. The resulting QCD multijet yield estimation as a function of the jet multiplicity for the pre-tagged and the b-tagged sample are listed in Table 7.7.

Table 7.6: Number of predicted QCD multijet events predicted with the Matrix Method and using the impact parameter significance d_0^{sign} in data corresponding to $2.9\,\text{pb}^{-1}$ with a given number of jets. Uncertainties for the Matrix Method are statistical only, for impact parameter significance statistical and systematic [121].

number of jets	low E_T^{miss} region	d_0^{sign}
pre-tagged		
1	79.14±7.73	50.6±4.90±11.7
2	25.36±4.21	14.5±2.70±3.40
3	8.07±2.42	4.73±1.52±1.13
≥4	3.49±1.58	1.49±0.95±0.47
b-tagged		
1	7.44±0.71	3.54±0.35±1.54
2	4.39±0.73	1.87±0.34±0.94
3	1.86±0.56	0.74±0.24±0.55
≥4	1.07±0.48	0.88±0.56±0.46

Table 7.7: Estimation of QCD multijet events used for the muon channel, predicted with the Matrix Method and the impact parameter significance. The uncertainties are broken down into correlated and un-correlated [121].

pre-tagged	b-tagged
$64.9 \pm 20.2 \pm 19.5$	$6.1 \pm 1.9 \pm 2.2$
$19.9 \pm 7.7 \pm 6.0$	$3.4 \pm 1.4 \pm 1.2$
$6.4 \pm 2.3 \pm 1.9$	$1.5 \pm 0.5 \pm 0.5$
$2.5 \pm 1.4 \pm 0.7$	$0.8 \pm 0.4 \pm 0.3$

7.3.1.2 Electron Channel

In the electron channel two different methods are used to estimate the QCD multijet background contribution, the "anti-electron" method and the "jet-electron" method. Both methods provide a shape template for the QCD multijet background sample. This is fitted together with the other MC samples to the low E_T^{miss} distribution of the data, allowing to predict the QCD multijet background in the high missing transverse energy region.

"anti-electrons": The "anti-electron" method employs an electron selection that is largely independent of the kinematic properties of the event. For this method all events of the e/γ stream with isolated electrons having $p_T > 20\,\text{GeV}$ and being detected in $|\eta| < 2.5$ are used. To obtain a sam-

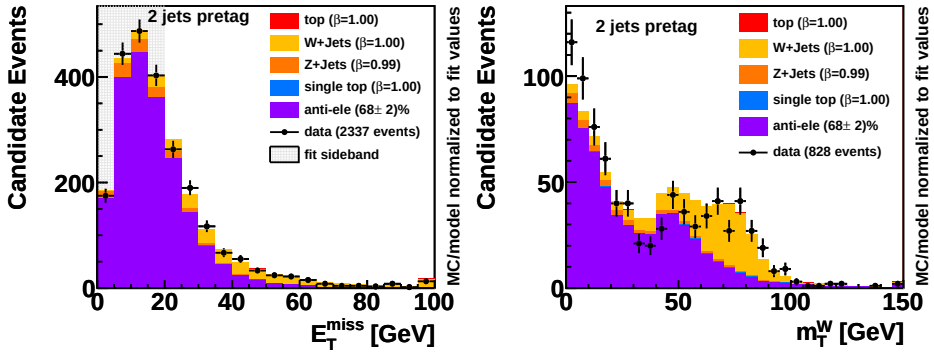

(a) (b)

Figure 7.13: Fit results and control plots for (a) E_T^{miss} and (b) W transverse mass distribution for the pre-tag selected data with exactly two jets for the anti-electron model. Shaded shows the side band where the fit is performed. Parameter β reflects the fitted results for MC based background with respect to the theoretical expectations [121].

ple with mis-identified leptons, one variable, originally designed to reject mis-identified leptons, is inverted. It turned out that requiring the pixel track quality cut (number of pixel, SCT, and B-layer hits) to fail yields best agreement with data. In case of absence of good electrons or muons, this "anti-electron" is chosen as the candidate electron. The fact that a jet object is treated as an EM object induces the problem of a mis-calibration of the missing transverse energy. This originates from the fact that the calibration is different for these two objects.

The estimation of the multijet contribution is done by a binned likelihood fit in the low missing transverse energy region ($E_T^{\text{miss}} < 20\,\text{GeV}$), in order to perform later a fit in the signal region to extract the QCD multijet background. Due to the restriction by low statistics, the fit is performed before the triangular cut, which is afterwards considered separately for each template. Figure 7.13 shows the final plot as well as the results for the binned likelihood fit (see legend).

"jet-electrons": To obtain a sample with jets that can mimic an electron, the same requirements have to be met for this jet as for the electron: a transverse energy of at least 25 GeV, within the fiducial η region ($|\eta| < 2.47$ and $1.37 < |\eta| < 1.52$), an EM fraction between 0.8 and 0.95, and at least four tracks within the jet.

As for anti-electrons, the missing transverse energy has to be corrected for jet-electrons. By scaling the jet-electron to the EM scale in the E_T calculation this is taken into account in this estimation method. This sample

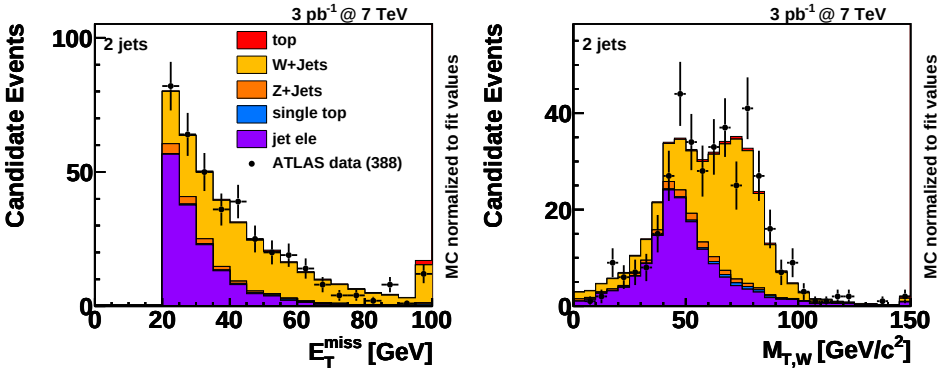

(a) (b)

Figure 7.14: Fit results for the jet-electron model. Shown are (a) E_T^{miss} and (b) W transverse mass distribution after full selection in the pre-tag data sample with exactly two jet [121].

is selected with a single jet trigger (`EF_Jet20`).

Plots for E_T^{miss} and the transverse mass of the W boson in the final sample are shown in Fig. 7.14. The results for estimated QCD multijet contribution are shown in Table 7.8 before and after applying the b-tagging requirement.

Systematic Uncertainties: The systematic uncertainties for both methods are obtained from a linearity test. Therefore pseudo-experiments were performed. For the MC simulated sample the contribution is taken from the Standard Model expectation in each jet multiplicity bin. The QCD multijet prediction method takes the number of expected events from a fit of the model to the data distribution. The QCD multijet contribution is varied between 0.5 and 1.5 to the fitted rate yielding a linear correlation between the simulated and the fitted QCD contribution. The uncertainty on the slope (in agreement with unity) in each jet multiplicity bin is taken as a systematic uncertainty of the method in this bin.

QCD Multijet Contribution for the Electron Channel: The estimated contribution of QCD multijet events obtained by the fitting a QCD multijet template obtained using the "electron-jets" and the "anti-electron" method is given in Table 7.8. They are listed for the pre-tag and b-tagged samples after all cuts as a function of the jet multiplicity.

In this study, the average of both methods was used. The resulting QCD multijet yield estimation as a function of the jet multiplicity for the pre-tagged and the b-tagged sample are listed in Table 7.9.

Table 7.8: Number of predicted QCD multijet events with a given number of jets for anti-electron models in electron channel. Only statistical uncertainties on the fit are shown [121].

number of jets	"jet-electrons"	"anti-electrons"
	pre-tagged	
1	578±17	455±4
2	160±6	220±4
3	42.3±3.1	70.7±2.9
≥ 4	18.9±2.7	36.1±2.8
	b-tagged	
1	23.5±1.5	20.3±1.6
2	14.5±1.8	18.3±1.7
3	3.5±1.2	6.3±0.9
≥ 4	3.5±1.8	6.0±1.0

Table 7.9: Estimation of QCD multijet events used for the electron channel, predicted with fits using the "electron-jet" and "anti-electron" method. The uncertainties are broken down into correlated and un-correlated [121].

pre-tagged	b-tagged
$516.0 \pm 87.0 \pm 19.0$	$21.9 \pm 2.3 \pm 2.5$
$190.0 \pm 42.0 \pm 9.0$	$16.4 \pm 2.7 \pm 2.9$
$56.5 \pm 20.1 \pm 5.5$	$4.9 \pm 2.0 \pm 1.9$
$27.5 \pm 12.2 \pm 4.9$	$4.8 \pm 1.8 \pm 2.6$

7.3.2 Estimation of the W+jets Background

The background contribution from W+jets events can be extracted from data. It was mentioned earlier in Sec. 3.2.3.1 (see Eq. 3.27), that the ratio of $W + n\,\text{jets}$ to $W + n + 1\,\text{jets}$ is expected to be approximately constant as a function of n. This allows to write the expected number of events for $W + n$ jets before b-tagging as

$$W^{n-\text{jets}}_{\text{pre-tagged}} = W^{2\,\text{jets}}_{\text{pre-tagged}} \sum_{i=2}^{n} (W^{2\,\text{jets}}_{\text{pre-tagged}} / W^{1\,\text{jet}}_{\text{pre-tagged}})^i \,, \tag{7.22}$$

where $W^{1\,\text{jet}}_{\text{pre-tagged}}$ ($W^{2\,\text{jets}}_{\text{pre-tagged}}$) is the number of W+1jet (W+2jets) events before tagging. In order to predict the number of events with tagged b-jets in the $W + n\,\text{jets}$ sample, the fraction $f^{\text{n-jets}}_{\text{tagged}}$ is used:

$$W^{\text{n-jets}}_{\text{tagged}} = W^{\text{n-jets}}_{\text{pre-tagged}} \cdot f^{\text{n-jets}}_{\text{tagged}} \,. \tag{7.23}$$

The fraction $f_{\text{tagged}}^{\text{n-jets}}$ is the fraction of events which contain at least one b-tagged jet and is defined as

$$f_{\text{tagged}}^{\text{n-jets}} = f_{\text{tagged}}^{\text{2-jets}} \cdot f_{2\to n}^{\text{corr}} \,. \tag{7.24}$$

Here $f_{2\to n}^{\text{corr}}$ is a correction factor which scales from the two jet exclusive sample to a sample with n jets that takes differences in flavor composition and tagging probabilities into account. It is estimated in MC simulated samples. The factor $f_{\text{tagged}}^{\text{2-jets}}$ is estimated with data as $(6.0 \pm 1.8(\text{stat.}) \pm 0.7(\text{syst.}))\%$ [122].

These two assumptions permit to predict the expected number of $W +$ n jets events in a tagged sample as

$$W_{\text{tagged}}^{n-\text{jets}} = W_{\text{pre-tagged}}^{2\,\text{jets}} \sum_{i=2}^{n} (W_{\text{pre-tagged}}^{2\,\text{jets}} / W_{\text{pre-tagged}}^{1\,\text{jet}})^i \cdot f_{\text{tagged}}^{n-\text{jets}} \,. \tag{7.25}$$

However, in this study the normalization for W+jets was estimated with maximum likelihood fit (see Sec. 7.6) and compared to the here presented estimation.

Other data-driven methods which yield a more accurate estimation of the W+jets background need more than the available statistics. Examples are the W/Z ratio and the charge asymmetry methods. The first uses the fact that the production ratio of W and Z bosons is well understood. The second estimates the W+jets content in a sample from the measured difference between the positive and negative lepton candidates and the known charge asymmetry of W bosons in association with jets. For details see [122].

7.4 Selected Events

The analysis is performed on the final selection sample, obtained by applying the selection criteria and correction factors to the simulation. A split-up into different jet multiplicities is performed considering all reconstructed jets with a transverse momentum larger than 25 GeV. Table 7.10 (7.11) shows the number of events for the electron (muon) channel split up into the one jet exclusive, two jet exclusive, three jet exclusive, and the four jet inclusive bin before the b-tagging. In Table 7.12 (7.13) the same is shown for the electron (muon) channel after applying the b-tag requirement. A signal-to-background ratio of about one is already obtained for the pre-tagged selection sample in the four jet inclusive bin, with W+jets being the main background contribution. Requiring at least one b-tagged jet enhances this value and yields a signal-to-background ratio for the three jet exclusive bin of almost one. Thus the usage of the three jet exclusive bin increases the statistics used in this measurement.

Figure 7.15 shows the corresponding jet multiplicity spectra after all selection criteria are applied, for the electron and muon channel respectively.

Table 7.10: Selected events for the electron channel in the different jet-multiplicity bins for signal and most relevant backgrounds before b-tagging. Last row shows the events selected in data. Only jets with $p_T > 25\,\text{GeV}$ have been considered.

Process	=1 jet	=2 jets	=3 jets	≥ 4 jets
$t\bar{t}$	1.7 ± 0.0	7.0 ± 0.1	13.3 ± 0.1	20.3 ± 0.1
W+jets	1152.0 ± 4.2	266.4 ± 1.5	58.2 ± 0.6	16.3 ± 0.3
QCD (est.)	516.0 ± 89.1	190.0 ± 43.0	56.5 ± 20.8	27.5 ± 13.1
Z+jets	19.1 ± 0.4	11.6 ± 0.3	4.8 ± 0.2	1.9 ± 0.1
Single top	4.3 ± 0.2	5.4 ± 0.2	2.2 ± 0.1	1.1 ± 0.1
Total bkg.	1691.3 ± 89.2	473.5 ± 43.0	121.7 ± 20.8	46.8 ± 13.1
Total MC	1693.0 ± 89.2	480.5 ± 43.0	135.0 ± 20.8	67.1 ± 13.1
Data	1814	404	120	56

Table 7.11: Selected events for the muon channel in the different jet-multiplicity bins for signal and most relevant backgrounds before b-tagging. Last row shows the events selected in data. Only jets with $p_T > 25\,\text{GeV}$ have been considered.

Process	=1 jet	=2 jets	=3 jets	≥ 4 jets
$t\bar{t}$	1.7 ± 0.0	7.2 ± 0.1	13.3 ± 0.1	20.1 ± 0.1
W+jets	1357.2 ± 4.4	309.2 ± 1.5	66.8 ± 0.7	19.3 ± 0.4
QCD (est.)	64.9 ± 28.1	19.9 ± 9.8	6.4 ± 3.0	2.5 ± 1.6
Z+jets	47.3 ± 0.6	13.9 ± 0.3	3.5 ± 0.2	1.4 ± 0.1
Single top	4.7 ± 0.2	4.9 ± 0.2	2.5 ± 0.1	1.0 ± 0.1
Total bkg.	1474.1 ± 28.4	348.0 ± 9.9	79.2 ± 3.1	24.2 ± 1.6
Total MC	1475.9 ± 28.4	355.2 ± 9.9	92.5 ± 3.1	44.3 ± 1.6
Data	1583	372	98	57

Table 7.12: Selected events for the electron channel in the different jet-multiplicity bins for signal and most relevant backgrounds after b-tagging. Last row shows the events selected in data. Only jets with $p_T > 25\,\text{GeV}$ have been considered.

Process	=1 jet	=2 jets	=3 jets	≥ 4 jets
$t\bar{t}$	0.6 ± 0.0	4.0 ± 0.0	8.8 ± 0.1	14.8 ± 0.1
W+jets	13.4 ± 0.5	7.4 ± 0.2	5.0 ± 0.1	2.2 ± 0.1
QCD (est.)	21.9 ± 3.4	16.4 ± 4.0	4.9 ± 2.7	4.8 ± 3.1
Z+jets	0.1 ± 0.0	0.3 ± 0.0	0.12 ± 0.0	0.1 ± 0.0
Single top	1.4 ± 0.1	2.8 ± 0.2	1.3 ± 0.1	0.7 ± 0.1
Total bkg.	36.8 ± 3.4	27.0 ± 4.0	11.4 ± 2.7	7.8 ± 3.1
Total MC	37.5 ± 3.4	30.9 ± 4.0	20.2 ± 2.7	22.6 ± 3.1
Data	30	21	14	17

Table 7.13: Selected events for the muon channel in the different jet-multiplicity bins for signal and most relevant backgrounds after b-tagging. Last row shows the events selected in data. Only jets with $p_T > 25\,\text{GeV}$ have been considered.

Process	=1 jet	=2 jets	=3 jets	≥ 4 jets
$t\bar{t}$	0.7 ± 0.0	4.1 ± 0.0	8.8 ± 0.1	14.7 ± 0.1
W+jets	16.3 ± 0.5	8.3 ± 0.2	6.5 ± 0.1	2.6 ± 0.1
QCD (est.)	6.1 ± 2.9	3.4 ± 1.8	1.5 ± 0.8	0.8 ± 0.5
Z+jets	0.3 ± 0.0	0.4 ± 0.0	0.1 ± 0.0	0.1 ± 0.0
Single top	1.7 ± 0.1	2.5 ± 0.2	1.4 ± 0.1	0.6 ± 0.1
Total bkg.	24.4 ± 2.9	14.7 ± 1.8	9.2 ± 0.8	4.1 ± 0.5
Total MC	25.0 ± 2.9	18.8 ± 1.8	18.1 ± 0.8	18.8 ± 0.5
Data	30	30	18	20

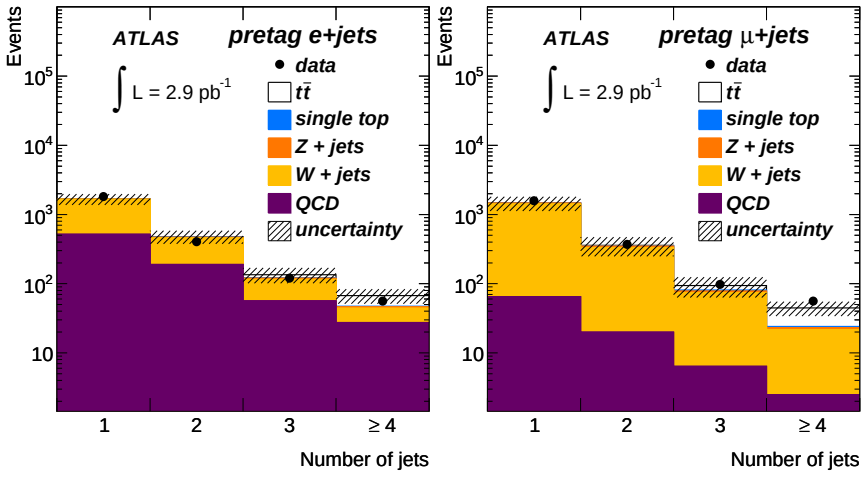

(a)

(b)

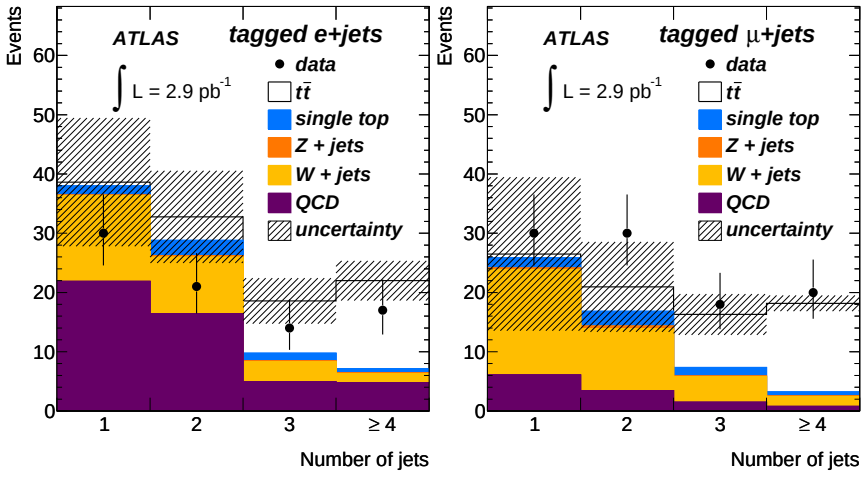

(c)

(d)

Figure 7.15: Jet multiplicity, i.e. number of jets with $p_T > 25\,\text{GeV}$, distributions in the selected sample in (left) the electron and (right) muon channel, (above) without and (below) with flavor tagging. All selection cuts except the requirement of at least four jets have been applied [9].

The background within the selected samples is dominated by W+jets events, which have the same final state signature as $t\bar{t}$ signal events. However, the final samples include important contributions from multijet events, particularly in the electron channel, due to imperfect reconstruction in the detector. The numbers shown are obtained from MC simulation, except for QCD multijet, where the estimation is obtained from data (see Sec. 7.3.1). A good agreement between data and the prediction by MC is observed for the number of selected events.

The lepton transverse momentum, the missing transverse energy, and the transverse mass of the reconstructed W boson candidate are shown in Fig. 7.16 and 7.17 for the three jet exclusive selection without and with flavor tagging, respectively. The same is shown for the four jet inclusive channel in Fig. 7.18 and 7.18, without and with the tagging of the b quark jet, respectively. The suppression of the W+jets contribution due to the flavor tagging requirement is clearly visible. A good agreement between data and the simulated samples was observed.

7.5 Top Quark Mass Reconstruction

The top quark pair production cross section is measured using a maximum likelihood fit to the invariant mass distribution of the reconstructed hadronic top quark candidate (Sec. 7.5.1). The algorithm used is described in Sec. 7.5.1. The template shape for the signal contribution was taken taken from MC simulation. While the shape for the QCD multijet background was estimated from data (see Sec. 7.5.2), the shape for the W+jets background was taken from MC (see Sec. 7.5.3), after validation studies using the available data statistics.

7.5.1 Algorithm and Performance

Several algorithms to reconstruct the hadronically decaying top quark have been studied. The choice for this measurement is the combination of three jets that yield the highest vector sum transverse momentum. A matching to the true partons of the hadronically decaying top quark with $\Delta R < 0.5$ yields for this algorithm an efficiency of about 25% to find the correct three-jet combination after event selection and when the partons from the hadronic top quark decay are within acceptance and well separated from other objects. This conclusion was taken from simulation study at a center-of-mass energy of 14 GeV, where top quarks have a high transverse momentum, so that this algorithm might not be quite the optimal choice for 7 TeV.

Other reconstruction algorithm that were studied are

- the three jets yielding the highest transverse momentum with one jet being tagged as a b quark jet with a tagging efficiency of 50%;

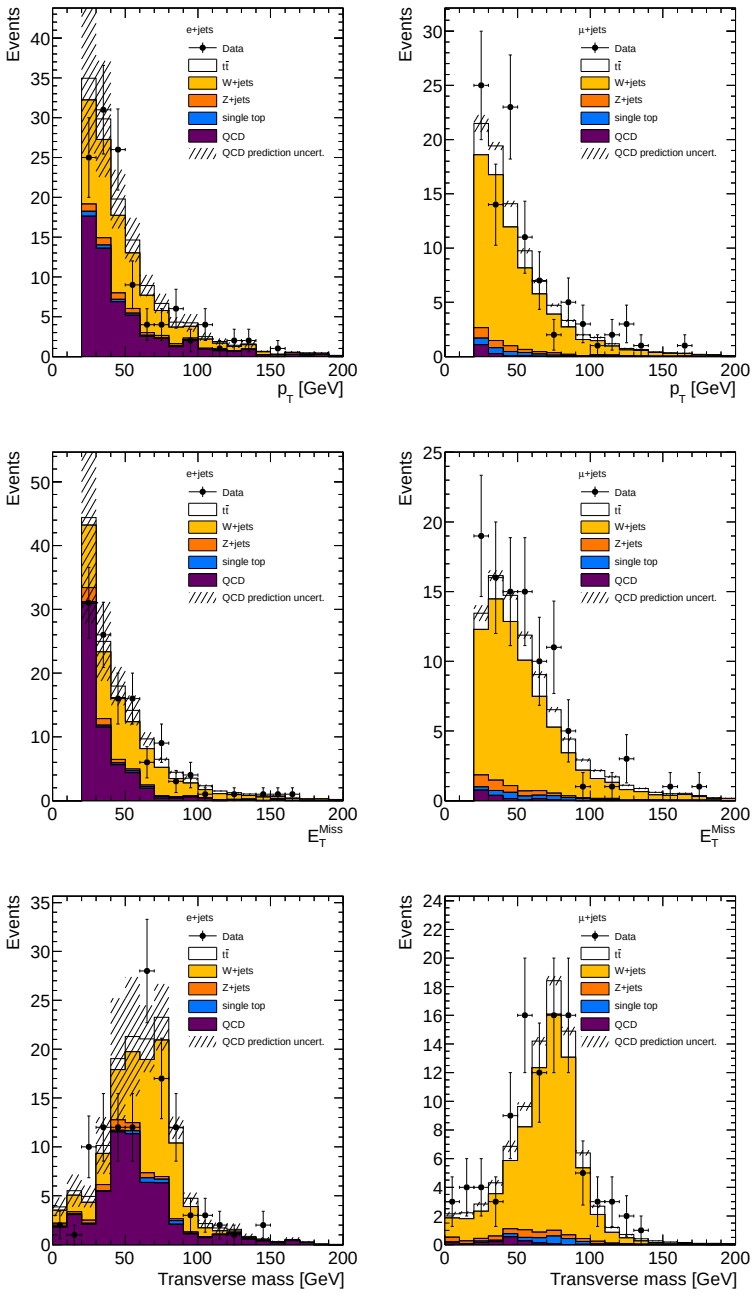

Figure 7.16: Transverse momentum of the lepton (above), the missing transverse energy (middle) and transverse mass of the leptonic W boson candidate for = 3-jets events passing the event selection in the electron (left) and muon (right) channel. All selection cuts have been applied, except the flavor tagging.

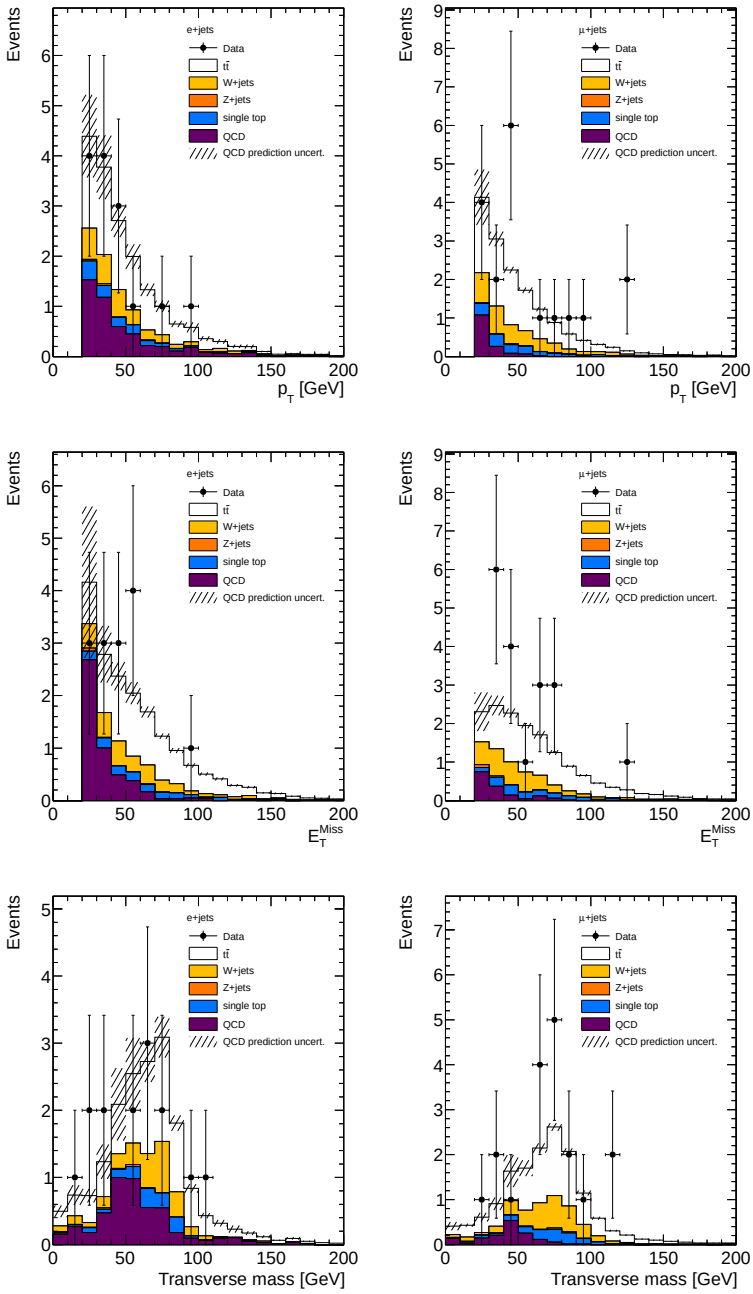

Figure 7.17: Transverse momentum of the lepton (above), the missing transverse energy (middle) and transverse mass of the leptonic W boson candidate for = 3-jets events passing the event selection in the electron (left) and muon (right) channel. All selection cuts have been applied, including the flavor tagging.

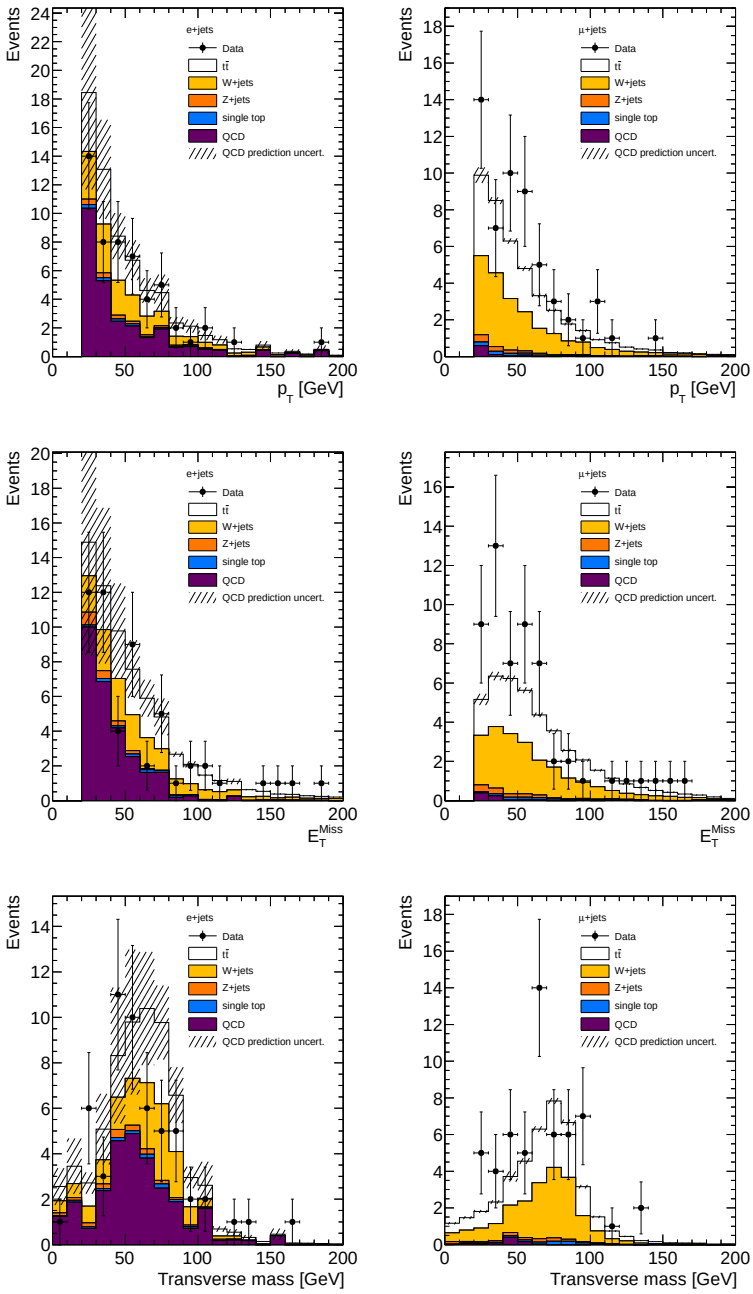

Figure 7.18: Transverse momentum of the lepton (above), the missing transverse energy (middle) and transverse mass of the leptonic W boson candidate for $\geq$ 4-jets events passing the event selection in the electron (left) and muon (right) channel. All selection cuts have been applied, except the flavor tagging.

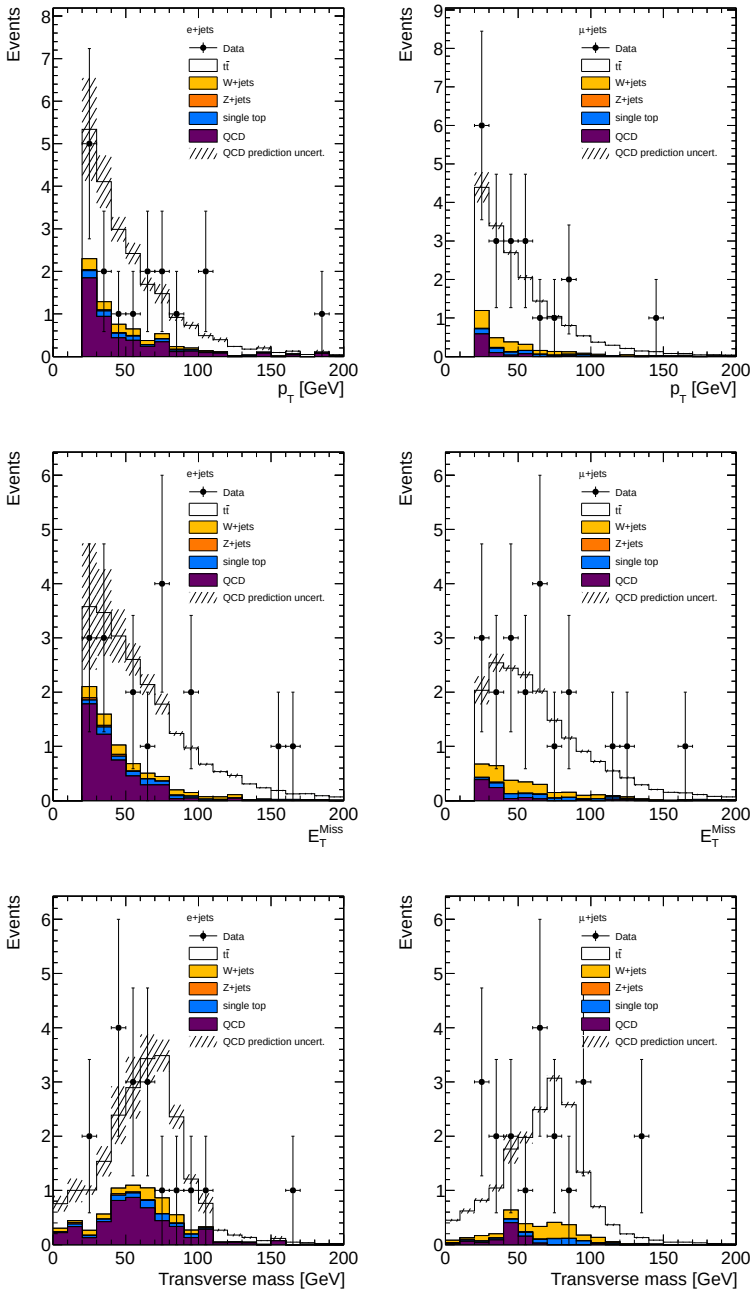

Figure 7.19: Transverse momentum of the lepton (above), the missing transverse energy (middle) and transverse mass of the leptonic W boson candidate for $\geq$ 4-jets events passing the event selection in the electron (left) and muon (right) channel. All selection cuts have been applied, including the flavor tagging.

- same as first but connecting the top quark mass with the mass of the W boson with

$$m_{jjb}^{\text{top}} \cdot \frac{m_W^{\text{PDG}}}{m_W^{\text{reco}}}\,, \tag{7.26}$$

  where m_W^{PDG} is the world-average W boson mass [17] and m_W^{reco} the one reconstructed mass from the two not-tagged jets. This method allows to reduce the contribution from JES to the systematic uncertainty as it largely cancels between m_{jjb}^{top} and m_W^{reco};

- starting from the W boson reconstructed with the two jets yielding the closest W boson mass to the world-average value [17] combined with
  - the jet yielding the closest top quark mass stated in [17];
  - the highest p_T jet tagged as a b quark jet;
  - the jet yielding the highest transverse momentum vector sum.

Theses algorithms yield a reconstruction efficiency up to 45%. The peak of the reconstructed top quark mass spectrum is narrower. However, the shape of the background is also distorted, peaking more strongly near the nominal top quark mass. This fact, together with the lack of a significant improvement in the expected $t\bar{t}$ cross section uncertainty from using more sophisticated mass reconstruction algorithms, motivated the choice of the less efficient but yet simpler and robust three jet combination for this early measurement.

7.5.2 Estimation of the QCD Multijet Background Shape

With data corresponding to only $2.9\,\text{pb}^{-1}$ and with a selection designed to get a $t\bar{t}$ sample as pure as possible, there is not enough data to use the data-driven methods explained in Sec. 7.3.1 to obtain both normalization and shape for QCD multijet distributions. Thus the QCD multijet template shape is derived from multijet enriched data samples, selected with the standard analysis cuts except the lepton requirements, which are inverted. Therefore, we require that the lepton fails at least one of the following identification criteria:

- one B-layer hit;
- the E/p requirement;
- the isolation criteria on the lepton.

These modified requirements allow to select samples with sufficiently high statistics. These samples are orthogonal to the analysis sample and thus diminish the real leptons from W/Z+jets and $t\bar{t}$ events. At the same

time, this event selection has been shown to provide a proper modeling of the three-jet mass distribution for the QCD multijet events selected in the signal sample, which can be predicted in the not-tagged case via the Matrix Method. A comparison between the three-jet mass distribution for not-tagged events with at least three jets between the Matrix Method prediction and the inverted-lepton sample can be found in Fig. 7.20 for the electron and muon channel. In both cases good modeling of the QCD multijet shape is obtained by the inverted-lepton selection within the limited statistical prediction of the Matrix Method prediction.

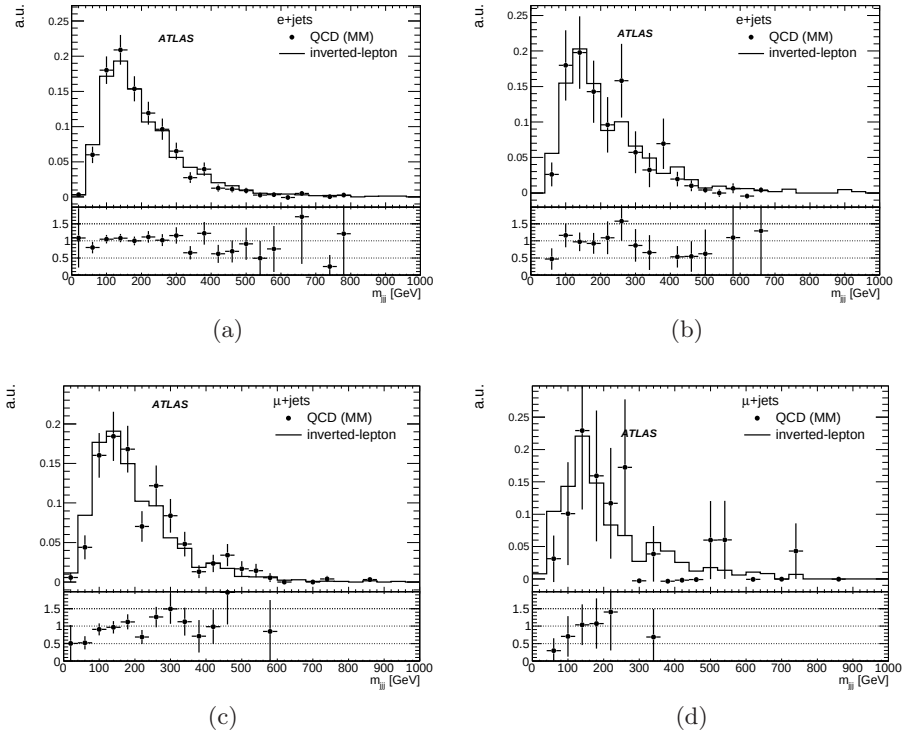

Figure 7.20: Comparison of the three-jet mass distribution for untagged $\ell+ \geq 3$ jets events between the Matrix Method prediction (dots with error bars) and the inverted-lepton selection (histogram) before (left) and after (right) E_T^{miss} plus triangular cuts for the electron (above) and muon channel (below).

Due to the small size of the data sample, the QCD multijet distributions obtained after requiring the presence of at least one identified b quark jet (a requirement which has been designed precisely to eliminate QCD multijet background) are subject to severe statistical fluctuations, making the QCD multijet shape estimation rather poor. To solve this problem an alternative

approach has been taken. Instead of using tagged samples we use distributions obtained before b-tagging and weight individual events by the average probability to tag a multijet event. This weight can be written for events with n_{jets} as

$$\omega = 1 - \prod_{i=0}^{n_{\text{jets}}} (1 - \text{TRF}(p_{T,i}, \eta_i)) \,, \tag{7.27}$$

where the Tag Rate Function (TRF) denotes the per jet tagging rate in QCD multijet events, which depends on the p_T and η of the jet.

The per jet tagging rate is measured in a sample of events with at least one jet, failing the lepton identification criteria (see above) and having no E_T^{miss} cut applied. Figure 7.21 shows the per-jet TRF as a function of jet p_T and η measured in the electron and muon channels. As it can be seen, the presence of a muon in the muon channel significantly enriches the heavy-flavor fraction of the QCD multijet background, thus leading to a higher per-jet tagging rate than in the electron channel.

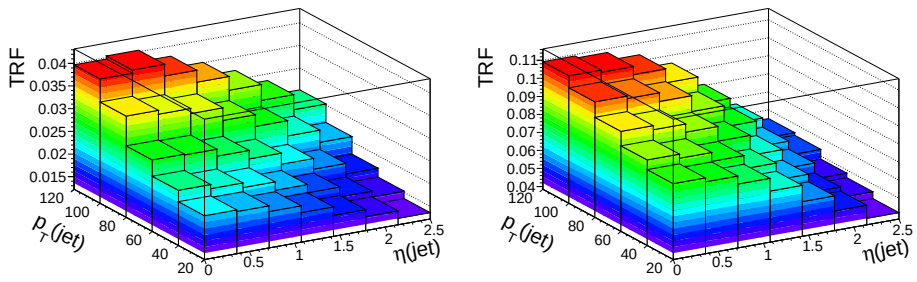

(a) (b)

Figure 7.21: Per-jet Tag Rate Function (TRF) in the (a) electron and (b) muon channel for QCD multijet enriched samples, as a function of p_T and η.

This weighting method corrects the bulk of the kinematic bias resulting from the b-tagging requirement, as demonstrated in Fig. 7.22, where the $H_T = \sum_i^{\text{jets}} p_{T,i}$ and three-jet mass distributions are compared between actual tagged lepton plus three jets events (selected with the inverted-lepton criteria and no E_T^{miss}), and untagged ones weighted through the above procedure.

7.5.3 Estimation of the W+jets Background Shape

The shape for the W+jets background template was taken from MC simulation. In order to validate the W+jets MC modeling with data, a W+jets

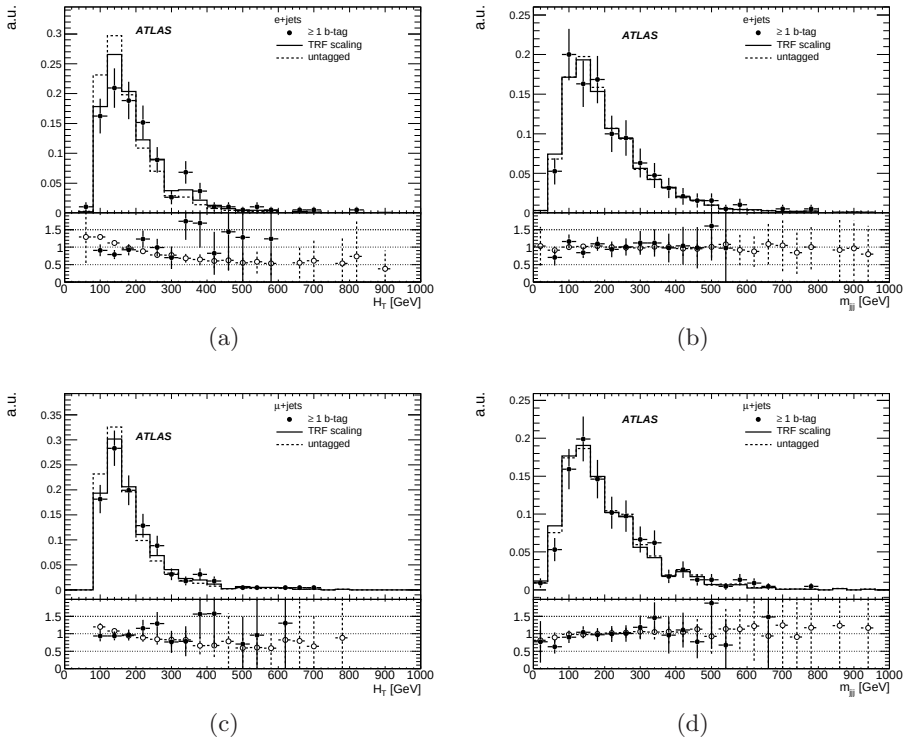

Figure 7.22: Comparison of H_T (left) and three-jet mass (right) distributions for purely no-tagged (dashed line), weighted no-tagged (full line), and tagged (dots with error bars) three jets inclusive events in the electron (above) and the muon channel (below) selected with the inverted-lepton criteria and without E_T^{miss} requirements.

dominated sample is obtained by requiring that there is no b-tagged jet in the event, in order to suppress the $t\bar{t}$ contamination to about 20%. This has the advantage of limiting any dependence on the assumed $t\bar{t}$ cross section in this comparison.

Figure 7.23 compares the W+jets shape of the three-jet mass distribution from simulation with the one obtained from data as described above. For the latter, the QCD multijet contamination estimated via the Matrix Method is subtracted, as well as other non-W backgrounds predicted by the simulation. The selection for the electron and muon channel was combined. At least three jets were required, with none of them tagged as a b quark jet. Good agreement is observed between the data and the MC prediction within the statistical uncertainties of the data.

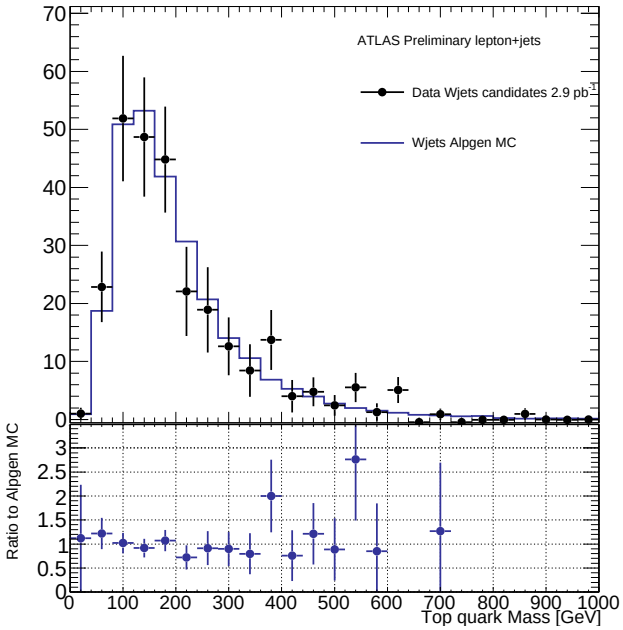

Figure 7.23: The three-jet invariant mass distribution comparing non-W background subtracted data and the W+jets MC prediction for events with three jets inclusive without a b-tagged jet. The distributions correspond to the combination of the electron and the muon channel.

7.6 The Fit Method

A maximum likelihood fit to the distribution of the three-jet invariant mass, as a correspondence to the hadronically decaying top quark mass, was performed. For the top quark candidate those three jets were selected, that form the highest vector sum p_T. Candidate events in the selected data sample are fitted to a weighted sum of templates corresponding to $t\bar{t}$, W+jets, QCD multijets, and the rest of physics backgrounds (i.e. single top, Z+jets, and diboson). The fit takes into account the full correlation of systematic uncertainties from both normalization and shape across processes as well as channels. It was performed minimizing the following likelihood function:

$$-2\ln\Big(L(k_{t\bar{t}}, k_{W+\text{jets}})\Big) \propto -2\sum_{i=0}^{N_{\text{bins}}} n_i \ln(\mu_i) - \mu_i \,, \tag{7.28}$$

with

$$\mu_i = k_{t\bar{t}} \cdot \mu_i^{t\bar{t}} + k_{W+\text{jets}} \cdot \mu_i^{W+\text{jets}} + k_{\text{QCD}} \cdot \mu_i^{\text{QCD}} + k_{\text{others}} \cdot \mu_i^{\text{others}} \,, \tag{7.29}$$

where n_i stands for the measured data events in bin i and μ_i for the MC prediction, dependent on the corresponding k-factors.

The scaling factors $k_{t\bar{t}}$ and $k_{W+\text{jets}}$, i.e. the scaling of the $t\bar{t}$ cross section and the amount of W+jets events in the sample, respectively, are fitted simultaneously. For the multijet background the factor k_{QCD} is set to one, as the QCD multijet sample is already normalized to the prediction by the data-driven method (see Sec. 7.3.1). The coefficient k_{other} of the minor background is set to one, corresponding to the Standard Model expectation. The uncertainties on k_{QCD} and k_{other} factors are propagated to the final result of the fit and the corresponding systematic uncertainties evaluated (see Sec. 7.6.1).

The template shape describing $t\bar{t}$ events is taken from simulation, as well as the shapes describing minor backgrounds like single top, Z+jets and diboson processes. Due to the small statistics of the present data sample ($2.9\,\text{pb}^{-1}$) the W+jets shape is also taken from simulation, although it is validated comparing the MC prediction to data (see Sec. 7.5.3). As explained in Sec. 7.3.1, data-driven methods have been developed to derive the template shape for the QCD multijet background. This brings the advantage that the QCD multijet background is not affected by physics modeling and jet energy scale (JES) uncertainties in the fit.

Figure 7.24 shows the corresponding three-jet mass distributions used as templates in the fits, i.e. the μ_i in Eq. 7.28, for $t\bar{t}$, W+jets, QCD multijets, and the combination of all other backgrounds, as an example for the muon channel with at least four jets.

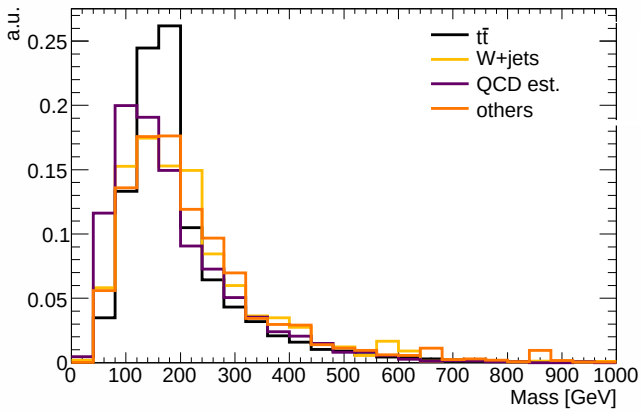

Figure 7.24: Template distributions used in fit for the muon channel with at least four jets. At least one b-tagged jet was required.

In order to provide the maximum sensitivity for this analysis, a combined fit of four channels is performed: electron and muon channel with the selections of three jets exclusive and four jets inclusive.

In Table 7.12 and 7.13 can be seen that the W+jets background contri-

bution in the four jet inclusive sample is relatively low. It is thus not possible to obtain a stringent result for $k_{W+\text{jets}}$, which in turn degrades the precision of $k_{t\bar{t}}$. A further constraint is obtained by fitting simultaneously the three jet exclusive sample that contains a larger fraction of W+jets events and still a sizable amount of $t\bar{t}$ events. The inclusion of the three jet exclusive sample in the fit corresponds to having about 67% additional signal with a signal-over-background ratio approximately one.

7.6.1 Systematic Uncertainties

In the measurement of the $t\bar{t}$ cross section numerous sources of uncertainty have been studied and considered. They are described in detail below.

7.6.1.1 Lepton Reconstruction, Identification, and Trigger

A good agreement between data and simulated events was found for the electron trigger, the reconstruction, and the identification efficiencies, being consistent within 2.3% or better statistical uncertainty. For muons the statistical uncertainty is determined as 1.2%. For details see Sec. 7.1 or [116].

The uncertainties on the lepton momentum scale and resolution was discussed in Sec. 7.2.2.3 (7.2.2.5) for electrons (muons).

7.6.1.2 Jet Energy Scale and Jet Reconstruction Efficiency

The uncertainty due to the jet energy scale (JES) was estimated by rescaling the four-vector of each reconstructed jet in MC up and down by a factor between 6% and 10%, corresponding to a variation by one sigma, depending on their transverse momentum and pseudo-rapidity (see Sec. 5.5.1). This procedure was not applied to the data-driven QCD multijet background. The affect on the missing transverse energy was corrected for by recalculating it using the rescaled jets instead.

The jet reconstruction efficiency is reproduced by the simulation in a residual systematic uncertainty at the percent level [123], which is taken as the systematic uncertainty.

7.6.1.3 B-tagging

Jets from data and simulation have been compared to estimated the uncertainties on the efficiency of the heavy flavor tagging of jets with the SV0 tagger (see Sec. 5.5.3). These efficiencies differ depending on the origin of the jet such that MC efficiencies for b and c quark jets have to be corrected by a factor of 5% to 12%, depending on the jet's transverse momentum. The obtained scaling factors underlie an uncertainty of 10% to 20% for jets tagged as b-jets, 20% to 40% for those tagged as c-jets, and about 20% for light jets [119].

Table 7.14: Correlated and uncorrelated uncertainties for the QCD multijet background normalization for the electron and muon channel, with the three jets exclusive and the four jet inclusive selection.

	Electron		Muon	
	=3 jets	$\geq$ 4 jets	=3 jets	$\geq$ 4 jets
correlated	20%	20%	47%	65%
uncorrelated	51%	56%	20%	20%

7.6.1.4 QCD Multijet Normalization

The shape of the QCD multijet background in the tagged samples was obtained from data and the normalization by using different methods for its estimate. Uncertainties on these normalizations originate from different source:

- the difference between estimates obtained using different control regions (muon channel) or different mis-identified lepton models (electron channel);
- the uncertainty of the fit for the fitting method;
- from the calibration of the methods using simulated multijet events (muon channel) or data events (electron channel).

These uncertainties are treated as uncorrelated between the electron and muon channel. The uncertainty of the mis-identification rate in the different control regions is treated fully correlated between jet bins. The rest of the components are taken as uncorrelated. In Table 7.14 these uncertainties are listed.

7.6.1.5 Other Backgrounds Normalization

The uncertainties for the theoretical predictions and thus the normalization of the smaller backgrounds are taken into account, namely Z+jets (100%), single top (10%), and diboson (5%).

The uncertainty on Z-jets is a conservative estimation to account for high jet multiplicities and the flavor content. Since the total contribution of Z+jets events to the final selected sample is very small, this uncertainty does not influence significantly the final result.

For single top the cross section obtained directly from MC@NLO was used [124]. Differences between this value and the one obtained with MCFM [81] at 7 TeV are of the order of 5% to 10%, with MC@NLO giving larger values [125]. On the other side, for the s- and Wt-channel single top production at NLO and next-to-next-to-leading logarithm (NNLL) cross

sections from 5% to 7% larger than those from MC@NLO have been calculated [126].

The diboson cross section and its uncertainty was taken from MCFM [81].

7.6.1.6 Ratio of 3-jet to 4-jet W+jets Yields

The W boson with associated jets as a background for semi-leptonic top quark decays was described in Sec. 3.2.3.1. As mentioned there, the description of a large number of associated jets can be estimated using the W+jets fraction (3 vs 4 jets). Comparing the predicted ratios of this scaling factor for the different MC generators and generator settings at parton level yields a difference of 24% [122].

7.6.1.7 Background Tag Fraction

Similar to the W+jets fraction (3 vs 4 jets), the tag fraction affects the fit of the three jet exclusive and four jet inclusive samples due to dependencies on the jet multiplicity of the W+jets background. The number of tagged jets is extrapolated from a sample of exactly three jets to the four jet inclusive sample by the ratio $f^{\text{corr}}_{=3\text{ jets}}$ that is defined as

$$f^{\text{corr}}_{=3\text{ jets}} = \frac{f^{\geq 4\text{ jets}}_{\text{tagged}}}{f^{=3\text{ jets}}_{\text{tagged}}} \,. \tag{7.30}$$

This value was estimated on ALPGEN W+jets MC studies under consideration of the three following (Gaussian) uncertainties:

- a fully correlated uncertainties of 300% for the $Wbb+$jets and $Wcc+$jets fraction and uncorrelated uncertainties of 100% on the $Wc+$jets fraction in the two jet exclusive sample;
- the uncertainty on the scaling factors for the efficiency of the b-tagging for b, c, and light jets is assumed. The tag fractions are measured separately for the three jet exclusive and the four jet inclusive samples yielding an additional 20% uncertainty on the fraction of the heavy flavor and 100% on the light jet components;
- a further contribution to the uncertainty is estimated varying several ALPGEN generator parameters that are known to influence the above mentioned ratios, e.g. the scale factor for the CKKW α_s scale (see Sec. 3.2.5). A conservative estimated was used, increasing the uncertainty by a factor of two yielding to 40% to 60% per ratio.

Since the contributions of the first and the second point are effectively canceled out in the ratio, the main contribution on the uncertainty of $f^{\text{corr}}_{=3\text{ jets}}$ originates from the last point, resulting in a total uncertainty of 24%.

7.6.1.8 W+jets Flavor Fraction Content

As discussed in Sec. 3.2.5, the heavy flavor content of W+jets is estimated using the MC simulation. An uncertainty on the prediction for the Wbb+jets, Wcc+jets, and Wc+jets background is taken into account in this study. The fraction of Wbb+jets and Wcc+jets was therefore varied by 100%, in a fully correlated way. For Wc+jets the variation was of 60%, uncorrelated to that of Wbb+jets and Wcc+jets. These uncertainties have been applied fully correlated to all jet multiplicities.

7.6.1.9 Background Shape

W+jets Shape: Due to the small size of the data sample, it is not possible to extract the template shape of W+jets using data-driven methods. The shape used in this study, obtained from the ALPGEN MC generator, was compared to variations of this generator and to the SHERPA MC.

Alternative W+jets models were compared by changing the default MC shape by distortions resulting from varying the choice of renormalization and fragmentation scale Q in the MC. The variations considered are $Q = m(W)$ and $Q = \sqrt{m^2(W) + p_T^2(W)}$, where $m(W)$ is the mass of the W bosons and $p_T(W)$ its transverse momentum. The default choice uses the sum of the p_T of all jets and was $Q = \sqrt{m^2(W) + \sum p_T^2(\text{jet})}$ [122].

Figure 7.25 (a) shows the three-jet invariant mass in samples of at least three jets with transverse momentum larger than 20 GeV and no b-tagged jets for the reference MC and the variations. Data candidates are also shown to demonstrate the goodness of the simulation. The largest discrepancy was observed in comparison to the SHERPA MC, which can be partially explained by the fact that the SHERPA MC was not tuned to data yet. Therefore, the SHERPA MC samples was used as an extreme model to estimate the uncertainty on the shape.

Figure 7.25 (b) and (c) show the leading and second leading jet p_T distributions, respectively, which clearly show that SHERPA predicts too hard jet p_T spectra.

QCD Multijet Shape: The QCD multijet shape is derived from a multijet enriched data sample by inverting lepton requirements and abandoning the b-tagging. The in such a way obtained shape has a softer spectrum in comparison to one estimated using the Matrix Method (see Sec. 7.3.1.1). In comparison to the W+jets samples, which in some way underlies a similar production process, the spectrum is harder. Figure 7.26 shows the comparison of the three jet invariant mass distribution for this multijet enriched sample as an example for the electron channel and the three jet exclusive selection.

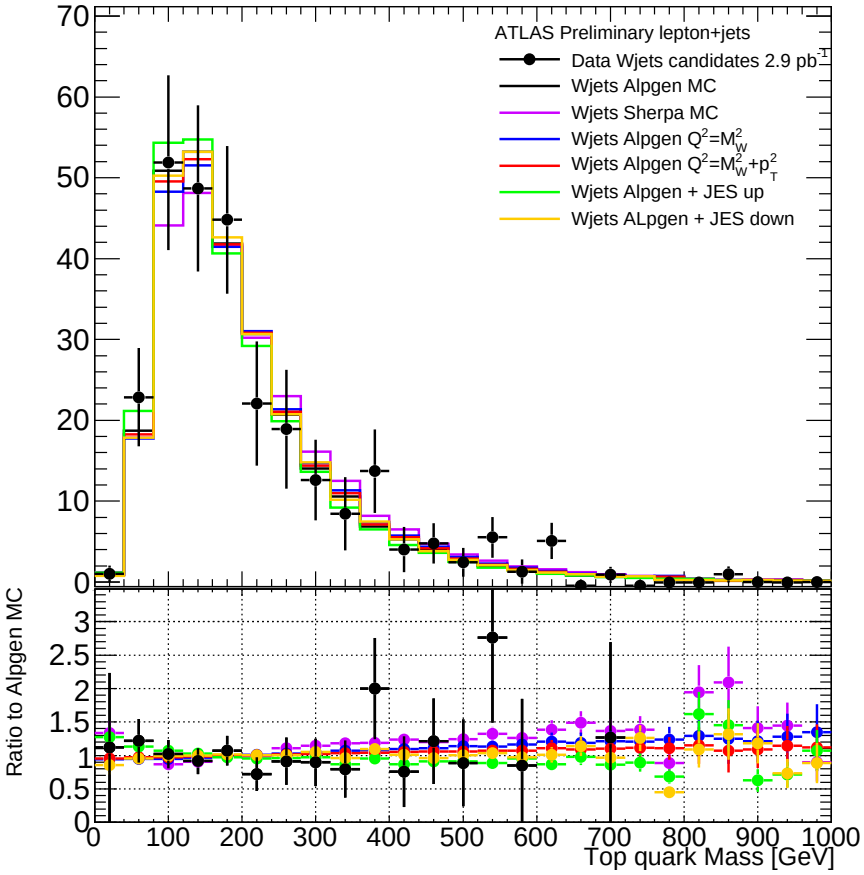

(a)

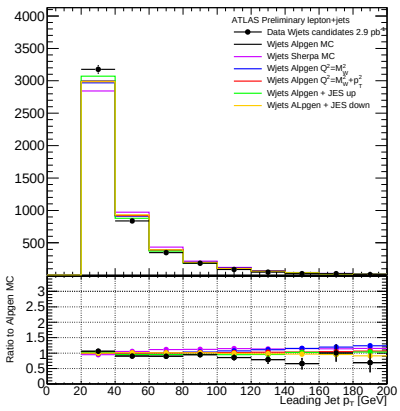

(b)

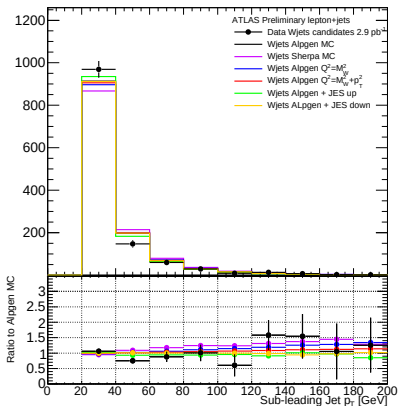

(c)

Figure 7.25: Distribution of (a) the three-jet mass, (b) the leading jet and (c) the second jet p_T for different W+jets MC samples. The effect of the variation of JES up on down on the reference ALPGEN MC is also shown. The distributions correspond to the electron and muon channels combined.

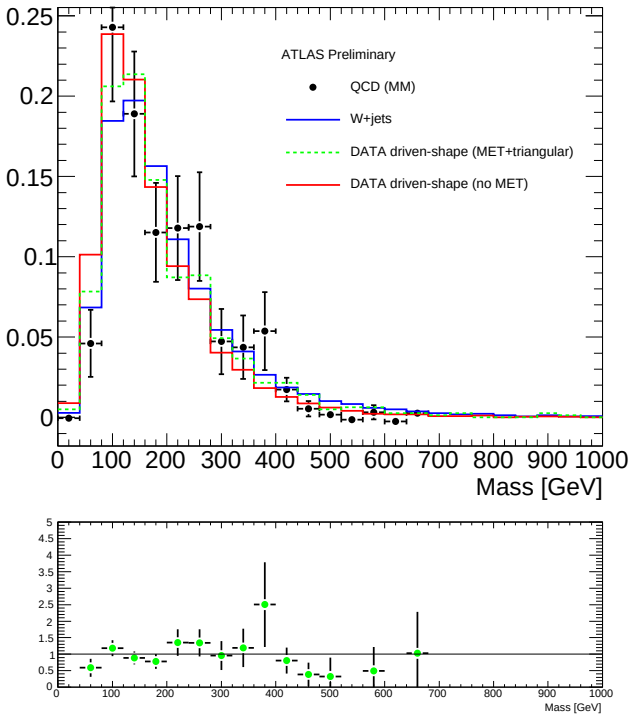

Figure 7.26: Three-jet invariant mass distributions for the multijet enriched data sample (green), a variation obtained without requirements on missing transverse energy and triangular cut (red) and W+jets MC (blue) in the electron channel. The distribution obtained from a tagged data sample using the matrix method is also shown as points with error bars. Below, the shape from the Matrix Method and the used one are compared.

7.6.1.10 $t\bar{t}$ Signal Modeling

NLO Simulation: In this analysis the $t\bar{t}$ signal MC samples was generated with MC@NLO (see Sec. 3.2.4). In order to take into account the uncertainty on the signal modeling, the MC@NLO sample was compared with a $t\bar{t}$ sample produced with POWHEG. POWHEG generates final states at NLO accuracy and was interfaced to both, PYTHIA and HERWIG.

Fragmentation: In order to give an estimate of the uncertainty caused by the parton shower simulation, two different hadronizations, i.e. HERWIG and PYTHIA, of the same POWHEG generator have been studied.

Initial and Final State Radiation: The uncertainty coming from initial state radiation (ISR) and final state radiation (FSR) parametrization on the

signal acceptance have been determined using AcerMC and the hadronization with PYTHIA [70]. The PYTHIA parameters have been varied in order to maximize or minimize the jet multiplicity due to ISR and FSR. These variations were performed in a range consistent with different models (MC@NLO+HERWIG, SHERPA 1.1.X, SHERPA 1.2.X, Q^2-ordered PYTHIA with different tunes, p_T-ordered PYTHIA with different tunes) [127].

Three different samples have been generated and studied: ISR varied up/down, FSR varied up/down, and the combination of ISR and FSR varied up/down. The uncertainty on the measured cross section has been assessed for each of them and the largest positive (up) and negative (down) uncertainties are taken.

Parton Density Function: The uncertainty raised by the PDF used for the signal MC generation was evaluated using the reweighing technique with different PDFs following the procedure described in [128, 129] (see Appendix A). An uncertainty of 2.5% on the signal acceptance has been considered. Uncertainties on the signal template shape have been neglected.

7.6.1.11 Luminosity

For the estimation of the luminosity ($2.9\,\mathrm{pb}^{-1}$) an uncertainty of 11% was taken into account. The main contribution originates from the uncertainties on the beam intensities. A conservative estimate of 10% was taken into account, mainly caused by the Direct-Current-Current-Transformator, which measures the total circulating current. Minor contributions are the length scale of the beam separation (2%), the effects of imperfect beam centering (2%), the emittance growth increasing the transverse beam size (3%), and the dependence on the mean number of interactions per crossing (2%) [113].

7.6.2 Expected Performance

The expected uncertainties for the $t\bar{t}$ production cross section measurement have been obtained by generating a large number of pseudo-experiments corresponding to the integrated luminosity in data. For this purpose Poisson fluctuations have been applied to the total expectation of signal and background, assuming $k_{t\bar{t}} = k_{W+\mathrm{jets}} = 1$. These fluctuation have been performed for both, the electron and the muon channel, in the three jet exclusive and the four jet inclusive channels.

In complete analogy to the fitting process on data (see Sec. 7.7.1), $k_{t\bar{t}}$ and $k_{W+\mathrm{jets}}$ have been fitted simultaneously combining the four channels. Figure 7.27 (a) shows the linearity of the fitting method for several variations of the signal sample variation ($k_{t\bar{t}}^{\mathrm{true}}$). No bias on the normalization of the signal sample was observed.

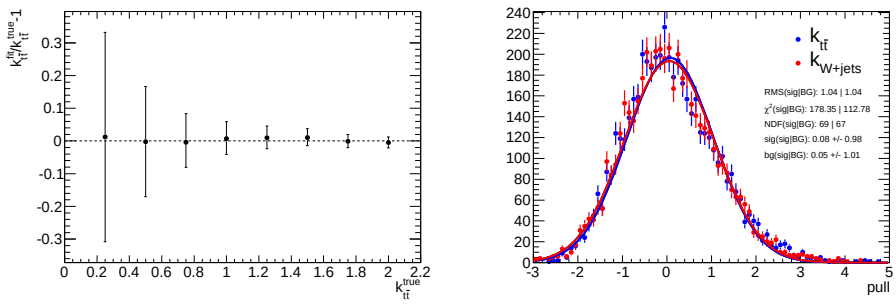

(a) (b)

Figure 7.27: (a) Linearity test of the fit for $k_{t\bar{t}}$ as a function of the true normalization. For each point 1000 pseudo-experiments have been performed. (b) Pull distribution for $k_{t\bar{t}}$ and $k_{W+\text{jets}}$ corresponding to 5000 pseudo-experiments. Errors are statistical only.

Figure 7.27 (b) shows the pull distribution for $k_{t\bar{t}}$ and $k_{W+\text{jets}}$ corresponding to 5000 pseudo-experiments. The root mean square of this distribution gives an estimate of the statistical uncertainty of this measurement. For the pull distributions of $k_{t\bar{t}}$ ($k_{W+\text{jets}}$) a mean of 0.08 (0.05) and a root mean square of 1.04 for both was measured. This ensures the correctness of the calibration of the fit, such that it represents a confidence level interval of 68%.

The shape and the normalization of the templates have been varied and fitted for the uncertainty estimation. The expected systematic uncertainty for each source (see Sec. 7.6.1) has been computed as the mean of the distribution of differences between the nominal fit results and the one obtained with the varied samples.

In order to keep the statistical fluctuation of the measurement low, the same pseudo experiments have been used for the nominal fit and for the estimation of the systematic uncertainties. A summary of the expected uncertainties for the measurement is shown in Table 7.15. The mean of the k-factors as well as the statistical uncertainty is listed, too. A detailed list of the expected uncertainties can be found in Appendix D.

The largest contribution to the systematic uncertainty is expected to come from the jet energy scale. Also the uncertainty originating from the flavor tagging yields an important contribution, as well as the uncertainty due to the QCD multijet normalization. These are followed by contributions arising from the background shape estimation, mainly from comparison with the sample generated with SHERPA.

Already with data corresponding to a luminosity of 2.9 pb^{-1} the statistical uncertainty is of the order of the total systematic uncertainty, (excluding

Table 7.15: Expected results of $k_{t\bar{t}}$ and $k_{W+\text{jets}}$ as well as for the uncertainties of the combined fit, for electron and muon simultaneously, of the three jets exclusive and four jets inclusive data for a sample of $2.9\,\text{pb}^{-1}$.

	$k_{t\bar{t}}$		$k_{W+\text{jets}}$	
k-factors	1.01		0.99	
Statistical Uncertainty (%)	+29.2	-27.0	+80.5	-75.3
Object selection				
Lepton Reco, ID, Trigger (%)	+2.1	-2.3	+2.2	-1.1
Jet energy scale (%)	+13.9	-10.5	+21.8	-27.6
b tagging (%)	+13.0	-8.5	+6.8	-5.6
Background rate				
QCD normalization (%)	+10.6	-9.5	+23.8	-21.6
Other background normalization (%)	+0.2	-0.2	+2.5	-2.3
Background modeling				
W+jets fraction (3 vs 4 jets) (%)	+3.5	-3.4	+3.2	-4.0
W+jets tag fraction (3 vs 4 jets) (%)	+3.5	-3.4	+3.2	-4.0
W+jets heavy flavor content	+2.1	-0.8	+2.3	-6.5
Background shape (%)	+7.3	-7.3	+23.8	-23.8
$t\bar{t}$ signal modeling				
ISR/FSR (%)	+9.9	-8.5	+13.6	-14.4
PDF (%)	+2.6	-2.4	+0.0	-0.0
Fragmentation (%)	+2.7	-2.7	+9.2	-9.2
NLO generator (%)	+3.7	-3.7	+15.4	-15.4
Total Systematic (%)	+26.2	-21.3	+46.9	-49.3
Lumi (%)	+12.5	-10.0	+2.9	-2.8
Total Uncertainty (%)	+41.2	-35.8	+93.2	-90.1

the uncertainty on the integrated luminosity).

7.7 Results

In this section the result of the top quark production cross section measurement is presented. The measured uncertainties are shown (Sec. 7.7.1), followed by the results of the template fit (Sec. 7.7.2). The obtained results for the W+jets background are compared to other studies performed in ATLAS (Sec. 7.7.3). Finally the significance of this measurement is discussed (Sec. 7.7.4).

Table 7.16: Results of $k_{t\bar{t}}$ and $k_{W+\text{jets}}$ as well as for the uncertainties of the combined fit, for electron and muon simultaneously, of the three jets exclusive and four jets inclusive data for a sample of 2.9 pb^{-1}.

	$k_{t\bar{t}}$		k_{W+jets}	
k-factors	0.79		1.03	
Statistical Uncertainty (%)	+35.6	-32.7	+76.5	-71.7
Object selection				
Lepton Reco, ID, Trigger (%)	+3.1	-2.7	+4.5	-5.4
Jet energy scale (%)	+29.2	-10.3	+13.9	-53.4
b tagging (%)	+12.3	-6.9	+7.4	-10.1
Background rate				
QCD normalization (%)	+12.4	-10.7	+21.3	-20.2
Other background normalization (%)	+0.2	-0.2	+2.4	-2.4
Background modeling				
W+jets fraction (3 vs 4 jets) (%)	+8.0	-8.8	+13.0	-12.9
W+jets tag fraction (3 vs 4 jets) (%)	+8.0	-8.8	+13.0	-12.9
W+jets heavy flavor content	+2.3	-1.5	+3.8	-5.0
Background shape (%)	+15.0	-15.0	+36.5	-36.3
$t\bar{t}$ signal modeling				
ISR/FSR (%)	+13.3	-16.6	+21.2	-13.2
PDF (%)	+2.6	-2.4	+0.0	-0.0
Fragmentation (%)	+0.7	-2.0	+3.0	-0.0
NLO generator (%)	+3.3	-3.0	+2.8	-2.8
Total Systematic (%)	+41.4	-30.8	+53.6	-72.4
Lumi (%)	+12.5	-10.0	+2.8	-2.9
Total Uncertainty (%)	+56.0	-46.1	+93.5	-102.0

7.7.1 Measured Uncertainties

In the final measurement of the $t\bar{t}$ cross section with data all sources of systematic uncertainties listed in Sec. 7.6.1 have been considered. In analogy to the estimation of the expected uncertainties in Sec. 7.6.2, the results are obtained for the combination of the three jet exclusive and the four jet inclusive and for the electron and the muon channel. A summary of the measured uncertainties is given in Table 7.16. A detailed list of the measured uncertainties can be found in Appendix E.

Comparing the outcome of the measurement to the expected uncertainties, a clear overestimation of the uncertainties for the jet energy scale (upper value larger by a factor of two) and the background shape uncertainties (both, up and down by a factor of two) can be observed. In general larger

Table 7.17: Measured inclusive $t\bar{t}$ cross section for the electron, muon, and the combination of both channels. The uncertainties represent the statistics, the systematic, and the uncertainty on the integrated luminosity.

Channel	Fitted cross section (pb)
electron	$98 \pm 58\ ^{+32}_{-26}\ ^{+12}_{-10}$
muon	$167 \pm 68\ ^{+42}_{-35}\ ^{+20}_{-18}$
electron and muon	$130 \pm 44\ ^{+34}_{-28}\ ^{+16}_{-13}$

uncertainties than expected are observed, as for instance for the uncertainty of ISR and FSR, for W+jets fraction (3 vs 4 jets), and the W+jets tag fraction (3 vs 4 jets). However, this is consistent within statistical fluctuations in data.

7.7.2 Template Fit Results

To obtain the cross section the measured k-factor is applied to the production cross section used for the MC simulation. The resulting measured cross sections for the $t\bar{t}$ production at the ATLAS experiment with $2.9\,\mathrm{pb}^{-1}$ is listed in Table 7.17. The estimated inclusive $t\bar{t}$ cross section is given for the electron and muon channel separately, as well as for the combination of the electron and muon channel. In all three cases the three jet exclusive and the four jet inclusive channel are combined. Since the measured systematic uncertainties are subject to large statistical fluctuations (see Sec. 7.7.1), the expected systematic uncertainties are reported instead.

Figure 7.28 shows the three-jet invariant mass distribution for the selected data in the electron and muon channels for the three jet exclusive and four jet inclusive samples. The result of the combined fit for the three jet exclusive and the four jet inclusive samples is shown in Fig. 7.29. Finally, Fig. 7.30 shows the result of the combined fit for the three jet and four jet together. In all figures the $t\bar{t}$ and W+jet contributions have been scaled according to the results of the fit.

7.7.3 W+jets Comparison to Other Studies

In addition to the $t\bar{t}$ normalization factor, the fit also determines the normalization factor for W+jets with at least four jets and at least one tagged as a b jet. Table 7.18 compares the results from the fit with an alternative data-driven estimate using a counting based method employing Berends scaling (see Sec. 3.2.3.1) [122]. A good agreement between the two methods was observed.

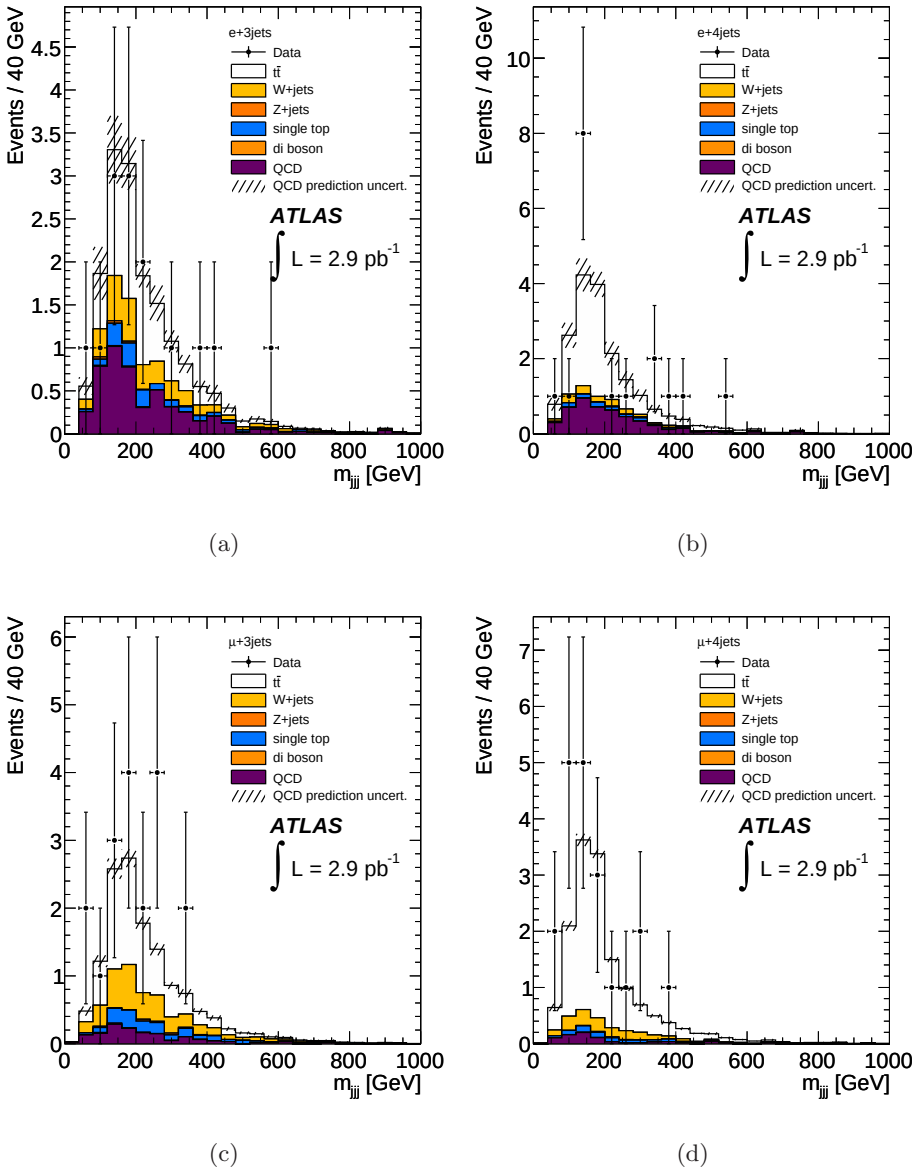

Figure 7.28: Three-jet invariant mass distribution for the selected data and the prediction for (a) the electron channel three jet exclusive and (b) four jet inclusive samples and for (c) the muon channel three jet exclusive and (d) four jet inclusive samples. The $t\bar{t}$ and W+jet contributions have been scaled according to the results of the fit.

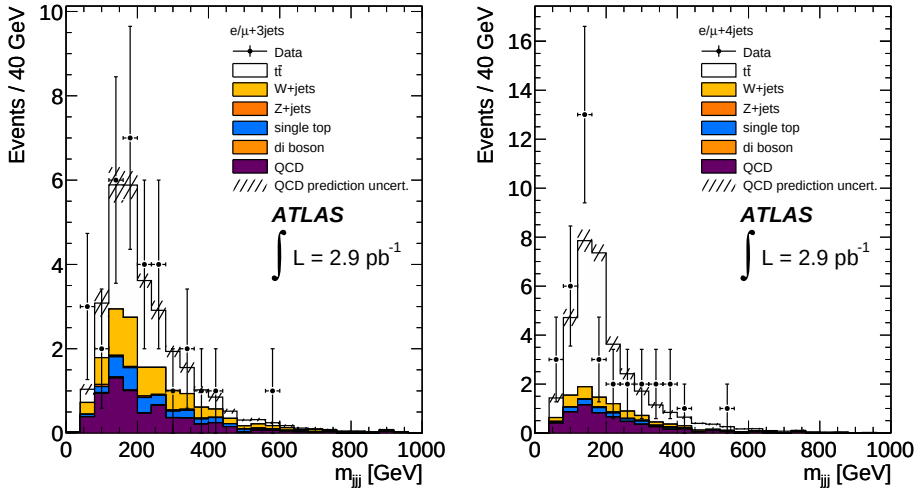

(a) (b)

Figure 7.29: Three-jet invariant mass distribution for the selected data and the prediction for the combined fit for (a) the three jet exclusive and (b) the four jet inclusive sample. The $t\bar{t}$ and W+jet contributions have been scaled according to the results of the fit.

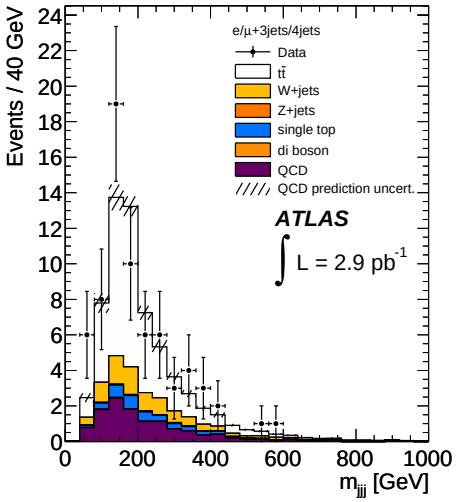

Figure 7.30: Three-jet invariant mass distribution for the selected data superimposed on the prediction for the combined fit. Electron and muon channel three jet exclusive and four jet inclusive samples are shown together. The $t\bar{t}$ and W+jet contributions have been scaled according to the results of the fit.

Table 7.18: Comparison of the measured W+jets background contribution in the selection sample with at least four jets, with at least on tagged as a b-jet. Yields are shown for the electron and muon channel for the measurement presented here and the counting based study in [122]. The first quoted uncertainty for each number is statistical, while the second one is coming from systematics.

channel	this measurement	counting based
electron	$2.2 \pm 1.6\,^{+1.0}_{-1.1}$	$1.9 \pm 0.7 \pm 0.9$
muon	$2.6 \pm 1.9\,^{+1.2}_{-1.3}$	$3.2 \pm 1.2 \pm 1.2$

7.7.4 Significance Calculation

The significance level quantifies the agreement between data and a null hypothesis H_0 making use of the so-called p-value. The p-value gives the probability that under the assumption of H_0 a result at least as extreme as the measured one is obtained. The null hypothesis is rejected if the p-value is smaller or equal a certain significance level α. For practical reasons, one maps α to the number of standard deviations N_σ a standard normal variate would have to be away from zero for the probability outside of $\pm N_\sigma$ to equal p [130]:

$$\alpha = 1 - \frac{2}{\sqrt{\pi}} \int_o^{N_\sigma/\sqrt{2}} e^{-t^2} dt \,. \tag{7.31}$$

7.7.4.1 Hybrid Bayesian-Frequentist Method

A hybrid-method of the Bayesian and Frequentist statistics was considered to estimate the significance of the results.

For the Frequentist approach a null hypothesis H_0 is selected and a critical region of sample space is defined that has probability α of containing the data under H_0. In case that the measurement lies within the critical region, H_0 is rejected. In this measurement the hypothesis H_0 is the Standard Model without the top quark.

The Bayesian approach gives a degree of believe for an unknown parameter to take on values in a certain region given by the data. It was used to take into account the systematic uncertainties in the significance estimation process, which is not possible in Frequentist statistics. The systematic uncertainties have been taken into account as Gaussian priors, i.e. Gaussian fluctuation of the background sample, taking into account correlations across processes as well as channels.

The template fit was performed with background samples only, i.e. the null hypothesis H_0. The observable $k_{t\bar{t}}$ was fitted in an ensemble testing of $3.7 \cdot 10^6$ pseudo experiments of these background-only samples. Events

with a fitted value of $k_{t\bar{t}}$ larger than or equal to the expected (measured) value are taken into account for the estimation of the expected (measured) p-value.

In order to control the computing time only those systematic uncertainties, that mainly contribute to the total uncertainty, have been considered:

- lepton identification (see Sec. 7.6.1.1);
- JES (see Sec. 7.6.1.2);
- b-jet tagging (see Sec. 7.6.1.3);
- QCD multijet normalization per channel, treated as uncorrelated across jet multiplicity bins (see Sec. 7.6.1.4);
- W+jets fraction (3 vs 4 jets) of W+jets yields (see Sec. 7.6.1.6);
- Z+jets, single top, and diboson cross sections (see Sec. 7.6.1.5);
- luminosity (see Sec. 7.6.1.11).

7.7.4.2 Evidence for Top Quark Production

Figure 7.31 shows the distribution of the fitted $k_{t\bar{t}}$ for $3.7 \cdot 10^6$ background-only pseudo-experiments. The measured $k_{t\bar{t}}$ factor is indicated by the vertical line at 0.790. Of the performed pseudo experiments 131 yield an expected

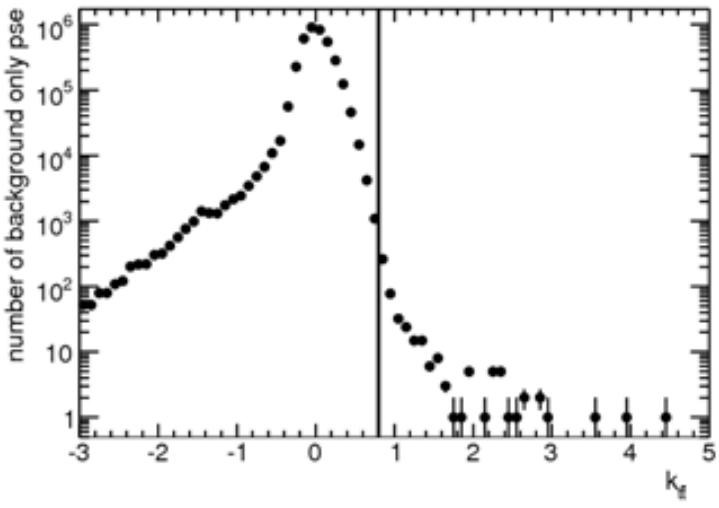

Figure 7.31: Distribution of fitted $k_{t\bar{t}}$ of $3.7 \cdot 10^6$ background-only pseudo-experiments. The vertical line at 0.790 shows the measured $k_{t\bar{t}}$ factor. There are 131 pseudo experiments above 1, and 530 above 0.790.

$k_{t\bar{t}} \geq 1.0$ which results into a expected p-value of $3.54 \cdot 10^{-5}$. This can be

Table 7.19: Inclusive top quark pair production measured in the semi-leptonic final state with three different methods, among them the one presented in this study. The uncertainties stated are statistical and systematical, respectively. Latter includes the uncertainty on the luminosity [9].

$\sigma_{t\bar{t}}$	Method
$142 \pm 34 \,^{+\,50}_{-\,31}$ pb	Counting
$130 \pm 44 \,^{+\,38}_{-\,30}$ pb	Fitted A (this measurement)
$118 \pm 34 \pm 34$ pb	Fitted B

translated into an expected significance level of $4.41\,\sigma$ for this inclusive $t\bar{t}$ cross section measurement with $2.9\,\mathrm{pb}^{-1}$. Above the measured $k_{t\bar{t}}$ of 0.79 a total of 530 pseudo-experiments were found, yielding a measured p-value of $1.43 \cdot 10^{-4}$.

The measured significance level amounts for $3.8\,\sigma$, providing an evidence for top quarks observed with the ATLAS detector.

7.8 Summary

The measurement of the inclusive top quark pair production cross section with a semi-leptonic final state at the ATLAS experiment at $\sqrt{s} = 7\,\mathrm{TeV}$ was presented. Data to an integrated luminosity of $2.9\,\mathrm{pb}^{-1}$ was analyzed and the top quark pair production cross section was measured to be

$$\sigma_{t\bar{t}}^{\mathrm{semilep}} = 130 \pm 44\,(\mathrm{stat.})\,^{+34}_{-28}\,(\mathrm{syst.})\,^{+16}_{-13}\,(\mathrm{lumi.})\,\mathrm{pb}\,, \tag{7.32}$$

corresponding to a significance of $3.8\,\sigma$. This measurement is one of the first with the ATLAS detector and was included in the first top quark publication [9]. Two additional measurements in the semi-leptonic channel showed a good agreement with the one presented in this work, all of them listed in Table 7.19.

The measurement in the channel with both top quark pairs decaying leptonically was presented at the same time [9], also showing a good agreement with the result presented in this study:

$$\sigma_{t\bar{t}}^{\mathrm{dilep}} = 151^{+78}_{-62}\,(\mathrm{stat.})\,^{+37}_{-24}\,(\mathrm{syst.}+\mathrm{lumi.})\,\mathrm{pb}\,. \tag{7.33}$$

All four measurements are summarized and compared with the theoretical prediction in Fig. 7.32. All measurements are found to be in agreement with each other as well as with Standard Model predictions of $\sigma_{t\bar{t}} = 164.6 \pm ^{11.4}_{15.7}\,\mathrm{GeV}$ [41, 47, 48] for $m_t = 172.5\,\mathrm{GeV}$.

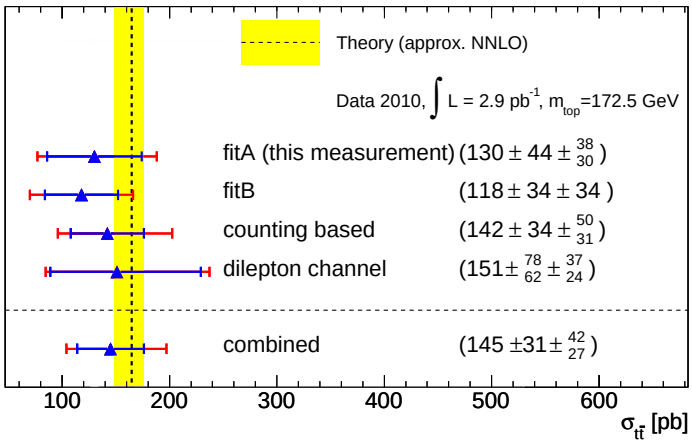

Figure 7.32: Summary of the top quark pair cross section measurements at the ATLAS experiment with data corresponding to $2.9\,\mathrm{pb}^{-1}$. Shown are all three measurements in the semi leptonic channel and the combined measurement in the di-leptonic channel as well as the theoretical prediction [41, 47, 48]. The combination the counting based method and the di-leptonic channel is shown ("combined") [9].

Chapter 8

Measurement of the Top Quark Pair Production Cross Section at $\sqrt{s} = 7\,\text{TeV}$ with $35\,\text{pb}^{-1}$

After performing the first study of top quark pair production using a small data set of $2.9\,\text{pb}^{-1}$, the complete data set collected in 2010 was analyzed, corresponding to an integrated luminosity of $35\,\text{pb}^{-1}$. The tenfold increase in statistics not only allowed a significant reduction in the statistical uncertainty of the top quark cross section measurement, but also led to further refinements in the object identification criteria improving the signal acceptance and suppressing backgrounds.

In addition, the large statistics allowed to consider for the first time exploiting the data itself to constrain the leading systematic uncertainties in the top quark cross section measurement. This was achieved by a judicious splitting of the data into orthogonal channels in such a way that the sensitivity to particular systematic uncertainties would be maximized. At the same time, a more sophisticated fitting technique was introduced to accomplish this goal.

Differences in the object identification with respect to those used in the early measurement are discussed in Sec. 8.1. The applied event selection and the resulting event yields are presented in Sec. 8.2. In Sec. 8.4 the profile likelihood fit in explained, followed by the results in Sec. 8.5. Finally, a summary is given in Sec. 8.6.

8.1 Physics Object Definition

The larger available data sample allowed a more detailed study and optimization of the object selection criteria used in the analysis. In the following the changes in these object selection criteria with respect to the earlier analysis using $2.9\,\mathrm{pb}^{-1}$ of data, as described in Sec. 7.1, are listed.

8.1.1 Electrons

The electron object requirements have been tightened significantly. The requirements applied in addition to those listed in Sec. 7.1.1 are:

- $\Delta\Phi < 0.02$ between the cluster position in the second layer of the EM calorimeter and the extrapolated track;
- an η and E_T dependent requirement on the cluster energy over track momentum (E/p);
- an η dependent requirement on the fraction of high threshold hits in the TRT;
- the difference between the measured number of TRT hits and the expected average number of TRT hits has to be within 15 hits;
- those electron candidates matching reconstructed conversion photons [131] are rejected;
- a stricter requirement for the track matching $|\Delta\eta|$ (< 0.005) and the impact parameter ($< 1.0\,\mathrm{mm}$).

For further details see [132].

These additional criteria allow to significantly reduce the contribution from the QCD multijet background in comparison to the analysis with $2.9\,\mathrm{pb}^{-1}$.

8.1.2 Muons

For the muon objects the same definition as described in Sec. 7.1.2 is used, with additional requirements on the hits:

- at least one B-layer hit (except when the track points to a known dead B-layer module);
- number of SCT hits plus the number of crossed dead SCT sensors larger than five (the number of crossed dead sensors was added);
- less than two pixel layers and SCT layers with absence of hits.

8.1.3 Jets and Flavor Tagging

The same jet objects as defined in Sec. 7.1.3 are used. The SV0 tagger was also used for flavor-tagging, with a slightly modified weight cut at 5.85 in order to maintain an average tagging efficiency of 50% for b-quark jets in $t\bar{t}$ events.

8.1.4 Missing Transverse Energy

The missing transverse energy is calculated as described in Sec. 5.6 for the extended data sample, taking into account the changes for the aforementioned object candidates. In comparison with the first measurement also taus, photons, and soft jets, corrected at the EM scale, are taken into account in the missing transverse energy reconstruction.

8.2 Event Selection and Event Yields

The event selection was further optimized in comparison to the analysis of the $2.9\,\mathrm{pb}^{-1}$ data set presented in Chapter 7. The requirement on the missing transverse energy in the electron channel was tightened to $E_T^{\mathrm{miss}} > 35\,\mathrm{GeV}$ to further suppress the background contribution from QCD multijet events. Further rejection was achieved by replacing the triangular cut by a requirements on the transverse mass of the reconstructed W boson candidate: $m_T(W) > 25\,\mathrm{GeV}$. For the muon channel the same requirements on the missing transverse energy as in the analysis with $2.9\,\mathrm{pb}^{-1}$ (see Sec. 7.2.1) were used. In summary, the following event selection requirements were made:

- exactly one (no) electron candidate and no (exactly one) muon candidate for the electron channel (muon channel). The selected candidate has to match the corresponding trigger object;
- a missing transverse energy of $E_T^{\mathrm{miss}} > 35\,\mathrm{GeV}$ ($E_T^{\mathrm{miss}} > 20\,\mathrm{GeV}$) for the electron (muon) channel;
- a transverse mass of the W boson candidates of $m_T(W) > 25\,\mathrm{GeV}$ and $m_T(W) > 60\,\mathrm{GeV} - E_T^{\mathrm{miss}}$ (triangular cut) for the electron and muon channel, respectively;
- the event contains either exactly three jets (three jets exclusive channel), exactly four jets (four jets exclusive channel), or at least five jets with $p_T > 25\,\mathrm{GeV}$ (five jets inclusive channel) within a pseudo rapidity of $|\eta| < 2.5$;
- exactly zero b-tagged jets, exactly one b-tagged jets, or at least two b-tagged jets;

Table 8.1: Scale factors for the b-tagging efficiency corresponding to the SV0 algorithm. [134].

p_T-range [GeV]	scale factor
20-25	0.872 ± 0.208
25-40	0.925 ± 0.105
40-60	0.942 ± 0.074
60-75	0.947 ± 0.102
75-90	0.947 ± 0.150
90-200	0.947 ± 0.200

representing a splitting of the data sample into 18 orthogonal channels, depending on lepton flavor, jet multiplicity or b-tagged jet multiplicity. Sec. 8.4.2 will discuss in detail the motivation for this channel breakdown.

The large available statistics and improved understanding of the data resulted in a more accurate determination of the data-to-MC scale factors.

The scale factor for reconstruction and identification of electrons was measured to be 1.000 ± 0.015, while the trigger scale factor was estimated as 0.995 ± 0.005. The uncertainties are statistical and an additional systematic uncertainty of 2% was taken into account. The η and E_T requirement on the cluster energy introduces a further correction between 0.9 and 0.99. For a detailed discussion see [132].

A correction of the electron energy scale was applied (not performed for the analysis with $2.9\,\mathrm{pb}^{-1}$): $E_{corr} = E/(1+\alpha)$, where the dimensionless parameter α varies between -0.02 and $+0.02$ as a function of η, in order to match the peak of the $Z \to e^+e^-$ invariant mass distribution between data and MC. In addition, a correction on the electron energy resolution was required in the MC, applied by over-smearing the electron energy in the simulation by an additional constant term of 1.1 (1.8) for $|\eta| < 1.4$ (> 1.4) [132].

The scale factor for the reconstruction and identification of muons was measured to be $0.997 \pm 0.001\,(\mathrm{stat.}) \pm 0.003\,(\mathrm{syst.})$ and $1.002 \pm 0.001\,(\mathrm{stat.}) \pm 0.001\,(\mathrm{syst.})$, respectively [132]. The scale factors for the muon trigger efficiency were parametrized in ϕ and η, varying between 0.92 and 1.0 with an uncertainty of around 1%. In the region $-0.5 < \eta < -0.4$ and $5\pi/16 < \pi < \pi/2$, a scale factor of 0.66 was applied. This is due to a lower trigger efficiency in data, caused by missing muon chambers in this region.

Corrections for the muon momentum scale and resolution were updated for the larger data set, taking into account different contributions from the Inner Detector and the Muon Spectrometer. For a detailed discussion see [133].

The scale factors for b-tagging efficiency are listed in Table 8.1. They

vary as a function of the jet transverse momentum, being about 0.9 for low p_T and 0.95 at high p_T.

The background contributions considered are the same as for the measurement with $2.9\,\mathrm{pb}^{-1}$ (see Chapter 7). The estimated fractions of $Wb\bar{b}$+jets and $Wc\bar{c}$+jets were scaled by a factor of 1.3, as determined in data using W+2-jet candidate events [135].

Applying the selection criteria and the corresponding scale factors yields the final sample used for the cross section measurement with the full 2010 data set. The yields, separated into the jet multiplicities, are listed for the electron channel in Table 8.2 (no b-tag), 8.3 (=1 b-tag), and 8.4 ($\geq$ 2 b-tags). The yields of the muon channel are shown in Table 8.5 (no b-tag), 8.6 (=1 b-tags), and 8.7 ($\geq$ 2 b-tags). A good agreement between the prediction from simulated MC events and data was observed. In the electron channel, with exactly three jets and exactly one tagged as a b quark jet, an upward fluctuation of the data was observed.

Also the distributions of kinematic variables show a good agreement between simulation and data. The distribution of the transverse mass of the W boson candidate, reconstructed from the corresponding lepton and the missing transverse energy, is drawn for the electron and muon channel in Fig. 8.1 and 8.2, respectively. In Appendix F the transverse momentum of the electron and the muon candidate for the electron and muon channel are shown in Fig. F.1 and F.2, respectively. Figure F.3 and F.4 show the distribution for the missing transverse energy in the electron and muon channel, respectively.

8.3 Systematic Uncertainties

Some of the systematics introduced for the evidence analysis in Sec. 7.6.1 changed as a result of new or more precise measurements in data from the increased available statistics, or the development of more refined prescriptions based on detailed MC studies. Here the main changes are summarized with respect to the systematic uncertainties discussed in Sec. 7.6.1.

The reconstruction and trigger efficiency for electrons and muons in MC simulation differs by 1.5% from data. For the identification a discrepancy of 3.5% was taken into account.

The uncertainty on the JES decreased in comparison to the study of $2.9\,\mathrm{pb}^{-1}$ by almost a factor of two (see Sec. 5.5.1). Uncertainties on the jet energy resolution and jet reconstruction efficiency were added. The jet reconstruction efficiency of the MC simulation agrees within 2% with the data, which is taken into account for as systematic uncertainty. This uncertainty was implemented by randomly rejecting 2% of the jets and re-doing the analysis. The resulting uncertainty was finally symmetrized. The jet energy resolution in MC is slightly better than that measured in data. A

Table 8.2: Selected events for the electron channel with no b-tagged jet. Only statistical uncertainties are shown, except for the QCD multijet background, where they are total uncertainties.

	= 2 jets	= 3 jets	= 4 jets	$\geq$ 5 jets
$t\bar{t}$	28.3 ± 0.4	42.1 ± 0.5	33.7 ± 0.5	22.8 ± 0.4
QCD	107.6 ± 61.0	51.2 ± 30.5	7.6 ± 5.9	4.5 ± 3.5
W+jets	2175.9 ± 8.7	529.4 ± 4.0	123.4 ± 1.8	34.3 ± 1.0
Z+jets	47.9 ± 2.1	24.9 ± 1.5	9.2 ± 0.9	4.3 ± 0.6
Single top	21.8 ± 0.3	9.6 ± 0.2	3.0 ± 0.1	1.0 ± 0.1
Dibosons	18.6 ± 0.2	5.6 ± 0.1	1.2 ± 0.0	0.2 ± 0.0
Total prediction	2400.2 ± 61.6	662.8 ± 30.8	178.2 ± 6.2	67.2 ± 3.7
Data	2449	621	182	58

Table 8.3: Selected events for the electron channel with one b-tagged jet. Only statistical uncertainties are shown, except for the QCD multijet background, where they are total uncertainties.

	= 2 jets	= 3 jets	= 4 jets	$\geq$ 5 jets
$t\bar{t}$	27.5 ± 0.4	56.3 ± 0.6	53.6 ± 0.6	37.5 ± 0.5
QCD	14.8 ± 7.6	10.5 ± 5.4	4.3 ± 2.5	2.5 ± 1.4
W+jets	68.9 ± 1.4	26.2 ± 0.8	8.5 ± 0.5	4.0 ± 0.3
Z+jets	1.1 ± 0.3	0.7 ± 0.3	0.7 ± 0.3	0.6 ± 0.2
Single top	18.8 ± 0.3	10.1 ± 0.2	3.5 ± 0.1	1.4 ± 0.1
Dibosons	1.1 ± 0.0	0.4 ± 0.0	0.1 ± 0.0	0.0 ± 0.0
Total prediction	132.2 ± 7.7	104.2 ± 5.6	70.7 ± 2.6	46.0 ± 1.5
Data	128	135	63	43

Table 8.4: Selected events for the electron channel with two or more b-tagged jet. Only statistical uncertainties are shown, except for the QCD multijet background, where they are total uncertainties.

	= 2 jets	= 3 jets	= 4 jets	$\geq$ 5 jets
$t\bar{t}$	5.7 ± 0.2	18.5 ± 0.3	22.5 ± 0.4	18.4 ± 0.3
QCD	0.3 ± 0.4	0.2 ± 0.3	0.8 ± 1.2	0.4 ± 0.4
W+jets	1.4 ± 0.2	1.3 ± 0.2	0.4 ± 0.1	1.1 ± 0.2
Z+jets	0.0 ± 0.0	0.1 ± 0.1	0.0 ± 0.0	0.0 ± 0.0
Single top	1.6 ± 0.1	1.7 ± 0.1	1.0 ± 0.1	0.5 ± 0.0
Dibosons	0.1 ± 0.0	0.0 ± 0.0	0.0 ± 0.0	0.0 ± 0.0
Total prediction	9.1 ± 0.6	21.8 ± 0.6	24.7 ± 1.3	20.4 ± 0.7
Data	6	38	24	25

Table 8.5: Selected events for the muon channel with no b-tagged jet. Only statistical uncertainties are shown, except for the QCD multijet background, where they are total uncertainties.

	= 2 jets	= 3 jets	= 4 jets	$\geq$ 5 jets
$t\bar{t}$	38.4 ± 0.5	59.3 ± 0.6	47.4 ± 0.6	30.5 ± 0.5
QCD	246.0 ± 12.4	97.2 ± 7.7	23.0 ± 3.9	15.3 ± 3.1
W+jets	4350.5 ± 12.3	969.1 ± 5.2	216.8 ± 2.4	56.7 ± 1.2
Z+jets	211.4 ± 4.5	58.1 ± 2.3	14.6 ± 1.2	4.8 ± 0.6
Single top	32.8 ± 0.4	14.0 ± 0.2	4.4 ± 0.1	1.3 ± 0.1
Dibosons	35.0 ± 0.2	9.5 ± 0.1	1.9 ± 0.1	0.4 ± 0.0
Total prediction	4914.2 ± 18.0	1207.1 ± 9.6	308.1 ± 4.8	109.0 ± 3.4
Data	4925	1131	302	105

Table 8.6: Selected events for the muon channel with one b-tagged jet. Only statistical uncertainties are shown, except for the QCD multijet background, where they are total uncertainties.

	= 2 jets	= 3 jets	= 4 jets	$\geq$ 5 jets
$t\bar{t}$	37.0 ± 0.5	76.9 ± 0.7	75.2 ± 0.7	53.3 ± 0.6
QCD	40.6 ± 4.2	23.8 ± 3.3	7.4 ± 1.5	3.7 ± 1.3
W+jets	129.8 ± 2.0	48.6 ± 1.1	16.2 ± 0.6	6.5 ± 0.4
Z+jets	5.4 ± 0.7	1.7 ± 0.4	0.9 ± 0.3	0.7 ± 0.2
Single top	28.1 ± 0.3	14.5 ± 0.2	5.0 ± 0.1	1.8 ± 0.1
Dibosons	1.9 ± 0.1	0.7 ± 0.0	0.2 ± 0.0	0.0 ± 0.0
Total prediction	242.9 ± 4.7	166.3 ± 3.6	104.9 ± 1.9	66.0 ± 1.5
Data	290	186	106	67

Table 8.7: Selected events for the muon channel with two or more b-tagged jet. Only statistical uncertainties are shown, except for the QCD multijet background, where they are total uncertainties.

	= 2 jets	= 3 jets	= 4 jets	$\geq$ 5 jets
$t\bar{t}$	7.2 ± 0.2	25.8 ± 0.4	32.6 ± 0.4	26.0 ± 0.4
QCD	0.8 ± 0.8	0.4 ± 0.9	1.3 ± 1.3	0.6 ± 0.6
W+jets	2.7 ± 0.3	2.4 ± 0.2	1.1 ± 0.2	1.1 ± 0.2
Z+jets	0.0 ± 0.0	0.1 ± 0.1	0.0 ± 0.0	0.1 ± 0.1
Single top	2.5 ± 0.1	2.7 ± 0.1	1.3 ± 0.1	0.7 ± 0.0
Dibosons	0.1 ± 0.0	0.1 ± 0.0	0.0 ± 0.0	0.0 ± 0.0
Total prediction	13.2 ± 0.9	31.5 ± 1.0	36.4 ± 1.5	28.5 ± 0.8
Data	14	39	40	33

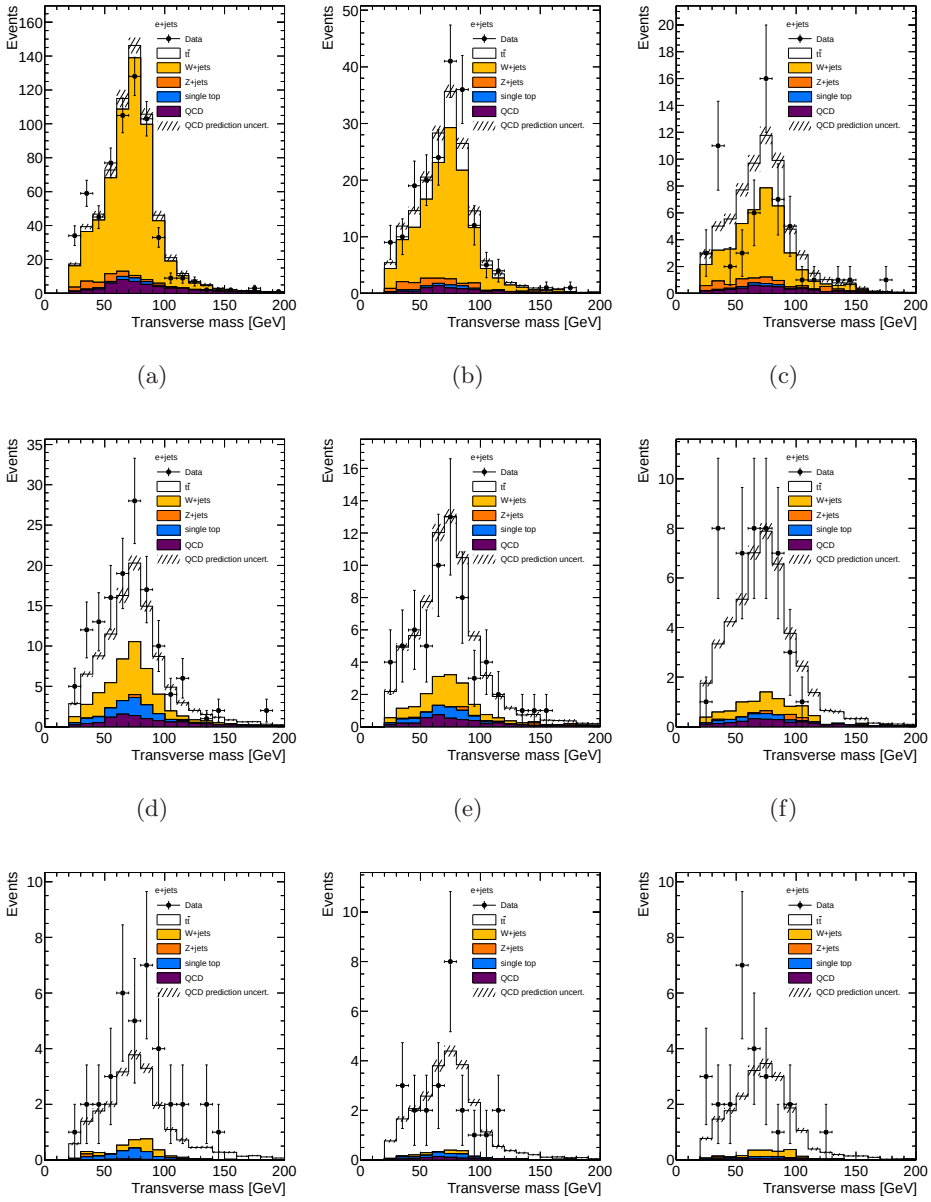

Figure 8.1: Transverse mass of the reconstructed W boson for the electron channel is shown, for (first row) no b-tagged jet, (second row) exactly one, and (last row) more than or equal two b-tagged jets. Different jet multiplicities are shown: (first column) three jets exclusive, (second column) four jets exclusive, and (last column) five jets inclusive. Uncertainties are statistical only for MC and include both statistical and systematic contributions for the QCD multijet background.

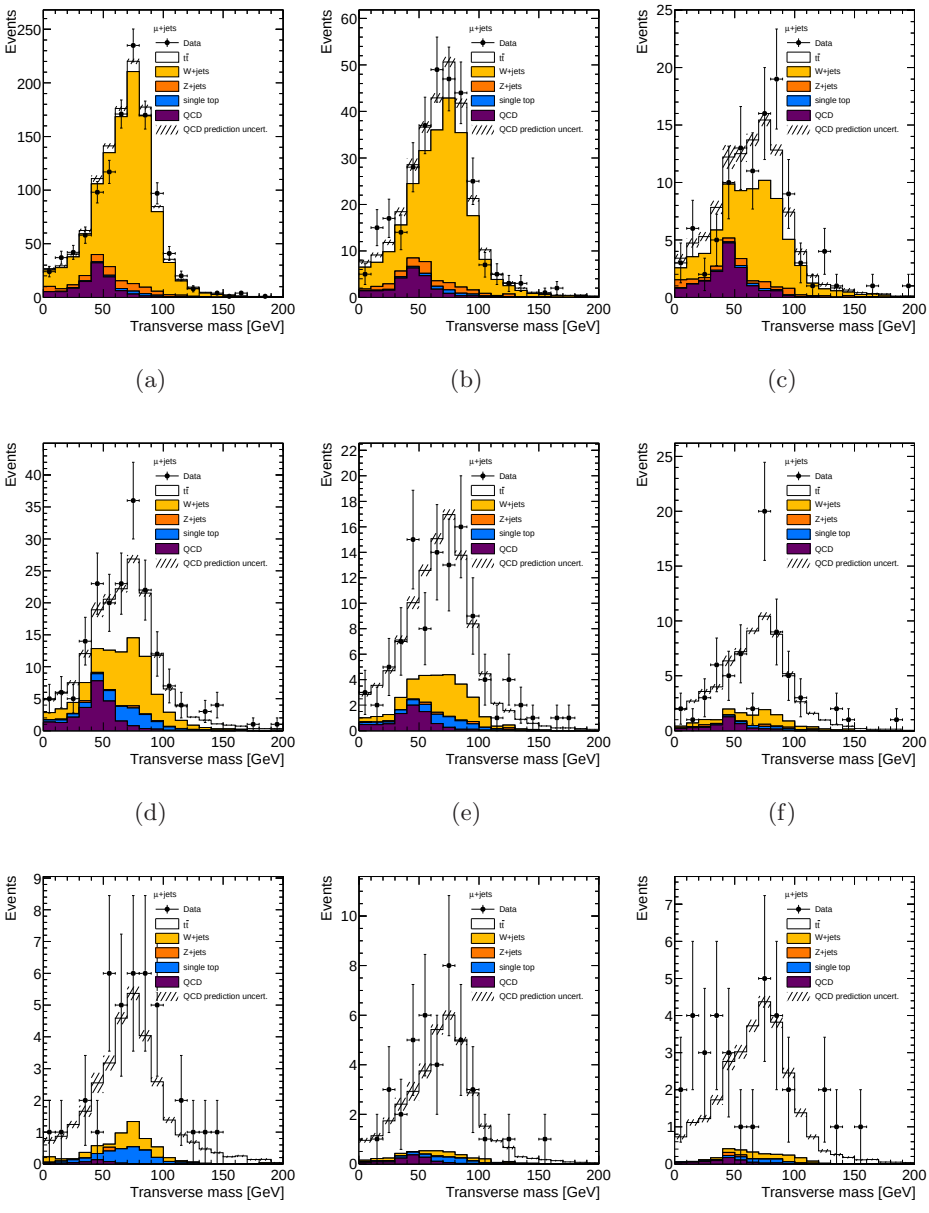

Figure 8.2: Transverse mass of the reconstructed W boson for the muon channel is shown, for (first row) no b-tagged jet, (second row) exactly one, and (last row) more than or equal two b-tagged jets. Different jet multiplicities are shown: (first column) three jets exclusive, (second column) four jets exclusive, and (last column) five jets inclusive. Uncertainties are statistical only for MCMC and include both statistical and systematic contributions for the QCD multijet background.

Table 8.8: Correlated uncertainties on the normalization of the QCD multijet background.

contribution	electron	muon
QCD normalization without b-tag	50%	30%
QCD normalization with b-tag	86%	40%

corresponding uncertainty was derived by comparing the result for the nominal MC with that after applying the required smearing of jet energies in the simulation to match the resolution in data. The resulting uncertainty was finally symmetrized. Details on the jet energy reconstruction for the complete 2010 data sample can be found in [107, 108].

Given the high statistics, the uncertainty in the QCD multijet background is dominated by the systematic uncertainty, which is treated as fully correlated between jet multiplicity bins. This correlated contribution distinguishes between the sample with and without b-tagged jets. The values are listed in Table 8.8.

Since the five jet inclusive bin was added in this analysis, an additional uncertainty on the ratio of 3-jet to 5-jet W+jets yields as predicted by ALPGEN was required, which was set to 48%, fully correlated with the existing 24% uncertainty on the ratio of 3-jet to 4-jet W+jets yields.

For the heavy flavor fraction in the W+jets background, an uncertainty of 50% for $Wb\bar{b}$+jets and $Wc\bar{c}$+jets, treated as fully correlated, and 40% for Wc+jets was estimated from data. Studies of the extrapolation to higher jet multiplicities with the ALPGEN yield an additional uncertainty. An uncertainty of 20% (40%, 60%) for the three jets exclusive (four jets exclusive, five jets inclusive) selection sample was applied, 100% correlated for $Wb\bar{b}$+jets and $Wc\bar{c}$+jets.

8.4 Profile Likelihood Fit

8.4.1 Method

In Sec. 7.6 the maximum likelihood fit was introduced. In the update of the $t\bar{t}$ cross section measurement with $35\,\mathrm{pb}^{-1}$ an improved method was used, including additional parameters (referred to as "nuisance parameters") to describe the effect of individual systematic uncertainties in the yields and shapes. A profile likelihood function was defined by introducing to the fit function in Eq. 7.28 a set of parameters $\vec{\alpha}$, one for each systematic uncertainty:

$$-2\ln\Big(L(k_{t\bar{t}}, k_{W+\mathrm{jets}}, \vec{s})\Big) \propto -2\sum_{i=0}^{N_{\mathrm{bins}}} n_i \ln(\mu_i) - \mu_i + \sum_{j=0}^{N_{\mathrm{syst}}} \alpha_j^2\,, \qquad (8.1)$$

where n_i stands for the measured data events in the bin i and μ_i for the total prediction. The latter is defined as

$$\mu_i = \sum_{\text{proc}} k_{\text{proc}} \cdot \mu_i^{\text{proc}} \left(1 + \sum_{j=1}^{N_{\text{syst}}} s_j^{\text{proc}} \right) , \tag{8.2}$$

with the first sum running over the number of processes ($t\bar{t}$, W+jets, QCD, or others) and the second sum runs over the number of systematic uncertainties (N_{syst}) considered. The factor $k_{t\bar{t}}$ ($k_{W+\text{jets}}$) multiplies the corresponding nominal cross sections of the $t\bar{t}$ signal (W+jets background). A scaling factor of one would correspond to the nominal Standard Model prediction of the corresponding cross section. The factors for the QCD multijet background and for other minor backgrounds were set to one. The scaling factors s_j^{proc} are defined for each of the j systematic uncertainties in terms of the nuisance parameters α_j as

$$s_j^{\text{proc}} = \alpha_j \left(\frac{f_j^{\text{proc,+}} - f_j^{\text{proc,-}}}{2} \right) + \alpha_j^2 \left(\frac{f_j^{\text{proc,+}} + f_j^{\text{proc,-}}}{2} \right) , \tag{8.3}$$

where $f_j^{\pm}$ correspond to the distributions varied by $\pm 1\sigma$ of the corresponding uncertainty j. This parametrization allows to include asymmetric systematic uncertainties while ensuring a continuous and differentiable function of the nuisance parameters, important for the numerical maximization of the likelihood.

The $-2 \ln L$ is minimized with respect to all parameters ($k_{t\bar{t}}$, $k_{W+\text{jets}}$, and $\vec{\alpha}$), where $k_{t\bar{t}}$ and $k_{W+\text{jets}}$ are free-floating parameters, while the nuisance parameters $\vec{\alpha}$ are subject to a Gaussian penalty term that constrain each of them to their a-priori uncertainties. In this formulation, the data can potentially exert further constraints on the magnitude of the systematic uncertainties, and reduce correspondingly their impact in the overall precision of the measurement. Additionally, the best fit to data may prefer a non-zero value for some nuisance parameters, representing modifications to the nominal model which may in some cases correct for existing biases (e.g. an upward fluctuation or systematic deviation in a correction efficiency as measured in a subsidiary control sample). Therefore, the fitted value of a nuisance parameter has the meaning of number of standard deviations from nominal preferred by the data, while its uncertainty is measured in units of the a-priori standard deviation for such uncertainty source. For example, a fitted nuisance parameter of $\alpha_j = -0.5 \pm 0.1$ should be interpreted as the data preferring a shift in the model corresponding to -0.5σ of the a-priori systematic uncertainty, and a reduction of the systematic uncertainty down to 10% of its original magnitude.

The 68% confidence level uncertainties on each of the parameters are obtained by varying the $-2 \ln L$ by ± 1 units. In the case of $k_{t\bar{t}}$ and $k_{W+\text{jets}}$,

the uncertainties returned by the fit include both statistical and systematic components. The uncertainty on the luminosity is considered separately.

Using the fitted parameters and their covariance matrix, it is possible to estimate the post-fit yields and their total uncertainties for all processes in each of the channels. This is done by generating random sets of ($k_{t\bar{t}}$, $k_{W+\text{jets}}$, $\vec{\alpha}$), modeled as Gaussians centered at the post-fit values and with uncertainties and correlations as given by their post-fit covariance matrix. The corresponding distributions of yields for each of the processes are computed as given by Eq. 8.2. The desired estimated post-fit yield and its uncertainty is given by the mean and standard deviation of each of such distributions.

8.4.2 Analysis Strategy

As compared to the previous measurement, in this measurement a further splitting of the data into jet multiplicity channels

- three jets exclusive;
- four jets exclusive;
- five jets inclusive;

and b-tagged jet multiplicity channels

- no b-tagged jet;
- exactly one b-tagged jet;
- at least two b-tagged jets;

was performed. Taking into account both, electron and muon channels, a total of 18 channels were combined in a global fit. This particular breakdown of the data was designed to maximize the sensitivity to particular systematic uncertainties, and thus the power of the data to constrain them.

The high jet multiplicity selection and the requirement of b-tagged jets enriches the number of $t\bar{t}$ events. This allows to be particularly sensitive to uncertainties on the $t\bar{t}$ modeling, e.g. the uncertainty on ISR and FSR, as well as fragmentation, since they affect the distribution of signal events as function of jet multiplicity, as demonstrated in Fig. 8.3. The uncertainties on the W+jets modeling can be better constrained at lower jet multiplicity and for events with no b-tagged jets, since these requirements yield a W+jets enriched sample. Also the uncertainty on the JES can be constrained due to the splitting into different jet multiplicities, since varying the jet energy of jets causes migrations in jet multiplicity. The choice of observable, three-jet mass, is also particularly sensitive to the JES owing to the accurately known value of the top quark mass. This is illustrated in Fig. 8.4.

In addition, the $t\bar{t}$ enriched sample obtained at high jet multiplicity allows to constrain b-tagging systematic uncertainties as, under the assumption that $B(t \to Wb) = 1$, the distribution of $t\bar{t}$ events in different b-tagged jet multiplicity bins is completely determined by the b-tagging efficiency (see Fig. 8.5). Similarly, uncertainties related to heavy flavor composition of W+jets can be constrained by examining the distribution of W+jets events as a function of b-tagged jet multiplicity bins at lower jet multiplicity.

8.5 Results

This section presents both expected and observed results for the measurement using an integrated luminosity of $35\,\mathrm{pb}^{-1}$, following the strategy outlined in Sec. 8.4.2.

8.5.1 Expected Performance of the Profile Likelihood Fit

The expected uncertainties on the measurement can be studied by performing a large number of pseudo-experiments, whereby the total signal-plus-background expectation (assuming $k_{t\bar{t}} = k_{W+\mathrm{jets}} = 1$ and $\vec{\alpha} = \vec{0}$) in each bin of the three-jet mass in the analyzed channels is fluctuated using Poisson statistics, and a fit to each pseudo-experiment is performed exactly as done in data. The same integrated luminosity as in the data was assumed. The means of the distributions of the fitted parameters can be used to verify the unbiasedness of the fit, and their RMS to estimate the uncertainties.

The mean values for $k_{t\bar{t}}$ and $k_{W+\mathrm{jets}}$ parameters and expected uncertainties from the combined fit to all channels yield

$$k_{t\bar{t}} = 1.02 \pm {}^{0.12}_{0.12}\,, \tag{8.4}$$

$$k_{W+\mathrm{jets}} = 0.98 \pm {}^{0.07}_{0.09}\,, \tag{8.5}$$

demonstrating the fit is unbiased and an overall precision of only 12% (excluding the uncertainty in the integrated luminosity) is expected for the measurement of the $t\bar{t}$ cross section. Figure 8.6 shows the distribution of the k-factor for the signal and the W+jets background from ensemble testing with 10,000 pseudo-experiments.

The expected results for the nuisance parameters with the profile likelihood fit are shown in Table 8.9. No significant bias on the nuisance parameters was observed within the statistical precision of the test. The expected uncertainty provides information about the constraining power of the data. Indeed, significant reductions in the uncertainties related to JES, b-tagging efficiency, $t\bar{t}$ modeling and W+jets modeling, are expected. For instance, the uncertainty on the JES is expected to be reduced down to 26% of the original uncertainty.

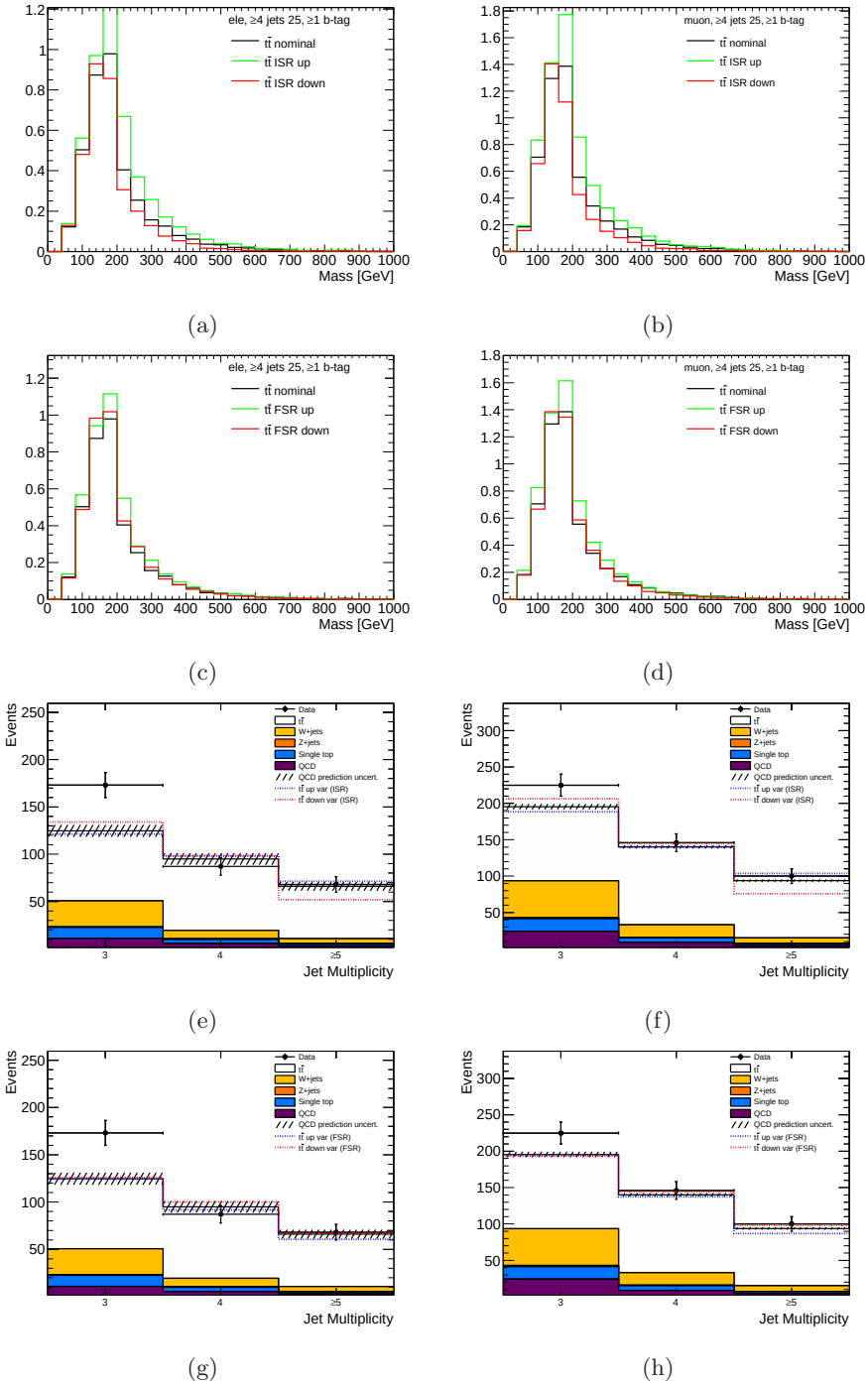

Figure 8.3: The invariant top mass distribution for the signal MC is shown for the up and down variation of (first row) ISR and (second row) FSR for at least four jets with at least one tagged as a b-jet. The electron channel is shown on the left, the muon channel on the right. Also shown is the distribution of the number of jets in the sample. Included are the one sigma variation for (third row) ISR, and (forth row) FSR.

Table 8.9: Expected results of the nuisance parameters fit from 200 pseudo-experiments. The fit was performed with the electron and muon channel in the =3-jet, =4-jet, ≥5-jet and zero-tag, =1-tag, ≥2-tag samples. The α correspond to the values of nuisance parameters that best fit the data and the $\Delta\alpha$ to the ranges covering the 68% confidence level.

Nuisance parameters	α	$\Delta\alpha$	
Object selection			
Jet energy scale	+0.03	+0.26	−0.26
Jet energy resolution	−0.10	+0.50	−0.42
Jet reco efficiency	−0.18	+1.03	−0.86
Lepton systematics	+0.03	+0.94	−0.93
BCtag	−0.07	+0.42	−0.39
Ltag	+0.02	+1.01	−1.01
Background rate			
QCDnorm corr e	+0.12	+0.87	−0.84
QCDnorm corr mu	−0.03	+0.89	−0.89
QCDnorm corr e btag	−0.02	+0.82	−0.77
QCDnorm corr mu btag	+0.00	+0.91	−0.88
$\sigma_{Z\text{jets}}$	+0.00	+1.03	−1.04
$\sigma_{\text{singleTop}}$	−0.01	+1.03	−1.03
Background modeling			
Berends scaling	−0.04	+0.33	−0.34
W+jets HFC meas	−0.01	+0.96	−0.95
W+jets HFQQ meas	−0.06	+0.76	−0.75
W+jets HFC theo	−0.02	+0.95	−0.93
W+jets HFQQ theo	+0.05	+0.82	−0.85
W+jets Sherpa	−0.04	+0.21	−0.22
W+jets iqopt2	−0.25	+0.95	−0.59
W+jets iqopt3	+0.01	+0.97	−0.96
QCD shape	+0.01	+0.77	−0.72
$t\bar{t}$ signal modeling			
ISR	−0.05	+0.31	−0.31
FSR	+0.04	+0.33	−0.33
Fragmentation	+0.01	+0.34	−0.37
NLO generator	+0.03	+0.40	−0.42

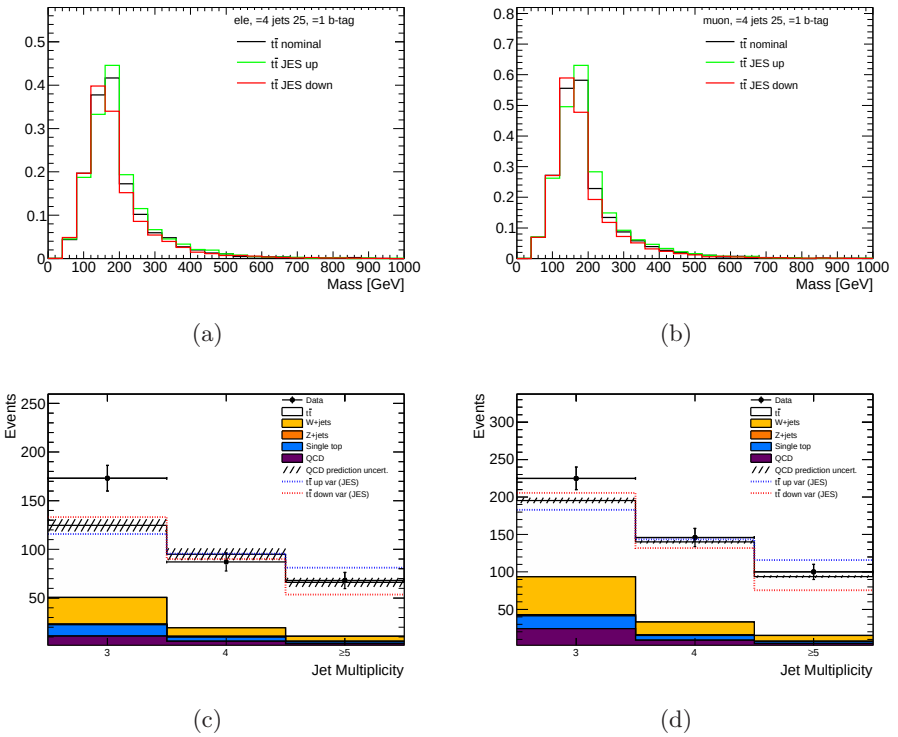

Figure 8.4: The invariant top mass distribution for the signal MC is shown for one sigma up and down variations of the JES uncertainty for (a) the electron and (b) the muon channel, with the selection of exactly four jets and exactly one b-tagged jet. The distribution of the number of jets in the sample with at least one b-tagged jet, including the one sigma variation for JES are shown for (c) the electron and (d) the muon channel.

In in Table. F.1 in Appendix F the correlation matrix for the nuisance parameters is shown. Strong anti-correlations (-0.64) between $k_{t\bar{t}}$ and the normalization of the QCD multijet background for the electron channel can be observed. The signal k-factor is also anti-correlated to the jet energy resolution (-0.17). The W+jets background is anti-correlated to the nuisance parameter for the uncertainty on heavy flavor tagging (-0.19) and the jet energy scale (-0.31). The uncertainty on the heavy flavor content of W+jets background estimated from the theory is correlated to the uncertainty on the normalization of the QCD multijet background (+0.45). The uncertainty on the light jet tagging efficiency is anti-correlated to the uncertainty on W+jets heavy flavor content from theory (-0.25), the W+jets normalization from SHERPA (-0.21) and the variations of the ALPGEN parameters, iqopt2 (+0.14) and iqopt3 (-0.21).

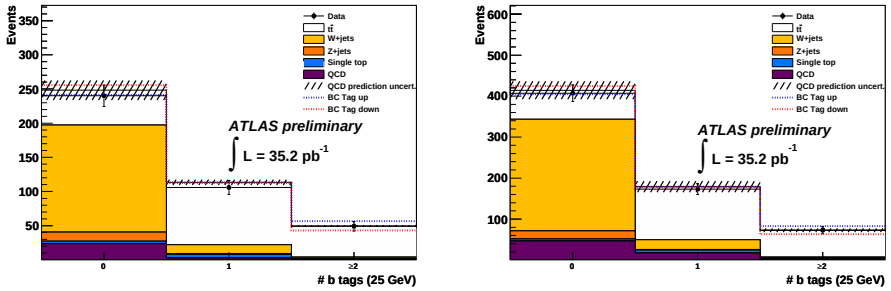

(a) (b)

Figure 8.5: The distribution of the number of b-tagged jets in the four jets inclusive sample, including the the one sigma variation for the b-tagging efficiency superimposed, for (a) the electron and (b) the muon channel [135].

Figure 8.7 shows further tests of the dependence of the expected results for the k-factors in presence of systematic shifts in the pseudo-data to verify that the nuisance parameters can actually absorb those effects leaving the k-factors unbiased. Figure 8.7 (a) and (b) show the dependence of the estimated $k_{t\bar{t}}$ as a function of injected biases on the JES and b-tagging efficiency. The largest bias observed is up to +4%, corresponding to shifts of $+1\sigma$ on the b-tagging efficiency with respect to the nominal value. Since the corresponding measured nuisance parameter in data will be only +0.8, the expected bias would be approximately 3%, much smaller than the overall expected precision on the measurement, and therefore no correction has been applied.

A similar study for $k_{W+\text{jets}}$ is shown in Fig. 8.7 (c) and (d). In this case a bias on the JES has an influence on the measured $k_{W+\text{jets}}$. This behavior is expected, since for the W+jets sample only changes of the shape due to the JES uncertainty were taken into account, and not of the acceptance, and thus by construction the measured $k_{W+\text{jets}}$ should include changes in the acceptance.

Figure 8.7 (e) and (f) demonstrate that different nuisance parameters yielding a-priori similar effects on the yields, can be disentangled by the fit giving the breakdown of channels used: the nuisance parameter for FSR is measured at the correct input value of zero in presence of biases to the JES in the pseudo-data. A similar conclusion is reached for the nuisance parameter describing the uncertainty on the $Wb\bar{b}$ and $Wc\bar{c}$ fractions with respect to biases on the b-tagging efficiency. This is in agreement with the expected correlations stated in the correlation matrix in Appendix F in Table F.1.

Also a linearity test for the two main sources of systematic uncertainty has been performed, in order to assure that the profile likelihood fit is able

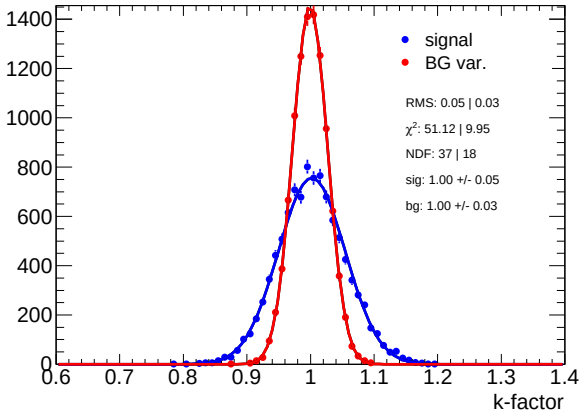

Figure 8.6: Distribution of the k-factors for the signal and W+jets background from ensemble testing with 10,000 pseudo-experiments for the combination of all channels.

to take possible shifts into account. Figure 8.8 (a) shows for the JES that the profile likelihood fit is able to take possible shifts of the systematics only with a small discrepancy into account. For the flavor tagging uncertainty a shift was observed, as shown in Fig. 8.8 (b). This small bias is responsible for the corresponding bias on $k_{t\bar{t}}$ shown in Figure 8.7 (b).

8.5.2 Cross Section Measurement

The results of the profile likelihood fit to all 18 channels, i.e. electron and muon data in the three jets exclusive, four jets exclusive, and five jets inclusive, as well as no, exactly one, and at least two b-tagged jets selection, are

$$k_{t\bar{t}} = 0.95^{+0.12}_{-0.11}\,, \tag{8.6}$$

$$k_{W+\text{jets}} = 1.04^{+0.08}_{-0.12}\,. \tag{8.7}$$

The stated uncertainties are the full combination of the statistical and the systematic uncertainties (not including the luminosity uncertainty). Correlations among the individual nuisance parameter uncertainties (see Table 8.10) have been taken into account for the results of the k-factors. The uncertainty on the luminosity is considered apart from this set of systematics and the contribution of the diboson cross-section and PDFs uncertainties to the total uncertainty were factorized and added in quadrature.

The results for the nuisance parameters are listed in Table 8.10. As explained earlier, the profile likelihood fit is able to restrict the systematic uncertainties using data. For the jet reconstruction efficiency data fa-

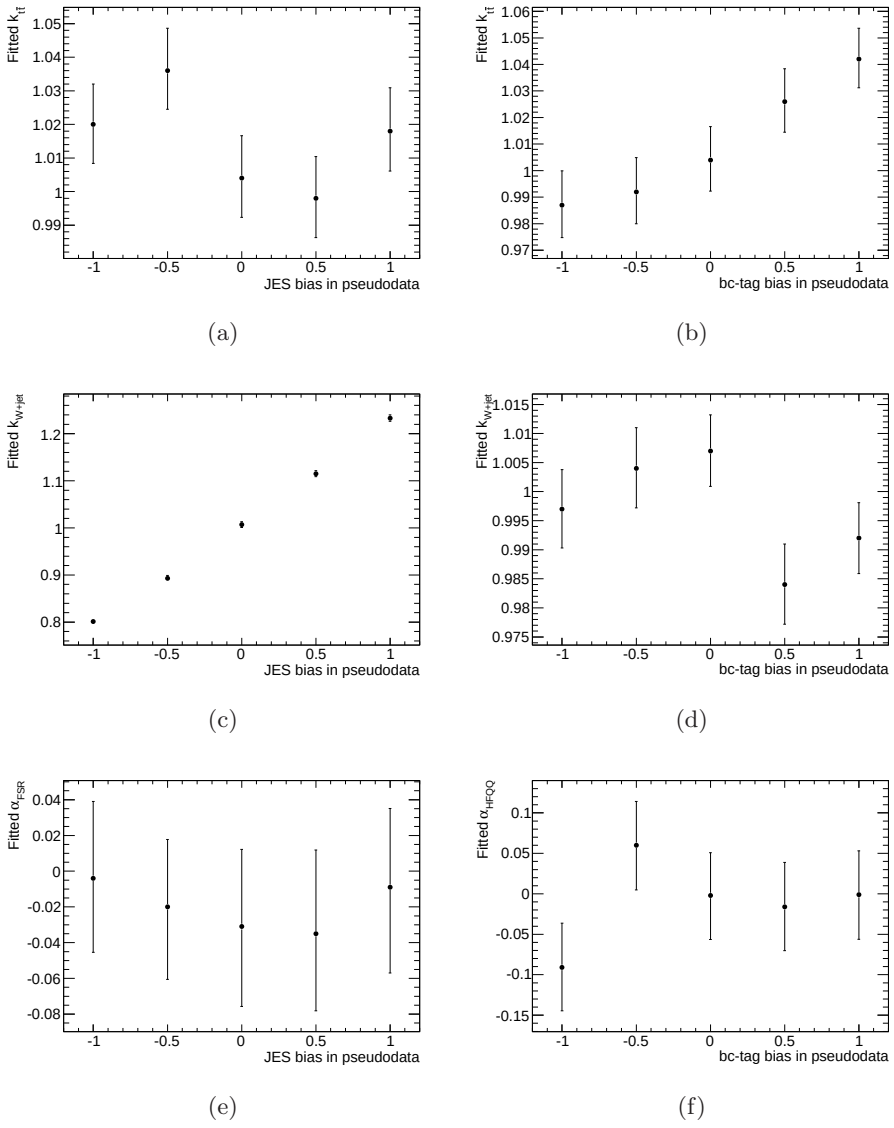

Figure 8.7: Cross checks of the profile likelihood fit. Correlation between main systematics and the fitted k-factors are shown (a-d). (e) and (f) show that the nuisance parameters for both are uncorrelated.

Table 8.10: Results of the nuisance parameters fit to electron and muon data in the =3-jet, =4-jet, ≥5-jet and zero-tag, =1-tag, ≥2-tag samples. The α correspond to the values of nuisance parameters that best fit the data and the $\Delta\alpha$ to the ranges covering the 68% confidence level.

Nuisance parameters	α	$\Delta\alpha$	
Object selection			
Jet energy scale	+0.62	+0.24	−0.31
Jet energy resolution	+0.00	+0.38	−0.38
Jet reco efficiency	−1.30	+0.47	−0.35
Lepton systematics	+0.41	+0.90	−0.90
BCtag	+0.80	+0.42	−0.40
Ltag	+0.28	+0.99	−1.00
Background rate			
QCDnorm ele	+0.26	+0.79	−0.78
QCDnorm muo	−0.04	+0.86	−0.86
QCDnorm ele corr btag	+0.57	+0.78	−0.76
QCDnorm muo corr btag	+0.07	+0.89	−0.87
$\sigma_{Z\text{jets}}$	+0.06	+1.00	−1.00
$\sigma_{\text{singleTop}}$	+0.24	+1.00	−1.00
Background modeling			
W+jets fraction (3 vs 4 jets)	−0.12	+0.34	−0.32
W+jets HFC measured	+0.23	+0.91	−0.92
W+jets HFQQ measured	+0.46	+0.72	−0.74
W+jets HFC theo.	+0.11	+0.83	−0.79
W+jets HFQQ theo.	−0.31	+0.79	−0.71
W+jets Sherpa	+0.36	+0.18	−0.18
W+jets iqopt2	+0.00	+0.48	−0.48
W+jets iqopt3	+0.00	+0.59	−0.59
QCD shape	−0.11	+0.64	−0.59
$t\bar{t}$ signal modeling			
ISR	−0.42	+0.29	−0.24
FSR	−0.60	+0.25	−0.32
Fragmentation	+0.39	+0.32	−0.31
NLO generator	−0.33	+0.40	−0.39

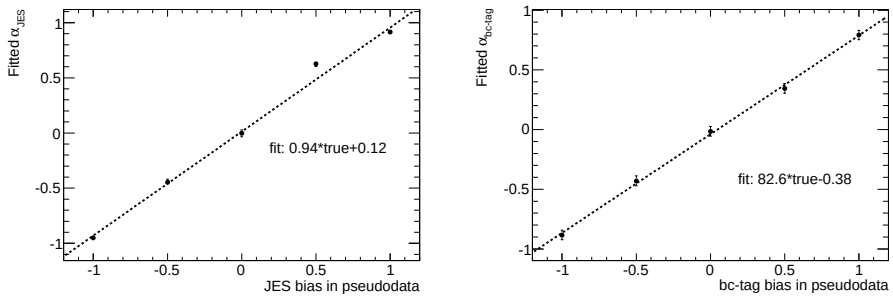

(a) (b)

Figure 8.8: The ability of the fit to take possible shifts of systematic into account is shown for (a) the JES and (b) the flavor tagging.

Table 8.11: Measured inclusive $t\bar{t}$ production cross section for the electron, muon, and the combination of both channels with $35\,\mathrm{pb}^{-1}$. The uncertainties represent the combination of the statistical together with the systematic uncertainties, and the uncertainty on the integrated luminosity.

Channel	Fitted cross section (pb)
electron	$193\ ^{+28}_{-27}\ ^{+7}_{-7}$
muon	$153\ ^{+26}_{-25}\ ^{+5}_{-5}$
electron and muon	$156\ ^{+20}_{-18}\ ^{+5}_{-5}$

vored an uncertainty of $1.3\,\sigma$ of the assumed value, with an uncertainty of $+0.47/-0.35\,\sigma$, in comparison to an expected constraining of only 0.18σ. No constraining was expected for the flavor tagging and the JES (see Sec. 8.5.1). The measurement clearly shows the constraining power of the data, since the nuisance parameter of $+0.62$ was estimated for JES, with only an uncertainty of around 0.3. Data preferred a larger uncertainty on flavor tagging of $0.8\,\sigma$, with an uncertainty of 50% on this value. Among the smaller contributions, the FSR contribution was constrained to $-0.6\,\sigma$ with an uncertainty of about 50%. For the other systematic uncertainties, which contribute significantly to the total uncertainty, the measured nuisance parameters are in agreement with the predicted uncertainty (see Sec. 8.5.3).

Multiplying the measured $k_{t\bar{t}}$ with the theoretical cross section used for the normalization of the signal sample results into the measured cross section. Table 8.11 shows the measured cross section for the top anti-top quark pair production at the ATLAS experiment with $35\,\mathrm{pb}^{-1}$. The estimated inclusive $t\bar{t}$ production cross section is given for the electron and muon channel

separately, as well as for the case of combining the electron and muon channel. In all three cases the three and four jet exclusive, and the five jet inclusive channel are combined, as well as the no b-tagged, exactly one, and at least two b-tagged jets selection. The full combination of the statistical and systematic uncertainties have been propagated as well.

The fitted cross section for the electron and muon channel differ because fitting the electron channel only the observed upward fluctuation in data (see Table 8.3) has a larger influence on the result. Furthermore, for the electron channel a different value for the JES is preferred. Both effects cause in the electron channel an increasing of the fitted $k_{t\bar{t}}$ and thus of the measured cross section, whereas combining both channels this effect is suppressed.

Table 8.12 shows the yields obtained with the procedure explained in Sec. 8.4.1 for the 18 channels analyzed in this measurement. The stated uncertainties are the combination of the systematic and statistic uncertainties, except luminosity. The yields are in agreement with those of the event selection presented in Sec. 8.4.1. The corresponding three-jet invariant mass distributions are shown in Figure 8.9 and 8.10 for the selected data in the electron and the muon channel, respectively, superimposed on the MC prediction for the simultaneous fit of the 18 channels. The resulting k-factors have been applied to the signal ($k_{t\bar{t}}$) and the $W+$jets background ($k_{W+\text{jets}}$). In all 18 channels a good agreement of data and the MC simulation is observed.

8.5.3 Comparison Between Measurements

The contributions of the individual uncertainties from the fit results were estimated as the difference in quadrature between the total uncertainty and the uncertainty obtained after having fixed the corresponding nuisance parameter to its fitted value. This allows to compare these results to the measurement with $2.9\,\text{pb}^{-1}$ obtained with the standard template fit as introduced in Sec. 7.6.

In this comparison the electron and muon channel have been combined and fitted for the three and four jets exclusive, together with five jets inclusive selection, for no b-tagged jet, exactly one b-tagged jet, and at least two b-tagged jets selection. Table 8.13 shows the results for the fit to the data corresponding to $35\,\text{pb}^{-1}$.

Table 8.14 shows the expected and measured k-factors for both analysis with the total uncertainties.

The total uncertainty on the $t\bar{t}$ cross section has been reduced by about a factor of three with respect to the measurement with $2.9\,\text{pb}^{-1}$. This is a major improvement given that with $2.9\,\text{pb}^{-1}$ the measurement had already comparable contributions from statistical and systematic uncertainties.

To understand the main reasons for the overall improvement it is useful to compare Table 7.15 and 8.13. On the one hand, it is observed an improve-

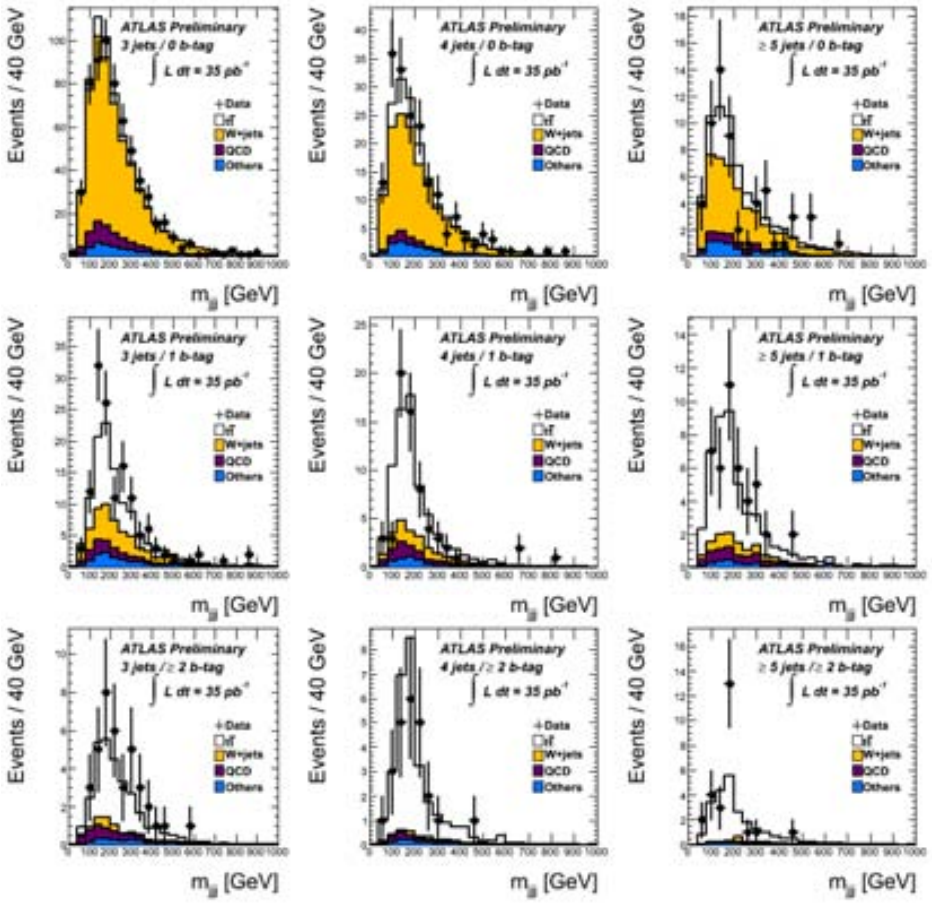

Figure 8.9: Invariant mass distribution, formed by the three jets with $p_T > 20\,\text{GeV}$ yielding the highest p_T vector sum for the electron channel: first row shows the no b-tag selection, the second the exactly one b-tag case, and the last the one with at least to b-tagged jets. The columns show from the left to the right the three jet exclusive, four jet exclusive, and the five jet inclusive selection [9].

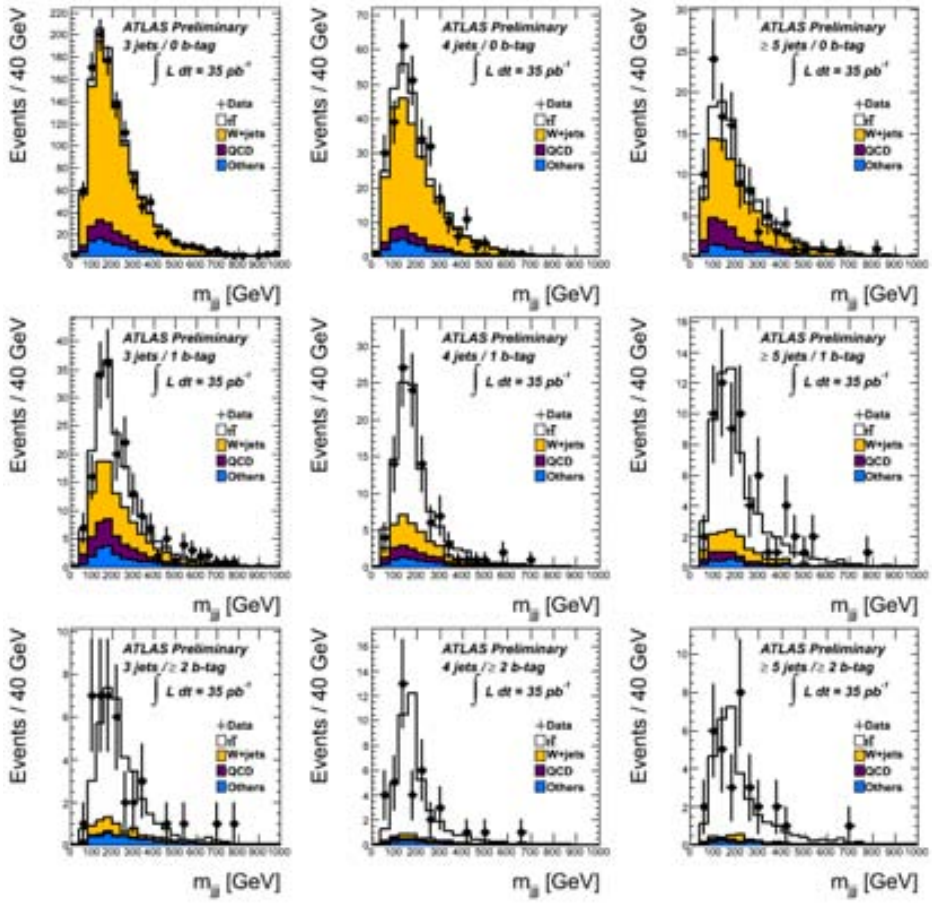

Figure 8.10: Invariant mass distribution, formed by the three jets with $p_T >$ 20 GeV yielding the highest p_T vector sum for the muon channel: first row shows the no b-tag selection, the second the exactly one b-tag case, and the last the one with at least to b-tagged jets. The columns show from the left to the right the three jet exclusive, four jet exclusive, and the five jet inclusive selection [9].

Table 8.12: Event yields measured with the profile likelihood fit for the 18 channels analyzed. The uncertainties are the combination of the systematic and statistic uncertainties, except luminosity.

	= 3 jets	= 4 jets	$\geq$ 5 jets
		electron channel	
		= 0 b-tagged jets	
$t\bar{t}$	36.3 ± 6.3	24.9 ± 4.3	17.2 ± 4.6
W+jets	493.9 ± 60.5	122.0 ± 18.9	36.6 ± 7.8
		= 1 b-tagged jets	
$t\bar{t}$	54.6 ± 7.8	49.1 ± 6.7	34.2 ± 6.9
W+jets	34.1 ± 8.3	11.8 ± 3.3	5.3 ± 1.8
		$\geq$ 2 b-tagged jets	
$t\bar{t}$	21.8 ± 3.8	25.9 ± 4.6	20.8 ± 4.2
W+jets	2.1 ± 0.7	0.8 ± 0.3	1.1 ± 0.4
		muon channel	
		= 0 b-tagged jets	
$t\bar{t}$	49.0 ± 7.8	37.5 ± 6.1	23.7 ± 6.9
W+jets	898.8 ± 110.3	210.3 ± 33.4	60.2 ± 13.1
		= 1 b-tagged jets	
$t\bar{t}$	74.8 ± 10.2	70.1 ± 9.0	48.7 ± 9.3
W+jets	64.6 ± 15.0	22.5 ± 5.8	8.8 ± 3.0
		$\geq$ 2 b-tagged jets	
$t\bar{t}$	30.3 ± 5.6	38.0 ± 6.5	29.2 ± 5.7
W+jets	3.9 ± 1.2	1.7 ± 0.8	1.3 ± 0.4

ment in the overall statistical precision beyond the expectation from luminosity scaling, mostly achieved through the larger number of channels used, which improved the overall sensitivity of the fit. In addition, the leading sources of systematic uncertainty in the $2.9\,\mathrm{pb}^{-1}$ measurements have been greatly reduced by using the constraining power of the data with $35\,\mathrm{pb}^{-1}$, leading to a reduction in the overall systematic uncertainty (excluding luminosity) of about a factor of 2.2. The uncertainty from JES and b-tagging have been reduced by a factor of 1.9 and 1.4, respectively. In addition, systematic uncertainties from $t\bar{t}$ modeling and background shape have been greatly reduced. Furthermore, the large uncertainty on the QCD normalization has been significantly reduced by an improved lepton identification and

Table 8.13: Results of the simultaneous fit of the electron and muon in the three jet exclusive sample, four jet exclusive, at least five jets and no b-tagged, exactly one, and at least two b-tagged jets. The contributions of the individual uncertainties from the fit results were estimated as the difference in quadrature between the total uncertainty and the uncertainty obtained after having fixed the corresponding nuisance parameter to its fitted value.

	$k_{t\bar{t}}$		$k_{W+\text{jets}}$	
k-factors	0.95		1.04	
Statistical Uncertainty (%)	+5.1	−5.0	+2.9	−2.8
Object selection				
Lepton Reco, ID, Trigger (%)	+1.9	−1.5	+1.9	−1.6
Jet energy scale (%)	+7.4	−5.5	+3.8	−4.5
b-tagging (%)	+8.5	−7.1	+1.4	−0.5
Backgrounds rate				
QCD normalization (%)	+4.0	−3.5	+3.1	−2.7
Other background normalization	+0.2	−0.6	+0.2	+0.5
Background modeling				
W+jets fraction (3 vs 4 jets) (%)	+2.7	−2.0	+0.9	−0.3
W+jets heavy flavor (%)	+5.4	−4.1	+0.9	−0.5
Background shape (%)	+1.2	+0.2	+1.1	−1.9
$t\bar{t}$ signal modeling				
ISR (%)	+2.3	−1.5	+1.0	−0.8
FSR (%)	+1.0	−0.2	+0.5	−0.0
PDF (%)	+1.7	−1.7	+1.7	−1.7
Fragmentation (%)	+1.2	−0.0	+0.5	−0.0
NLO generator (%)	+0.9	−0.0	+0.8	−0.3
Total Systematics (%)	+11.7	−10.6	+6.7	−10.9
Total Uncertainty (%)	+12.7	−11.7	+7.3	−11.4

Table 8.14: Comparison of the measured top quark pair production cross section with data corresponding to a luminosity of $2.9\,\mathrm{pb}^{-1}$ and $35\,\mathrm{pb}^{-1}$. Shown are the total uncertainties.

Analyzed luminosity	$k_{t\bar{t}}$	$k_{W+\mathrm{jets}}$
	expected	
$2.9\,\mathrm{pb}^{-1}$	$1.01\,^{+0.42}_{-0.39}$	$0.99\,^{+0.92}_{-0.89}$
$35\,\mathrm{pb}^{-1}$	$1.02\,^{+0.12}_{-0.12}$	$0.98\,^{+0.07}_{-0.09}$
	measured	
$2.9\,\mathrm{pb}^{-1}$	$0.79\,^{+0.44}_{-0.36}$	$1.03\,^{+0.96}_{-1.05}$
$35\,\mathrm{pb}^{-1}$	$0.95\,^{+0.12}_{-0.11}$	$1.04\,^{+0.08}_{-0.12}$

optimized event selection. Finally, a major improvement in the uncertainty on the integrated luminosity (reduced from 11% to 3.4%), was achieved.

8.6 Summary

The measurement was updated with a data sample corresponding to a luminosity of $35\,\mathrm{pb}^{-1}$, about one order of magnitude more than available for the analysis in Chapter 7, and the overall precision of the measurement was improved by about a factor of three relative to that with $2.9\,\mathrm{pb}^{-1}$.

Figure 8.11 shows a comparison with other measurements of the top quark pair production cross section in the semi-leptonic channel using flavor tagging at the ATLAS detector. The presented result is one of the most precise measurements and in good agreement with the other existing measurements in the same channel, as well as with the theoretical predictions. This result was recently released as preliminary result from the ATLAS collaboration [108].

The presented result is compatible and in a good agreement with the theoretical prediction as well as with other analysis performed in ATLAS.

Figure 8.12 compares results of from the Tevatron (DØ and CDF) and LHC (ATLAS and CMS) experiments. For the DØ experiment the results for the lepton plus jets final state [136] as well as the combined result are shown [137], as well as for the CDF experiment, [138] and [139] respectively. Also the result from the CMS collaboration was obtained in the lepton plus jets final state [140]. The presented measurement is in a good agreement with results from other experiments. The top quark pair production cross section was measured at center-of-mass energies much larger than

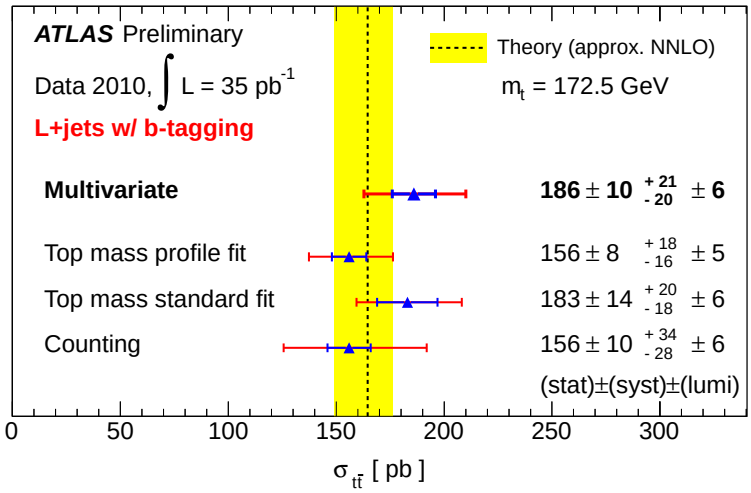

Figure 8.11: Summary of the top quark pair production cross-section measurements in the single-lepton channel with b-tagging using data corresponding to an integrated luminosity of $35\,\mathrm{pb}^{-1}$. Each measurement is quoted with its statistical, systematic and luminosity uncertainty. The yellow band corresponds to the theory uncertainty [41, 47, 48]. This study is stated as "Top mass profile fit" [108].

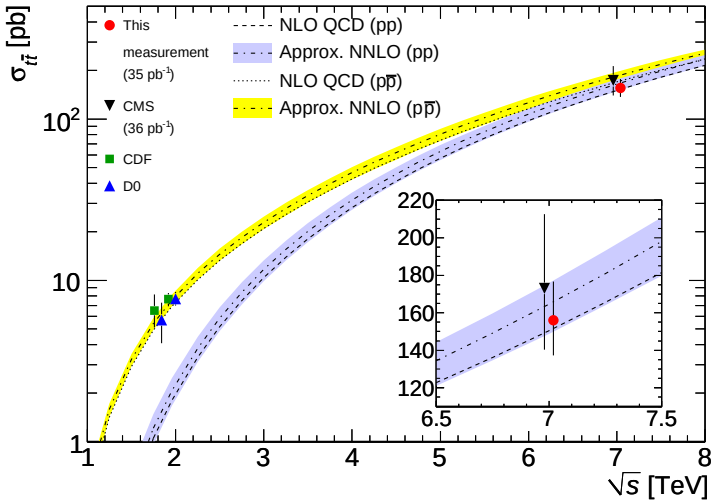

Figure 8.12: Results for the inclusive top quark production cross section from DØ [136, 137], CDF [138, 139], CMS [140], and the presented measurement for ATLAS [108]. The theory curves are taken from [76], assuming a top quark mass of 172.5 GeV, and take uncertainties on the PDF into account.

those achieved at the TEVATRON, yielding a very good agreement with the theoretical predictions.

Chapter 9

Summary and Prospects

The measurement of the top quark pair production cross section in proton-proton collisions at $\sqrt{s} = 7\,\text{TeV}$ with the ATLAS experiment was presented. Following a selection for top quark pair events decaying in the semi-leptonic channel, signal and background templates for the invariant mass of the hadronic top quark candidate were fitted to the data, taking into account systematic uncertainties. The electron and muon channel were analyzed, as well as their combination. In order to improve the precision of the measurement, the three jet exclusive and four jet inclusive selections were analyzed simultaneously and combined in the final result. Using data corresponding to an integrated luminosity of $2.9\,\text{pb}^{-1}$, the production cross section was measured to be

$$130 \pm 44\,(\text{stat.})\,^{+34}_{-28}\,(\text{syst.})\,^{+16}_{-13}\,(\text{lumi.})\,\text{pb}\,, \tag{9.1}$$

with comparable contributions from statistic and systematic uncertainties. The significance estimated for this measurement was 3.8 standard deviations, corresponding to evidence for top quark pair production in the semi-leptonic channel. This result has been published in the European Physical Journal C [9].

In an update of the measurement with the complete data collected in 2010, corresponding to a luminosity of $35\,\text{pb}^{-1}$, the cross section was measured with significantly higher accuracy. Following the intrinsic improvements in the object identification and event selection resulting from the larger data set, the analysis strategy was adjusted to respond to the demand of greater control of systematic uncertainties to achieve a precise measurement. The fitting method was enhanced to a profile likelihood fit, using nuisance parameters in order to allow data to restrict the contribution from systematic uncertainties. For the measurement the electron and muon channel have been analyzed in combination. Furthermore three jet selections (three jets exclusive, four jets exclusive, and five jets inclusive) and three flavor tagging sets (no b-tagged jets, exactly one b-tagged jets, and two or

more b-tagged jets) have been combined, resulting in

$$156\,^{+20}_{-18}\,(\text{stat.+syst.})\,^{+5}_{-5}\,(\text{lumi.})\,\text{pb}\,. \tag{9.2}$$

The measurement presented in this work is in good agreement with the theoretical prediction and other measurements performed at the ATLAS and the CMS experiment, and represents one of the most precise measurements from the LHC experiments with an integrated luminosity of $35\,\text{pb}^{-1}$.

Already after a short time of running the LHC, very promising results have been obtained with the early data. With the complete data collected in the year 2010, the precision of this measurement has reached the 10% level. This precision is comparable to the not precise single measurements at the TEVATRON experiments, achieved after a decade of running and detailed data analysis.

During 2011 and 2012 the per-beam energy of the LHC will remain at 3.5 TeV while the instantaneous luminosity will be increased steadily up to about $3 \cdot 10^{33}\,\text{cm}^{-2}\text{s}^{-1}$ [141]. The goal for 2011 is to deliver an integrated luminosity of about $3\,\text{fb}^{-1}$ to the experiments.

Already in Summer 2011 data corresponding to around $1\,\text{fb}^{-1}$ will be available. The technique developed in this measurement will allow to continue to exploit the large data sets to constrain the effect of systematic uncertainties and achieve unprecedented levels of precision in the cross section measurement. Indeed, preliminary results suggest that a precision on the $t\bar{t}$ cross section measurement in the semi-leptonic channel well below 5% can be achieved with about $0.7\,\text{fb}^{-1}$ of data. Achieving this milestone will required much more detailed studies on systematic uncertainties affecting the measurement, as well as refinements on the models used to parametrize their effects. This technique is expected to also be applicable to other measurements and searches, improving our ability to precisely test the Standard Model predictions and potentially discover new physics effects.

In view of the achievements in the early phase of the LHC, the coming years will be "[..] a very exciting time for particle physics" [142].

Appendix A

Parton Density Functions

Parton Density Functions (PDFs) account for the sub-structure of the colliding protons. At sufficient high energies the constituents of the proton can be resolved to gluons and so-called sea quarks, in addition to the valence quarks ($u\,u\,d$). The PDF $f_i(x, Q^2)$ gives the probability for the parton i to carry the fraction x of the four-momentum of the proton in a momentum transfer of Q^2. The factorization ansatz is used to predict the cross section for a partonic[1] sub-process $q_i q_j \to X$ (see Eq. 3.17). Therefore the short distance process, i.e. the partonic hard scatter cross section for this particular process, is folded with the long distance part, the PDF.

The PDFs can not be calculated by perturbative QCD, but have to be determined experimentally. Therefore structure functions are used, which are measured in deep-inelastic scattering (DIS) processes and are defined as

$$F_i(x, Q^2) = \sum_{a=q,g} C_{i,a} \otimes f_a(x, Q^2)\,. \tag{A.1}$$

$C_{i,a}$ is the so-called DIS coefficient function. The PDFs can be estimated by fitting the $F_i(x, Q^2)$ to data. Figure A.1 shows such fits of F_2 for the combined data of Hadron Elektron Ring Anlage (HERA) collected from 1994 until 2000 [143], as well as from BCDMS [144] and NMC [145].

Since electrons do not couple to gluons, the PDF for gluons can only be estimated at HERA from higher order corrections. The resulting large uncertainties at $x > 0.1$ are mainly constrained by measurements of the inclusive jet cross section with Run I data from the Tevatron.

In this measurement the PDF set CTEQ6 [75] from fits of the CTEQ collaboration was used. For the generation of the main backgrounds the CTEQ6L1 set was used. It uses LO formulas for the strong coupling $\alpha_s(Q)$ with $\Lambda^{4\,\text{flavor}}_{\text{QCD}} = 0.215\,\text{GeV}$ [78]. The generation of the signal process was performed using the PDF set CTEQ6.6, which uses NLO estimations for $\alpha_s(Q)$ and takes this higher-order effects into account.

[1] Here q_i denotes quarks and also gluons.

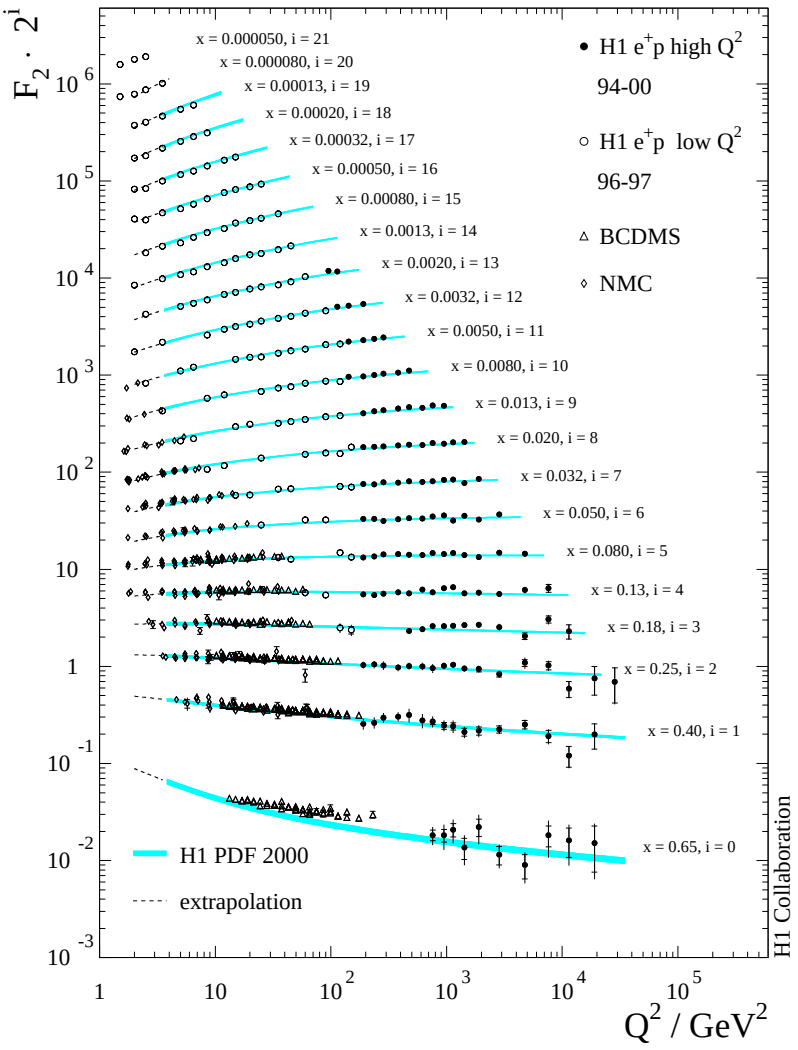

Figure A.1: The proton structure function F_2 is shown for the combined data from 1994 until 2000 of e^+p collisions at HERA. The error bands represent the corresponding Standard Model expectation determined from the H1 PDF 2000 fit. The dashed curves show the backward extrapolation of the fit to values below the minimum Q^2. Also shown are the F_2 data from BCDMS and NMC, which are not used in the fit. The error bars represent statistic and total errors [143].

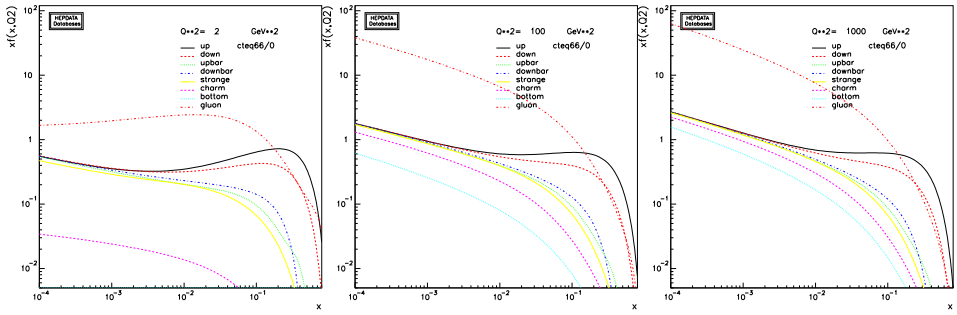

(a) (b) (c)

Figure A.2: CTEQ6.6 PDF for quarks and gluons as a function of x for (a) $Q^2 = 2\,\mathrm{GeV}$, (b) $Q^2 = 100\,\mathrm{GeV}$, and (c) $Q^2 = 1\,\mathrm{TeV}$ [146].

In the recent general purpose set CTEQ6.6, an independent strangeness parametrization was implemented, constrained by DIS data. Already in the former version (CTEQ6.5) heavy-quark effects in perturbative QCD have been included, which were improved to better agree with DIS heavy-flavor production data. Furthermore the x-range was extended towards lower values. CTEQ6.6 also yields a better agreement with measurements of the charm production at HERA. Further details are given in [75].

The PDF set CTEQ6.6M includes 44 eigenvectors corresponding to 22 uncertainties of the parton parameters, varied up and down. Additional two uncertainties with respect to CTEQ6.5M originate from the free strangeness parametrization. By comparing those variations the uncertainty contribution of the PDF set to the cross section measurement can be estimated [128, 129].

Figure A.2 shows the PDFs for quarks and gluons for different values of Q^2 for CTEQ6.6. The contribution form u and d quarks are dominant with respect to other quarks up to low values of x, while gluons prevail all quark contributions for $x < 0.15$.

Appendix B

Luminosity

Beside the center-of-mass energy, the instantaneous luminosity is an important property to characterize particle accelerators. As a simplification a Gaussian transverse beam profile can be assumed, such that the instantaneous luminosity can be written as

$$\mathcal{L}_{\text{inst}} = \frac{f\, B\, n_p^2}{4\pi\, \sigma_x\, \sigma_y}, \tag{B.1}$$

where f is the rotation frequency (at the LHC 11245.5 Hz) of the B colliding bunches, each consisting of n_p protons (about 10^{11}). The beam width σ_x (σ_y) in the x (y) direction at the LHC is about $60\,\mu$m [147].

In general the instantaneous luminosity is distinguished from the integrated luminosity. The instantaneous luminosity quantifies the number of collisions in a certain area per unit time, whereas the integrated luminosity

$$\mathcal{L}_{\text{int}} = \int_{t_i}^{t_e} \mathcal{L}_{\text{inst}}\; dt\,, \tag{B.2}$$

is commonly used to specify the amount of processes with a certain cross section recorded by the detector. In high energy physics the integrated luminosity is often referred to as just luminosity. This nomenclature is adapted in this document.

The instantaneous luminosity is measured in units of $\text{cm}^{-2}\text{s}^{-1}$. For the integrated luminosity the unit barn ($1\,\text{b} = 10^{-24}\,\text{cm}^{-2}$) was introduced, to have an easier handle of the large amounts of events collected in high energy experiments.

Appendix C

Monte Carlo Samples

This appendix presents the MC samples that have been used for the analysis. The process generator, cross section, number of generated events and corresponding integrated luminosity are shown. Table C.1 includes the $t\bar{t}$ signal and single top MC samples. Diboson processes are summarized in Table C.2. Table C.3 and C.4 present the W+jets samples. W+jets with heavy flavor jets samples are listed in Table C.5. For the Z+jets MC samples see Table C.6. Finally, Tables C.7 to C.10 show the QCD multijet MC samples.

Table C.1: Top-pair and single top MC samples used in this analysis.

Process	Generator	Section (pb)	Events	$\mathcal{L}\,(\mathrm{pb}^{-1})$
$t\bar{t}$ non-had	MC@NLO	89.023	773167	9661.8
$t\bar{t}$ non-had	POWHEG+HERWIG	89.406	199882	2235.7
$t\bar{t}$ non-had	POWHEG+PYTHIA	89.406	199838	2235.2
$t\bar{t}$ non-had ISR down	AcerMC+PYTHIA	89.092	199844	2243.1
$t\bar{t}$ non-had ISR up	AcerMC+PYTHIA	89.092	199829	2243.0
$t\bar{t}$ non-had FSR down	AcerMC+PYTHIA	89.092	199838	2243.1
$t\bar{t}$ non-had FSR up	AcerMC+PYTHIA	89.092	199811	2242.7
$t\bar{t}$ non-had ISR-FSR down	AcerMC+PYTHIA	89.092	199794	2242.6
$t\bar{t}$ non-had ISR-FSR up	AcerMC+PYTHIA	89.092	199885	2243.6
Wt-chan	MC@NLO	14.581	8856	607.4
t-chan (e)	MC@NLO	7.152	2966	414.7
t-chan (μ)	MC@NLO	7.176	5983	833.8
t-chan (τ)	MC@NLO	7.128	3030	425.1
s-chan (e)	MC@NLO	0.469	8424	17961.6
s-chan (μ)	MC@NLO	0.468	4254	9089.7
s-chan (τ)	MC@NLO	0.470	8480	18119.7

Table C.2: Diboson MC samples used in this analysis, generated with HERWIG.

Process	Cross Section (pb)	Events	$\mathcal{L}\,(\mathrm{pb}^{-1})$
WW	11.75	249837	21262.7
ZZ	0.977	249725	255603.9
WZ	3.432	249380	72663.2

Table C.3: W+jets MC samples used in this analysis, generated with ALPGEN+HERWIG.

Process	Cross Section (pb)	Events	$\mathcal{L}\,(\mathrm{pb}^{-1})$
$W(e\nu)$ + 0 jets	8434.23	1381931	163.8
$W(e\nu)$ + 1 jets	1577.46	258408	163.8
$W(e\nu)$ + 2 jets	460.06	188896	410.6
$W(e\nu)$ + 3 jets	123.10	50477	410.0
$W(e\nu)$ + 4 jets	30.87	12991	420.8
$W(e\nu)$ + 5 jets	8.42	3449	409.6
$W(\mu\nu)$ + 0 jets	8461.19	1386038	163.8
$W(\mu\nu)$ + 1 jets	1563.06	255909	163.7
$W(\mu\nu)$ + 2 jets	457.87	187860	410.3
$W(\mu\nu)$ + 3 jets	123.34	50887	412.6
$W(\mu\nu)$ + 4 jets	31.35	12991	414.4
$W(\mu\nu)$ + 5 jets	8.54	3498	409.6
$W(\tau\nu)$ + 0 jets	8339.67	1365491	163.7
$W(\tau\nu)$ + 1 jets	1557.70	254753	163.5
$W(\tau\nu)$ + 2 jets	459.45	188446	410.2
$W(\tau\nu)$ + 3 jets	123.98	50472	407.1
$W(\tau\nu)$ + 4 jets	31.35	12996	414.5
$W(\tau\nu)$ + 5 jets	8.54	3998	468.1

Table C.4: W+jets MC samples used in this analysis, generated with SHERPA.

Process	Cross Section (pb)	Events	$\mathcal{L}\,(\mathrm{pb}^{-1})$
$W(e\nu)$ + jets	10634.13	1998286	192.8
$W(\mu\nu)$ + jets	10645.35	1997537	187.6
$W(\tau\nu)$ + jets	10519.69	1998340	190.0

Table C.5: W+heavy flavor+jets MC samples used in this analysis, generated with ALPGEN+HERWIG.

Process	Cross Section (pb)	Events	$\mathcal{L}\,(\mathrm{pb}^{-1})$
$Wb\bar{b}$ + 0 jets	3.90	6499	1666.4
$Wb\bar{b}$ + 1 jets	3.17	5500	1735.0
$Wb\bar{b}$ + 2 jets	1.71	2997	1752.6
$Wb\bar{b}$ + 3 jets	0.73	1500	2054.8
$Wc\bar{c}$ + 0 jets	127.5	252558	1980.8
$Wc\bar{c}$ + 1 jets	103.2	206448	2000.1
$Wc\bar{c}$ + 2 jets	51.7	103477	2001.5
$Wc\bar{c}$ + 3 jets	16.9	33989	2011.2
Wc or $\bar{c}$ + 0 jets	431.3	862565	1999.9
Wc or $\bar{c}$ + 1 jets	160.1	320379	2001.1
Wc or $\bar{c}$ + 2 jets	42.5	84899	1997.6
Wc or $\bar{c}$ + 3 jets	9.9	19992	2019.4
Wc or $\bar{c}$ + 4 jets	2.3	4995	2171.6

Table C.6: Z+jets MC samples used in this analysis, generated with ALPGEN+HERWIG.

Process	Cross Section (pb)	Events	$\mathcal{L}\,(\mathrm{pb}^{-1})$
$Z(ee)$ + 0 jets	807.52	304216	376.7
$Z(ee)$ + 1 jets	162.63	63440	58.6
$Z(ee)$ + 2 jets	49.17	19497	396.5
$Z(ee)$ + 3 jets	13.66	5499	402.6
$Z(ee)$ + 4 jets	3.29	1499	455.6
$Z(ee)$ + 5 jets	0.98	500	510.2
$Z(\mu\mu)$ + 0 jets	802.39	303947	378.8
$Z(\mu\mu)$ + 1 jets	162.02	62996	388.8
$Z(\mu\mu)$ + 2 jets	48.31	18993	393.1
$Z(\mu\mu)$ + 3 jets	13.54	5497	406.0
$Z(\mu\mu)$ + 4 jets	3.42	1499	438.3
$Z(\mu\mu)$ + 5 jets	0.98	499	509.2
$Z(\tau\tau)$ + 0 jets	802.03	303359	378.2
$Z(\tau\tau)$ + 1 jets	158.60	63481	400.3
$Z(\tau\tau)$ + 2 jets	49.29	19492	395.5
$Z(\tau\tau)$ + 3 jets	13.42	5497	409.6
$Z(\tau\tau)$ + 4 jets	3.54	1499	423.4
$Z(\tau\tau)$ + 5 jets	0.85	499	587.1

Table C.7: Light-quark QCD multijet MC samples used in this analysis, generated with ALPGEN+HERWIG. The Jn refers to p_T slicing, with J3 at higher p_T than J2, etc. The muon filter requires one true muon with $p_T > 10\,\text{GeV}$ and $|\eta| < 2.8$. and a fourth with $p_T > 17\,\text{GeV}$.

Process	Cross Section (pb)	Events	$\mathcal{L}\,(\text{pb}^{-1})$
Muon filtered			
J1p2	28343.0	279895	9.88
J1p3	1008.0	10497	10.41
J2p2	27927.0	279895	10.02
J2p3	10660.9	86425	8.11
J2p4	1248.9	12500	10.01
J2p5	148.4	1500	10.11
J3p2	3004.2	29988	9.98
J3p3	3709.0	37483	10.11
J3p4	1224.9	12491	10.20
J3p5	359.1	3997	11.13
4 jets $p_T > 17\,\text{GeV}$ and 3 jets $p_T > 25\,\text{GeV}$ filtered			
J1p2	103065.0	1022910	9.92
J1p3	21247.0	212332	9.99
J2p2	72979.7	728709	9.99
J2p3	166732.3	1643429	9.86
J2p4	256204.9	2560009	9.99
J2p5	57103.6	571248	10.00
J3p2	10881.4	108952	10.01
J3p3	110727.1	1105688	9.99
J3p4	167584.0	1665908	9.94
J3p5	54371.7	543559	10.00

Table C.8: Light-quark QCD multijet MC samples used in this analysis, generated with ALPGEN+HERWIG. The Jn refers to p_T slicing, with J3 at higher p_T than J2, etc. These samples are unfiltered.

Process	Cross Section (pb)	Events	$\mathcal{L}\,(\mathrm{pb}^{-1})$
J4p2	12064.	120832	10.02
J4p3	24138.	240671	9.97
J4p4	17319.	173373	10.01
J4p5	7777.	77946	10.02
J4p6	3088.	30920	10.01
J5p2	269.	80843	300.53
J5p3	640.	192170	300.27
J5p4	625.	187681	300.29
J5p5	383.	114819	299.79
J5p6	217.	65384	301.31

Table C.9: QCD $b\bar{b}$ MC samples used in this analysis, generated with ALPGEN+HERWIG. The Jn refers to p_T slicing, with J3 at higher p_T than J2, etc. No filter was applied.

Process	Cross Section (pb)	Events	$\mathcal{L}(\mathrm{pb}^{-1})$
J4p0	66.4	1000	15.06
J4p1	443.1	4495	10.14
J4p2	553.6	5996	10.83
J4p3	370.9	3998	10.78
J4p4	228.6	2497	10.92
J5p0	1.3	500	384.62
J5p1	8.5	2995	352.35
J5p2	15.0	4990	332.67
J5p3	14.1	4491	318.51
J5p4	13.7	4491	327.81

Table C.10: QCD $b\bar{b}$ MC samples used in this analysis, generated with ALPGEN+HERWIG. The Jn refers to p_T slicing, with J3 at higher p_T than J2, etc.

Process	Cross Section (pb)	Events	$\mathcal{L}$(pb^{-1})
Muon filtered			
J1p0	13741.0	137975	10.04
J1p1	859.7	9000	10.47
J2p0	5071.0	50981	10.05
J2p1	4009.5	40441	10.09
J2p2	1105.9	11498	10.40
J2p3	230.6	2499	10.84
J2p4	43.4	500	11.52
J3p0	384.5	4000	10.40
J3p1	1162.3	11996	10.32
J3p2	658.2	6999	10.63
J3p3	231.1	2498	10.81
J3p4	86.6	1000	11.55
4 jets $p_T > 17$ GeV and 3 jets $p_T > 25$ GeV filtered			
J1p0	480.0	5499	11.46
J1p1	553.9	5997	10.83
J2p0	251.0	2999	11.95
J2p1	1865.7	18996	10.18
J2p2	7003.4	70471	10.06
J2p3	2734.1	27491	10.05
J2p4	692.3	6999	10.11
J3p0	40.2	499	12.41
J3p1	1510.3	15494	10.26
J3p2	4768.0	47978	10.06
J3p3	2483.1	24986	10.06
J3p4	952.1	9996	10.50

Appendix D

Expected Uncertainties

In this appendix a detailed split-up of the expected uncertainties is given for the object modeling (Table D.1), the background rate (see Table D.2), the background modeling (see Table D.3), and the signal modeling (Table D.4).

Table D.1: Expected uncertainties for the object modeling systematics. Bold numbers are the square sum of the indented split up.

Object selection	$k_{t\bar{t}}$		$k_{W+\text{jets}}$	
Lepton Reco, ID, Trigger (%)	**+2.08**	**-2.27**	**+2.21**	**-1.06**
elIdtrig (%)	+1.60	-1.70	+0.60	-0.30
muIdtrig (%)	+1.30	-1.40	+1.50	-1.00
ele offset (%)	+0.00	-0.40	+0.50	-0.00
ele smear (%)	+0.00	-0.40	+1.30	-0.00
mu offset (%)	+0.00	-0.00	+0.50	-0.20
mu smear (%)	+0.30	-0.00	+0.30	-0.00
Jet energy reconstruction (%)	**+13.89**	**-10.50**	**+21.80**	**-27.58**
Jet reconstruction efficiency(%)	+4.00	-0.00	+0.00	-6.10
Jet energy scale (%)	+13.30	-10.50	+21.80	-26.90
b tagging (%)	**+13.00**	**-8.50**	**+6.83**	**-5.55**
BCtag (%)	+13.00	-8.50	+6.80	-5.40
Ltag (%)	+0.10	-0.20	+0.60	-1.30

Table D.2: Expected uncertainties for the background rate systematics. Bold numbers are the square sum of the indented split up.

background rate	$k_{t\bar{t}}$		$k_{W+\text{jets}}$	
QCD normalization (%)	**+10.61**	**-9.54**	**+23.77**	**-21.56**
QCD corr ele (%)	+4.50	-4.30	+8.50	-6.50
QCD corr mu (%)	+0.50	-0.50	+5.40	-4.80
QCD uncorr ele3 (%)	+1.40	-1.70	+16.80	-14.00
QCD uncorr ele4 (%)	+9.40	-8.20	+11.50	-12.70
QCD uncorr mu3 (%)	+0.90	-1.10	+6.90	-6.40
QCD uncorr mu4 (%)	+1.00	-1.00	+1.10	-1.10
Other background normalization (%)	**+0.22**	**-0.22**	**+2.47**	**-2.31**
Xsect Zjets (%)	+0.20	-0.20	+0.90	-0.70
Xsect dibosons (%)	+0.00	-0.00	+0.10	-0.10
Xsect singleTop (%)	+0.10	-0.10	+2.30	-2.20

Table D.3: Expected uncertainties for the background modeling systematics. Bold numbers are the square sum of the indented split up.

background modeling	$k_{t\bar{t}}$		$k_{W+\text{jets}}$	
W+jets fraction (3 vs 4 jets) (%)	**+3.50**	**-3.40**	**+3.20**	**-4.00**
W+jets tag fraction (3 vs 4 jets) (%)	**+3.50**	**-3.40**	**+3.20**	**-4.00**
W+jets heavy flavor content	**+2.14**	**-0.76**	**+2.34**	**-6.51**
Wjets HFC (%)	+0.40	-0.30	+0.80	-1.20
Wjets HFQQ (%)	+2.10	-0.70	+2.20	-6.40
background shape (%)	**+7.34**	**-7.31**	**+23.78**	**-23.80**
QCD shape (%)	+0.80	-0.30	+1.70	-2.00
Wjets Sherpa (%)	+7.20	-7.20	+23.40	-23.40
Wjets iqopt2 (%)	+1.10	-1.10	+3.50	-3.50
Wjets iqopt3 (%)	+0.50	-0.50	+1.60	-1.60

Table D.4: Expected uncertainties for the $t\bar{t}$ signal modeling systematics.

$t\bar{t}$ signal modeling	$k_{t\bar{t}}$		$k_{W+\text{jets}}$	
ISR/FSR (%)	+9.85	-8.46	+13.60	-14.40
PDF (%)	+2.60	-2.40	+0.00	-0.00
Fragmentation (%)	+2.72	-2.72	+9.18	-9.18
NLO generator (%)	+3.70	-3.70	+15.40	-15.40

Appendix E

Measured Uncertainties

In this appendix a detailed split-up of the uncertainties measured with $2.9\,\mathrm{pb}^{-1}$ is given for the object modeling (Table E.1), the background rate (see Table E.2), the background modeling (see Table E.3), and the signal modeling (Table E.4).

Table E.1: Measured uncertainties for the object modeling systematics. Bold numbers are the square sum of the indented split up.

Object selection	$k_{t\bar{t}}$		k_{W+jets}	
Lepton Reco, ID, Trigger (%)	**+3.05**	**-2.67**	**+4.52**	**-5.36**
elIdtrig (%)	+2.50	-2.50	+2.40	-2.30
muIdtrig (%)	+0.40	-0.50	+3.20	-3.00
ele offset (%)	+1.60	-0.00	+0.00	-3.40
ele smear (%)	+0.00	-0.70	+1.80	-0.00
mu offset (%)	+0.00	-0.40	+1.10	-0.00
mu smear (%)	+0.60	-0.00	+0.00	-1.70
Jet energy reconstruction (%)	**+29.15**	**-10.30**	**+13.90**	**-53.37**
Jet reconstruction efficiency(%)	+6.10	-0.00	+0.00	-9.60
Jet energy scale (%)	+28.50	-10.30	+13.90	-52.50
b tagging (%)	**+12.30**	**-6.91**	**+7.43**	**-10.14**
BCtag (%)	+12.30	-6.90	+7.30	-10.10
Ltag (%)	+0.10	-0.40	+1.40	-0.90

Table E.2: Measured uncertainties for the background rate systematics. Bold numbers are the square sum of the indented split up.

bkg rate	$k_{t\bar{t}}$		k_{W+jets}	
QCD norm (%)	**+12.38**	**-10.68**	**+21.25**	**-20.18**
QCDnorm corr ele (%)	+4.80	-4.40	+6.40	-4.90
QCDnorm corr mu (%)	+0.80	-0.80	+7.10	-6.80
QCDnorm uncorr ele3 (%)	+1.90	-2.40	+13.60	-11.30
QCDnorm uncorr ele4 (%)	+10.90	-9.00	+9.60	-11.40
QCDnorm uncorr mu3 (%)	+2.00	-2.00	+9.00	-8.80
QCDnorm uncorr mu4 (%)	+1.80	-1.80	+1.40	-1.40
Other bkg norm (%)	**+0.22**	**-0.22**	**+2.42**	**-2.42**
Xsect Zjets (%)	+0.20	-0.20	+1.00	-1.00
Xsect dibosons (%)	+0.00	-0.00	+0.10	-0.10
Xsect singleTop (%)	+0.10	-0.10	+2.20	-2.20

Table E.3: Measured uncertainties for the background modeling systematics. Bold numbers are the square sum of the indented split up.

bkg modeling	$k_{t\bar{t}}$		k_{W+jets}	
W+jets fraction (3 vs 4 jets) (%)	**+8.00**	**-8.80**	**+13.00**	**-12.90**
W+jets tag fraction (3 vs 4 jets) (%)	**+8.00**	**-8.80**	**+13.00**	**-12.90**
W+jets heavy flavor content	**+2.26**	**-1.50**	**+3.80**	**-5.03**
W+jets HFC (%)	+1.60	-1.50	+3.80	-3.80
W+jets HFQQ (%)	+1.60	-0.00	+0.00	-3.30
bkg shape (%)	**+14.98**	**-14.97**	**+36.47**	**-36.25**
QCD shape (%)	+0.50	-0.10	+4.00	-0.00
W+jets Sherpa (%)	+14.20	-14.20	+34.40	-34.40
W+jets iqopt2 (%)	+4.10	-4.10	+9.80	-9.80
W+jets iqopt3 (%)	+2.40	-2.40	+5.90	-5.90

Table E.4: Measured uncertainties for the $t\bar{t}$ signal modeling systematics.

$t\bar{t}$ signal modeling	$k_{t\bar{t}}$		k_{W+jets}	
ISR/FSR (%)	+13.33	-16.61	+21.21	-13.17
PDF (%)	+2.60	-2.40	+0.00	-0.00
Fragmentation (%)	+0.68	-1.95	+2.97	-0.00
NLO generator (%)	+3.30	-3.00	+2.80	-2.80

Appendix F

Control Plots and Correlation Matrix for Analysis with 35 pb^{-1}

In this appendix the distributions of the transverse momentum of the electron and muon candidate in the corresponding channel are shown in Fig. F.1 and F.2, respectively. Also the distribution of the missing transverse energy for the electron and muon channel is drawn in Fig. F.3 and F.4. The correlation matrix of the expected nuisance parameters from 200 pseudo experiments is listed in Table F.1.

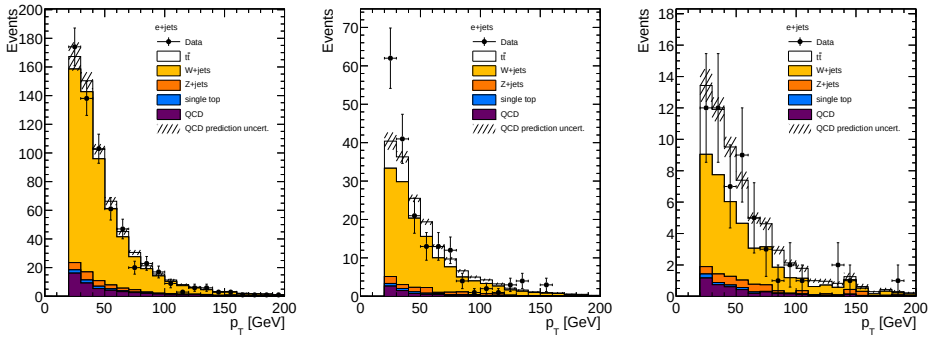

(a) (b) (c)

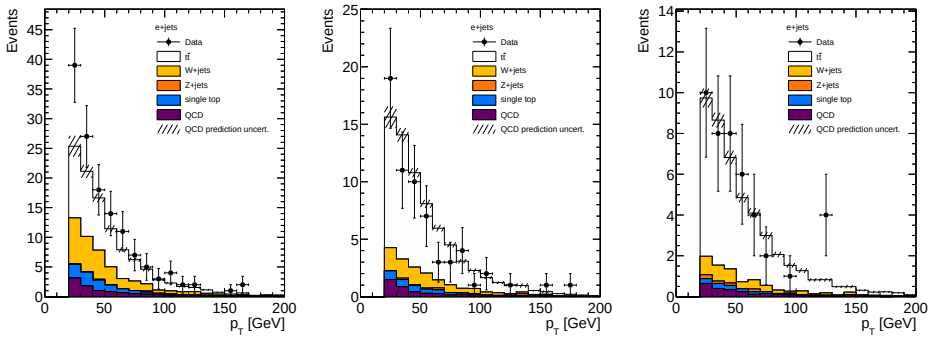

(d) (e) (f)

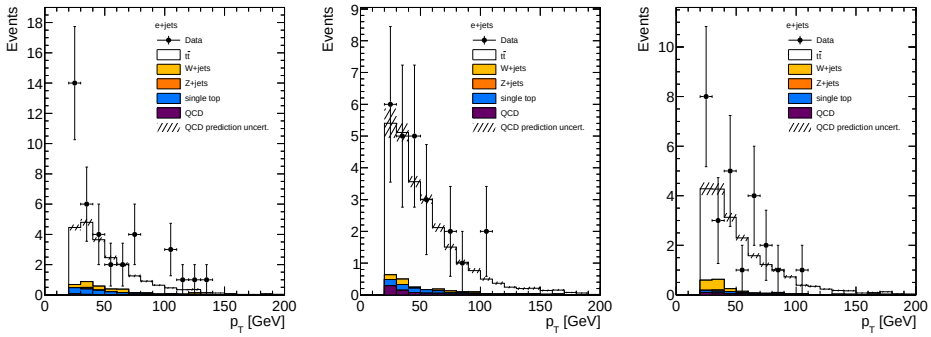

(g) (h) (i)

Figure F.1: Transverse momentum of the electron candidate in the electron channel is shown, for (first row) no b-tagged jet, (second row) exactly one, and (last row) more than or equal two b-tagged jets. Different jet multiplicities are shown: (first column) three jets exclusive, (second column) four jets exclusive, and (last column) five jets inclusive. Uncertainties are statistical only plus systematical for QCD multijet background.

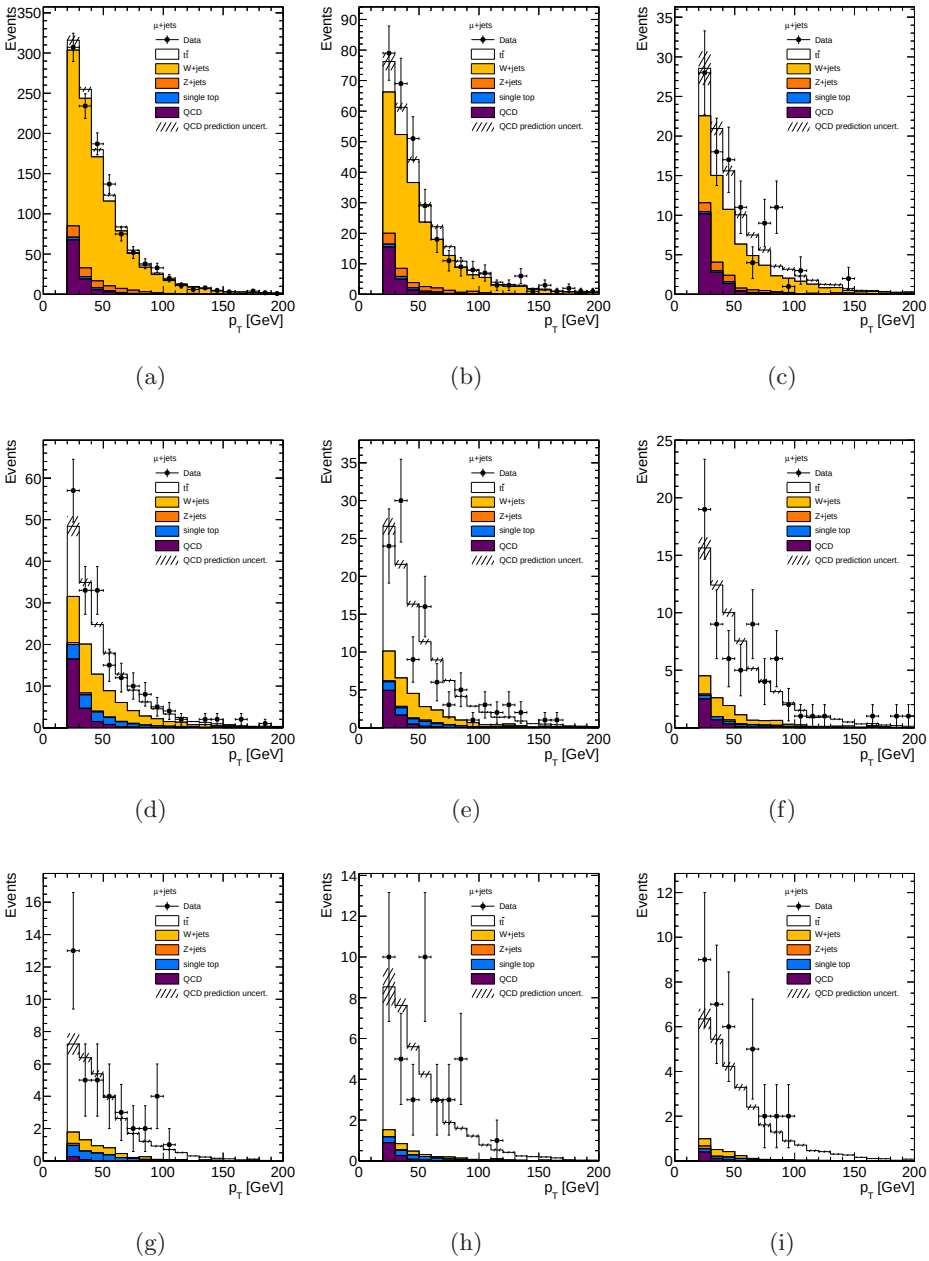

Figure F.2: Transverse momentum of the muon candidate in the muon channel is shown, for (first row) no b-tagged jet, (second row) exactly one, and (last row) more than or equal two b-tagged jets. Different jet multiplicities are shown: (first column) three jets exclusive, (second column) four jets exclusive, and (last column) five jets inclusive. Uncertainties are statistical only plus systematical for QCD multijet background.

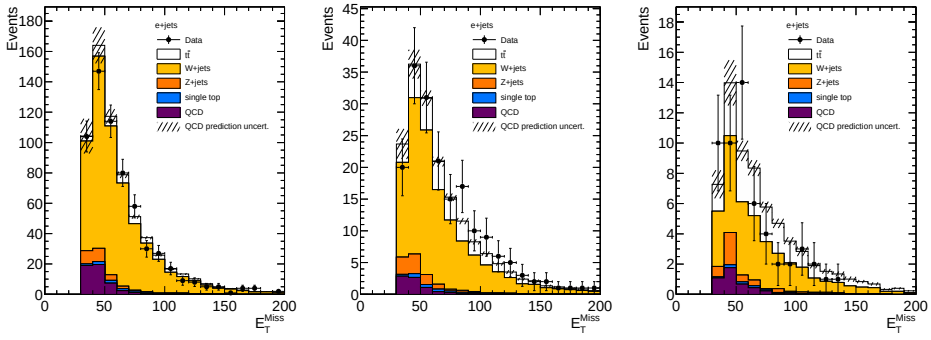

(a)

(b)

(c)

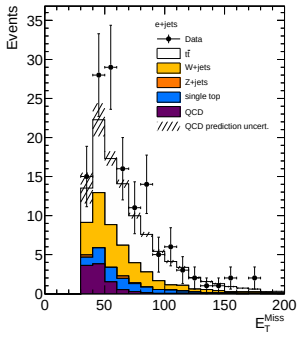

(d)

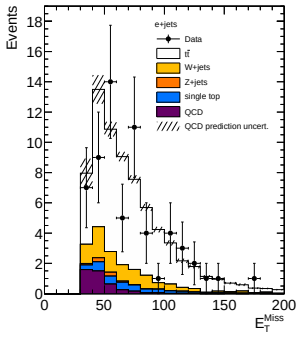

(e)

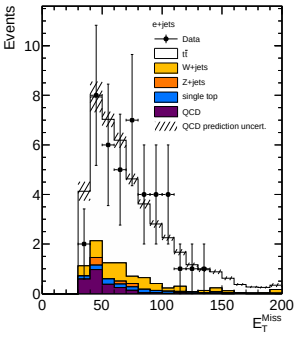

(f)

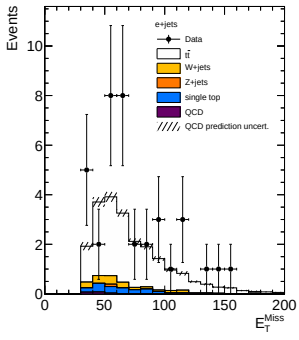

(g)

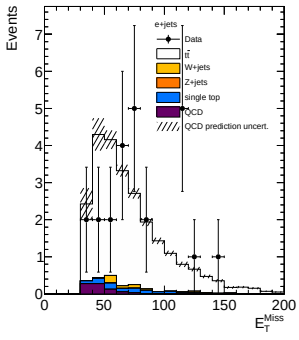

(h)

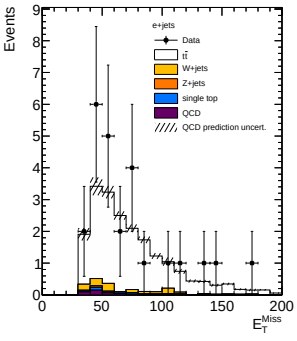

(i)

Figure F.3: Missing transverse energy of the electron channel is shown, for (first row) no b-tagged jet, (second row) exactly one, and (last row) more than or equal two b-tagged jets. Different jet multiplicities are shown: (first column) three jets exclusive, (second column) four jets exclusive, and (last column) five jets inclusive. Uncertainties are statistical only plus systematical for QCD multijet background.

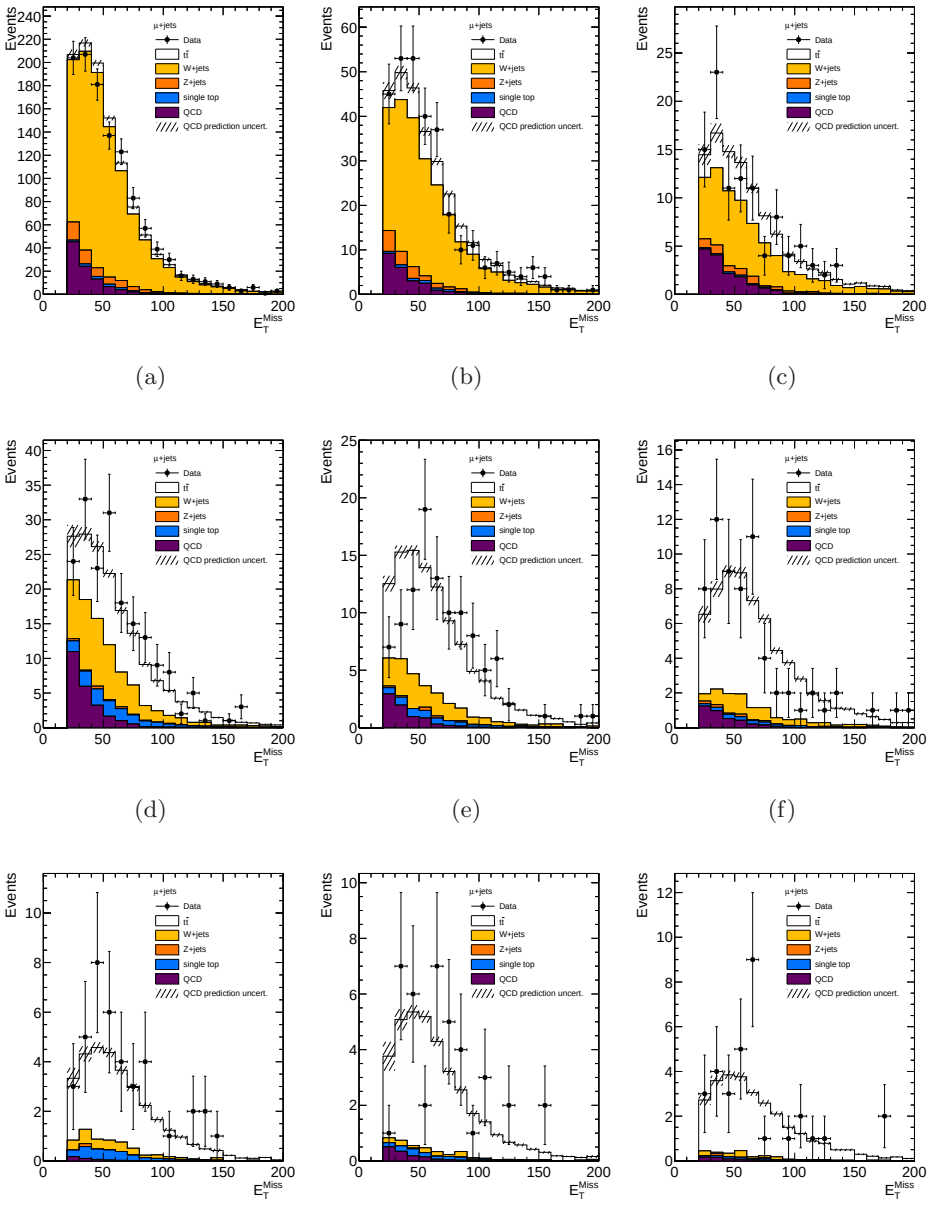

Figure F.4: Missing transverse energy of the muon channel is shown, for (first row) no b-tagged jet, (second row) exactly one, and (last row) more than or equal two b-tagged jets. Different jet multiplicities are shown: (first column) three jets exclusive, (second column) four jets exclusive, and (last column) five jets inclusive. Uncertainties are statistical only plus systematical for QCD multijet background.

Table F.1: Correlation Matrix for the profile likelihood fit for 200 pseudo experiments, each scaled corresponding to a luminosity of $35\,\mathrm{pb}^{-1}$. The row titles are symmetric to the column titles.

$k_{t\bar{t}}$	$k_{W+\mathrm{jets}}$	BCtag	jet energy resolution	jet energy scale	jet reconstruction efficiency	lepton systematics	light jet tag	QCDnorm corr ele	QCDnorm corr ele btag	QCDnorm corr mu	QCDnorm corr mu btag	QCDshape	Wjets Berends	Wjets HFC meas	Wjets HFC theo	Wjets HFQQ meas	Wjets HFQQ theo	Wjets Sherpa	Wjets iqopt2	Wjets iqopt3	cross section Zjets	cross section singleTop	ttbar FSR	ttbar fragmentation	ttbar ISR	ttbar NLO
+1.00	−0.06	−0.09	−0.17	−0.04	−0.13	−0.03	−0.19	−0.64	−0.04	−0.20	−0.06	−0.25	−0.06	−0.02	+0.00	−0.02	−0.43	−0.04	+0.11	+0.00	+0.03	−0.04	+0.04	−0.03	−0.00	−0.21
−0.06	+1.00	−0.19	+0.02	−0.31	−0.04	+0.03	+0.17	+0.17	+0.02	+0.05	+0.03	+0.07	+0.05	+0.02	−0.00	−0.04	+0.12	+0.07	−0.00	+0.11	−0.03	−0.06	+0.25	−0.03	−0.03	−0.26
−0.09	−0.19	+1.00	−0.11	+0.11	+0.05	−0.03	+0.05	+0.03	+0.00	+0.04	+0.00	−0.03	−0.05	−0.00	+0.00	−0.01	−0.02	−0.01	−0.00	−0.00	−0.01	−0.00	−0.01	−0.01	−0.01	−0.10
−0.17	+0.02	−0.11	+1.00	+0.03	+0.05	−0.02	+0.04	+0.02	−0.02	−0.03	−0.02	−0.06	−0.03	+0.00	−0.00	+0.00	+0.03	+0.01	+0.01	−0.01	−0.02	+0.01	+0.00	−0.02	+0.00	−0.07
−0.04	−0.31	+0.11	+0.03	+1.00	−0.10	−0.03	−0.11	−0.04	−0.00	+0.00	−0.01	−0.14	−0.01	+0.01	−0.00	−0.01	−0.07	+0.02	−0.03	−0.00	+0.02	+0.01	+0.01	−0.01	−0.01	+0.12
−0.13	−0.04	+0.05	+0.05	−0.10	+1.00	−0.02	+0.04	+0.02	−0.03	−0.05	−0.04	−0.11	−0.06	−0.01	+0.00	−0.01	+0.01	+0.00	−0.02	+0.01	−0.01	+0.01	−0.01	−0.02	−0.00	+0.01
−0.03	+0.03	−0.03	−0.02	−0.03	−0.02	+1.00	−0.08	+0.02	+0.00	+0.03	−0.01	+0.03	−0.02	−0.03	−0.00	+0.02	+0.06	+0.07	−0.07	−0.00	+0.03	+0.00	−0.00	+0.00	+0.00	−0.01
−0.19	+0.17	+0.05	+0.04	−0.11	+0.04	−0.08	+1.00	+0.09	−0.00	−0.02	+0.02	+0.15	+0.05	−0.06	−0.00	+0.01	−0.25	−0.21	+0.14	−0.21	+0.04	−0.03	+0.04	+0.01	−0.01	+0.07
−0.64	+0.17	+0.03	+0.02	−0.04	+0.02	+0.02	+0.09	+1.00	−0.03	+0.07	+0.02	+0.01	+0.00	+0.01	+0.00	+0.01	+0.45	+0.05	+0.02	+0.03	−0.16	+0.00	−0.03	−0.01	+0.00	+0.07
−0.04	+0.02	+0.00	−0.02	−0.00	−0.03	+0.00	−0.00	−0.03	+1.00	−0.02	−0.01	−0.05	−0.03	−0.00	+0.00	+0.00	+0.02	−0.01	+0.01	−0.01	−0.00	+0.00	−0.00	−0.01	+0.00	+0.00
−0.20	+0.05	+0.04	−0.03	+0.00	−0.05	+0.03	−0.02	+0.07	−0.02	+1.00	+0.01	−0.25	−0.05	+0.02	+0.00	+0.01	+0.20	−0.02	+0.00	+0.00	−0.04	−0.00	−0.01	−0.01	+0.00	+0.02
−0.06	+0.03	+0.00	−0.02	−0.01	−0.04	−0.01	+0.02	+0.02	−0.01	+0.01	+1.00	−0.08	−0.05	−0.02	+0.00	+0.02	+0.04	+0.01	−0.00	+0.01	+0.00	−0.00	+0.00	−0.01	+0.00	−0.00
−0.25	+0.07	−0.03	−0.06	−0.14	−0.11	+0.03	+0.15	+0.01	−0.05	−0.25	−0.08	+1.00	−0.10	+0.02	−0.00	+0.01	+0.02	−0.02	+0.00	+0.05	−0.00	+0.02	−0.04	−0.03	+0.00	+0.04
−0.06	+0.05	−0.05	−0.03	−0.01	−0.06	−0.02	+0.05	+0.00	−0.03	−0.05	−0.05	−0.10	+1.00	−0.02	+0.00	+0.05	+0.01	+0.02	−0.01	+0.02	−0.00	+0.00	−0.01	−0.02	+0.00	−0.04
−0.02	+0.02	−0.00	+0.00	+0.01	−0.01	−0.03	−0.06	+0.01	−0.00	+0.02	−0.02	+0.02	−0.02	+1.00	−0.00	+0.09	+0.04	+0.03	−0.02	+0.01	+0.01	+0.01	+0.01	+0.00	+0.00	+0.00
+0.00	−0.00	+0.00	−0.00	−0.00	+0.00	−0.00	−0.00	+0.00	+0.00	+0.00	+0.00	−0.00	+0.00	−0.00	+1.00	+0.00	−0.00	−0.00	−0.00	−0.00	−0.00	+0.00	−0.00	+0.00	+0.00	−0.00
−0.02	−0.04	−0.01	+0.00	−0.01	−0.01	+0.02	+0.01	+0.01	+0.00	+0.01	+0.02	+0.01	+0.05	+0.09	+0.00	+1.00	+0.00	−0.02	+0.01	+0.02	+0.03	+0.00	−0.02	−0.00	−0.00	+0.01
−0.43	+0.12	−0.02	+0.03	−0.07	+0.01	+0.06	−0.25	+0.45	+0.02	+0.20	+0.04	+0.02	+0.01	+0.04	−0.00	+0.00	+1.00	+0.03	−0.10	+0.05	+0.01	−0.00	+0.03	−0.01	−0.01	−0.03
−0.04	+0.07	−0.01	+0.01	+0.02	+0.00	+0.07	−0.21	+0.05	−0.01	−0.02	+0.01	−0.02	+0.02	+0.03	−0.00	−0.02	+0.03	+1.00	+0.08	−0.15	+0.01	−0.01	+0.02	+0.00	+0.00	−0.03
+0.11	−0.00	−0.00	+0.01	−0.03	−0.02	−0.07	+0.14	+0.02	+0.01	+0.00	−0.00	+0.00	−0.01	−0.02	−0.00	+0.01	−0.10	+0.08	+1.00	+0.01	−0.01	−0.01	+0.01	+0.00	−0.00	+0.01
+0.00	+0.11	−0.00	−0.01	−0.00	+0.01	−0.00	−0.21	+0.03	−0.01	+0.00	+0.01	+0.05	+0.02	+0.01	−0.00	+0.02	+0.05	−0.15	+0.01	+1.00	+0.33	−0.00	+0.03	+0.01	+0.00	−0.01
+0.03	−0.03	−0.01	−0.02	+0.02	−0.01	+0.03	+0.04	−0.16	−0.00	−0.04	+0.00	−0.00	−0.00	+0.01	−0.00	+0.03	+0.01	+0.01	−0.01	+0.33	+1.00	+0.01	−0.00	−0.01	−0.00	−0.01
−0.04	−0.06	−0.00	+0.01	+0.01	+0.01	+0.00	−0.03	+0.00	+0.00	−0.00	−0.00	+0.02	+0.00	+0.01	+0.00	+0.00	−0.00	−0.01	−0.01	−0.00	+0.01	+1.00	−0.00	+0.00	−0.00	+0.01
+0.04	+0.25	−0.01	+0.00	+0.01	−0.01	−0.00	+0.04	−0.03	−0.00	−0.01	+0.00	−0.04	−0.01	+0.01	−0.00	−0.02	+0.03	+0.02	+0.01	+0.03	−0.00	−0.00	+1.00	−0.00	+0.00	−0.01
−0.03	−0.03	−0.01	−0.02	−0.01	−0.02	+0.00	+0.01	−0.01	−0.01	−0.01	−0.01	−0.03	−0.02	+0.00	+0.00	−0.00	−0.01	+0.00	+0.00	+0.01	−0.01	+0.00	−0.00	+1.00	−0.00	−0.01
−0.00	−0.03	−0.01	+0.00	−0.01	−0.00	+0.00	−0.01	+0.00	+0.00	+0.00	+0.00	+0.00	+0.00	+0.00	+0.00	−0.00	−0.01	+0.00	−0.00	+0.00	−0.00	−0.00	+0.00	−0.00	+1.00	−0.01
−0.21	−0.26	−0.10	−0.07	+0.12	+0.01	−0.01	+0.07	+0.07	+0.00	+0.02	−0.00	+0.04	−0.04	+0.00	−0.00	+0.01	−0.03	−0.03	+0.01	−0.01	−0.01	+0.01	−0.01	−0.01	−0.01	+1.00

Acronyms

ALFA	Absolute Luminosity For ATLAS
ALICE	A Large Ion Collider Experiment
AOD	analysis object data
ATLAS	A Toroidal LHC ApparatuS
BR	branching ratio
CERN	European Organization for Nuclear Research
CDF	Collider Detector at Fermilab
CKM	Cabibbo-Kobayashi-Maskawa
CMS	Compact Muon Solenoid
CSC	Cathode Strip Chamber
DAQ	Data Acquisition
DIS	deep-inelastic scattering
DQ	Data Quality
DESY	Deutsches Elektron Synchrotron
EF	Event Filter
EM	electromagnetic
EW	electroweak
FCal	Forward Calorimeter
FCNC	flavor changing neutral current
FSR	final state radiation
GEANT4	GEometry ANd Tracking 4

GIM	Glashow-Iliopoulos-Maiani
GRL	Good Runs List
HEC	Hadronic End-cap Calorimeter
HERA	Hadron Elektron Ring Anlage
HLT	High Level Trigger
ISR	initial state radiation
JES	jet energy scale
L1	Level 1
L2	Level 2
LAr	Liquid Argon
LEAR	Low Energy Antiproton Ring
LEIR	Low Energy Ion Ring
LEP	Large Electron-Positron Collider
LHC	Large Hadron Collider
LHCb	Large Hadron Collider beauty
LINAC2	Linear Accelerator 2
Lips	Lorentz invariant phase space
LIS	Laser Ion Source
LO	leading order
LUCID	LUminosity measurement using Cerenkov Integrating Detector
MC	Monte Carlo
MDT	Monitored Drift Tubes
MNS	Maki-Nakagawa-Sakata
MSSM	Minimal Supersymmetric extension of the Standard Model
NLO	next-to-leading order
NNLO	next-to-next-to-leading order
NLL	next-to-leading logarithm

NNLL	next-to-next-to-leading logarithm
PDF	Parton Density Function
POWHEG	Positive Weight Hardest Emission Generator
PS	Proton Synchrotron
PSB	Proton Synchrotron Booster
QCD	Quantum Chromo Dynamics
QED	Quantum Electro Dynamics
RDO	Raw Data Object
RFQ	Radio Frequency Quadrupole
RPC	Resistive Plate Chamber
ROD	Read-Out Driver
ROI	Region of Interest
SCT	Semiconductor Tracker
SLAC	Stanford Linear Accelerator Center
SPS	Super Proton Synchrotron
TDAQ	Trigger and Data Acquisition
TGC	Thin Gap Chamber
TileCal	Tile Calorimeter
TRF	Tag Rate Function
TRT	Transition Radiation Tracker
ZEUS	Zearch to Elucidate Underlying Symmetry
ZDC	Zero-Degree Calorimeter

Bibliography

[1] J. J. Thomson, Philosophical Magazine **44**, 293 (1897), Facsimile from Stephen Wright, Classical Scientific Papers, Physics (Mills and Boon, 1964).

[2] S. L. Glashow, Nucl. Phys. **22**, 579 (1961).

[3] S. Weinberg, Phys. Rev. Lett. **19**, 1264 (1967).

[4] A. Salam, Nobel Symposium Stockholm; Almquvist and Wiksell , 367 (1968).

[5] S. W. Herb *et al.*, Physical Review Letters **39**, 252 (1977).

[6] The ALEPH Collaboration, The DELPHI Collaboration, The L3 Collaboration, The OPAL Collaboration, and The SLD Collaboration, The LEP Electroweak Working Group and The SLD electroweak and Heavy Flavour Group, Physics Reports **427**, 257 (2006), arXiv:hep-ex/0509008v3.

[7] The CDF Collaboration, Physical Review Letters **74**, 2626 (1995), arXiv:hep-ex/9503002v2.

[8] The D0 Collaboration, Physical Review Letters **74**, 2632 (1995), arXiv:hep-ex/9503003v1.

[9] The ATLAS Collaboration, The European Physical Journal C **71**, 1 (2011), arXiv:1012.1792v2 [hep-ex].

[10] F. Halzen and A. D. Martin, *Quarks and Leptons: An Introductory Course in Modern Particle Physics* (Wiley, 1984).

[11] M. E. Peskin and D. V. Schroeder, *An Introduction To Quantum Field Theory* (Westview Press, 1995).

[12] P. Schmüser, *Feynman-Graphen und Eichtheorien für Experimentalphysiker* (Springer, 1995).

[13] C. Berger, *Elementarteilchenphysik: Von den Grundlagen zu den modernen Experimenten* (Springer, Berlin Heidelberg New York, 2008).

[14] V. D. Barger and R. J. Phillips, *Collider Physics: Revised Edition*, Upd sub ed. (Westview Press, 1996).

[15] LEP EWWG, LEP EWWG home page, `http://lepewwg.web.cern.ch/LEPEWWG/`, 2010.

[16] E. Noether and M. A. Tavel, Gott.Nachr. , 235 (1918), Gott.Nachr.1918:235-257,1918; Transp.Theory Statist.Phys.1:186-207,1971.

[17] K. Nakamura, J. Phys. G: Nucl. Part. Phys. 37 075021 (2010).

[18] BES Collaboration *et al.*, Physical Review Letters **88**, 101802 (2002).

[19] T. van Ritbergen and R. G. Stuart, Physical Review Letters **82**, 488 (1999).

[20] L. Chau and W. Keung, Physical Review Letters **53**, 1802 (1984).

[21] L. Wolfenstein, Physical Review Letters **51**, 1945 (1983).

[22] Super-Kamiokande Collaboration, Physics Review Letters **81**, 1562 (1998).

[23] C. Rubbia, Reviews of Modern Physics **57**, 699 (1985).

[24] P. Bagnaia *et al.*, Physics Letters B **129**, 130 (1983).

[25] A. S. Goldhaber and M. M. Nieto, Reviews of Modern Physics **82**, 939 (2010), arXiv:0809.1003v5 [hep-ph].

[26] The ALEPH Collaboration, The DELPHI Collaboration, The L3 Collaboration, The OPAL Collaboration, and The LEP Electroweak Working Group for Higgs Boson Searches, Physics Letters B **565**, 61 (2003), arXiv:0809.1003v5 [hep-ph].

[27] The CDF Collaboration, The D0 Collaboration, the Tevatron New Physics, and Higgs Working Group, arXiv:1007.4587v1 [hep-ex] (2010).

[28] V. C. Rubin and J. Ford, W. Kent, The Astrophysical Journal **159**, 379 (1970).

[29] K. Kodama *et al.*, Physics Letters B **504**, 218 (2001), arXiv:hep-ex/0012035v1.

[30] A. Djouadi, arXiv:hep-ph/0503172v2 (2005), Phys.Rept.457:1-216,2008.

[31] J. R. Incandela, A. Quadt, W. Wagner, and D. Wicke, Progress in Particle and Nuclear Physics **63**, 239 (2009), arXiv:0904.2499v3 [hep-ex].

[32] A. Sirlin, Physical Review D **22**, 971 (1980).

[33] The ALEPH Collaboration, The CDF Collaboration, The DO Collaboration, The DELPHI Collaboration, The L3 Collaboration, The OPAL Collaboration, The SLD Collaboration, The LEP Electroweak Working Group, The Tevatron Electroweak Working Group and The SLD electroweak heavy flavour groups, arXiv:0911.2604v2 [hep-ex] (2009), CERN-PH-EP/2009-023.

[34] Tevatron Electroweak Working Group, CDF, and D0 Collaborations, arXiv:1007.3178v1 [hep-ex] (2010), FERMILAB-TM-2466-E, TEVEWWG-TOP-2010-07, CDF-NOTE-10210, D0-NOTE-6090.

[35] C. Quigg, arXiv:0801.1345v3 [hep-ph] (2004), FERMILAB-Conf-04/049-T.

[36] C. Quigg, Physics Today **50**, 20 (1997), arXiv:hep-ph/9704332v1.

[37] M. Jezabek and J. H. Kühn, Nuclear Physics B **314**, 1 (1989).

[38] Tevatron Electroweak Working Group, for the CDF Collaboration, and the D0 Collaboration, arXiv:0908.2171v1 [hep-ex] (2009), FERMILAB-TM-2440-E.

[39] V. M. Abazov, Physics Review Letter **106**, 022001 (2011), arXiv:1009.5686v1 [hep-ex].

[40] The CDF Collaboration, arXiv:1006.4597v1 [hep-ex] (2010), Fermilab-Pub-10-207-E.

[41] U. Langenfeld, S. Moch, and P. Uwer, arXiv:0907.2527v1 [hep-ph] (2009).

[42] S. Moch, Journal of Physics G: Nuclear and Particle Physics **34**, 995 (2008), arXiv:0803.0457v2 [hep-ph].

[43] D. Chakraborty, J. Konigsberg, and D. Rainwater, Annual Review of Nuclear and Particle Science **53**, 301 (2003), arXiv:hep-ph/0303092v1.

[44] N. Kidonakis, E. Laenen, S. Moch, and R. Vogt, Physical Review D **64**, 114001 (2001).

[45] W. Bernreuther, A. Brandenburg, Z. G. Si, and P. Uwer, Nuclear Physics B **690**, 81 (2004), arXiv:hep-ph/0403035v1.

[46] R. Bonciani, S. Catani, M. L. Mangano, and P. Nason, Nuclear Physics B **529**, 424 (1998), arXiv:hep-ph/9801375v2.

[47] M. Beneke, M. Czakon, P. Falgari, A. Mitov, and C. Schwinn, arXiv:0911.5166v1 [hep-ph] (2009).

[48] S. Moch and P. Uwer, Physical Review D **78**, 034003 (2008), arXiv:0804.1476v2 [hep-ph].

[49] ATLAS Top Working Group, Top physics monte carlo page, `https://twiki.cern.ch/twiki/bin/view/AtlasProtected/TopMC`, 2010.

[50] S. Frixione, P. Nason, and B. R. Webber, Journal of High Energy Physics **2003**, 007 (2003), arXiv:hep-ph/0305252v2.

[51] S. Frixione and B. R. Webber, Journal of High Energy Physics **2002**, 029 (2002), arXiv:hep-ph/0204244v2.

[52] R. Schwienhorst, C. Yuan, C. Mueller, and Q. Cao, Physical Review D **83**, 034019 (2011), arXiv:1012.5132v1 [hep-ph].

[53] The CDF Collaboration, arXiv:1101.0034v1 [hep-ex] (2010), submitted to Physical Review D.

[54] P. Langacker, Reviews of Modern Physics **81**, 1199 (2009), arXiv:0801.1345v3 [hep-ph].

[55] The CDF Collaboration, Phys. Rev. Lett. **103**, 101803 (2009), arXiv:0907.1269v3 [hep-ex].

[56] The D0 Collaboration, **D0 Note 5882-CONF** (2009).

[57] G. Mahlon and S. J. Parke, Physical Review D **81**, 074024 (2010), arXiv:1001.3422v2 [hep-ph].

[58] G. Mahlon, arXiv:hep-ph/9811219v1 (1998).

[59] M. Beneke *et al.*, arXiv:hep-ph/0003033v1 (2000).

[60] R. Guedes, R. Santos, and M. Won, arXiv:1007.2992v1 [hep-ph] (2010), Talk presented at ICWS2010 / ILC2010.

[61] The D0 Collaboration, Physics Letters B **682**, 278 (2009), arXiv:0908.1811v2 [hep-ex].

[62] S. Catani, arXiv:hep-ph/0005233v1 (2000), CERN–TH/2000-073.

[63] F. A. Berends, H. Kuijf, B. Tausk, and W. T. Giele, Nuclear Physics B **357**, 32 (1991).

[64] T. Gleisberg *et al.*, Journal of High Energy Physics **2009**, 007 (2009), arXiv:0811.4622v1 [hep-ph].

[65] T. Sjostrand, S. Mrenna, and P. Skands, arXiv:hep-ph/0603175v2 (2006), JHEP 0605:026,2006.

[66] G. Marchesini *et al.*, Computer Physics Communications **67**, 465 (1992).

[67] T. Gleisberg *et al.*, Journal of High Energy Physics **2004**, 056 (2004), arXiv:hep-ph/0311263v1.

[68] H. Baer, F. E. Paige, S. D. Protopescu, and X. Tata, hep-ph/0312045 (2003).

[69] M. L. Mangano, F. Piccinini, A. D. Polosa, M. Moretti, and R. Pittau, Journal of High Energy Physics **2003**, 001 (2003), arXiv:hep-ph/0206293v2.

[70] B. P. Kersevan and E. Richter-Was, hep-ph/0405247 (2004).

[71] J. M. Butterworth, J. R. Forshaw, and M. H. Seymour, Zeitschrift für Physik C: Particles and Fields **72**, 637 (1996), arXiv:hep-ph/9601371v1.

[72] K. Assamagan *et al.*, ATLAS Note **ATL-SOFT-INT-2010-002** (2010).

[73] S. Catani, F. Krauss, B. R. Webber, and R. Kuhn, Journal of High Energy Physics **2001**, 063 (2001), arXiv:hep-ph/0109231v1.

[74] S. Frixione, P. Nason, and C. Oleari, Journal of High Energy Physics **2007**, 070 (2007), arXiv:0709.2092v1 [hep-ph].

[75] P. M. Nadolsky *et al.*, Physical Review D **78**, 013004 (2008), arXiv:0802.0007v3 [hep-ph].

[76] M. Aliev *et al.*, Computer Physics Communications **182**, 1034 (2011), arXiv:1007.1327v1 [hep-ph].

[77] S. Frixione, E. Laenen, P. Motylinski, C. White, and B. R. Webber, Journal of High Energy Physics **2008**, 029 (2008), arXiv:0805.3067v1 [hep-ph].

[78] J. Pumplin *et al.*, Journal of High Energy Physics **2002**, 012 (2002).

[79] S. Allwood-Spires *et al.*, ATLAS Note **ATL-PHYS-INT-2010-132** (2010).

[80] R. Gavin, Y. Li, F. Petriello, and S. Quackenbush, 1011.3540 (2010).

[81] J. M. Campbell and R. K. Ellis, Physical Review D **60**, 113006 (1999), arXiv:hep-ph/9905386v2.

[82] J. Caron, The LHC injection complex, `http://cdsweb.cern.ch/record/841568`, 1993.

[83] C. Hill and R. Scrivens, CERN hadron linacs, `http://linac2.home.cern.ch/linac2/default.htm`, 2008.

[84] J. Caron, Accelerators chain of CERN : operating and approved projects, 2001.

[85] K. Schindl, CERN – division PS – LHC-PS project, `http://ps-div.web.cern.ch/ps-div/LHC-PS/LHC-PS.html`, 1998.

[86] A. Rey, AB OP SPS operation presentation, `http://ab-dep-op-sps.web.cern.ch/ab-dep-op-sps/SPS_Presentation.htm`, 2010.

[87] J. Gillies, R. Jacobsson, and O. Lenz, LHC underground structure, `http://keyhole.web.cern.ch/keyhole/reception/lhc_underground.jpg`, 1997.

[88] X. Cid Vidal and R. Cid, Taking a closer look at LHC, `http://www.lhc-closer.es/php/index.php?i=1&s=3&p=1&e=0`, 2010.

[89] S. Gilardoni and C. Carli, Ions for LHC (I-LHC) home page, `http://project-i-lhc.web.cern.ch/project-i-lhc/Overview.htm`, 2007.

[90] The ATLAS Collaboration, Journal of Instrumentation **3**, 003 (2008).

[91] J. Pequenao, Event cross section in a computer generated image of the ATLAS detector, 2008, CERN-GE-0803022 01.

[92] The ATLAS Collaboration, arXiv:0901.0512 (2009).

[93] The ATLAS TileCal Collaboration, **ATL-TILECAL-PUB-2008-001** (2010).

[94] R. G. Newton, American Journal of Physics **44**, 639 (1976).

[95] E. Torrence, ATLAS data summary, `http://atlas.web.cern.ch/Atlas/GROUPS/DATAPREPARATION/DataSummary/`, 2011.

[96] N. Soni and ATLAS Collaboration, arXiv:1006.5426v1 [hep-ex] (2010).

[97] The ATLAS Collaboration, ATLAS Note **ATL-COM-DAQ-2010-013** (2010).

[98] D. O. Damazio *et al.*, ATLAS Note **ATLAS-CONF-2010-030** (2010).

[99] J. Allison, IEEE Trans. Nulc. Sci. **53**, 270 (2006).

[100] S. Agostinelli *et al.*, Nuclear Instruments and Methods in Physics Research Section A: Accelerators, Spectrometers, Detectors and Associated Equipment **506**, 250 (2003).

[101] T. Cornelissen *et al.*, ATLAS Note **ATL-SOFT-PUB-2007-007** (2007).

[102] E. Bouhova-Thacker *et al.*, ATLAS Note **ATL-INDET-PUB-2009-001** (2009).

[103] K. Prokofiev and f. t. A. Collaboration, arXiv:1010.1483v1 [physics.ins-det] (2010), Presented at Hadron Collider Physics Symposium 2010, Toronto, Canada.

[104] P. Billoir and S. Qian, Nuclear Instruments and Methods in Physics Research Section A: Accelerators, Spectrometers, Detectors and Associated Equipment **311**, 139 (1992).

[105] G. P. Salam, arXiv:0906.1833v2 [hep-ph] (2009).

[106] The ATLAS collaboration, ATLAS Note **ATLAS-CONF-2010-056** (2010).

[107] The ATLAS Collaboration, ATLAS Note **ATLAS-CONF-2011-032** (2011).

[108] The ATLAS collaboration, ATLAS Note **ATLAS-CONF-2011-035** (2011).

[109] B. Heinemann, F. Hirsch, and S. Strandberg, ATLAS Note **ATLAS-CONF-2010-042** (2010).

[110] The ATLAS collaboration, ATLAS Note **ATLAS-CONF-2010-099** (2010).

[111] A. Canepa *et al.*, ATLAS Note **ATL-PHYS-INT-2010-135** (2010).

[112] Cabrera Urban *et al.*, ATLAS Note **ATL-COM-PHYS-2011-132** (2011).

[113] The ATLAS Collaboration, ATLAS Note **ATLAS-COM-CONF-2010-062** (2010).

[114] The ATLAS Collaboration, ATLAS Note **ATLAS-COM-CONF-2011-034** (2011).

[115] A. Hoecker, B. Heinemann, and E. Torrence, Luminosity and run statistics plots for 2010 beam data, `https://twiki.cern.ch/twiki/bin/view/AtlasPublic/RunStatsPublicResults2010`, 2010.

[116] N. Benekos *et al.*, ATLAS Note **ATL-PHYS-INT-2010-131** (2010).

[117] M. Aharrouche *et al.*, ATLAS Note **ATL-PHYS-INT-2010-126** (2010).

[118] The ATLAS Collaboration, ATLAS Note **ATLAS-CONF-2010-038** (2010).

[119] B. Alvarez *et al.*, ATLAS Note **ATL-PHYS-INT-2010-133** (2010).

[120] The D0 Collaboration, Physical Review D **76**, 092007 (2007), arXiv:0705.2788v1 [hep-ex].

[121] B. Abi *et al.*, ATLAS Note **ATL-PHYS-INT-2010-139** (2010).

[122] Acharya *et al.*, ATLAS Note **ATL-PHYS-INT-2010-136** (2010).

[123] J. Arguin *et al.*, ATLAS Note **ATL-PHYS-INT-2010-134** (2010).

[124] S. Frixione, E. Laenen, P. Motylinski, and B. R. Webber, Journal of High Energy Physics **2006**, 092 (2006).

[125] J. Campbell, R. K. Ellis, and F. Tramontano, Physical Review D **70**, 094012 (2004), arXiv:hep-ph/0408158v1.

[126] N. Kidonakis, 1005.3330 (2010), PoS DIS2010:196,2010.

[127] A. Shibata *et al.*, ATLAS Note **ATL-COM-PHYS-2009-334** (2009).

[128] The ATLAS Top Working Group, ATLAS Note **ATL-PHYS-INT-2010-138** (2010).

[129] T. A. collaboration, ATLAS Note **ATL-PHYS-PUB-2009-086** (2009).

[130] L. Demortier, CDF Note **8662** (2007).

[131] H. Abreu *et al.*, ATLAS Note **ATL-PHYS-INT-2010-137** (2010).

[132] N. Benekos *et al.*, ATLAS Note **ATL-COM-PHYS-2011-123** (2011).

[133] T. A. collaboration, ATLAS Note **ATLAS-CONF-2011-046** (2011).

[134] J. Stillings, FlavourTagging analysis 16, `https://twiki.cern.ch/twiki/bin/view/AtlasProtected/Analysis16`, 2011.

[135] M. Bosman *et al.*, ATLAS Note **ATL-COM-PHYS-2011-111** (2011).

[136] The D0 Collaboration, D0 Note **D0 note 6037-CONF** (2010).

[137] The D0 Collaboration *et al.*, Physical Review D **67**, 012004 (2003).

[138] The CDF Collaboration *et al.*, Physical Review D **64**, 032002 (2001).

[139] The CDF Collaboration, CDF Note **Conf. Note 10137** (2010).

[140] The CMS Collaboration, arXiv:1106.0902v1 [hep-ex] (2011).

[141] Carli, CERN Notes **CERN-ATS-2011-005** (2011).

[142] CERN Press Office, Council appoints CERNs next director general, `http://public.web.cern.ch/press/pressreleases/Releases2007/PR10.07E.html`, 2007.

[143] The H1 Collaboration, The European Physical Journal C - Particles and Fields **30**, 1 (2003), arXiv:hep-ex/0304003v1.

[144] A. C. Benvenuti *et al.*, Physics Letters B **223**, 485 (1989).

[145] M. Arneodo *et al.*, Physics Letters B **364**, 107 (1995), arXiv:hep-ph/9509406v2.

[146] M. Whalley and J. Bentham, The durham HepData project, `http://hepdata.cedar.ac.uk/`, 2010.

[147] The ATLAS Collaboration, arXiv:1101.2185v1 [hep-ex] (2011).

Acknowledgment

An erster Stelle möchte ich meinen Eltern danken, die mich in jeglicher Hinsicht unterstützt, ermutigt und korrigiert haben. Ihr habt Vieles einfacher gemacht, was ohne euch wohl gar nicht möglich gewesen wäre.

Muchas gracias a mi supervisor Aurelio. Fuiste una fuente de inspiración y ha sido un placer y un honor trabajar contigo.

También me gustaría agradecer al Top Group del IFAE. Aurelio, Clément, Jordi, Lluisa, Luca y Martine, muchas gracias por hacer esta tesis posible y por compartir estos años de investigación conmigo.

Imma, moltes gràcies per a supervisar-me al principi i per a ajudar-me també al final.

Within the ATLAS collaboration a lot of people helped to make this dissertation possible and deserve my deep thanks. Special thanks to everybody in the Top Working Group for pushing forward this analysis towards publication.

Y que hubieran sido esos años sin mis compañeros del despacho?! Carlos, gracias por tu apoyo. . . y los mapas. Estel, moltes gràcies per crear tots aquests programes amb noms tan freakis amb mi. Jordi, merci per a totes aquestes rialles. Chiara, grazie mille per tutte le torte.. senza cioccolato. Y Garo, guapísimo, gracias por mostrarme que emacs no es inútil.

Danke auch an die Jungs vom Lindenplaya, die immer für Senf und Musik gesorgt haben. BAM!

Eskerrik asko nire euskara taldeari deskonektatzen laguntzeagatik.. hori da!

Eskerrik asko nire family-ari: Gerard, Uxue, Urko eta Ixa. Bartzelonara iritsi nintzenetik, bizitza ez litzateke berdina izango zuek gabe. Gerard, quants quilòmetres hem fet junts?

Schwesti! Danke fuer die Europa-Flatrate und für's Zuhören. Schön, dass es dich gibt.

Eskerrik asko Aratz nirekin zure bizitza konpartitzeagatik. Azkenean Bartzelonan elkarrekin gaude eta ez dakit zer izan daitekeen hori baino hobea. Mila esker beti laguntzeagatik, zure pazientzia mugagabeagatik eta guztiagatik! Izugarri maite zaitut!